Ultrafast vibrational dynamics of nucleobases and base pairs in solution and DNA oligomers

DISSERTATION

zur Erlangung des akademischen Grades

DOCTOR RERUM NATURALIUM

(Dr. rer. nat.)

im Fach Physik

eingereicht an der

Mathematisch-Naturwissenschaftlichen Fakultät

der Humboldt-Universität zu Berlin

von

Dipl.-Phys. Christian Greve

Präsident der Humboldt-Universität zu Berlin

Prof. Dr. Jan-Hendrik Olbertz

Dekan der Mathematisch-Naturwissenschaftlichen Fakultät

Prof. Dr. Elmar Kulke

Gutachter:

1. Prof. Dr. Thomas Elsässer
2. Prof. Dr. Oliver Benson
3. Prof. Dr. Wolfgang Zinth

Eingereicht am 10.06.2014
Tag der Disputation: 17.09.2014

Abstract

This work contributes to a deeper understanding of the vibrational potential energy surface and vibrational and structural dynamics on the femto- to picosecond time scale of nucleobases, base pairs, and hydrated DNA. Linear, nonlinear ultrafast pump-probe and two-dimensional photon echo infrared spectroscopy combined with exciton model and ab initio calculations are used to analyze vibrational NH stretching excitations of the DNA components at different levels of molecular complexity.

Monomeric adenosine and thymidine nucleobases in nonpolar solution reveal the magnitude of mechanical couplings and vibrational anharmonicities in the absence of hydrogen bonding. This allows to determine the eigenstate wavefunctions of the single- and double-excited states in adenosine as delocalized normal and partly localized modes, respectively. Population lifetimes of the NH stretching excitations in adenosine are determined as several picoseconds, while the single NH stretching mode of thymidine decays faster with a time constant of one picosecond.

The formation of interbase hydrogen bonds in adenosine-thymidine (A·T) base pairs leads to significant changes in vibrational dynamics and to highly congested vibrational line shapes. The number of A·T dimer associated bands is found to exceed the number of local NH stretching states. This is explained by anharmonic couplings to a low-frequency hydrogen bond mode and by enhanced state mixing with fingerprint combination and overtone modes (Fermi resonances), in particular involving the NH_2 bending state. A significant hydrogen bonding induced lifetime shortening to sub-picosecond values as well as an ultrafast vibrational excitation transfer are observed. The NH stretching excitations are found to be highly inhomogeneously broadened due to structural inhomogeneity, while ultrafast fluctuations in the hydrogen-bonding geometries are absent.

The study of double-helical hydrated guanine-cytosine (G·C) oligomer films in comparison to previous studies on G·C base pairs in nonpolar solution points to a significant impact of hydration already for a low level of humidity. Measurements at variable water content allow to discern the base pair NH stretching modes from the OH stretching excitations of the water shell. Weak interbase "horizontal" vibrational couplings are found, while clear indications for "vertical" intrastrand vibrational couplings are absent. At low humidity, the base pairs exhibit a high degree of structural inhomogeneity, while neither the NH stretching excitations nor the remaining water molecules show ultrafast spectral diffusion. At full hydration, vibrational interbase couplings and interbase hydrogen bonding interactions remain unchanged, but the water shell shows spectral diffusion on a time scale of 250 fs, i.e. decelerated to the case of bulk water. The water shell is found to serve as an efficient heat sink for high-energy vibrational excitations as indicated by the formation of a hot ground state on the femtosecond time scale.

As a side project, the Fermi resonance effect of the NH_2 bending overtone with fundamental NH stretching states is studied in ternary mixtures of aniline, DMSO, and CCl_4. The enhancement of Fermi resonances upon hydrogen bonding is quantitatively captured through an exciton model. Moreover, polarization-resolved 2D-IR spectroscopy is demonstrated as an important tool for the analysis of overtone spectra of molecules in solution.

Contents

1 Introduction

1.1 Hydrogen bonding and DNA

Covalent bonds and non-covalent interactions between atoms, functional groups, and ions determine the structure and function of biomolecules [1–4]. Among the non-covalent interactions, hydrogen bonding forces are probably the most important ones. A hydrogen bond represents a structural motif, where a proton is typically covalently bound to a donor atom (X) and electrostatically bound to an electronegative acceptor atom (Y), forming a X-H··Y structural motif with the H··Y distance falling below the sum of the H and Y van der Waals radii. For the most abundant class of weakly hydrogen-bonded systems, the H··Y interaction energies are around 2-30 kJ/mol (20-310 meV per bond) corresponding to typically 1-15 % of the binding energy provided by covalent bonds [5]. Intra- and intermolecular hydrogen bonds play a defining role for the secondary structure of the deoxyribonucleic acid (DNA) [1]. Hydrogen-bonded nucleobase pairs adenine-thymine and guanine-cytosine attached to two coiled backbones of repetitive sugar-phosphate units form the famous double-helix DNA structure [6]. In combination with π stacking interactions, the combined effect of numerous nucleobase-nucleobase hydrogen bonding forces is strong enough to stabilize this native double-stranded DNA structure, while the hydrogen bonding interactions are sufficiently weak to enable DNA and RNA polymerase enzymes to transiently separate the two strands during replication and transcription, respectively [4]. Hydrogen bonding ensures the complementarity of nucleobase pairing and, therefore, constitutes the central ingredient for unambiguous duplication and read-out of the genetic code given by the nucleobase sequence. The specific arrangements of hydrating water molecules have been found to be crucial for stabilization of the native DNA structure [7], replication and transcription processes [8], and the site-specific recognition of DNA by restriction enzymes [9] and other proteins [10]. The equilibrium structure of hydrated DNA has been determined with a precision of a fraction of a bond length through X-ray and neutron diffraction methods [2,11–15] and nuclear magnetic resonance (NMR) measurements [16–18].

While the time-averaged structural properties of the double-helix are fairly well understood, much less is known about the dynamic processes on the microscopic scale involving structural fluctuations and hydrogen bonding dynamics. Dynamic processes relevant to structure and function of DNA occur over time scales ranging from femtoseconds to hours. During replication of the human genome, a single polymerase enzyme synthesizes 50 base pairs per second, while the full replication of the human genome - due to the multitude of enzymes working on each chromosome - takes about 20 hours [19]. Water molecules in the first hydration shell of DNA, i.e. those water molecules directly interacting with DNA, exchange with outer shell water molecules on the pico- to nanosecond time scale [20–23], while rotational dynamics of water molecules near the DNA interface occurs within few to tens of picoseconds [24]. In the second and outer hydration shell regions of DNA, hydrogen bond breakage and (re)formation in the hydrogen-bonded water network take place on the time scale of one picosecond with fluctuations in hydrogen bond strength occurring within few tens to hundreds of femtoseconds [22,24], which is similar to the behavior of bulk water [25–29].

In order to access even the fastest of such processes, numerous methods have been developed. Multidimensional NMR methods such as nuclear Overhauser effect spectroscopy (NOESY) and nuclear magnetic relaxation dispersion (NMRD) measurements were used to unravel structural dynamics down to time scales of hundreds of picoseconds [16–18, 30, 31]. Although the molecular

interpretation of magnetic relaxation rates rests on a rigorous theoretical foundation, it is not always straightforward due to the biomolecular complexity [18]. NMRD and NOESY methods require theoretical models to indirectly provide information on dynamical structural processes in the nano- to 100 picosecond regime, while ultrafast DNA-water dynamics are inaccessible. DNA solvation dynamics on pico- and sub-picosecond time scales, averaged over a large spatial volume, were studied by measuring the collective response of the molecular environment upon electronic excitation through time-resolved fluorescence Stokes shift (TRSS) spectroscopy with a fluorescent probe embedded into or attached to the DNA structure, where the dynamic Stokes shift directly reflects the rate of molecular reorganization of the fluorophore's environment [23,32–34]. Extracting the correct microscopic picture from the collective reorganization dynamics around the fluorophore poses a scientific challenge, often providing conflicting interpretations [23,32,35–37]. Ultrafast time-resolved X-ray diffraction techniques are promising [38–40], but are so far not capable of resolving dynamics in complex biomolecular systems. Molecular dynamics simulations have significantly contributed to an in-depth understanding of the fastest molecular structural processes [22,29,35,41], but require an experimental benchmark.

With the advent of ultrashort tunable infrared laser pulses in the last decade, time-resolved nonlinear vibrational spectroscopy with femtosecond time resolution took on a leading role for the spectroscopic observation of ultrafast structural processes of molecules in solution [42–44]. Vibrational excitations - often highly localized on a molecular subunit in contrast to electronic excitations - dynamically reflect fluctuating couplings to intra- and intermolecular degrees of freedom and, hence, constitute sensitive local probes of temporal changes in the environment. Mapping of the temporal response of vibrational marker modes to multiple ultrashort light pulses has developed into an extremely powerful technique with unprecedented time resolution for the analysis of anharmonic vibrational couplings, dephasing processes, vibrational energy redistribution and relaxation, and structural dynamics in DNA and its hydration shell [45–53]. In particular, two-dimensional vibrational spectroscopy [45, 46], which correlates the excitation frequency of a molecules with its detection frequency at a later time, provides direct insight into vibrational coupling patterns, excitation transfer and frequency fluctuation dynamics. This enables the determination of underlying line broadening mechanism and ultrafast structural dynamics even in a highly inhomogeneous molecular environment as found in DNA.

1.2 Motivation and relevant questions

The main goal of this thesis is to gain a profound understanding of vibrational couplings and vibrational and structural dynamics of double-helical DNA in combination with its hydration shell. The complexity of vibrational line shapes and dynamics in DNA arises from the variety of possible coupling mechanisms such as intramolecular couplings within the DNA nucleobases, interstrand couplings between hydrogen-bonded nucleobase pairs, intrastrand couplings among vertically stacked nucleobases, and couplings to and within the surrounding hydration shell [48, 50, 52, 54–57]. The magnitudes of these couplings determine vibrational energy flow pathways and time scales of vibrational energy deactivation in DNA and contribute to the remarkable photostability of DNA. Up to now, the relevance of these various contributions is not thoroughly understood. Moreover, the multitude of vibrational modes and potential coupling mechanisms in the nucleobases and DNA did not allow for an in depth understanding of vibrational spectroscopic signatures of nucleobases and DNA.

In order to quantify the impact of these different contributions on vibrational line shapes and dynamics, the isolated nucleobases in nonpolar waterfree solution are analyzed first. The results serve as a benchmark for a subsequent study of hydrogen-bonded nucleobase pairs in nonpolar waterfree solution. Afterwards, double-helical DNA oligomer films with a hydration shell of variable

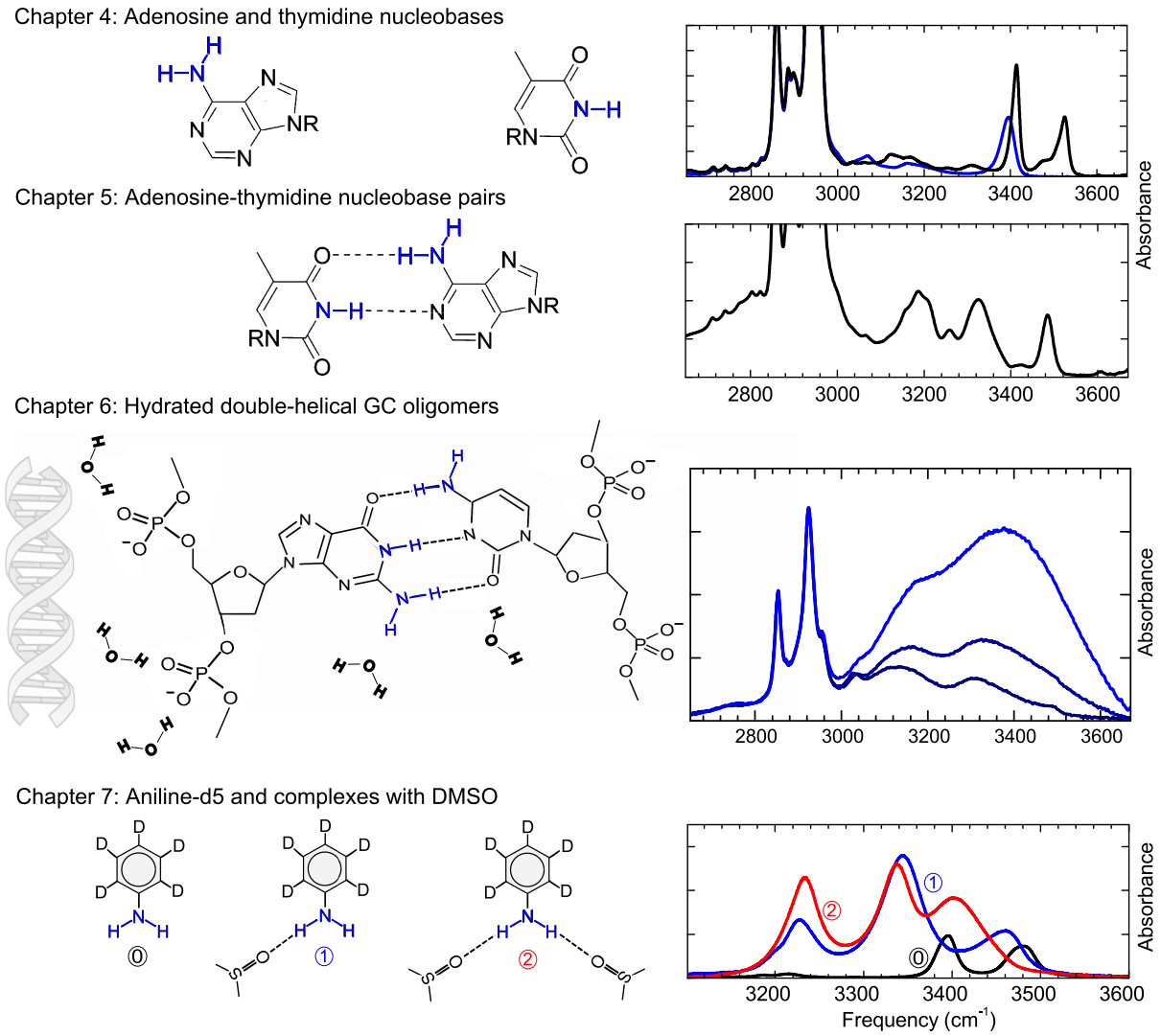

Figure 1.1: *Left: The molecular systems studied in the different chapters of this thesis from top to bottom: adenosine and thymidine monomers and adenosine-thymidine base pairs in chloroform solution, double-helical guanine-cytosine (G·C) 23-mer film at different humidity, and aniline-d5 uncomplexed and complexed with one and two DMSO molecules in CCl_4 solution. Their corresponding linear infrared spectra in the range of NH and OH stretching excitations are given on the right with the intense narrow bands at 2800-3000 cm^{-1} arising from CH stretching contributions.*

size are addressed. As a side project, we study a model system to better understand the influence of hydrogen bonding on Fermi resonances and vibrational line shapes. The thereby analyzed molecular structures of adenosine and thymidine nucleobases, adenosine-thymidine base pairs, double-helical guanine-cytosine oligomers, and complexes of aniline-d5 and DMSO are sketched in Figure 1.1. In this work, we use NH and OH stretching excitations as local probes for hydrogen bonding interactions and fluctuating intra- and intermolecular couplings in vibrational linear and ultrafast nonlinear pump-probe and two-dimensional polarization-resolved photon echo spectroscopy. Using these methods, we contribute to answers to the following major questions:

- What are the vibrational line shapes, dynamics, mechanical couplings, and anharmonicities

of NH stretching excitation in adenosine and thymidine monomer, and which is the proper eigenstate description for the single- and double-excited NH stretching states?

- Does the formation of intermolecular hydrogen bonds in adenosine-thymidine (A·T) nucleobase pairs lead to significant interbase couplings of NH stretching excitations? How does the increase in effective couplings to overtones and combination fingerprint modes and low-frequency hydrogen bond modes upon hydrogen bond formation affect vibrational line shapes, population relaxation, and the eigenstate character of NH stretching excitations in A·T pairs? Are there notable spectroscopic differences between different A·T pairing geometries?

- What is the effect of the sugar-phosphate backbone, counterions, and - in particular - a variable degree of hydration on vibrational line shapes and dynamics in double-helical guanine-cytosine (G·C) oligomers compared to the situation in isolated waterfree G·C nucleobase pairs? Is there a notable effect of vibrational couplings between stacked nucleobase pairs? What is the role of the hydration shell during vibrational relaxation, and how does the water shell around DNA behave in comparison to bulk water in terms of ultrafast structural fluctuations?

- Can the enhancement of Fermi resonances due to hydrogen bonding cause intrinsically weak overtone transitions to become as strong as allowed fundamental transitions of hydrogen-bonded NH stretching vibrations? Can we give a *quantitative* description of the Fermi resonance effect, and how does hydrogen bonding induced changes in the Fermi resonance effect impact vibrational relaxation pathways in a model system of aniline-DMSO complexes?

1.3 Outline

This work is structured as follows: In chapter 2, the underlying theory of vibrational line shapes, vibrational relaxation, and (non)linear vibrational spectroscopy using diagrammatic perturbation theory is presented and the concepts of ultrafast pump-probe and photon-echo spectroscopy are introduced. Chapter 3 deals with our experimental realizations with particular focus on the phase-resolved measurement of the absorptive nonlinear molecular response in a heterodyne-detected polarization-resolved two-dimensional photon echo experiment. Chapter 4 summarizes some aspects of the existing knowledge in the literature on vibrational and structural dynamics of DNA nucleobases and hydrated DNA, highlighting those issues that are of relevance for this work.

In chapter 5, the potential energy surface of NH stretching excitations in adenosine and thymidine nucleobases in chloroform solution is analyzed, providing intermode couplings, anharmonicities, and lifetimes of the single-excited states. Such parameters will be compared to results from quantum-chemical calculations and combined with simple excitonic model calculations to characterize the single- and double-excited NH stretching eigenstates in the picture of normal modes and local modes. The results from this chapter serve as reference for the following chapters.

In chapter 6, the adenosine and thymidine nucleobases will be studied in the presence of two interbase hydrogen bonds in chloroform solution forming A·T base pairs, where hydrogen bonding will be demonstrated to lead to significant changes in line shapes, vibrational dynamics, and the character of NH stretching eigenstates. H/D exchange experiments, two-color pump-probe measurements, and 2D-IR spectra will reveal the presence of anharmonic intra- and intermolecular couplings within NH stretching excitations and to low-frequency hydrogen bond modes, ultrafast energy transfer within the NH stretching manifold, and a prominent role of Fermi resonances for the vibrational line shapes in A·T pairs.

In chapter 7, the ultrafast 2D-IR signatures of NH and OH stretching excitations in double-helical guanine-cytosine oligomers at two different levels of hydration will be measured and com-

pared to the situation in G·C base pairs in waterfree solution, thereby providing insight into the effect of hydrating water molecules and the backbone on intra- and interbase couplings and the extend of vibrational couplings between stacked base pairs. Such measurements allow to distinguish the ultrafast dynamic signatures of water molecules in the first and second hydration shell.

In chapter 8, the hydrogen-bonding induced enhancement in the Fermi resonance effect between the fundamental NH stretching states and the NH_2 bending overtone state in tertiary mixtures of aniline, DMSO, and CCl_4 will be studied, stimulated by our conclusion about the importance of Fermi resonances for the NH stretching manifold of A·T nucleobase pairs. Thereby, more information is provided about the effect of a different degree of hydrogen bonding on a NH_2 amino group. A quantitative analysis of the Fermi resonance enhancement in oscillator strength in the linear vibrational spectrum will be provided through an excitonic model. Polarization-resolved 2D-IR spectroscopy will be demonstrated as a powerful tool to study the vibrational overtone manifold. As an outlook, we present two-color pump-probe measurements to characterize vibrational relaxation pathways in the presence and in the absence of hydrogen bonding of aniline to DMSO. This thesis will be concluded with a summary in chapter 9.

2 Time-resolved nonlinear infrared spectroscopy

Linear infrared spectroscopy provides time-averaged vibrational line shapes that give very limited insight into the the specific broadening mechanisms and underlying ultrafast processes such as vibrational relaxation and dephasing dynamics or structural fluctuations. In contrast, the nonlinear interaction of multiple optically coherent ultrashort light pulses with the ensemble of oscillators allows to follow even the fastest vibrational and structural processes in real time. Here the manipulation of quantum coherent molecular states is analyzed by measuring the emitted nonlinear signal field following the induced macroscopic coherent polarization of the molecular ensemble.

In this chapter, the concepts relevant for an understanding of the experimental results of this thesis will be presented. After introducing anharmonic couplings as the basis for vibrational anharmonicity, the effect of coupling on the wave function character of vibrational modes as local or normal modes will be analyzed. The theoretical framework of ultrafast (non)linear spectroscopy is introduced, based on perturbation theory to propagate the density matrix. Redfield theory and the Kubo model are presented to incorporate and explain the physical basis of vibrational relaxation and dephasing. The rest of the chapter is devoted to the properties and measurement of the third order nonlinear response in ultrafast pump-probe and three-pulse photon echo spectroscopy. Special focus is put onto the manifestation of molecular couplings in 2D spectra and the manipulation of the nonlinear response via polarization control of the excitation light pulses.

2.1 Vibrational molecular couplings

Vibrational couplings between intra- and intermolecular modes define structural, dephasing and excitation relaxation dynamics. Their characterization is therefore the basis of any in-depth understanding of molecular dynamics.

In principle, all internal vibrational and rotational degrees of freedom in a large N-atomic molecule can be analyzed by calculating the 3N-6 dimensionless internal vibrational modes Q_i in a Taylor expansion of the potential energy surface leading to the Hamiltonian:

$$H = \sum_{i}^{3N-6} \frac{p_i^2}{2m_i} + \sum_{i\neq j}^{3N-6} \frac{1}{2} G_{ij} p_i p_j + V_0 + \sum_{i}^{3N-6} f_i^{(1)} Q_i + \frac{1}{2!} \sum_{ij}^{3N-6} f_{ij}^{(2)} Q_i Q_j + \frac{1}{3!} \sum_{ijk}^{3N-6} f_{ijk}^{(3)} Q_i Q_j Q_k + \frac{1}{4!} \sum_{ijkl}^{3N-6} f_{ijkl}^{(4)} Q_i Q_j Q_k Q_l + ... \tag{2.1}$$

with $f^{(n)}_{k_1 k_2 ... k_n} = \left(\frac{\partial^n V}{\partial Q_{k1} \partial Q_{k2} ... \partial Q_{kn}} \right)_0$ the force constant of nth order, and G_{ij} the Wilson G-matrix elements [58–60][a]. If higher expansion terms than second order are neglected in the harmonic oscillator approximation, vibrational excitations are described as delocalized collective motions,

[a] The molecular potential energy is best described using the 3N-6 *internal coordinates* S_t, e.g. curvilinear internal coordinates specified by bond lengths and angles, which are separated from the translational and rotational center of mass motion of the molecule. In contrast, the kinetic energy is best described in the 3N *cartesian displacement coordinates* ξ_i of the N atoms. Both coordinates are related by a matrix B, whose coefficients B_{ti} depend on the

which are independent from each other (normal modes). Anharmonic correction terms in the Hamiltonian (2.1) will be particularly large in the presence of hydrogen-bonding. They can be treated perturbatively in the eigenstate representation of the harmonic oscillator normal modes and the energy levels of the vibrational eigenstates in the case of purely quadratic anharmonicity in the absence of vibrational degeneracy are obtained as [61–63]:

$$\frac{E(n_1, n_2, .., n_k)}{\hbar} = \sum_i \omega_i (n_i + \frac{1}{2}) + \sum_{i \leq j} x_{ij} (n_i + \frac{1}{2})(n_j + \frac{1}{2}) \tag{2.5}$$

with ω_i the normal mode frequency of mode i, n_i the number of quanta in that mode, x_{ii} the diagonal anharmonicity and x_{ij} the intermode anharmonicity parameters of the coupled vibrations $\omega_{i,j}$. The anharmonicity parameters x_{ij} are related to the corresponding cubic and quartic derivatives (anharmonic couplings) of the potential energy surface in a complex way [62,64,65]) and typically have negative values. There are two effects of vibrational anharmonicity: first, in the presence of anharmonic coupling between a mode i and k the 01 and 12 transition frequencies of mode i become dependent on the degree of excitation n_k in mode k. The frequency shifts depend on the magnitude of their intermode off-diagonal anharmonicity x_{ik} and the two modes i and k are said to be coupled to each other. Second, even in the vibrationally cold molecule the transition frequencies ω_{01} and ω_{12} will be downshifted compared to its harmonic values due to diagonal and off-diagonal anharmonicity, and energetic level spacing reduces with higher quantum numbers:

$$\begin{aligned} \omega_{01}(n_k) &= \omega_1 + 2x_{11} + \sum_{k \leq i} x_{1k}(n_k + \frac{1}{2}) \\ \omega_{12}(n_k) &= \omega_{01}(n_k) + 2x_{11} \end{aligned} \tag{2.6}$$

The difference D_{ii} between the ω_{12} and ω_{01} transition frequency of mode i is given by twice the intramode anharmonicity x_{ii}, while the combination mode with one quantum both in mode i and k is downshifted by a value D_{ik} given by the off-diagonal anharmonicity x_{ik} compared to the sum of the fundamental transitions E_{10} and E_{01}. The anharmonic shifts are sketched in Figure 2.1.

The normal mode concept was originally developed for largely delocalised excitations in highly coupled solid state systems [66]. The validity of this approach in smaller molecular system with several rather isolated, diverse chemical subunits becomes questionable [67,68]. Also the molecular complexity addressable in this way is limited unless high molecular symmetry allows for simplifications based on group theory. The question arises under what molecular parameters and degree

molecular equilibrium geometry:

$$S_t = \sum_i^{3N} B_{ti} \xi_i \tag{2.2}$$

with t∈{1,2...,3N-6}. The Wilson G matrix elements can then be defined as:

$$G_{tt'} = \sum_i^{3N} \frac{1}{m_i} B_{ti} B_{t'i} \tag{2.3}$$

with m_i the effective mass of the internal coordinate S_i. This allows to write the vibrational kinetic energy T in the most general way as

$$T = \sum_{tt'} \frac{1}{2} G_{tt'} p_t p_{t'} = \sum_t \frac{p_t^2}{2m_t} + \sum_{t \neq t'} \frac{1}{2} G_{tt'} p_t p_{t'} \tag{2.4}$$

with P_t the momentum conjugate to the internal coordinate S_t. When the internal coordinates S_t and $S_{t'}$ are mutually orthogonal on one another, then $G_{tt'}$ will be zero for t≠t'. In general, this does not have to be the case, and there can be a coupling between the momenta of different internal coordinates p_i and p_j. In the cartesian coordinate system, the momenta are all mutually orthogonal, and the kinetic energy term (2.4) reduces to the well-known equation $T = \sum p_i^2/(2m_i)$.

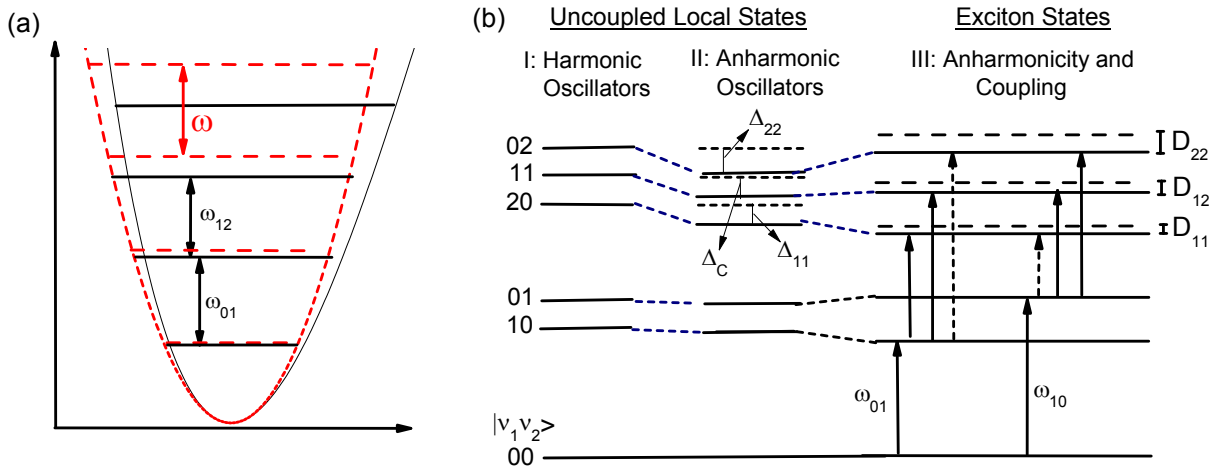

Figure 2.1: *(a) Effects of anharmonic couplings on the vibrational level scheme of a selected mode. (b): Two coupled anharmonic oscillators forming a six-level system of zero-, one- and two quantum states labelled $|\upsilon_1\upsilon_2>$, with υ_1 and υ_2 the number of quanta in the two modes. In the absence of anharmonicity and coupling, the energies of the two-exciton states are the sum of the energies of the one-exciton states (I). Anharmonicity leads to a downshift in single- and especially double-excited states, indicated by the local mode diagonal Δ_{11}, Δ_{22} and combination tone anharmonicity Δ_C (II). The presence of both intermode coupling and anharmonicity leads to additional changes in eigenstate energies (III). The energy differences between the 0-1 and 1-2 transition frequencies between the excitonic states are specified by the diagonal D_{11}, D_{22} and the off-diagonal D_{12} anharmonicities. The degree of normal mode and local mode character in the exciton states depends on their intermode coupling, anharmonicity parameters and the energetic separation of the uncoupled local states.*

of excitation an eigenstate description in terms of highly localized excitations in weakly coupled vibrational modes is valid.

A system of two near degenerate coupled oscillators including the double excited states can be described by the Hamiltonian [69]

$$H = \hbar \left(\sum_{n=1}^{2} \omega_m a_m^\dagger a_m + J[a_1^\dagger a_2 + a_2^\dagger a_1] + \Delta_{11} a_1^\dagger a_1^\dagger a_1 a_1 + \Delta_{22} a_2^\dagger a_2^\dagger a_2 a_2 + 2\Delta_C a_1^\dagger a_2^\dagger a_1 a_2 \right) \tag{2.7}$$

with $a_m^\dagger / a_m$ the creation/annihilation operators for excitation in mode m, J the bilinear coupling, and Δ_{mm} and Δ_C the anharmonic downshifts of the over- and combination tones. This Hamiltonian is obtained by truncating the Taylor expansion of the potential energy after fourth order, transforming the internal coordinates Q_i into the bosonic creation ($a^\dagger$) and annihilation (a) operators [70] with $Q_i \propto (a_i + a_i^\dagger)$, and retaining only the quantum conserving terms. Therefore, the excitonic Hamiltonian provides a good description only for coupled nearly degenerate states, while otherwise higher order Taylor expansion terms as well as non-quantum conserving terms need to the included. In the local mode basis {|01>, |10>, |02>, |20>, |11>} ($|mn\rangle$ indicates m quanta in mode 1 and n quanta in mode 2), the excitonic Hamiltonian is written as:

$$H = \hbar \begin{pmatrix} \omega_1 & J & & & \\ J & \omega_2 & & & \\ & & 2\omega_1 - \Delta_{11} & 0 & \sqrt{2}J \\ & & 0 & 2\omega_2 - \Delta_{22} & \sqrt{2}J \\ & & \sqrt{2}J & \sqrt{2}J & \omega_1 + \omega_2 - \Delta_C \end{pmatrix} \tag{2.8}$$

For the single excited non-interacting states {|01>, |10>}, the time-independent vibrational off-diagonal coupling term J will induce a certain degree of mode mixing of the local eigenstates depending on the ratio of coupling strength to energy separation in the uncoupled local modes. Diagonalisation of the one-exciton manifold provides the new eigenvalues $E_{\pm}$ for the coupled system [70]:

$$E_{\pm} = \bar{E} \pm \sqrt{\delta^2 + J^2} \qquad \text{with} \qquad \bar{E} = \hbar\frac{\omega_1 + \omega_2}{2} \qquad \text{and} \qquad \delta = \hbar\frac{\omega_1 - \omega_2}{2} \tag{2.9}$$

with the corresponding new eigenvectors given as

$$\begin{aligned} |\Psi_+\rangle &= cos\left(\frac{\Theta}{2}\right) e^{-i\frac{\varphi}{2}} |01\rangle + sin\left(\frac{\Theta}{2}\right) e^{i\frac{\varphi}{2}} |10\rangle \\ |\Psi_-\rangle &= -sin\left(\frac{\Theta}{2}\right) e^{-i\frac{\varphi}{2}} |01\rangle + cos\left(\frac{\Theta}{2}\right) e^{i\frac{\varphi}{2}} |10\rangle \end{aligned} \tag{2.10}$$

and the angles Θ and φ defined by

$$tan(\Theta) = \frac{J}{\delta} \qquad \text{and} \qquad J_{12} = J_{21} e^{i\varphi} \ . \tag{2.11}$$

In the case of weak coupling ($\frac{J}{\delta} << 1$), the mixing angle Θ is close to zero, indicating negligible mode mixing. The unperturbed modes $\{|01>, |10>, \}$ are still the correct eigenfunctions, being localized along the corresponding bond axis. In the contrary situation of the coupling J being much bigger than the energy gap between the unperturbed eigenenergies, significant mode mixing will occur. In this case the symmetric and asymmetric combinations of the unperturbed eigenfunctions are the new highly delocalised normal mode eigenfunctions where the sign of the coupling J determines their respective energetic position.

The intensities of vibrational transitions are related to their corresponding transition dipole matrix elements. The nuclear dipole moment is expanded in the internal local coordinates Q_i:

$$\mu = \mu_0 + \sum \left(\frac{\partial \mu}{\partial Q_i}\right)_0 Q_i + \sum \left(\frac{\partial^2 \mu}{\partial Q_i \partial Q_j}\right)_0 Q_i Q_j + ... \tag{2.12}$$

with μ_0 the permanant dipole moment. The oscillator strength of a certain vibrational transition along a local coordinate Q_i with an eigenstate change $|\nu> \rightarrow |\nu'>$ is dependent on the overlap integral $<\nu|\mu(Q_i)|\nu'>$. Truncation of the dipole moment at the linear order gives:

$$\left\langle \nu|\mu(Q_i)|\nu' \right\rangle = \mu(Q_i) \left\langle \nu|\nu' \right\rangle + \left(\frac{\partial \mu}{\partial Q_i}\right) \left\langle \nu|Q_i|\nu' \right\rangle \tag{2.13}$$

The first term is zero for orthogonal vibrational states, and the second term specifies the oscillator strength. For a linear dipole moment function, the symmetry of the harmonic oscillator eigenstates leads to the allowance of only single-quantum transitions $\Delta\upsilon = \pm 1$ in the harmonic case due to the $<\nu|Q_i|\nu'>$ term. However, higher orders in the Taylor expansion (2.12) as well as deviations from the harmonic oscillator eigenstates in the presence of an anharmonic potential may lead to weak allowance of multi-quantum overtone and combination tone transitions. Their intensities decrease with increasing $\Delta\upsilon = \upsilon' - \upsilon$.

The transition dipole moments of the mixed states in equation (2.10) are given as linear combinations of the two local uncoupled transition dipoles and transform identically to the decoupled eigenstates in the presence of coupling [69]. Therefore, the knowledge of the mixing angle Θ also reveals the orientation of the new transition dipole moments and allows for a rough calculation of the corresponding linear IR spectral intensity ($\propto \mu^2$). Any vibrational mode coupling will lead to a transfer in oscillator strength. This may have particularly drastic results if a dipole-allowed

fundamental transition is anharmonically coupled to a close to resonant, harmonically forbidden overtone transition. The concomitant enhancement in oscillator strength of the dark state due to mode mixing is known as the Fermi resonance effect. The often unexpected occurrence of highly absorbing overtone bands modifies vibrational line shapes and may lead to erroneous assignments of vibrational bands. Fermi resonances will be revealed as a crucial ingredient in the understanding of the NH stretching mode pattern in DNA nucleobase pairs in chapter 6. In chapter 8, we will give a quantitative description of the impact of hydrogen bonding on the degree of Fermi resonance enhancement in vibrational overtone transitions.

In the case of degenerate local states with $\omega_1 = \omega_2 =: \omega_0$, the single excited modes are given as asymmetric and symmetric eigenstates. In this case, the two-exciton Hamiltonian (2.8) in the local mode basis $\{|02>, |20>, |11>\}$ is given as:

$$H^{(2)} = \hbar \begin{pmatrix} 2\omega_0 - \Delta_0 & 0 & \sqrt{2}J \\ 0 & 2\omega_0 - \Delta_0 & \sqrt{2}J \\ \sqrt{2}J & \sqrt{2}J & 2\omega_0 - \Delta_C \end{pmatrix} \quad . \tag{2.14}$$

Here $\Delta_{11} = \Delta_{22} =: \Delta_0$ is the identical diagonal anharmonicity for both oscillators. The new eigenvalues of the double-excited states are obtained by diagonalisation, which yields [69]:

$$\begin{aligned} &E_{20} = 2\omega_0 - \frac{\Delta_0 + \Delta_C}{2} + \frac{2J}{sin\theta}; \qquad E_{11} = 2\omega_0 - \Delta_0; \qquad E_{02} = 2\omega_0 - \frac{\Delta_0 + \Delta_C}{2} - \frac{2J}{sin\theta} \\ &\text{with the mixing angle} \qquad \theta = arctan\left(\frac{4J}{\Delta_0 - \Delta_C}\right) \end{aligned} \tag{2.15}$$

with the corresponding eigenstates:

$$\begin{aligned} |\Psi_{20}\rangle &= sin(\theta/2)\,|1,1\rangle - \frac{cos(\theta/2)}{\sqrt{2}}\,(|2,0\rangle + |0,2\rangle) \\ |\Psi_{11}\rangle &= \frac{1}{\sqrt{2}}\,(|2,0\rangle - |0,2\rangle) \\ |\Psi_{02}\rangle &= cos(\theta/2)\,|1,1\rangle + \frac{sin(\theta/2)}{\sqrt{2}}\,(|2,0\rangle + |0,2\rangle) \end{aligned} \tag{2.16}$$

Depending on the interplay between intermode coupling J and anharmonic downshifts Δ_0 and Δ_C, the two-exciton states may be a mixture of the local mode states $\{|02\rangle, |20\rangle, |11\rangle\}$. Such mixing may lead to weak allowance of harmonically forbidden three-quantum transitions such as $|01\rangle \rightarrow |20\rangle$ or $|10\rangle \rightarrow |02\rangle$.

When a vibrational eigenstate in the single or double exciton manifold is only weakly influenced by coupling to other modes such that mode mixing is negligible, this state is said to be well described in the local mode picture [71, 72]. In the opposite case of heavy mode mixing, the normal mode picture applies. However, often the intermediate situation is found. Physical quantities, such as the vibrational eigenfrequencies obtained by diagonalisation of the Hamiltonian, are independent of the chosen basis set, since the local and normal mode descriptions are linked by a mere basis set transformation. The basis providing the "best" description is distinguished from others by having the system Hamiltonian as close to being in diagonal form as possible.

In many cases, the conventional normal mode description of molecular vibrations turned out to be inefficient at high vibrational energies. Vibrational overtone states of small to medium-sized molecules containing XH hydrogen-stretching oscillators (X= C, N, O, Si) have been studied extensively using a basis set of localized vibrational excitations. Hydrogen-stretching modes are distinguished from other vibrational modes by three facts. First, the low mass of the hydrogen atom gives a high XH stretching frequency well seperated from fundamental frequencies of other

vibrational modes. This makes XH stretching states less affected by couplings to other modes (still, Fermi resonances can play an important role). Second, of all vibrational modes, the XH stretching modes have the highest frequency shift upon hydrogen bonding and therefore provide a sensitive probe for hydrogen bonding strength and dynamics: While OH or NH stretching modes red-shift by several hundreds of wavenumbers already for medium strong hydrogen-bonds, C=O stretching modes experience typically not more than 30 cm^{-1} frequency shifts upon hydrogen-bonding. Therefore, it can be more instructive to study the hydrogen bond donor groups instead of the acceptor units. Third, the vibrational anharmonicity in XH stretching modes is high. This can be understood by assuming a Morse oscillator, where the anharmonic correction term in the potential energy is inversely proportional to the (small) reduced mass of the XH system [73]. When climbing the vibrational ladder, the increasing influence of anharmonicity has been shown to increasingly localize the higher-lying vibrational states in most cases. Several authors have analyzed the transition from normal mode to local mode behavior as a function of energy and molecular parameters [74, 75].

Still, for each molecular system the detailed situation of the vibrational eigenstates needs to be experimentally verified. Ab initio calculations, such as those implemented in quantum chemistry programs as Gaussian [76], may predict anharmonicity constants and underlying couplings only with limited reliability. In contrast, ultrafast four wave mixing pump-probe and photon echo spectroscopy can be used to extract some of these parameters experimentally through the analysis of peak positions and intensities (see section 2.5). In this thesis, the molecular wave function character of single- and double-excited NH stretching states will be analyzed in various molecular systems with and without the presence of hydrogen bonding.

2.2 Nonlinear polarization and density matrix formalism

In the following sections, the excitation of molecular states with optical driving fields as the basis of ultrafast spectroscopy will be considered. Molecules in solution are described with the statistical density operator approach. The field-induced time-dependent macroscopic polarization P is given as the ensemble-averaged expectation value of the dipole operator,

$$P(t) = \langle \mu \rho(t) \rangle \tag{2.17}$$

with ρ the density operator and $\langle\rangle$ indicating averaging over the molecular ensemble. The temporal behavior of the density operator is best analyzed in the interaction picture. Here the total Hamiltonian $H(t) = H_0 + V_I(t)$ can be separated into the time-independent system Hamiltonian H_0 and the external light-matter interaction $V_I(t) = -\vec{\mu}_I \vec{E}(t)$ in the dipole approximation. The latter term is assumed to be weak allowing a treatment in perturbation theory. While the studied molecular system is treated as a quantum system, the light field E(t) is considered classical. With $U_0(t, t_0) = e^{-\frac{i}{\hbar} H_0 (t - t_0)}$, the unitary system time evolution operator, and $\mu_I(t) = U_0(t, t_0) \mu U_0^\dagger(t, t_0)$ the transition dipole moment in the interaction picture, the density matrix in the interaction picture $\rho_I(t) = U_0^\dagger(t, t_0) \rho(t) U_0(t, t_0)$ shows a time evolution described by the Liouville-von Neumann equation:

$$\frac{d}{dt} \rho_I(t) = -\frac{i}{\hbar} \left[V_I(t), \rho_I(t) \right] \tag{2.18}$$

It can be formally solved by integration and iteratively plugging into itself to yield an expansion in terms of increasing orders of the electric fields E_i:

$$\rho_I(t) = \rho_0(t_0) + \sum \rho_I^{(n)} \tag{2.19}$$

$$\text{with} \qquad \rho_I^{(n)}(t) = \left(\frac{-i}{\hbar}\right)^n \int_{t_0}^{t} dt_n \int_{t_0}^{t_n} dt_{n-1} ... \int_{t_0}^{t_2} dt_1 \vec{E}_n(t_n)\vec{E}_{n-1}(t_{n-1})...\vec{E}_1(t_1) \\ [\vec{\mu}_{In}(t_n), [\vec{\mu}_{In-1}(t_{n-1}), ... [\vec{\mu}_{I1}(t_1), \rho_I(t_0)]] ...] \tag{2.20}$$

This yields the macroscopic polarization of the system $P(t)$ as the Taylor expansion in powers of the exciting fields E_i (t)

$$P(t) = Tr(\mu\rho(t)) = \sum P^{(n)}(t) \tag{2.21}$$

with $P^{(n)}$ the nonlinear polarization of order n:

$$P^{(n)}(t) = \left(\frac{-i}{\hbar}\right)^n \int_{t_0}^{t} dt_n \int_{t_0}^{t_n} dt_{n-1} ... \int_{t_0}^{t_2} dt_1 \vec{E}_n(t_n)\vec{E}_{n-1}(t_{n-1})...\vec{E}_1(t_1) \\ \langle\vec{\mu}(t) [\vec{\mu}_n(t_n), [\vec{\mu}_{n-1}(t_{n-1}), ... [\vec{\mu}_1(t_1), \rho(t_0)]] ...]\rangle \tag{2.22}$$

$$= \int_0^\infty d\tau_n \int_0^\infty d\tau_{n-1} ... \int_0^\infty d\tau_1 \vec{E}_n(t-\tau_n)\vec{E}_{n-1}(t-\tau_n-\tau_{n-1})...\vec{E}_1(t-\tau_n-...-\tau_1)R^{(n)}(\tau_n, \tau_{n-1}, ..., \tau_1) \tag{2.23}$$

In the last step a coordinate transform from absolute times to time intervals τ_n was employed by setting $t_1 = 0, \tau_1 = t_2 - t_1, ..., \tau_n = t - t_n$. The nonlinear polarisation of order n is obtained as the convolution of the nth order nonlinear response function with the exciting light pulses E_i. The nth order nonlinear molecular response function $R^{(n)}$ contains the full microscopic information on molecular dynamics that is necessary to describe any nth order nonlinear optical process:

$$R^{(n)}(\tau_n, ..., \tau_1) = \left(\frac{-i}{\hbar}\right)^n \Theta(\tau_1)\Theta(\tau_2)...\Theta(\tau_n) \langle\vec{\mu}(\tau_n + ... + \tau_1) \\ \times [\vec{\mu}_n(\tau_{n-1} + ... + \tau_1), ..., [\vec{\mu}_1(0), \rho(-\infty)] ...] \tag{2.24}$$

Here the Heaviside function enforces causality, ensuring the nonlinear response occurs only after the corresponding electric field interactions. Evaluation of the nested commutators for a two-level system shows the nth order nonlinear response function to be a sum of 2^n tensors that are each given by a (n+1)-point dipole correlation function. Only half of them are independent from each other, and the others are their complex conjugates.

According to the convolution in equation (2.23), a precise measurement of the nonlinear response requires the electric field envelopes to be sufficiently short compared to the dynamics of the response functions. This demand is fulfilled for the systems studied in this thesis. Some of the phase factors originating from the time evolution of the response function may cancel with the highly oscillating electric field phase factors if the laser frequencies ω_i match the transition frequencies ω_{ij} of the molecular system [77]. Such terms will change in time rather slowly and give substantial values after integration. The rotating wave approximation therefore implies that only resonant field excitations are considered.

The time-dependent macroscopic polarization P(t) will act as a source term in Maxwell´s equations:

$$\vec{\nabla}^2\vec{E}(\vec{r}, t) - \frac{1}{c^2}\frac{\partial^2\vec{E}(\vec{r}, t)}{\partial t^2} = \frac{4\pi}{c^2}\frac{\partial^2\vec{P}(\vec{r}, t)}{\partial t^2} \tag{2.25}$$

This will lead to radiation of a coherent signal field with a 90° phase shift into a specific phase matched direction $\vec{k}_S$ through macroscopic interference of the members of the ensemble. If the nonlinear medium has a slap geometry of length l with 0<z<l and the polarization wave vector

$\vec{k}_P = \sum \pm \vec{k}_i$ ($\vec{k}_i$: wave vector of light pulses E_i) fulfills $k_p l \gg 1$ and is aligned along z axis, the generated signal field E_S is obtained in the weak signal limit as [78]:

$$\Rightarrow E_S(\vec{r},t) = i\frac{2\pi\omega_S}{nc} l\vec{P}(t) sinc\left(\frac{\Delta kl}{2}\right) e^{\frac{i\Delta kl}{2}} e^{i\vec{k}_S\vec{r}-i\omega_S t} + c.c. \tag{2.26}$$

with sinc (x) = sin(x)/x, c the speed of light, n the index of refraction, and $\Delta k = |\vec{k}_S - \vec{k}_P|$ the wave-vector mismatch between the polarization wave vector $\vec{k}_P$ and the wave vector of emitted signal $\vec{k}_S$. Substantial signal emission occurs only in the phase-matched direction with $\Delta kl << \pi$. In the infrared domain, the sample size is typically much larger than the exciting wavelengths; therefore interference of the coherent third order signals from different molecules will lead to highly directed signal emission.

Double-sided Feynman diagrams

The various terms contributing to the nonlinear polarization in equation (2.23) are distinguished by their specific pathway of field induced density matrix evolution. The nonlinear response functions as well as the striking light fields are incorporated into double-sided Feynman diagrams. They allow for a compact notation and visualization of the stepwise density matrix manipulation due to absorption and emission events. Two vertical lines represent the time evolution of the bra and ket states of the density operator with the time running upwards. The manipulated populations (diagonal density matrix elements) and coherences (off-diagonal density matrix elements) are written between the two vertical lines. Excitation/de-excitation of the corresponding bra or ket states are designated through inward/outward pointing arrows while action on the left/right line means manipulation of the ket/bra state. An arrow pointing to the right implies an optical driving field with phase $e^{i\omega t + i\vec{k}\vec{r} + i\phi}$ while an arrow going to the left implies interaction with the complex conjugate field. Each light-matter interaction adds the corresponding dipole matrix element $\mu_{i,j}$ of the interaction. As each interaction on the bra side of the density matrix provides a minus sign from the commutator, each diagram carries a sign $(-1)^\beta$ with β the number of interactions working on the bra side. The finally emitted signal field is indicated by a dashed arrow which by convention always points to the right. The signal field is characterized by its wave vector $\vec{k}_S = \sum \vec{k}_i$ and frequency $\omega_S = \sum \omega_i$ which are dictated by the sum of the incident wave vectors and frequencies for the specified Feynman diagram. Only pathways that end in a population state give a nonzero signal contribution since the last step in calculating the nonlinear polarization is tracing over $\mu\rho(t)$.

In the absence of external driving fields, the coherences of the density matrix are subject to dephasing, while the population states experience relaxation and transfer. These aspects are covered in the following two sections.

Vibrational energy relaxation

Deactivation of vibrational populations in liquid-phase systems occurs via internal vibrational cascaded redistribution into anharmonically coupled intra- and intermolecular rovibrational modes typically on femto- to picosecond time scales.[b] Understanding the detailed relaxation pathway is of crucial importance for many chemical, physical and biological processes such as vision, molecular photostability, energy transport in photosynthetic light-harvesting complexes, and electron transfer processes [79–81].

For large molecular systems in solution such as those studied here, it is impossible to know the entire microscopic state. However, one is typically interested only in the detailed behavior of

[b] In contrast, radiative relaxation is negligible for purely vibrational transitions due to the ω^3-dependence of the Einstein A coeffcient for spontaneous emission.

a small vibrational subsystem H_S with local coordinates Q. The remaining degrees of freedom are attributed to a thermal bath H_B with local coordinates q which is treated with quantum statistical methods and a system bath interaction term V:

$$\begin{aligned} H &= H_S(Q) + H_B(q) + V \\ &= \sum_a \hbar\omega_a \left|a\right\rangle \left\langle a\right| + H_B + \sum_{a,\alpha} \left|a\right\rangle V_{a\alpha} \left\langle \alpha\right| \end{aligned} \tag{2.27}$$

Here {a} forms a basis of the subsystem H_S and $\{\alpha\}$ a basis of the bath Hamiltonian. The relevant degrees of freedom in the subsystem H_S are analyzed using the reduced density operator that is obtained from the full system density matrix by tracing over the bath states:

$$\sigma_{mn}(t) = Tr_B\{\rho_{mn}\} = \sum_\alpha \langle \alpha m|\rho|\alpha n\rangle \tag{2.28}$$

Regarding the dynamics in the bath as rapid compared to the relaxation dynamics of the system, the bath can be considered to stay always in equilibrium (Markovian approximation). In order to incorporate detailed vibrational relaxation effects into the nth order response functions, the density matrix elements are propagated using Redfield theory [82–84] during the field-free time intervals τ_i. For weak system-bath coupling, this interaction can be treated as a time-dependent perturbation to second order and the time evolution of the reduced density matrix elements σ_{ab} is given by the Redfield equation:

$$\frac{\partial \sigma_{ab}}{\partial t} = -i\omega_{ab}\sigma_{ab} + \sum_{cd} R_{ab,cd}\sigma_{cd} \tag{2.29}$$

Here σ_{ab} are the reduced density matrix elements and R the Redfield relaxation tensor, both written in the subsystem eigenstate basis, and ω_{ab} are the system transition frequencies. The elements of the Redfield tensor are related to the transfer rates $\Gamma_{ab,cd}$ between the diagonal and off-diagonal reduced density matrix elements. The Redfield tensor elements $R_{ab,cd}$ are given as [85–87]:

$$R_{ab,cd} = \Gamma^+_{db,ac} + \Gamma^-_{db,ac} - \delta_{db}\sum_r \Gamma^+_{ar,rc} - \delta_{ac}\sum_r \Gamma^-_{dr,rb} \tag{2.30}$$

$$\begin{aligned} \text{with} \qquad \Gamma^+_{db,ac} &= \frac{1}{\hbar^2}\int_{-\infty}^{\infty} dt\, \langle V_{db}(t)V_{ac}(0)\rangle\, e^{i\omega_{ac}t} \\ \Gamma^-_{db,ac} &= \frac{1}{\hbar^2}\int_{-\infty}^{\infty} dt\, \langle V_{db}(t)V_{ac}(0)\rangle\, e^{i\omega_{db}t} \\ V_{ab}(t) &= e^{iH_Bt/\hbar}V_{ab}e^{-iH_Bt/\hbar} \end{aligned} \tag{2.31}$$

Here $V_{ab}(t)$ is a matrix element of the coupling operator in the basis of the subsystem H_S in the Heisenberg representation, where the time dependency arises from coupling to fluctuating bath modes. $\langle\rangle$ indicates averaging over the bath states, ω_{ab} is the energy gap between states in H_S, and δ_{ab} the Kronecker delta. The tetradically notated Redfield tensor elements describe both population relaxation ($R_{aa,aa}$) and transfer ($R_{aa,bb}$) as well as coherence relaxation ($R_{ab,ab}$) and transfer ($R_{ad,cd}$). The transition rates are obtained by Fourier transformation of the bath-averaged two-point interaction correlation functions evaluated at ω_{ab} [85,88,89]. This is the time-domain version of Fermi´s Golden Rule. These interaction correlation functions can, for example, be calculated using classical molecular dynamics simulations, which sample a huge number of trajectories to extract the variable interaction force constants.

Evaluating the equations (2.31) and (2.30) gives the master equation, which describes the net change of population in a certain state:

$$\begin{aligned} \frac{\partial \sigma_{aa}(t)}{\partial t} &= \sum_{b \neq a} w_{ab}\sigma_{bb}(t) - \sum_{k \neq a} w_{ka}\sigma_{aa}(t) \\ \text{with} \qquad w_{ab} &= -R_{aa,bb} = \frac{1}{\hbar^2}\int_{-\infty}^{\infty} dt\, \langle V_{ba}(t)V_{ab}(0)\rangle\, e^{i\omega_{ba}\tau} \end{aligned} \tag{2.32}$$

Fluctuating system-bath couplings leading to fluctuating intramolecular interaction terms ("off-diagonal disorder") form the basis of any energy relaxation, and decoherence.

Vibrational dephasing

The dephasing of vibrational coherences in the absence of external optical driving fields results from time-dependent modulations of the potential energy surface due to fluctuating intra- and intermolecular interactions V with the thermally populated bath modes. Provided the system-bath interactions are a weak perturbation, the fluctuations $\delta\omega_{01}(t)$ in vibrational transition frequencies around an ensemble-averaged value ω_{01} will be small and the system´s quantum state remains unchanged. After coherent excitation of the dipole oscillators in the ensemble, variations in their individual frequencies will lead to dephasing of their corresponding ensemble-averaged vibrational coherences.

A basic phenomenological description of decoherence was given by Bloch [90] that incorporates the bath modes in a statistical approach to define a time-independent T_2 relaxation time for damping of coherences. It is applicable when there is a clear separation in time scales between the system dynamics and the bath dynamics. For molecular solution-phase systems studied in this thesis, vibrational dynamics in the system occur on multiple time scales ranging from femtoseconds to seconds, which makes the Bloch approach inadequate.

An advanced model is obtained by considering the linear response function following the Feynman diagram in Figure 2.3 (a). For a transition dipole moment independent of the nuclear bath coordinates Q (Condon approximation), $R^{(1)}$ is given as:

$$R^{(1)}(t) = \langle \mu_{01}(t)\mu_{10}(0)\rho(-\infty)\rangle = i\mu_{01}^2 e^{-i\omega_{01}t}\left\langle exp\left(-i\int_0^t \delta\omega_{01}(\tau)d\tau\right)\right\rangle \tag{2.33}$$

with $\langle\rangle$ indicating the ensemble average over all excited oscillators. If the transition frequency fluctuations follow Gaussian statistics, the ensemble-averaged exponential term can be calculated exactly by truncating the expansion of the ensemble-averaged exponential term in orders of $\delta\omega_{01}$ after second order (second order cumulant approximation [78]). Gaussian fluctuation dynamics are typically justified according to the central limit theorem due to the high degree of statistically fluctuating and interacting bath degrees of freedom. This allows the introduction of the line shape function g(t) [78] for a system in equilibrium:

$$\left\langle exp\left(-i\int_0^t \delta\omega_{01}(\tau)d\tau\right)\right\rangle = e^{-g(t)} \qquad \text{with} \qquad g(t) = \frac{1}{2}\int_0^t\int_0^{\tau'} d\tau' d\tau'' \overbrace{\langle \delta\omega_{01}(\tau'')\delta\omega_{01}(0)\rangle}^{C(\tau'')} \tag{2.34}$$

The two-point frequency fluctuation correlation function (FFCF) $C(\tau)$ describes the degree of correlation between molecular transition frequencies for two different points in time. A prominent analytical approach for the description of $C(\tau)$ was given by Kubo [91]:

$$C(t) = \Delta\omega^2 e^{-\frac{t}{\tau_C}} \tag{2.35}$$

It assumes a mono-exponential decay with the correlation time τ_C that starts from an initial value at t = 0 given by the variance of the frequency fluctuations $\Delta\omega^2$. This yields the line shape function g(t), which can be considered in two limiting cases:

$$\begin{aligned} g(t) =& \Delta\omega^2\tau_C^2\left(e^{-\frac{t}{\tau_C}} - 1 + \frac{t}{\tau_C}\right) \\ =& \begin{cases} \Delta\omega^2\tau_C t & \text{for} \quad \tau_C\Delta\omega \ll 1 \quad (1) \text{ homogeneous limit} \\ \frac{\Delta\omega^2 t^2}{2} & \text{for} \quad \tau_C\Delta\omega \gg 1 \quad (2) \text{ inhomogeneous limit} \end{cases} \end{aligned} \tag{2.36}$$

(1): For fast frequency modulations the FFCF $C(t)$ shows a delta-like behavior $C(t) = \frac{\delta(t)}{T_2^*}$ with T_2^* the pure dephasing time. This leads to a Lorentzian absorption line shape with a FWHM of $\Delta\nu = 1/(\pi T_2^*)$ that is smaller than the frequency fluctuation amplitude (motional narrowing). The finite T_1 population lifetime gives an additional contribution to dephasing for an isolated vibrational two-level system, since in the density matrix a relaxation of diagonal states is unavoidably connected to a decay in the off-diagonal components [46]:

$$\frac{1}{T_2} = \frac{1}{2T_1} + \frac{1}{T_2^*} \tag{2.37}$$

(2): For slow frequency modulations $C(t) = \Delta\omega^2$ is constant providing a Gaussian line shape with a FWHM given by the frequency fluctuation amplitude $\Delta\omega$. The band shape directly reflects the static inhomogeneity of transition frequencies within the molecular ensemble.

For hydrogen bonded systems, inhomogeneous broadening typically arises from variations in hydrogen bond strength, structure, and the local environment around the vibrational chromophores. Energy gap fluctuations can sometimes occur on time scales comparable to the femtosecond to picosecond range typically covered by ultrafast spectroscopic experiments, allowing for direct observation of gradual frequency shifts (spectral diffusion). Vibrational dephasing dynamics dictate the linear absorption spectra:

$$\sigma(\omega) = \frac{1}{2\pi} Re \int_{-\infty}^{\infty} dt e^{i(\omega-\omega_{01})t - g(t)} \tag{2.38}$$

Inversion of the above equation yielding the line shape function g(t) gives only poor results in the presence of experimental noise. In contrast, time-resolved spectroscopic approaches allows one to directly follow frequency fluctuation dynamics and population and phase relaxation via pump-probe and 2D photon echo spectroscopy.

2.3 Vibrational line shapes in the presence of hydrogen bonding

The formation of a hydrogen bond significantly affects vibrational line shapes and dynamics, in particular those of XH stretching modes. Most prominent is a redshift of the XH stretching frequency upon formation of a XH··Y hydrogen bond, which results from a softening in the covalent X-H bond due to a reduction in the harmonic force constant. The hydrogen bonding induced polarization of the electron density distribution around the XH molecular motif leads to changes in the electron-electron and electron-core interaction terms, which - according to the Born-Oppenheimer picture [92] - affects the molecular potential energy surface, increases vibrational anharmonicity and, hence, reduces the energy separation of the vibrational ground and first excited states.

Theory predicts that hydrogen bond formation leads to anharmonic coupling between the high-frequency XH stretching mode (local coordinate q, momenta p, and reduced mass m) and the low-frequency X-Y hydrogen bond mode (local coordinate Q, momenta P, and reduced mass M) [93].

Assuming an anharmonic coupling term between two harmonic oscillators, a high-frequency XH stretching and low-frequency hydrogen bond mode, and neglecting bilinear intermode coupling, kinetic energy coupling terms, and higher order expansion terms, the XH··Y system can be described by the Hamiltonian:

$$\begin{aligned} H(Q,q) =& \frac{p^2}{2m} + \frac{1}{2}m\omega^2 q^2 + \frac{P^2}{2M} + \frac{1}{2}M\omega^2 Q^2 + KQq^2 \\ =& \frac{p^2}{2m} + \frac{1}{2}m\omega_{eff}^2 q^2 + \frac{P^2}{2M} + \frac{1}{2}M\omega^2 Q^2 \\ \text{with} \qquad & \omega_{eff}(Q) = \omega\sqrt{1 + Q\frac{2K}{m\omega^2}} \approx \omega + Q\frac{K}{m\omega} \end{aligned} \tag{2.39}$$

with ω_{eff} the effective XH stretching frequency in the presence of hydrogen bonding and $K = (\frac{\partial^3 V}{\partial Q \partial^2 q})_0$ the cubic anharmonic force constant. We find that the presence of an anharmonic coupling term makes the effective XH stretching frequency scale approximately linearly with the R(X..Y) heavy atom distance. Therefore, the observed XH stretching frequency directly reflects the hydrogen bond strength. Correlations between spectroscopic and crystallographic data of various crystals indeed showed this linear dependence over a large range, with notable differences for NH··N and NH··O hydrogen bonds [94, 95] as shown in Figure 2.2 (a). The slope of stretching frequency to heavy atom distance critically depends on the cubic anharmonic coupling term of the potential energy surface as well as on the environment. Thus, such empiric correlations have only limited value for the prediction of the hydrogen bond strengths in an unknown molecular system. Moreover, the validity of these relations for solution phase systems is unclear.

Moreover, different mechanisms lead to spectral line broadening upon hydrogen bond formation. Intra- and intermolecular couplings of hydrogen stretching modes with fluctuating solvent degrees of freedom are reflected in the line broadening of hydrogen stretching transitions:

- Fluctuating hydrogen-bonding interactions combined with a shortened vibrational lifetime lead to faster vibrational T_2 dephasing and, hence, enhanced homogeneous broadening.
- A heterogeneous distribution of hydrogen bond lengths and hydrogen bonding geometries may give rise to enhanced inhomogeneous broadening.
- Anharmonic couplings of XH stretching vibrations to low-frequency hydrogen bond modes (see above) lead to formation of vibrational sidebands with their respective intensities given by the corresponding Frank-Condon overlap (detailed explanation on page 85 in the context of adenosine-thymidine base pairs).
- The red-shift in the XH stretching transition frequency reduces the energy gap to fingerprint overtone and combination tone states, allowing enhanced mode mixing with harmonically forbidden overtone and combination tone modes (Fermi resonances), which may provide significant oscillator strength for the Fermi resonance enhanced peaks.

Already for a single XH stretching mode, such processes may lead to a break-up into a multitude of lines with a highly unpredictable lineshape and substructure (see the linear spectra of various molecular amine systems in Figure 2.2). The disentanglement of the linear spectra then can be only achieved by comprehensive experimental and theoretic analysis, as we will do in chapter 6 for the linear spectrum of A·T base pairs.

In addition, for XH stretching modes, one observes a substantial enhancement of oscillator strength upon hydrogen bonding, which is a direct result of the increased polarization of the electron density leading to an increased change in dipole moment along the vibrational XH stretching local coordinate Q (increase in $\partial\mu/\partial Q$; compare page 10). A calculation for hydrogen-bonded phenol

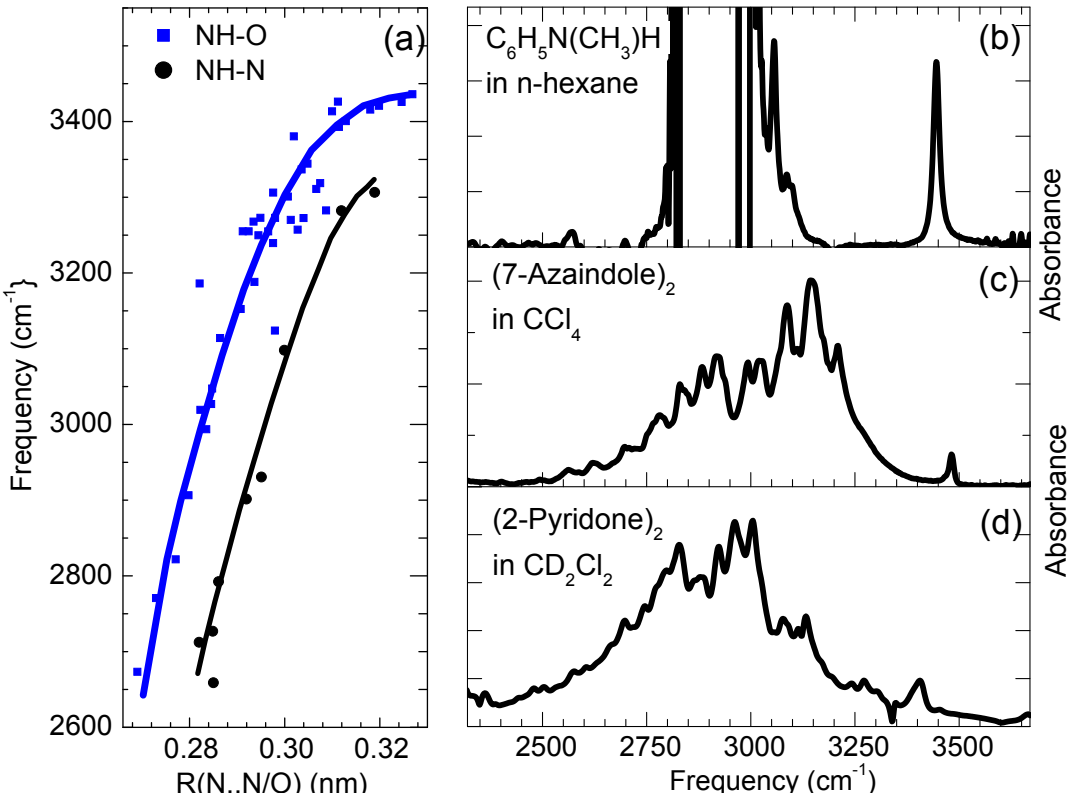

Figure 2.2: *(a) The NH stretching frequency in the presence of NH··O (blue dots) and NH··N (black dots) hydrogen bonds as a function of the R(N..N/O) heavy atom distance for various crystalline molecular systems including fit lines (reproduced from ref [94, 95]). (b,c,d) Infrared absorption spectra for various amine molecules in the range of NH stretching vibrations with hydrogen bonding increasing from top to bottom. The strong absorption at 2800-3100 cm^{-1} in (b) arises from CH stretching modes.*

complexes with truncation of the dipole moment expansion $\mu(Q) = \mu_0 + \mu_1 Q + \mu_2 Q^2$ after the quadratic term (cf. equation (2.12)) showed that not only the linear term but also the quadratic term increase upon hydrogen bond formation, and hence, contribute to the oscillator strength enhancement [96].

The energetic shift of particular vibrational states upon hydrogen bond formation may lead to notable changes in the effective coupling between different states, which results in modified intermode mixing and altered vibrational eigenstates and, hence, in modified energy flow pathways and population lifetimes. XH stretching modes experiencing hydrogen bonding are shifted closer to energetic degeneracy with fingerprint overtone and combination tone states.

2.4 Third-order response and experimental techniques

Since in the case of isotropic solution phase system the even order nonlinear response orientationally averages to zero, the third order nonlinear response is often the lowest observable optical nonlinearity:

$$P^{(3)}(t) = \int_0^\infty d\tau_3 \int_0^\infty d\tau_2 \int_0^\infty d\tau_1 \vec{E}(t-\tau_3)\vec{E}(t-\tau_3-\tau_2)\vec{E}(t-\tau_3-\tau_2-\tau_1)R^{(3)}(\tau_3,\tau_2,\tau_1) \qquad (2.40)$$

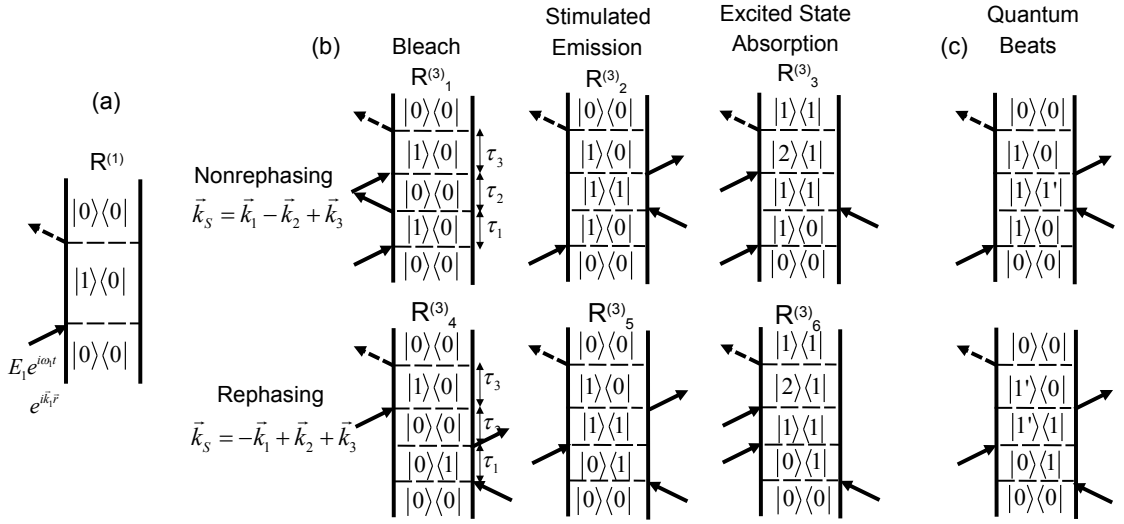

Figure 2.3: *Independent Feynman diagrams for linear (a) and third order signals (b, c) for a three-level system. (b) Bottom row: Rephasing pathways that generate a photon echo signal show a reverse coherence evolution in the τ_1 and τ_3 period while nonrephasing pathways (shown on the top row) do not. (c) Additional pathways for coherent multi-mode excitation producing quantum beats.*

$$\text{with } R^{(3)}(\tau_3,\tau_2,\tau_1) = \left(\frac{-i}{\hbar}\right)^3 \Theta(\tau_3)\Theta(\tau_2)\Theta(\tau_1)\sum_{\alpha=1}^{6}\left[R^{(\alpha)}(\tau_3,\tau_2,\tau_1) - R^{*(\alpha)}(\tau_3,\tau_2,\tau_1)\right] \tag{2.41}$$

It is important to note that the measurement of any third order signal requires at least an anharmonic three level system and is not possible in a two level systems, as will be shown below. The third-order nonlinear response of a vibrational anharmonic three-level system has six independent Feynman diagrams as shown in Figure 2.3 (b). Here initially only vibrational ground state population is assumed, which for room temperature experiments (kT $\approx$ 200 cm^{-1}) on high-frequency vibrations is clearly fulfilled. The coherence created by the first pulse will dephase during the first coherence evolution period τ_1 and then be transferred into a population state by the second pulse. This can be either population in the ground or single excited state, which may relax due to T_1 relaxation during the population waiting time τ_2. Pathways including a $|2\rangle\langle 0|$ coherence during the τ_2 interval are here neglected since its typically fast decoherence gives these pathways notable signal strength only for waiting times close to zero. The third pulse creates a dephasing coherence evolving either as $|1\rangle\langle 0|$ or $|2\rangle\langle 1|$ coherence, which leads finally to emission of the nonlinear signal bringing the system back into a $|1\rangle\langle 1|$ or $|0\rangle\langle 0|$ ground state.

The second order cumulant approximation with strictly correlated fluctuations on the ω_{01} and ω_{12} transition gives for both transitions identical line shape functions [97] and yields the third response functions of Figure 2.3 (b) as:

$$\begin{aligned}
R_2(\tau_1,\tau_2,\tau_3) =& R_1 = \frac{i}{\hbar^3}\mu_{01}^4 e^{-i\omega_{01}(\tau_3+\tau_1)} e^{-g(\tau_1)-g(\tau_2)-g(\tau_3)+g(\tau_1+\tau_2)+g(\tau_2+\tau_3)-g(\tau_1+\tau_2+\tau_3)} \\
R_3(\tau_1,\tau_2,\tau_3) =& -\frac{i}{\hbar^3}\mu_{01}^2\mu_{12}^2 e^{-i((\omega_{01}-\Delta)\tau_3+\omega_{01}\tau_1)} e^{-g(\tau_1)-g(\tau_2)-g(\tau_3)+g(\tau_1+\tau_2)+g(\tau_2+\tau_3)-g(\tau_1+\tau_2+\tau_3)} \\
R_5(\tau_1,\tau_2,\tau_3) =& R_4 = \frac{i}{\hbar^3}\mu_{01}^4 e^{-i\omega_{01}(\tau_3-\tau_1)} e^{-g(\tau_1)+g(\tau_2)-g(\tau_3)-g(\tau_1+\tau_2)-g(\tau_2+\tau_3)+g(\tau_1+\tau_2+\tau_3)} \\
R_6(\tau_1,\tau_2,\tau_3) =& -\frac{i}{\hbar^3}\mu_{01}^2\mu_{12}^2 e^{-i((\omega_{01}-\Delta)\tau_3-\omega_{01}\tau_1)}) e^{-g(\tau_1)+g(\tau_2)-g(\tau_3)-g(\tau_1+\tau_2)-g(\tau_2+\tau_3)+g(\tau_1+\tau_2+\tau_3)}
\end{aligned} \tag{2.42}$$

The phase evolution of R_{4-6} acquired in the first coherence time period τ_1 is reversed in

the conjugate coherence period τ_3, showing a "rephasing" character and leading to a revival of macroscopic polarization providing the photon echo signal, unlike the nonrephasing (virtual echo) response functions R_{1-3}. Rephasing pathways show phase-matched signal emission in the $-\vec{k}_1+\vec{k}_2+\vec{k}_3$ direction while nonrephasing pathways lead to signal emission in the $+\vec{k}_1-\vec{k}_2+\vec{k}_3$ direction. For pathways $R_{1,2,4,5}$ only involving transitions between the ground and first excited state, the signal field shows an emission frequency $\omega_S = \sum \omega_i$ equal to the excitation frequency ω_{01}. In contrast, the pathways $R_{3,6}$ show emission at the anharmonically downshifted frequency ω_{12}. In the absence of vibrational anharmonicity Δ and electrical anharmonicity $\mu_{12} \neq \sqrt{2}\mu_{10}$ and for identical T_2 dephasing dynamics in the various coherence states addressed, the Feynman pathways R_{1-6} would show completely destructive interference, eliminating any third order signal [64].

The line shape function g(t) (defined in equation 2.34) and, thus, the frequency-frequency correlation function completely defines the third-order (and linear) response. It is the key ingredient in linking the spectroscopic observables to the microscopic molecular dynamics.

Spectroscopic techniques

Different experimental approaches for measuring the vibrational third-order response function at different degree of completeness and accuracy exist, which can be grouped into pump-probe spectroscopy, two-dimensional (2D) transient hole-burning spectroscopy, four wave mixing 2D photon echo spectroscopy in transient grating, two-pulse or three-pulse realization, and coherent Raman scattering (CRS) [98–101]. The latter, employing a sequence of three non-resonant optical pulses with the first two coincident in time, the second stokes/antistokes-shifted and the third pulse finally generating a strong coherent Raman-shifted background-free signal, addresses only T_2 dephasing processes in vibrational coherences. It is insensitive to population dynamics and has been used for studying Raman-active vibrational manifolds and dephasing dynamics in liquids [99, 102]. Vibrational energy relaxation (T_1 population dynamics) can be measured with experimental sequences of resonant IR pump excitation followed by delayed spontaneous Raman scattering [98, 103] monitoring changes of vibrational "parent" population and occurrence of new Raman-shifted bands. However, this technique suffers from low signal intensities making it often hard to discriminate the signal from the elastic Rayleigh scattering and/or fluoresence contributions. In this thesis, we therefore make extensive use of IR-pump IR-probe transient absorption spectroscopy and femtosecond three-pulse photon echo spectroscopy, using two respectively three optically coherent light pulses to create and manipulate quantum coherent system molecular states that are finally analyzed by measuring the emitted third-order nonlinear signal field following the induced oscillating coherent polarization of the molecular ensemble.

Pump-probe spectroscopy

Directly accessing overtone transitions in linear spectroscopy is - due to vibrational selection rules - very inefficient compared to sequential single quantum excitation pathways. In third-order pump-probe spectroscopy, mainly changes in populations in a molecular system induced by a strong broadband pump pulse are monitored by a non-collinear time-delayed broadband weak probe pulse probing at the same or a different wavelength for different pump-probe delays. Changes in transmission are recorded by dispersion of the probe beam in a spectrometer and detection in time-integrating square-law detector arrays (see Figure 2.4 (b)). If in resonance with a vibrational fundamental transition ω_{01}, the excitation by the pump pulse will make the probe beam experience a reduced absorption at the same frequency due to both the reduction of ground state population (bleach) and the stimulated emission from the newly populated excited state. Moreover an enhanced absorption component of the $1 \rightarrow 2$ transition at ω_{12} will appear (see Figure 2.4 (c,d)), the energy difference $\omega_{01} - \omega_{12}$ giving the diagonal anharmonicity. While the decay in the enhanced

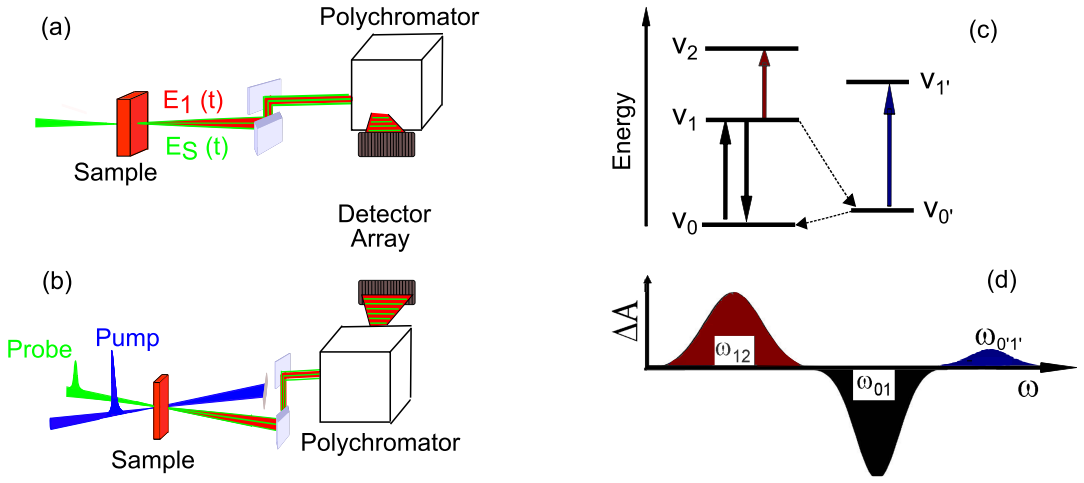

Figure 2.4: *Sketch of (a) linear absorption and (b) nonlinear third order pump-probe experiments. (c): Different contributions to the transient absorption signal of an anharmonic three-level system including a possible "hot ground state" signal with the corresponding transient spectrum in (d).*

absorption signal for increasing pump-probe delays directly reflects the excited state T_1 lifetime, the recovery dynamics of the bleach signal is affected by the available population relaxation and transfer pathways which eventually delocalize the excess energy into the low-frequency bath modes, leading to multi-exponential bleach recovery dynamics. The heated bath may couple to the fundamental molecular transition, leading to a shift in transition frequency that relaxes back to its original value only after the complete thermal equilibration of the probed volume which occurs on the time scale of macroscopic heat conduction (ns-μs). When studying weakly hydrogen-bonded stretching oscillators the increase in sample temperature may lead to weakening or breaking of hydrogen bonds which would lead to an enhanced absorption "hot ground state" signal [104, 105], typically occurring at blue shifted 0-1 frequencies and growing in on the time scale of vibrational cooling.

The pump-probe signal is given as the change of absorbance induced by the pump pulse:

$$\begin{aligned}\Delta A(\omega,\tau_2) &= -\,log\left(\frac{I_{pr}(\omega,\tau_2)}{I^0_{pr}(\omega}\right) = -log\left(\frac{\int dt\,|E_{Pr}(\omega)+E_S(\omega,\tau_2)|^2}{\int dt\,|E_{Pr}(\omega)|^2}\right)\\ &\approx -2\frac{\int dt Re\left\{E_{Pr}(\omega)E^*_S(\omega,\tau_2)\right)}{\int dt\,|E_{Pr}(\omega)|^2}\end{aligned} \tag{2.43}$$

with I_{pr}/I^0_{pr} the probe intensity with/without pump, in the limit of a weak signal intensity as compared to the probe pulse intensity. In the slowly varying envelope approximation, this yields the absorbance change as proportional to the imaginary part of the nonlinear third-order polarization $P^{(3)}(\omega)$ at frequency ω [78]:

$$E_S(\omega,\tau_2) = \frac{4\pi\omega}{n(\omega)c}\frac{Im\left\{P^{(3)}(\omega,\tau_2)/E_{pr}(\omega)\right\}|E_{pr}(\omega)|^2}{\int d\omega\,|E_{Pr}(\omega)|^2} \tag{2.44}$$

with $E_{pr}(\omega) = \int E_{pr}(t)e^{i\omega t}$ and $P^{(3)}(\omega) = \int P^{(3)}(\tau_3)e^{i\omega\tau_3}$.

In the context of coherent spectroscopy, the absorbance change is understood as interference between the probe and the emitted third-order signal fields corresponding to the different Feynman diagrams shown in Figure 2.3 (b) under the rotating wave approximation. For the following discussion, strict time ordering is assumed with the pump pulse preceding the probe pulse. The

Feynman pathways can be grouped into bleach ($R_{1,4}$), stimulated emission ($R_{2,5}$) and excited state contributions ($R_{3,6}$), depending on the nature of the transition of the probe beam k_{Pr}. The detector records the phase-matched signal components with $\vec{k}_1 = -\vec{k}_2$ emitted in the probe pulse direction with $\vec{k}_S = \vec{k}_{pr}$, requiring two interactions within the envelope of the pump pulse and one interaction within the envelope of the probe pulse. The phase matching condition thus leads for both rephasing and nonrephasing pathways to signal emission collinear to the probe pulse which ensures measurement of completely absorptive line shapes. No explicit time ordering between the first two interactions is possible and the phase evolution between the first two pulses can be neglected which leads to identical responses from the top and bottom pathways in Figure 2.3 (b,c). If the pump pulse bandwidth spans two close-to-resonant modes, coherent excitation may induce excited state wave packet dynamics that will modulate the pump-probe signal as a function of pump-probe delay (quantum beats pathways, Figure 2.3 (c)). The oscillation period is given by the frequency splitting of their fundamental frequencies. For delays exceeding the time scale of vibrational dephasing only incoherent population relaxation/transfer processes are measured.

During temporal overlap of pump and probe beam, additional Feynman pathways with the probe beam preceding one or both of the pump excitations arise. These "coherent artifact" spikes mask dynamic features near the zero pump-probe delay. Alternatively, they can be viewed as resulting from interference of the probe beam with pump light scattered from the spatially modulated refractive index grating in the sample induced by Kerr interactions during pulse overlap. Conventional pump-probe signals grow in around zero delay with a rise time given by the pump-probe cross correlation width. For large negative delays (the probe pulse arrives before the pump pulse), no pump-induced absorbance changes such as population relaxation or transfer can be measured due to causality of the third-order nonlinear signal. However, a different kind of signal is observed, which is the perturbed free induction decay (PFID) signal [106–108]: The vibrational coherence induced by the probe pulse will radiate a free induction decay signal collinear to the incoming probe pulse and enter the detector. However, only its pump-induced perturbations in strength and frequency will be measured in the pump-probe experiment. The perturbed free induction decay signals can be also explained from the interference of the probe field with third-order signal contributions arising from Feynman diagramms that show a sequence of pulse interactions with one interaction of the probe field first followed by two delayed interactions with the pump field. Spectral dispersion of the probe pulse with sufficient spectral resolution enables measurement of the full PFID signal (probe and PFID signal are sufficiently stretched in time to interfere despite the fact that they leave the sample at different times), which provides a measure of the dephasing time T_2.

Pump-probe spectroscopy was established as an extremely powerful technique for the analysis of vibrational energy relaxation pathways and coherence dynamics as well as for structural dynamics and structure determination. Additional insight is obtained from polarization-selective measurements of the time-dependent anisotropy, providing information on the time scale of resonant intermolecular energy transfer and orientational diffusion [109, 110].

Coherent two-dimensional spectroscopy

The nuclear potential energy surface of complex molecules such as DNA nucleobases leads to highly congested vibrational spectra, making unique peak assignments in linear or one dimensional transient absorption spectra often impossible. Two-dimensional (2D) spectroscopy allows one to reduce the spectral congestion by spreading it over an additional spectral dimension [45, 111–113]. We use the 2D Fourier transform three pulse photon echo approach. It uses three ultrashort non-collinear excitation pulses with variable time delay, which generates a nonlinear signal in a background-free phase-matched direction that is recorded in amplitude and phase by spectral interferometry with a fourth weak local oscillator pulse (see Figure 2.5). The pulse delay between the first two pulses (coherence time τ_1) is scanned while the delay between the second and third pulse (waiting time τ_2)

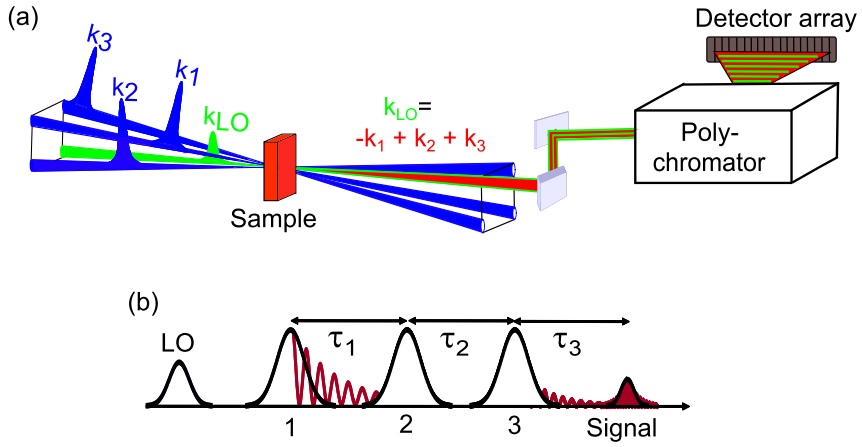

Figure 2.5: *(a) Sketch of the Fourier transform three pulse 2D-IR setup in box-CARS geometry with the pulse sequence shown below (b). The photon echo (rephasing) signal emitted in the background-free direction is field-resolved detected by spectral interferometry with a local oscillator (LO) pulse.*

stays fixed. The spectrometer provides the detection frequency axis, while the excitation frequency axis is obtained by a Fourier Transform method of the signal field with respect to the coherence time τ_1 (details on Fourier-transform spectral interferometry are given in section 3.3). The 2D frequency domain signal $E_{Sig}(\omega_3, \omega_1, \tau_2)$ shows the dephasing dynamics of vibrational coherences in two evolution periods $\tau_{1,3}$ separated by a delay τ_2, thus correlating the excitation of a system at a certain dipole oscillation frequency ω_1 with the probability of observing it at a final emission frequency ω_3 at a later waiting time τ_2 in the ensemble-averaged system. Essentially the 2D plots give the third order susceptibility $\chi^{(3)}$ which is the frequency domain representation of the third-order temporal response functions:

$$\chi^{(3)}(\omega_1, \omega_3, \tau_2) = \int\int_{-\infty}^{\infty} d\tau_1 d\tau_3 e^{-i(\omega_1\tau_1 + \omega_3\tau_3)} R^{(3)}(\tau_1, \tau_2, \tau_3) \tag{2.45}$$

In the last 10 years the positions, signs, amplitudes and line shapes of the signals in 2D-IR spectra have provided extensive insight into the vibrational eigenstates of the system under study, couplings [47, 113, 114] and molecular structure in peptides, proteins and DNA [53, 115–121]. Moreover they helped to reveal vibrational relaxation and transfer dynamics, hydration and structural dynamics [25, 122–124] and were used for studying dynamics exclusively on surfaces and interfaces based on second-order up-conversion of the nonlinear signal with a visible pulse [125].

The non-collinear pulse geometry yields the rephasing and nonrephasing third-order signal contributions in two different directions, $k_1 - k_2 + k_3$ and $-k_1 + k_2 + k_3$. However, exchanging the time ordering of the first two pulses ($\tau_1 < 0$) allows one to measure both contributions in the same direction of the detector. The nonlinear signal field of an anharmonic three level system in 2D frequency space in the semi-impulsive limit can be calculated by Fourier transformation of the response functions $R_1 - R_6$ from equation (2.42) with respect to τ_1 and τ_3. FT of the sum of $R_1 - R_3$ yields the nonrephasing, FT of the sum of $R_4 - R_6$ the rephasing 2D signals as shown in Figure 2.6 (a), (b). The nonrephasing and rephasing signals show dispersive phase-twisted line shapes aligned along the anti-diagonal and diagonal frequency axes, respectively. 2D-IR spectra with absorptive line shapes can be generated by taking the real part of the sum of rephasing and nonrephasing signal contributions [126](Figure 2.6 (c)). Here the dispersive wings almost cancel, leaving absorptive line shapes with well-defined position, sign and narrow shape. The latter is especially important if the

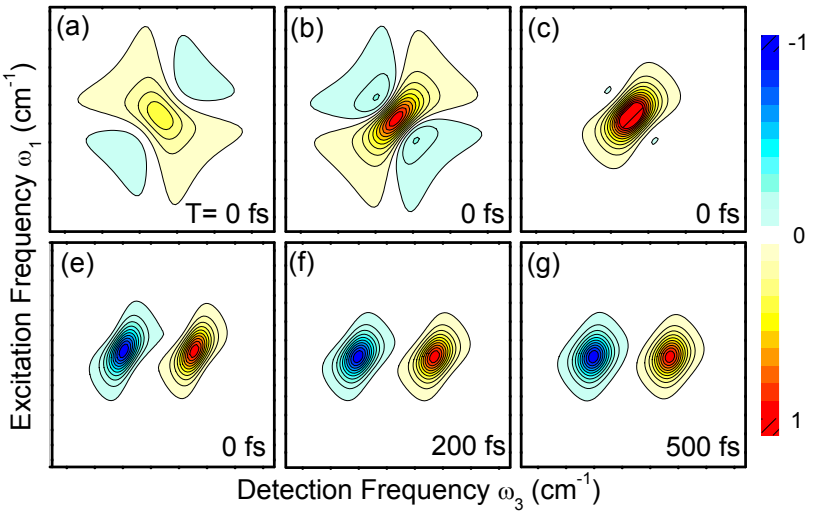

Figure 2.6: *Calculated nonlinear signal field of an anharmonic three-level system in 2D frequency space using the response functions (2.42) and assuming a Kubo line shape function g(t) (2.36) with a correlation time τ_C of 500fs. (a) Nonrephasing signal. (b) Rephasing echo signal. (c) Absorptive 2D-IR signal. (e-g): Band reshaping with waiting time indicative of spectral diffusion.*

pulse bandwidth covers a high density of vibrational states, as is typically the case for the systems studied in this work.

The waiting time dynamics of 2D line shapes allow one to extract the FFCF $C(\tau)$ and thus the line shape function g(t). For waiting times τ_2 shorter than the correlation time τ_C (inhomogeneous case), the nonrephasing signal is weak compared to the rephasing signal, aligning the absorptive signal along the frequency diagonal corresponding to an intense echo signal for $\tau_1 = \tau_3$ in the time domain [127]. When the molecular frequency memory is lost ($\tau_2 \gg \tau_C$, equally strong rephasing and nonrephasing signals lead to a more round absorptive line shape and the one-to-one correlation between excitation and detection frequency is lost. The FFCF is a measure of the dynamics with which a molecule samples the different frequencies within an inhomgenously broadened vibrational band. Gradual changes in the transition frequency in a selected molecule, which can be followed on the experimental time scale, are known as spectral diffusion. They result from either structural fluctuations or from close-to-resonant energy transfer. $C(\tau)$ can be approximated by the ratio of rephasing/nonrephasing signal intensity, the ellipticity of the 2D line shape [128], and the slope of the center line [129,130] connecting signal maxima for cuts at fixed detection frequency [c]. Line shape analysis of 2D-IR spectra is a powerful approach for analyzing structural dynamics in molecules. In chapter 7, we will use the center line slope method for extracting the frequency fluctuation dynamics of local OH stretching excitations as an indirect probe for structural dynamics in the hydration shell of DNA.

2.5 Molecular couplings in 2D-IR spectroscopy

One of the outstanding capabilities of 2D-IR spectroscopy is to resolve, quantify, and follow molecular vibrational couplings on ultrafast time scales. Two anharmonic, independent oscillators, as

[c] For isolated vibrational transitions, photon echo peak shift measurements [131–133] proved most useful for studying solvation dynamics.

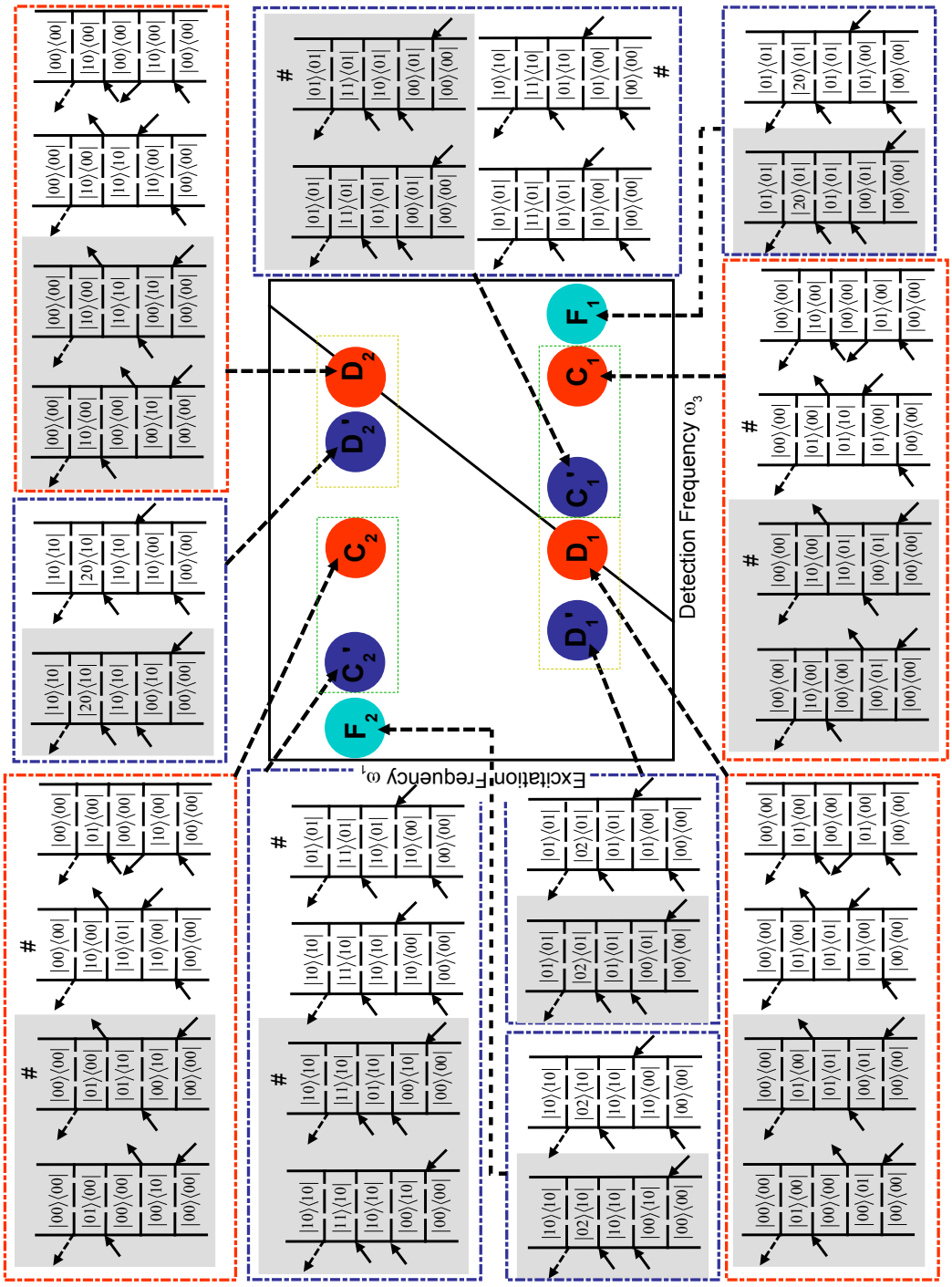

Figure 2.7: *Feynman diagrams contributing to the 2D-IR spectrum of two anharmonically coupled oscillators assuming initially only population of the ground state. Pathways with rephasing character are highlighted in gray while those involving interstate coherences are marked with a diamond. Population transfer pathways are not included.*

arising from, e.g., two strongly localized and remote excitations within the same molecule or arising from different non-hydrogen-bonded molecular species, will show a 2D spectrum with two pairs of "diagonal" peaks corresponding to their individual 0-1 and and red-shifted excited state 1-2 transitions being red-shifted by their individual diagonal anharmonicity. In the presence of coupling

additional cross peaks occur. Two modes are said to be coupled to each other when the second- or higher-order derivatives of the potential energy surface with respect to the two corresponding local coordinates are nonzero. Anharmonic coupling terms will lead to the situation that the excitation of one mode changes the transition frequency of the other one. Including the double-excited states in a system of two coupled anharmonic oscillators with fundamental frequencies ω_{01} and ω_{10}, there are six energy levels. These produce eight peaks in a 2D spectrum all aligned with their excitation frequency ω_1 at either of the two fundamental frequencies but with their detection frequencies ω_3 identical to one of the six dipole-allowed single quantum transitions (see Figure 2.7 and 2.1 (b)). They can be grouped in two diagonal features $(D_1; D_1'/D_2; D_2')$ and two cross peak features $(C_1; C_1'/C_2; C_2')$, each split into a pair. Each 2D-IR peak is distinguished by its pathways of stepwise coherence and population state manipulation induced by the three excitation pulses, as indicated by their corresponding Feynmann pathways in Figure 2.7 with their sign +/- indicated by the red/blue color coding. Those pathways with rephasing character are highlighted in gray and evolve with conjugate coherences during the τ_1 and τ_3 period, providing phase factors with opposite sign. The positive diagonal (D_1, D_2) and cross peaks (C_2, C_1) arise from evolution between only the two fundamental transitions, while the negative signals describe excitation pathways also involving the double excited state manifold. All diagonal peaks involve excitation of only one of the two oscillators which goes up to the overtone excited states (ES) for the negative diagonal peaks D_1', D_2'. The positive cross peaks (C_2, C_1) arise from mixed excitation of the two fundamental frequencies ω_{01} and ω_{10}. In the case of the negative cross peaks C_1', C_2', excitation of the combination mode is involved in the process of density matrix manipulation. In the strong coupling limit ($|V| >> \hbar|(\omega_2 - \omega_1)|$ and for diagonal anharmonicities $\Delta_{1,2}$ exceeding the coupling |V|, the two-exciton states become heavily mixed leading to a weak allowance of single photon transitions that change more than one quantum and produce weak additional harmonically forbidden features F and F'.

Half of the cross peak pathways involve interstate coherences (pathways marked with diamonds in Figure 2.7) during the waiting time period leading to a slight oscillatory component in their intensity with waiting time with the difference frequency $\Delta\omega$ between the two fundamental transition frequencies [134], as reflected in their response functions $R(\tau_2) \propto e^{-i(\omega_{01}-\omega_{10})\tau_2-\Gamma\tau_2}$. Underdamped quantum beats require the interstate dephasing time $1/\Gamma$ to be longer than the inverse difference frequency $\Delta\omega$. In the absence of coupling, the cross peaks C_1 and C_1' as well as C_2 and C_2' would exactly cancel to zero. If the pulse bandwidth spans multiple vibrational modes, this allows in many cases to distinguish two (coupled) vibrational modes from the same molecule from two independent modes from different molecules. This differentiation is of great value for peak assignments in spectra of multi-molecular mixtures.

Two-dimensional IR spectra allows one to map out the single and double exciton manifold while the excitonic energy level positions and transition dipole intensities and directions are encoded in peak positions and intensities. The splittings of the diagonal- and cross-peak pairs are related to their intermode coupling V and the anharmonic downshift of the overtones and combination modes in a complex way [46, 69]. Anharmonicity and coupling parameters are obtained as fit values in the Hamiltonian 2.8 such, that its diagonalisation reproduces the observed excitonic eigenfrequencies shown in the 2D-IR peak pattern. Simultaneously this yields the corresponding excitonic eigenstates.

Population relaxation typically makes up most of the waiting time dynamics in 2D-IR spectra and occurs via modes that are often dark to the experiment. For highly complex line shapes with fundamental and excited state transitions heavily overlapping in conventional pump-probe spectra, the additional frequency axis in 2D-IR spectroscopy is the only way to unravel individual T_1 lifetimes reliably. If population transfer occurs between two coherently excited modes (see 2.8 (a) and (b)), it can be directly followed due to changes in cross peak intensities C_1 and C_2 as a function

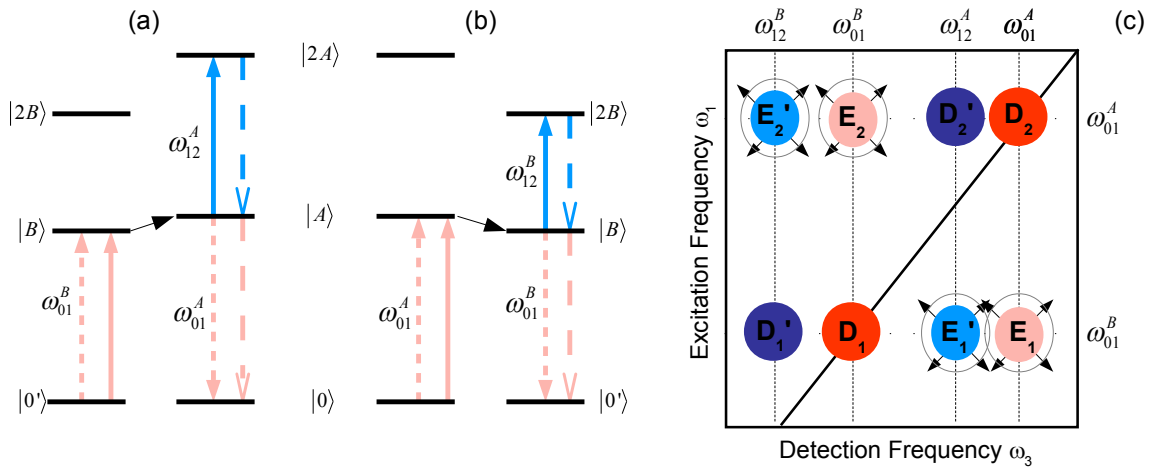

Figure 2.8: *Ladder diagrams for energetic (a) uphill and (b) downhill population transfer between two near degenerate anharmonic vibrational modes, occurring in the waiting time period τ_2. (c) Corresponding 2D spectrum for two modes without anharmonic coupling between them. In the presence of population transfer new peaks E_2, E_2' and E_1, E_1' will grow in. If both modes are already anharmonically coupled, $E_{1,2}$ cross peak intensities will change differently than the diagonal peaks at identical emission frequency. The ω_3 peak position of E_2', E_1' contrasts to the case of anharmonically coupled modes in the absence of energy transfer.*

of waiting time τ_2. Their dynamics reflect both the population exchange kinetics as well as the T_1-lifetime of that mode to which population is shifted, leading to involved rate equations [135, 136]. Therefore, for the new cross peaks to become clearly visible, the population transfer has to be typically faster than the T_1 lifetime of the transferred mode. On an identical time scale, new enhanced absorption signals with negative sign will grow in at detection frequencies shifted from the fundamental frequencies $\omega_{1,2}$ by the *diagonal* anharmonicity of that oscillator to which the excitation was transferred. If energy-wise only downhill or also uphill population transfer occurs depends on the ratio of frequency separation of the involved modes compared to the thermal energy kT. For single color 2D-IR experiments with 300 cm^{-1} pulse bandwidth, observable population transfer will, thus, often involve transfer in both directions.

Population transfer requires anharmonic mode coupling to vibrational modes accepting the difference energy. This makes population transfer especially probable between nearly degenerate states due to the high density of molecular low-frequency modes. Structural fluctuations enabling spectral diffusion may be helpful in bridging the energy gap [137]. Hydrogen-bond breaking or formation processes during the waiting period can lead to a dynamic growth of cross peak intensities in a similar way as with population transfer. Therefore, distinction between both processes may be difficult. In many cases, cross peaks will already exist for $\tau_2 = 0$. This observations shows instantaneous anharmonic couplings mediated via through-bond mechanical or through-space dipole dipole interactions. Population transfer will then lead to cross peak intensity dynamics that are different from those found for the diagonal peaks.

Polarization anisotropy and relative transition dipoles angles

So far, the orientational contribution of relative dipole directions in the sequence of field interactions to the third order response was neglected. Actually, the amplitudes of peaks in 2D-IR spectra reflect both the strength and direction of the four transition dipoles interacting with the various linearly

polarized light fields. According to equation (2.24) and (2.40), the heterodyne detected third order signal of one particular Feynman diagram in the semi-impulsive limit can be related to the four-point dipole correlation function:

$$\langle \mu_a(0)\mu_b(t_1)\mu_c(t_2)\mu_d(t_3)\rangle \, E_1E_2E_3E_{LO} \tag{2.46}$$

with $\mu_a(t)$ the transition dipole moment at time t, projected on the laboratory fixed electric field vector $\hat{a}$. Each field interaction excites a subset of molecules with non-perpendicular transition dipole orientations with respect to the exciting field polarization. In the absence of field interactions, their dipole orientations may change due to rotational diffusion or intermolecular energy transfer. The finally emitted signal will depend on the polarization geometry, the molecular transition dipole orientations contained in the detailed excitation pathway, and the time scales of dipole reorientation processes. For sufficiently short coherence time $\tau_{1,3}$ scan ranges as dictated by the T_2 dephasing times and for sufficiently short waiting time periods (limited by T_1 lifetimes), dipole reorientation dynamics can be neglected and molecular transition dipole orientations can be assumed time-independent. This assumption is valid for the molecules studied here. Regarding changes in transition dipole orientation as independent from vibrational amplitude motions, the orientational component of (2.46) can be abbreviated as

$$\langle a_\alpha b_\beta c_\gamma d_\delta\rangle \equiv \left\langle (\hat{\mu}_\alpha\cdot\hat{a})(\hat{\mu}_\beta\cdot\hat{b})(\hat{\mu}_\gamma\cdot\hat{c})(\hat{\mu}_\delta\cdot\hat{d})\right\rangle \tag{2.47}$$

with a_α the projection of the transition dipole unit vector $\hat{\mu}_\alpha$ onto the electric field polarization direction $\hat{a}$, etc.. In the most general case of an arbitrary polarization geometry of the exciting field vectors with relative polarization angles θ_{ab} and relative angles of the involved transition dipoles $\theta_{\alpha\beta}$, the orientational part of the heterodyned third-order signal of a certain Feynman pathway is given as [138]:

$$\begin{aligned}\langle a_\alpha b_\beta c_\gamma d_\delta\rangle = 1/30\,[&\langle cos\theta_{\alpha\beta}cos\theta_{\gamma\delta}\rangle\,(4cos\theta_{ab}cos\theta_{cd}-cos\theta_{ac}cos\theta_{bd}-cos\theta_{ad}cos\theta_{bc})\\ &+\langle cos\theta_{\alpha\gamma}cos\theta_{\beta\delta}\rangle\,(4cos\theta_{ac}cos\theta_{bd}-cos\theta_{ab}cos\theta_{cd}-cos\theta_{ad}cos\theta_{bc})\\ &+\langle cos\theta_{\alpha\delta}cos\theta_{\beta\gamma}\rangle\,(4cos\theta_{ad}cos\theta_{bc}-cos\theta_{ab}cos\theta_{cd}-cos\theta_{ac}cos\theta_{bd})\end{aligned} \tag{2.48}$$

The ensemble average $\langle\rangle$ is over all possible alignments that are each weigthed by the probability $P(\theta_{\alpha\beta})$ of finding a certain transition dipole orientation $\theta_{\alpha\beta}$:

$$\langle cos\theta_{\alpha\beta}cos\theta_{\gamma\delta}\rangle = \int_0^{2\pi} d\varphi \int_0^{\pi} d\theta sin\theta P(\theta_{\alpha\beta})P(\theta_{\gamma\delta})cos\theta_{\alpha\beta}cos\theta_{\gamma\delta} \tag{2.49}$$

Here we consider only isotropically oriented molecules, which is the situation in the solution-phase systems studied here, and look at absorptive 2D spectra in the all-parallel polarization condition ZZZZ ($\hat{a}=\hat{b}=\hat{c}=\hat{d}$) and the cross polarized configuration ZZXX ($\hat{a}=\hat{b}$, $\hat{c}=\hat{d}$ and $\theta_{ac}=90°$). In the experiment a, b, c indicate the three excitation pulses k_1, k_2, k_3 and d is the local oscillator pulse.

a) Diagonal peaks: For diagonal peaks D_i arising from pathways with excitation in only one oscillator, integration in spherical coordinates gives for the ratio of peak intensity in ZZZZ ($S_{D_i}^{ZZZZ}$) vs in ZZXX configuration ($S_{D_i}^{ZZXX}$) an enhancement of diagonal peak intensity by a factor of 3 [46, 138]

$$\frac{S_{D_i}^{ZZZZ}}{S_{D_i}^{ZZXX}} = \frac{\langle (a_\alpha)^4\rangle}{\langle (a_\alpha)^2(c_\alpha)^2\rangle} = \frac{1/5}{1/15} = 3 \tag{2.50}$$

b) Cross peaks: The ratio of cross peak intensities C_i in ZZZZ ($S_{C_i}^{ZZZZ}$) relative to their intensity in ZZXX polarization configuration ($S_{C_i}^{ZZXX}$) can be shown to depend on the relative transition

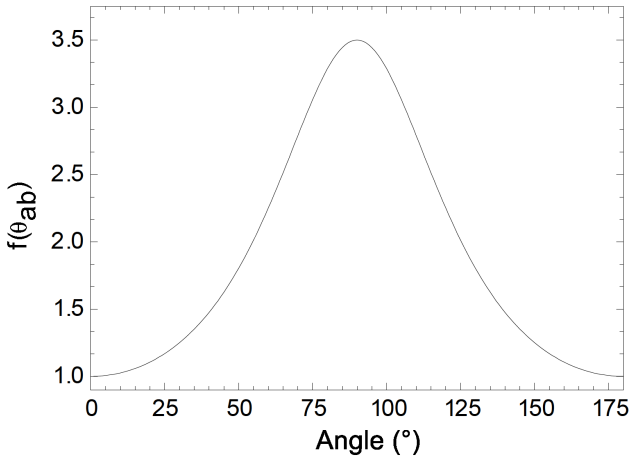

Figure 2.9: *Scaling factor between the ratio of cross peak to diagonal peak intensity in ZZXX configuration and between the same ratio in ZZZZ configuration for absorptive 2D-IR spectra, given by equation (2.52). It is plotted as a function of the relative transition dipole angle.*

dipole angle θ_{ab} [46]:

$$\frac{3S_{C_i}^{ZZXX}}{S_{C_i}^{ZZZZ}} = \frac{10 - P_2(\theta_{ab})}{4P_2(\theta_{ab}) + 5} = f(\theta_{ab}) \tag{2.51}$$

with $P_2(\theta_{ab}) = 1/2(3cos^2\theta_{ab} - 1)$ the second order Legendre polynomial of θ. The factor 3 in the above equation arises from the difference in diagonal peak intensity in ZZXX and ZZZZ configuration [46] and can be substituted by the corresponding scaling of diagonal peak intensities:

$$f(\theta_{ab}) = \frac{S_{C_i}^{ZZXX}}{S_{D_i}^{ZZXX}} \frac{S_{D_i}^{ZZZZ}}{S_{C_i}^{ZZZZ}} \tag{2.52}$$

Equation (2.52) compares ratios of peaks within the same 2D spectra, recorded in different polarization geometries, which reduces the error due to possible drifts in laser intensity. The function $f(\theta_{ab})$ is shown in Figure 2.9. It gives the relative enhancement factor of cross peak intensities compared to diagonal peak intensities upon a change in polarization condition ZZZZ to ZZXX. This ratio is directly related to the relative angle between the two coupled fundamental transition dipoles. Thus relative transition dipole angles can be extracted from two separately recorded sets of 2D-IR spectra. In the case of localized vibrations, transition dipole directions are closely following the axis of molecular bonds, which shows polarization-dependent 2D-IR spectroscopy contains structural sensitivity. On the other hand, if the molecular structure is known from the start, this angular information helps with the spectroscopic assignment of vibrational peaks. The waiting time period has to be chosen as small as possible to minimize possible errors due to to population transfer which could affect the cross peak intensities.

In highly congested and inhomogenously broadened spectra as found for DNA helices, strong diagonal features completely mask the weaker cross peak features. The fact that diagonal features scale down by roughly a factor of three in ZZXX configuration as compared to ZZZZ configuration while the cross peak intensities scale differently for nonparallel transitions allows one to construct a diagonal-peak-free 2D spectra from such two separate sets of spectra by manual subtraction [46,139]:

$$S = S^{ZZZZ} - 3S^{ZZXX} \tag{2.53}$$

Alternatively, an *in situ* elimination of diagonal peaks with a single 2D scan is possible for certain polarization conditions [52,54,140–142] due to destructive interference of the generated signal fields.

The $(\hat{a}/\hat{b}/\hat{c}/\hat{d}) = (60°/\ \text{-}60°/\ 0°/\ 0°)$ polarization geometry measures a similar response as before: $1/4(S^{ZZZZ} - 3S^{ZZXX})$. However, since the laser noise in the "two" measurements is inherently correlated, the peak suppression is of higher quality.

3 Experimental

In this work, molecular systems in liquid phase are examined in terms of their vibrational eigenstate character, energy relaxation pathways, and transient structural changes. Such experiments require ultrashort coherent infrared pulses for excitation and the detection of weak ultrashort nonlinear signal fields. This chapter will show in detail how both demands are experimentally fulfilled and particularly emphasize the details of our realization of photon echo spectroscopy with Fourier-transform spectral interferometry to yield absorptive 2D-IR spectra. The chapter closes with a quality assessment of the generated IR pulses and the experimental capabilities of polarization anisotropy in our 2D-IR spectra.

3.1 Generation of ultrashort mid-IR pulses

In this thesis we probe molecular dynamics with local vibrational marker modes with eigenfrequencies of 1600 - 3600 cm^{-1}. In this frequency range there are only few tunable, table-top sized broadband laser sources providing the necessary sub-100fs IR pulses.[a] The low cross sections of purely vibrational transitions call for high peak powers laser with pulse energies in the micro-joule range for sufficient nonlinear signal intensity. We use a commercial amplified solid-state titanium-sapphire [144] (Al_2O_3) (Ti:Sa) laser system followed by optical parametric down-conversion in a home-built setup. The Ti:Sa laser medium features a large tuning range, distinguished gain bandwidth, and high pump-power tolerance, making it nowadays the standard workhorse for most experiments in ultrafast optics.

Laser system

The laser system consists of a Ti:Sa oscillator (Micra 5, Coherent) whose pulses seed a chirped-pulse amplifying (CPA) system (Legend Elite, Coherent) as sketched in Figure 3.1. The oscillator unit consists of a continuous wave $Nd:YVO_4$-based diode-pumped laser (Verdi, Coherent) running at 532 nm (frequency-doubled) that is pumping a Ti:Sa crystal in a ring cavity. Intracrystal Kerr lensing allows one to coherently couple the longitudinal cavity modes (modelocking), which leads to generation of 35 fs pulses centered around the 800 nm fundamental wavelength with 100 nm bandwidth. The out-coupled pulses have a pulse energy around 5nJ at a repetition rate of 80 MHz.

In the CPA unit, a lens-grating combination first induces a positive chirp on the pulse hereby stretching it to about 400 ps. A quarter wave plate combined with a Pockels cell operated as a switchable quarter wave plate allows one to selectively incouple and trap an isolated seed pulse in the regenerative amplifier ring cavity. The Ti:Sa amplifier crystal is pumped with a pulsed (AOM Q-switched) frequency-doubled 22 W Nd:YLF laser (Evolution-30 Coherent) running at a 1kHz repetition rate. Depletion of population inversion by the seed pulse during 15 round trips in the cavity leads to a gain in seed pulse energy by a factor $> 10^6$. A polarizing beam splitter and a

[a] Quantum cascade lasers [143] using cascaded unipolar intersubband transitions in repeated multiple quantum well semiconductor hetero-structures with electronic pumping can be designed for the required frequency range by proper choice of layer thicknesses, but pulse durations stay limited to nanoseconds. The same limitation holds for conventional p-n-injection IV-VI lead-salt diode lasers. Synchronously pumped color-center lasers using defects in alkali-halide crystals as gain medium may provide pulse durations down to picoseconds at a minimum frequency of 2500 cm^{-1}, however only with limited long term stability of the gain medium.

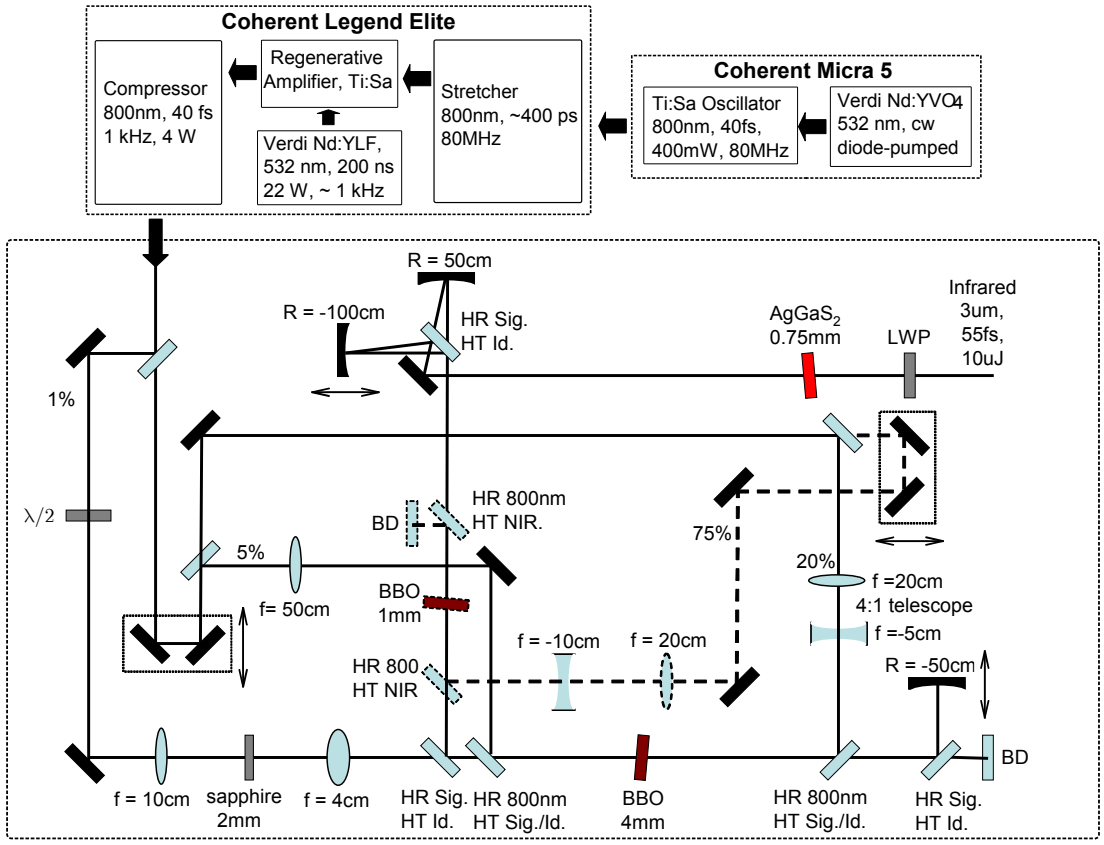

Figure 3.1: *Setup for generating ultrashort IR pulses. Pulses of a Ti:Sa oscillator are amplified in a regenerative chirped pulse amplifier laser system and converted in the IR by difference frequency generation in a $AgGaS_2$ crystal of two intense signal and idler pulses created by threefold optical parametric amplification. The dashed third amplification step is only there for the 2D-IR and single-color pump-probe experiments performed around 3µm. HR: high reflection, HT: high transmission, BD: beam dump, λ/2: half-wave plate, LWP: long wave pass filter.*

second Pockels cell outcouple the amplified pulse, which gets recompressed in a multipass grating arrangement. In this way, output pulses of 40 fs with 4 mJ pulse energy at a 1 kHz repetition rate are produced. The laser setup is sketched in the upper part of Figure 3.1.

Optical parametric frequency conversion

Generation of tunable mid-IR pulses is achieved by optical parametric frequency conversion of the 800 nm pulses [145]. A homebuilt optical parametric amplifier (OPA) system based on a BBO crystal creates two intense near-IR pulses, which are difference-frequency-mixed in a (non-isotropic) crystal with significant second order susceptibility.

In an optical parametric amplifier, an intense pump pulse ("fundamental", $\vec{k}_1, \omega_1$) interacts in a nonlinear second order process with a weak seed pulse ("signal", $\vec{k}_2, \omega_2$). This leads both to amplification of the signal and generation of an "idler" wave ($\vec{k}_3, \omega_3$) at the difference frequency $\omega_3 = \omega_1 - \omega_2$ with an idler intensity depending on the wave vector mismatch $\Delta\vec{k}$ and the interaction length L:

$$I_3 = I_3^0 sinc^2(|\Delta k| L/2) \tag{3.1}$$

$$\Delta\vec{k} = \vec{k}_1 + \vec{k}_2 - \vec{k}_3 \tag{3.2}$$

Equation (3.2) mirrors the momentum conservation condition, indicating that coherent frequency conversion is only effective for identical phase velocities of the individual fundamental and converted light fields (phase matching). The refractive index dependency on the light field polarization direction in birefringent crystals allows one to passively fulfill phase matching even in the presence of dispersion. For collinear beams, the phase matching condition (3.2) transforms into:

$$0 = n_1(\omega_1)\omega_1 + n_2(\omega_2)\omega_2 - n_3(\omega_3)\omega_3 \tag{3.3}$$

For an uniaxial crystal, a light field with polarization parallel to the plane of optical axis and light propagation direction experiences the "extraordinary" refractive index that depends on the relative angle between polarization direction and optical crystal axis. In contrast, when polarized perpendicular to this plane the light pulse sees the (constant) "ordinary" refractive index. Adjusting the incoming field polarizations and tuning the optical crystal angle allows one to achieve phase matching for a narrow range of mixed frequencies. In "type I" phase matching, the two lower frequency waves have the same polarization, while in "type II" phase matching their polarizations are orthogonal [146].

The detailed parametric frequency converter is schematically shown in Figure 3.1. 1 mJ of the incoming 800 nm pulse is separated into four components, which are used to feed a four-step optical amplification process. 1% of the incoming energy is split off, polarization-rotated by 90°, and focused in a 2 mm sapphire crystal to generate an optical-to-near IR super-continuum [147, 148] via self-phase modulation in a single optical filament. A 5% 800 nm pump pulse is temporally and spatially shifted to collinearly overlap with the refocused white-light pulse in a 4 mm thick BBO (Beta-barium borate, β-BaB_2O_4) crystal where parametric amplification of a near IR signal component from the white-light continuum takes place. The amplified signal is split from the remaining 800nm and the generated idler component with dichroic mirrors, and is then retro-reflected and refocused by a concave mirror with tunable delay into the BBO crystal. Here it is overlapped and amplified by a 800 nm pump pulse containing 20% of the initial 800 nm pulse energy. The pump beam diameter has been reduced with a 4:1 telescope to roughly adapt signal and pump beam sizes. Again the amplified signal component is filtered out with the help of dichroic mirrors. It is boosted in a third amplification step in a second 1 mm BBO crystal to a combined signal (1.2-1.6 μm) and idler (2.4-1.6 μm) power of about 200 μJ. The optical amplification stages each use type II phase matching.

The longest obtainable (idler) wavelengths are limited by the onset of absorption in the BBO crystal above 2.6 μm, which does not allow to cover the full range of vibrational NH stretching modes, and therefore requires a difference-frequency generation (DFG) process. Since the spatial position of signal and idler components are slightly shifted due to walk-off effects in the crystals, both components are split from each other with dichroic mirrors to precisely tune their spacial and temporal overlap with an additional delay stage in the arm of the signal beam in a 0.75 mm thick $AgGaS_2$ crystal. Separation and recombination of signal and idler pulses have been shown to suppress noise and enhance the shot-to-shot stability [149]. DFG in the crystal creates mid-IR output pulses using type I phase matching with center frequencies tunable between 2.7 and 10 μm wavelength. Remaining near-IR and 800 nm components are filtered out by a longpass filter. This setup is used to provide IR pulses around 3.3 μm, with a bandwidth above 250 cm^{-1}, and an energy up to 10 μJ (corresponding to a visible-to-mid-IR power conversion efficiency around 1 %). The shot-to-shot stability of up to 0.2 % rms in the center of the pulse spectrum is extraordinarily good due to the multistep frequency conversion process, exceeding the 800 nm input pulse characteristics. These pulses provide the input for single color pump-probe and 2D-IR measurements around 3 micron. The pulse duration measured with frequency resolved optical gating is around (55±5) fs (see section 3.4).

In order to monitor the systems temporal and spectral response at vibrational modes distinct from those which are pumped, an amplified Coherent Libra-USP-HE Ti:Sa laser system is used to seed two separate parametric frequency converters, each of which are very similar to the one described above except that they use only two amplification stages with subsequent DFG (the third amplification stage indicated by dashed lines in Figure (3.1) does not exist). In this way, independently tunable pump and probe pulses with center frequencies between 2.7 and 10 μm are obtained with pulse energies around 2 μJ and pulse durations around 100 fs, as given by cross correlation measurements.

3.2 Two-color pump-probe spetup

The two separate parametric frequency converters are combined with the two-color pump-probe experiment shown in Figure 3.2. The setup uses an additional reference probe beam that is generated by reflection of the probe beam on the front and backside of a low-dispersive BaF_2 wedge. Both reflections carry an energy of approximately 80 nJ corresponding to a few percent of the pump pulse energy. To ensure that the probe beam experiences a homogeneously excited sample, the beam diameters of the probe pulses are enlarged by a 1.5:1 telescope prior to focusing into the sample by a 30° off-axis parabolic mirror. The focal spot size of the probe beam is therefore reduced by a factor of two compared to that of the pump beam (300 μm). The probe reference beam transmits through the sample slightly outside of the pumped region. The pump beam is blocked for every second pulse by a chopper, which is running on half the lasers repetition rate of 0.5 kHz and synchronized to the Pockels cells of regenerative amplifier cavity. An optical delay line provides a well-defined shift before the pump beam is focused by the same off-axis parabolic mirror described before.

After the sample, both probe pulses are focused in a polychromator and dispersed onto the two lines of a liquid-nitrogen cooled HgCdTe (mercury cadmium telluride, MCT) array detector with 2x64 pixels. The individual MCT detector pixels react with a change in resistivity upon IR radiation, leading to a change in bias current that is integrated over a gate pulse provided by the CPA system. The obtained voltage is proportional to the incoming spectral intensity component and read out by a fast analog-to-digital converter allowing for spectrally-resolved single shot data acquisition. The absorbance change is then measured as:

$$\Delta A(\omega, T) = -log\left[\left(\frac{I^0_{Pr}}{I^0_{Ref}}\right) \cdot \left(\frac{I_{Ref}}{I_{Pr}}\right)\right] \tag{3.4}$$

with I_{Pr} and I^0_{Pr} the spectral probe intensity with and without pump, I_{Ref} and I^0_{Ref} the spectral reference beam intensity with and without pump, and T the pump-probe delay. The reference beam allows one to largely compensate for shot-to-shot laser intensity fluctuations, thus enhancing the pump-probe signal-to-noise ratio by almost an order of magnitude compared to when no reference beam is used. Spatial and temporal overlap of the broadband pump and broadband probe beam in the sample is found by monitoring the strong pump-induced absorbance changes in a thin germanium sample. The two-photon absorption spike during pulse overlap allows one to measure the pump-probe cross correlation giving a measure of the pulse duration and the time-zero position (see also section 3.4).

3.3 Heterodyne-detected three pulse photon echo setup

For the most comprehensive measurement of the third order response function, an additional experimental time delay, introduced by splitting the pump pulse into two pulses, leads to multidimensional spectra via application of multiple Fourier transform (FT) algorithms. Multidimensional

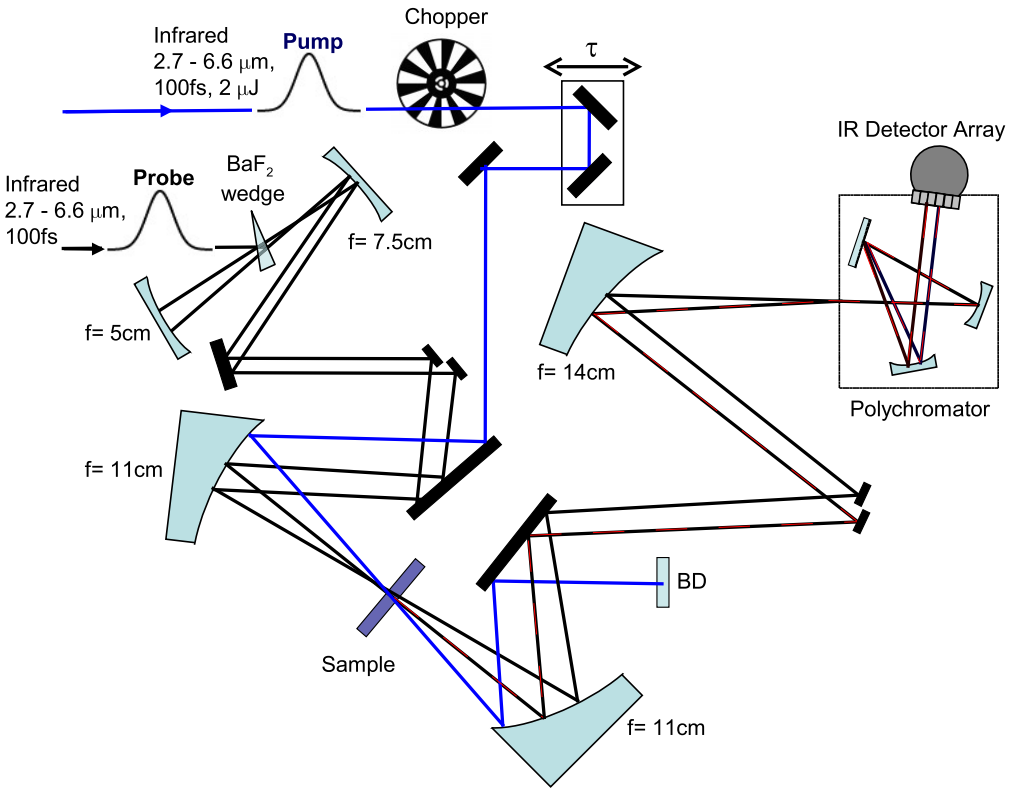

Figure 3.2: *Two-color spectrally dispersed pump-probe setup where the generated third order signal (dashed red line) is self-heterodyned by the probe pulse. A reference pulse is used to compensate for laser intensity fluctuations.*

spectroscopy was first realized in nuclear magnetic resonance (NMR) FT spectroscopy [150, 151]. The dephasing dynamics in hyperfine spin transitions in molecules in an external magnetic field have been probed with multiple radio-frequency pulses to provide structural sensitivity via the assignment of cross peaks to nuclear Ovenhauser effect or scalar spin-spin mediated couplings. However, the micro- to nanosecond resolution of NMR is too slow for directly addressing the various time scales of intra- and intermolecular interactions in liquids going down to the femtosecond time scale. In the optical domain, 7th order/5th order Raman spectroscopy probing the electronic polarizability was first used to map the nonlinear response in 3D/2D frequency dimensions [152–156][b]. The first 2D-IR spectra were based on a dynamic hole-burning approach operating completely in the frequency domain with a narrow-band pump pulse and a short (broadband) probe pulse where the pump center frequency was scanned [118]. Even though the experimental alignment and pulse duration requirements are easier to fulfill, the necessary compromise between time and frequency resolution along the ω_1 frequency axis are considerable draw-backs. Especially for probing ultrafast dephasing and population relaxation dynamics in hydrogen-bonded solution-phase systems, the typical pump pulse duration of 500fs would compromise any dynamic information. Alternatively, the narrow-band pump pulse can be substituted with a collinear femtosecond double pulse pair of tunable delay, as obtained from an Michelson interferometric setup or a pulse shaper [157, 158]. Due to the collinearity of the first two excitation pulses, rephasing and nonrephasing signal contributions are then simultaneously detected and their separation requires extensive phase cycling

[b] Third-order CRS provides the same one-dimensional information as spontaneous Raman scattering [152].

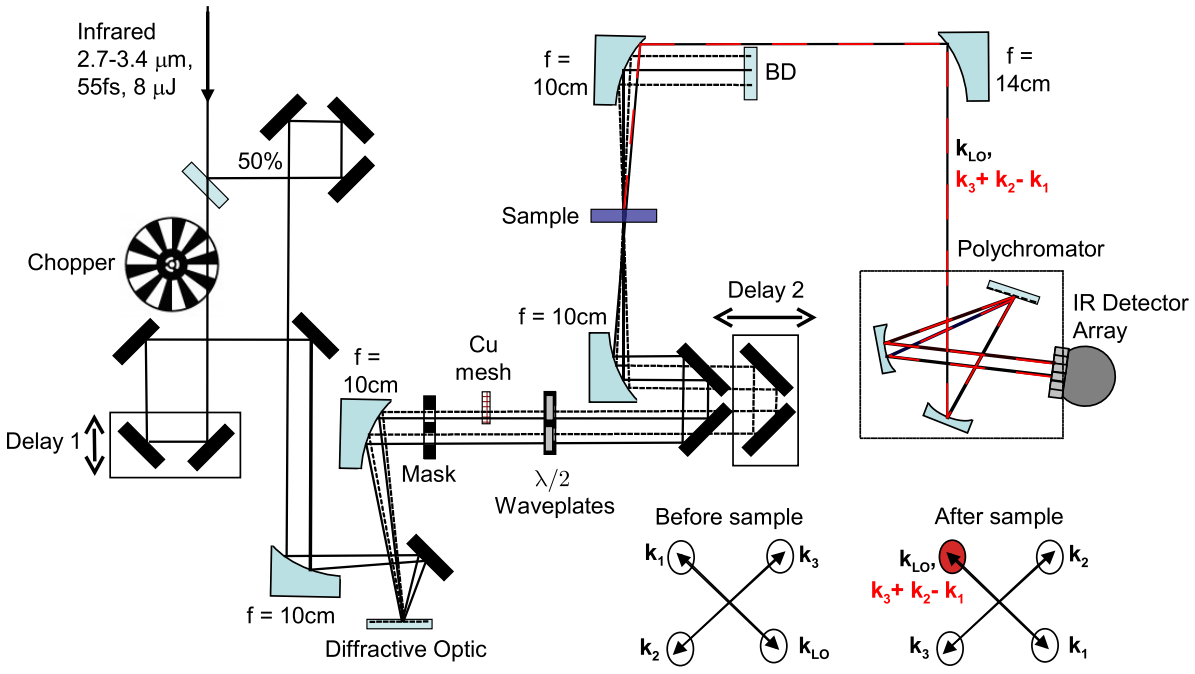

Figure 3.3: *2D-IR three pulse photon echo setup with passive phase stabilization. The generated nonlinear signal is heterodyne detected with a local oscillator pulse to enable phase resolved signal detection using Fourier-transform spectral interferometry.*

procedures [159].

Therefore, we instead use the completely non-collinear three pulse photon echo geometry using four femtosecond infrared pulses. Here, three excitation pulses denoted k_1, k_2, k_3 generate a third-order nonlinear signal into a background-free, phase-matched direction that is different for the rephasing/nonrephasing signal contribution ($-\vec{k}_1 + \vec{k}_2 + \vec{k}_3$/ $\vec{k}_1 - \vec{k}_2 + \vec{k}_3$). The signal field is heterodyned with a fourth weak local oscillator pulse k_{LO} and spectrally dispersed for interferometric phase-resolved signal detection [160, 161] on a square-law time-integrating array detector. The detailed 2D-IR setup is shown in Figure 3.3. The incoming mid-IR pulses of 55 fs pulse duration are first divided by an ordinary 50:50 beam splitter with one pulse being time-shifted by a first optical delay stage 1 and blocked for every second pulse by an optical chopper running at half the repetition rate of the CPA system. Both beams travel parallel on the same height and are focused by a 90° off-axis parabolic mirror onto a reflective optical grating (diffractive optic), which is designed to diffract 35 % of the incoming light into both ± 1 diffraction orders in vertical direction. After recollimation by a second parabolic mirror, a mask blocks all other diffraction orders, leaving only 4 replica IR pulses traveling on the corners of a square (box-car geometry). The polarization of each pulse is individually rotated by zero-order MgF_2 $\lambda/2$ waveplates. The two pulses k_2 and k_{LO} traveling at a lower height hit a second optical delay stage 2, while the upper two pulses k_1 and k_3 hit a fixed retroreflector. In total, the first delay stage 1 shifts both k_1 and k_2, while delay stage 2 shifts both k_2 and k_{LO}. The pulse k_3 stays fixed at all times and is retarded with respect to the local oscillator pulse k_{LO} by traversing a 0.5 mm thick CaF_2 window, which induces a delay of about 850 fs. Often the LO pulse will therefore be the first pulse to transverse the sample and remain unaffected by possible distortions due to transient sample absorption induced by the other pulses. After the LO pulse is attenuated with a copper mask by two orders of magnitude, all four

pulses are focused into the sample by another 90° off-axis parabolic mirror. Their beam diameter in the focus is about 120 μm as measured with the knife-edge technique.

In the experiment, for a few fixed waiting times τ_2 the coherence time τ_1 is scanned to cover the full dephasing process of the system occurring after the coherent excitation by the first pulse. The setup allows to independently shift the three excitation pulses against each other: while delay stage 2 sets the delay between the first two pulses (τ_1, coherence time), delay stage 1 needs to be incremented in concert with the coherence time to ensure a constant delay between the second and third pulse (τ_2, population time) in the case of positive coherence times. In contrast, when pulse k_2 arrives before k_1 ($\tau_1 < 0$), delay stage 1 stays fixed at the desired population time position. For the rest of this manuscript, the coherence time will be addressed as τ and the waiting time as T.

All four pulses are aligned noncollinear to one another when hitting the sample. The theoretical treatment of photon echo spectroscopy in chapter 2 yielded the photon echo signal as arising from a stepwise third-order light-matter interaction with the signal field propagation direction k_S given by the phase-matching condition. Alternatively, the signal field can be viewed as stemming from a diffraction process: The first two excitation pulses $\vec{k}_1$ and $\vec{k}_2$ generate a spatial intensity and refractive index grating with a grating vector $\Delta\vec{k}_{12} = \vec{k}_2 - \vec{k}_1$. For resonant excitation, this may transform into a population grating, which decays due to population relaxation and molecular diffusion. Finally, the third pulse k_3 gets diffracted from this grating into the background-free direction $\vec{k}_S^{\pm} = \vec{k}_3 \pm \Delta\vec{k}_{12}$, with $\vec{k}_S^{+}$ indicating the emission direction of the photon echo field and $\vec{k}_S^{-}$ indicating the propagation direction of the virtual echo.

The box-cars geometry ensures that the generated signal field $\vec{k}_S^{+}$ travels collinear to the LO pulse, which allows the reference pulse to "heterodyne" the nonlinear signal (see the right bottom part of Figure 3.3). Both pulses are focused onto the entrance of a spectrometer and spectrally dispersed by a grating onto a single-line, liquid-nitrogen cooled HgCdTe (mercury cadmium telluride, MCT) detector array with 16 pixels yielding spectral intensities on a shot-to-shot basis as explained before. For coverage of a desired spectral bandwidth, the tilting angle of the grating is changed to measure several weakly overlapping spectral windows. The chopper blocks for every second shot the two excitation pulses k_1 and k_2 while k_3 and k_{LO} stay unaffected. The setup can therefore also be used as a single-color pump-probe spectrometer. Here the k_3 pulse, attenuated to a few percent, serves as probe and k_1 or k_2 as pump pulse, while the remaining pulses are blocked. The absorbance change ΔA is then measured as

$$\Delta A(\omega, T) = -log(I_{Pr}^0/I_{Pr}) \tag{3.5}$$

with I_{Pr}/I_{Pr}^0 the probe intensity with/without the pump pulse and T the pump-probe delay. This also allows one to easily find the spatial and temporal overlap in the sample of all excitation pulses defining the time zero position for the two delay stages in a way identical to that explained above. While pump-probe measurements allow covering a big range of delays (limited only by the extension of the delay stage) with narrow step size and are fairly quick, the recording of only one 2D spectra takes 30-90 minutes, corresponding to 150-450 coherence time delays with step sizes of 4 fs (depending on the dephasing time of the system). Therefore, the number of recordable waiting times is typically limited to a maximum of 12 due to the limited long-term laser stability.

Fourier-transform spectral interferometry

The setup allows one to record the LO spectrum ones with and without the contribution from the nonlinear third order signal. Subtraction of two subsequently recorded spectra therefore directly yields the spectral interference pattern $I_{SI}(\omega_3, \tau, T)$ between the LO and the nonlinear signal field

for a given coherence time τ and waiting time T:

$$\begin{aligned} I_{SI}(\omega_3,\tau,T) =& \left| \int_0^\infty \left(E_{sig}(\tau_3,\tau,T) + E_{LO}(t_{LO}-\tau_3)\right) e^{i\omega_3\tau_3} d\tau_3 \right|^2 - I_{LO}(\omega_3) \\ \approx& 2Re\left\{ \int E_{Sig}(\tau_3,\tau,T) e^{i\omega_3\tau_3} d\tau_3 \int E^*_{LO}(\tau_3-\tau_{LO}) e^{-i\omega_3(\tau_3-\tau_{LO})} d\tau_3 \right\} \\ =& 2Re\left\{ E_{LO}(\omega_3) E_{Sig}(\omega_3) e^{-i\omega_3\tau_{LO}} \right\} \end{aligned} \tag{3.6}$$

Here τ_{LO} is the delay between k_3 and LO, E_{LO} is the LO field for $\tau_{LO} = 0$, and the weak homodyne signal intensity component was neglected. The combined frequency resolution of grating and detection array (i.e. the pixel size) of about 8 cm^{-1} is sufficient to stretch both the LO and signal field in time to more than 1.8 ps. Therefore, they will interfere on the detector despite being completely time-separated when hitting the sample. The spectral interference fringes have a period inversely proportional to the delay between signal and the LO. While any scattering contributions from k_3 into the direction of the local oscillator are suppressed, interferences with scattered k_1 and k_2 light can be hard to distinguish from the wanted coherent nonlinear signal. This enforces the use of samples with sufficiently high optical quality, even though the FT procedure explained below allows for filtering out these unwanted contributions to a big extent. The amplification in the heterodyne detection allows one to measure signal intensities as low as few tens of pico-joules.

To extract the complex signal field from the measured frequency-domain interference traces, a Fourier-transform algorithm is used [162]. Defining $f(\omega_3) = E_{LO}(\omega_3)E_{Sig}(\omega_3)$, the (real-valued) interference signal can be written as:

$$I_{SI}(\omega_3,\tau,T) = 2Re\left\{ f(\omega_3) e^{i\omega_3\tau_{LO}} \right\} = 2\left[f(\omega_3) e^{i\omega_3\tau_{LO}} + f^*(\omega_3) e^{-i\omega_3\tau_{LO}} \right] \tag{3.7}$$

Therefore, the inverse FT of the frequency domain interference signal yields two contributions in the time domain which are symmetric around zero (see Figure 3.4 (b)):

$$FT^{-1}\left\{ I_{SI}(\omega_3,\tau,T) \right\} = \tilde{I}_{SI}(\tau_3,\tau,T) = f(\tau_3-\tau_{LO}) + f(-\tau_3-\tau_{LO}) \tag{3.8}$$

The coherent signal has to obey causality and is emitted only after the arrival of the third pulse. Therefore contributions $f(-\tau_3 - \tau_{LO})$ at negative times have to be discarded. Of interest are only those heterodyned signal contributions that occur at a similar time as the arrival of pulse 3. Therefore, a super-Gaussian window function centered around $t = \tau_{LO}$ is applied to pick out the coherent signal contributions which allows one to filter out scattering and transient absorption signals to some extent. Back-fourier transformation of the so-selected signal gives the complex signal field $E_{Sig}(\omega_3)$ for a given coherence time τ and waiting time T (see Figure 3.4 (c)):

$$E_{Sig}(\omega_3,\tau,T) = FT\left[\Theta(t) FT^{-1}(I_{SI}(\omega_3,\tau,T) \right] \tag{3.9}$$

with $\Theta(t)$ indicating a Super-Gaussian filter function (i.e. as indicated in Figure 3.4 (b)). Even though the initially measured interference term is a real valued quantity, this procedure allows one to recover both the amplitude and the phase of the nonlinear signal field, stressing the mutual dependence of the imaginary and real part given by the Kramers-Kronig relation.

A change Δt_i of the absolute arrival times of the optical pulses k_i will translate in a changing spectral interference pattern for a rephasing signal as:

$$\begin{aligned} &I_{SI}(\omega_3,\tau,T) = 2Re\left\{ E_{LO}(\omega_3) E_{Sig}(\omega_3) e^{i\phi} e^{-i\omega\tau_{LO}} \right\} \\ &\text{with } \phi = \omega(-\Delta t_1 + \Delta t_2 + \Delta t_3 - \Delta t_{LO}) = \omega(\Delta\tau_1 - \Delta\tau_{LO}) = (\phi_3 - \phi_1) + (\phi_2 - \phi_{LO}) \end{aligned} \tag{3.10}$$

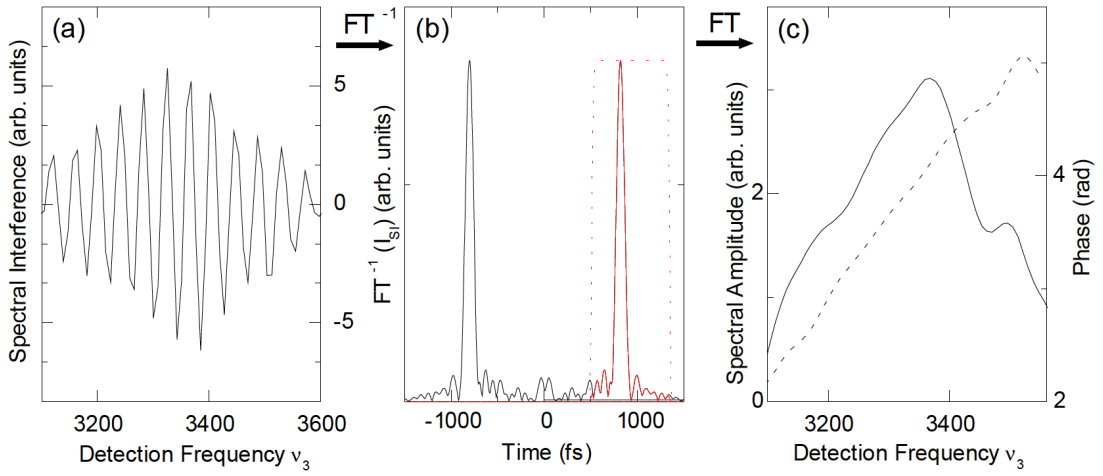

Figure 3.4: *(a): Interference pattern in spectral domain for a given coherence and waiting time. (b): Inverse Fourier transform delivers the corresponding time domain trace. (c): Spectral amplitude (solid line) and phase (dotted line) obtained by Fourier transforming only those time domain components selected by a super-Gaussian filter function (red dots in (b)).*

Here ϕ_i indicates the phase drifts of the individual pulses, $\Delta\tau_1$ a change in the coherence time and $\Delta\tau_{LO}$ a change in the delay between k_3 and k_{LO}. This equation has two important repercussions:

First, for a stable long-term interferometric signal, the total phase ϕ defined in the latter equation has to be stabilized to zero. In principle, mechanical shifts in the position of optical elements in the path of the individual beams may lead to temporal phase drifts. In the setup after the generation of two phase-locked pulse pairs (k_1, k_2) and (k_3, k_{LO}) by the diffractive optics, the pulses k_1 and k_3 hit the same optical elements which is also true for k_2 and k_{LO}. Therefore any phase jitter due to spacial shifts in mirror positions will affect k_1 and k_3 as well as k_2 and k_{LO} in the same way, canceling the total phase ϕ in equation (3.10) to zero. This passive phase stabilization scheme [163, 164] reduces phase fluctuations to below $\lambda/120$ at 3 micron during a period of hours and is more easily implemented than active-phase stabilization schemes requiring interferometric reference measurements for feedback [165].

Second, in our setup a change $\Delta\tau_1$ in the coherence time is inevitably connected to an identical shift in the time position of the local oscillator pulse $\Delta\tau_{LO}$, since pulse k_2 and k_{LO} hit the same movable mirror used for setting the τ_1 delay. Therefore according to equation (3.10), for a certain detection frequency the interference amplitudes during a scan in coherence time will not show an oscillatory signal as a function of frequency ω_1. Instead only the envelope of the nonlinear response function is measured (see Figure 3.5 (a)) and the experiment is performed in the fully "rotating frame". Since no longer a highly oscillating signal (period around 10fs for 3 microns) but only its envelope needs to be measured, measuring in the rotating frame enables under-sampling, which allows one to reduce measurement time. Otherwise the highest frequency component in the coherence dephasing process, i.e. the highest recordable emission frequency, dictates the maximum possible step size of the coherence scan according to the Nyquist theorem. We did not make use of under-sampling but used a 4fs step size. In order to recover oscillations with the right system fundamental frequency, the complex signal field $E_{Sig}(\omega_3, \tau, T)$ is multiplied with a factor $e^{-i\omega_3(\tau-\tau_{LO})}$ (see Figure 3.5 (b)).

Since now the spectral amplitude and the phase of the nonlinear signal field is known, it can be Fourier-transformed with respect to the coherence time τ. This generates the excitation frequency axis, yielding the nonlinear third order susceptibility as a function of detection and

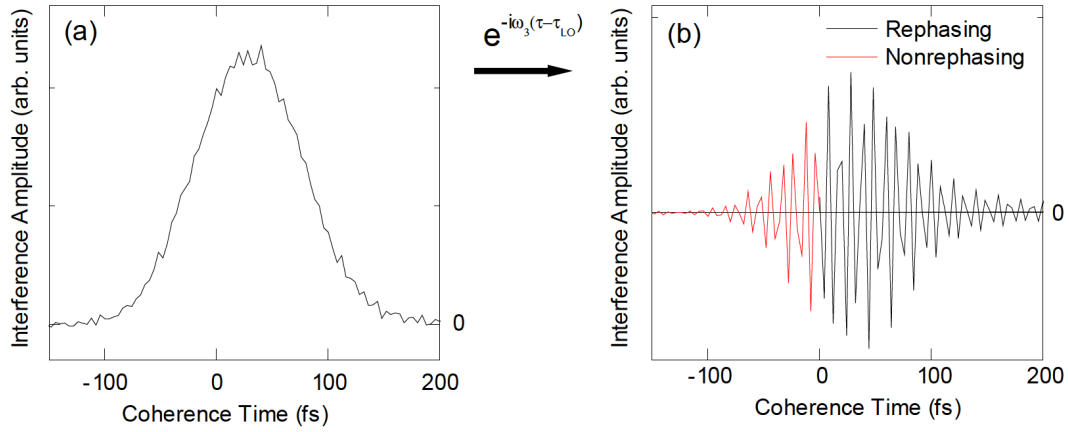

Figure 3.5: *Interference amplitude vs. coherence time for a selected detection frequency (a) in the full rotating frame where the LO temporal position moves in concert with the delay τ_1. Multiplication with a phase factor $e^{-i\omega_3(\tau-\tau_{LO})}$ yields oscillations with the fundamental frequency ω_1 (its real part is plotted in (b)).*

excitation frequency. A good signal-to-noise 2D spectra free of artifacts requires the scan range of the coherence time τ to cover the complete dephasing process to avoid truncation effects in the FT. At the same time τ should not exceed twice the dephasing time T_2 to prevent noise fluctuation dynamics from entering the 2D spectrum. The sensitivity to noise fluctuations therefore limits the effective resolution in the detection frequency direction. For high coherence times we use zero-padding by roughly a factor of 2 (adding zeros to the time domain data) to enhance the point density in ω_3-direction after the FFT procedure.

This procedure is applied for both the $\tau > 0$ and the $\tau < 0$ time domain yielding the rephasing and nonrephasing 2D spectra. The sum of both yields a complex-valued 2D spectrum where the real part shows the absorptive and the imaginary part the dispersive nonlinear third order response. However, in order to clearly separate these two components, the absolute phase of the nonlinear complex signal needs to be measured, i.e., especially the absolute temporal delay of the LO-pulse with interferometric precision. Here we make use of the projection-slice theorem, which states that the real part of the 2D spectrum integrated over the ω_1 frequency equals a spectrally dispersed pump-probe transient absorption measurement:

$$I_{PP}(\omega_3, T) = Re\left\{\int d\omega_1 S_{2D}(\omega_1, T, \omega_3) e^{i\Phi_0 + i\omega_3 \Delta t}\right\} \tag{3.11}$$

A constant phase offset Φ_0 as well as a linear phase factor $\omega_3 \Delta t$ accounting for uncertainties in the delay between k_3 and the LO is varied until the best agreement between both measurements is achieved, which allows one to fix the delay up to a fraction of a femtosecond. Typical qualities of this "phasing" process are shown in Figure 3.6 for different molecular systems. The properly phased 2D spectra is divided by the square root of the independently measured LO spectral intensity to correct for the heterodyning amplification process. In order to roughly correct for reabsorption processes within the sample, the complex signal field is additionally divided by the sample transmission. Finally, the 2D spectra is divided by the scaling factor used to fit the pump-probe and the projected 2D data, which corrects for slow drifts in laser intensity for different waiting time spectra.

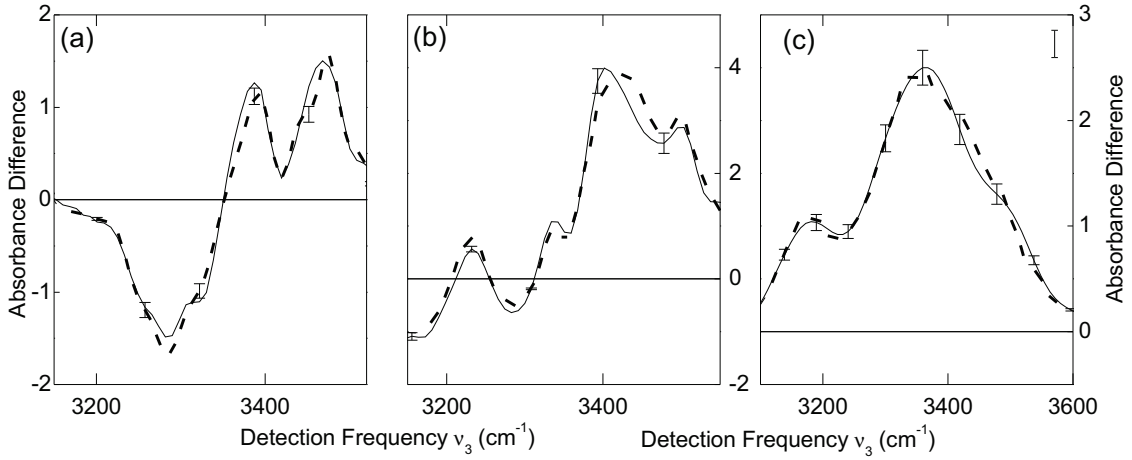

Figure 3.6: *In order to set the absolute phase of the nonlinear signal, the spectrally dispersed pump-probe spectra (dashed line) are compared with with the real part of ω_1-integrated 2D spectra (solid line) for different molecular systems each at 150 fs waiting time. Good agreement is achieved when deviations are not higher than 7% (see error bars).(a): Aniline monomer, (b): Aniline$-(DMSO)_2$, (c): G·C oligomers 0% R. H.*

3.4 Characterization measurements

IR pulse characterisation

A proper characterization of the employed ultrashort IR pulses is crucial to understand the measured third-order signals of a molecular system. The spectral amplitude and phase completely define the temporal behavior of any optical pulse. However, typical nanosecond response times of current photo detectors are too slow to directly follow the oscillating field of an mid-IR pulse. A linear device, e.g. a Michelson interferometer or a grating spectrometer coupled to a time-integrating detector, cannot measure the spectral phase of an isolated pulse, only its spectral intensity [162]. We therefore make use of second and third order nonlinearities to analyze our mid-IR pulses. In intensity cross-correlation measurements, a reference pulse and the probe pulse of interest cross noncollinearly with tunable delay T in a nonlinear media with non-vanishing second-order susceptibility and the (instantaneously) generated nonlinear signal is measured by a time-integrating detector:

$$G_2(T) \propto \int_{-\infty}^{\infty} dt |E(t)E_{Ref}(t-T)|^2 = \int_{-\infty}^{\infty} dt I(t) I_{Ref}(t-T) \tag{3.12}$$

This second-order intensity cross-correlation function $G_2(T)$ allows one to estimate the pulse duration if a certain temporal shape is assumed. If both pulses have Gaussian temporal shapes and identical pulse duration, $G_2(T)$ will be also Gaussian with a FWHM exceeding the pulse duration of I(t) by a factor $\sqrt{2}$. Similar deconvolution factors exist for $sech^2$ shaped pulses (1.543) which is why for smoothly varying pulse shapes, even without proper knowledge of the pulse shape, the pulse duration can be obtained within an error of 10%. In our experiments, we use the two-photon absorption nonlinearity in a 70 μm thin germanium/ indium arsenide semiconductor (band gap $\approx$ 0.67 eV/ 0.35 eV @ 300 K) for analyzing pulses of 3 respectively 6 microns. The simultaneous presence of two mid-IR photons ($3\mu m \approx 0.41eV$) allows with a certain probability for exceeding the band gap which reflects in an enhancement of absorption for both beams during pulse overlap. The two setups described above operated as pump-probe spectrometers with spectrally integrated detection easily allow one to measure the absorbance change of the probe beam. For a weak probe

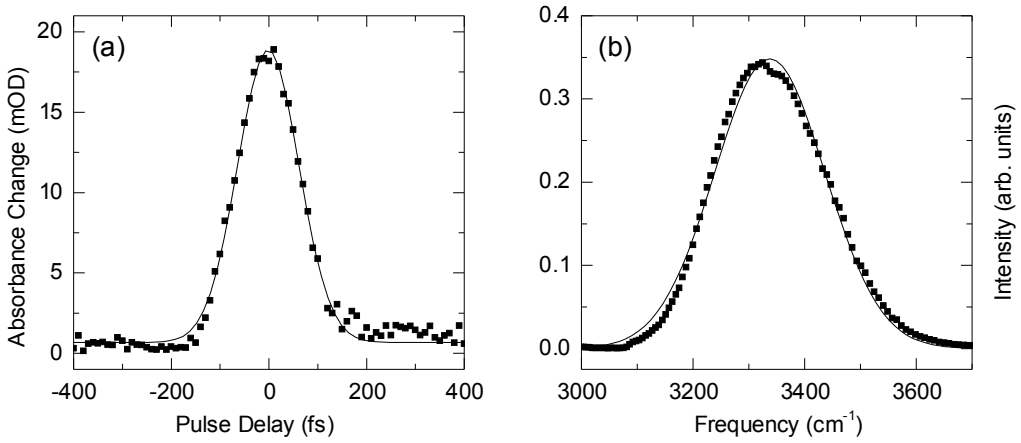

Figure 3.7: *(a) Typical pump-probe cross-correlation measurement using the two-photon absorption signal in Ge for 3 micron pulses. The FWHM of 150 fs implies a pulse duration around 105 fs. (b) Spectral intensity distribution with a FWHM of 240 cm^{-1}.*

pulse, $\Delta A(T)$ is in first approximation proportional to the intensity cross correlation signal $G_2(T)$. In addition, the pump reference pulse needs to be sufficiently attenuated to prevent notable two-photon absorption already from the reference pulse which otherwise would lead to a long-lived absorption signal due to the generation of free excitons in the substrate, overlaying the desired pump-probe two photon absorption signal. A typical intensity cross correlation measurement in the mid-IR two-color pump-probe setup yields pulse durations around 100 fs while the spectral bandwidth is around 250 cm^{-1} (see Figure 3.7). The time bandwidth product $\tau\Delta\upsilon = 0.76$ implies not perfectly transform-limited pulses.

A complete reconstruction of the temporal shape (except for the carrier envelope phase) of ultrashort pulses is possible using frequency-resolved optical gating (FROG) [166]. We use the transient-grating (TG)-diffraction variant, where two noncollinear beams overlapped in a $\chi^{(3)}$ medium generate a nonlinear refractive index grating (the gate), from which a third beam is diffracted with variable delay T in its phase-matched direction. A FROG trace is obtained by measuring the power spectrum of the diffraction signal as a function of the delay, known as a spectrogram. The noncollinear three pulse photon echo setup described above allows one to direct measure the third-order intensity autocorrelation function:

$$G_{TG}(T) = \int_{-\infty}^{\infty} dt|E(t)E(t-T)E*(t-T)|^2 = \int_{-\infty}^{\infty} dtI(t)I^2(t-T) \tag{3.13}$$

Typical FROG traces recorded with a 0.5 mm thin CaF_2 sample without and with chirp compensation are shown in Figure 3.8 (a) and (b). Since CaF_2 shows a negative second-order dispersion in contrast to most other materials, the addition of a sufficient amount of CaF_2 in all optical paths allows one to compensate for some of the quadratic temporal phase [167] introduced during previous optical mixing and propagation through filters and beam splitters. A complex iterative algorithm in principle allows one to recover the complete spectral amplitude and phase from the spectrogram. However, assuming a Gaussian temporal pulse shape the pulse duration σ can be already estimated from the spectrogram:

$$\sigma = \frac{\sigma_{G_{TG}}}{\sqrt{3/2}} \tag{3.14}$$

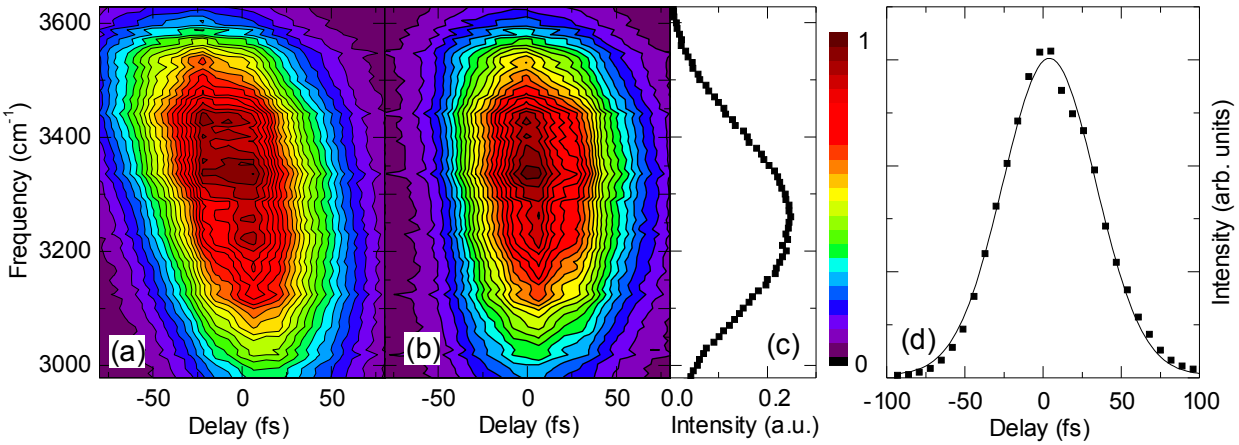

Figure 3.8: *Typical transient-grating FROG traces of the (a) uncompensated negatively chirped and (b) chirp-compensated 3 micron pulses by inserting 8mm CaF_2 into the optical beam path. (c) Pulse spectrum with a FWHM of about 350 cm^{-1}. (d) FROG signal intensity as a function of the waiting time from (b), integrated over frequency with a Gauss fit (solid line) with FWHM of 70 fs. The estimated pulse duration of 57 fs yields a time-bandwidth product $\Delta\omega\tau$ of 0.60 close to the value for a transform-limited Gaussian pulse (0.44).*

Here $\sigma_{G_{TG}}$ is the FWHM of the spectrogram integrated over frequency. The obtained pulse durations of $\sigma = (57\pm 5)$fs for typical linear chirp-compensated 3 micron pulses gives time-bandwidth products around 0.60 indicating nearly transform-limited ultrafast pulses. Typical pulse parameters of ultrafast mid-IR pulses used in the 2D-IR and two-color pump-probe setup are summarized in table 3.1.

Setup	Experiment	Bandwidth (FWHM)(cm^{-1})	Pulse Duration (fs)	Time-Bandwidth Product
2-color Pump-Probe	Cross-correlation	240	105	0.76
2D-IR	TG-FROG	350	55	0.60

Table 3.1: *Typical pulse parameters for different experimental conditions.*

Polarization anisotropy in 2D-IR spectra

As explained in the previous chapter, since the nonlinear response results from the successive molecular interactions with 4 polarized light fields, the nonlinear third order signals depend on the angles between all the involved molecular transition dipoles. This allows one to extract relative transition dipole angles from the different scaling of cross and diagonal peaks with polarization as well as the suppression of particular peaks in the 2D-IR spectrum. The accomplishable quality of both aspects, i.e. the error bars, is now analyzed looking at the NH stretching region of the $Aniline\cdot\cdot(DMSO)_2$ molecule. The double hydrogen-bonded amino group not only ensures high IR cross sections, but also the relative transition dipole orientations are already quite well understood from the linear IR spectra [168] (see chapter 8).

In the 3100-3500 cm^{-1} region, this molecule shows three strong IR transitions (see Figure 3.9

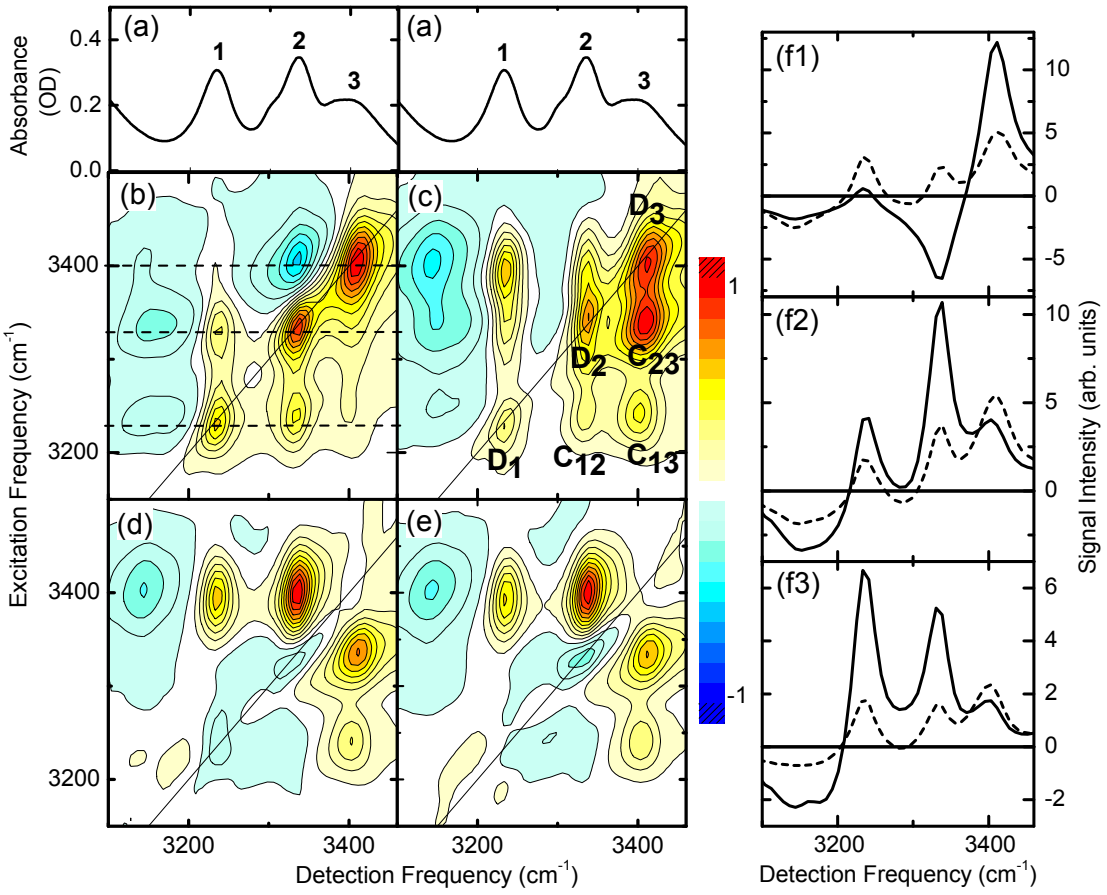

Figure 3.9: *Polarization-anisotropy effects studied on the Aniline−$(DMSO)_2$ molecule. (a) Linear FT-IR spectra in the 3100-3500 cm^{-1} region with two parallel transitions labeled 1 and 2 and a third band 3 with perpendicular dipole orientation. (b) Absorptive 2D-IR spectra in ZZZZ and (c) ZZXX polarization configuration at 200fs waiting time with labeling of the positive peaks. (d) Calculated difference spectra ZZZZ- 2.4 ZZXX. (e) 2D-IR spectra recorded in (60°/-60°/0°/0°) polarization geometry with a 200fs waiting time. (f1-f3) Horizontal slices along the 2D spectra in (b) (solid lines) and in (c) (dashed lines) for different excitation frequencies of 3400 cm^{-1} (f1), 3330 cm^{-1} (f2) and 3230 cm^{-1} (f3).*

(a)): two low-frequency bands at 3235 (Fermi-resonance enhanced NH_2-bending overtone) and 3350 cm^{-1} (symmetric NH-stretch fundamental) labeled as band 1 and 2 that are perfectly parallel to each other, and a third high frequency band at 3400 cm^{-1} (asymmetric NH stretch fundamental, band 3) perpendicular to either of the two. Absorptive 2D-IR spectra in (k_1, k_2, k_3, k_{LO}) = ZZZZ and ZZXX polarization geometry with a waiting time of 200fs are shown in Figure 3.9 (b) and (c). In the following only the positive (yellow-red) cross peaks below the diagonal are considered due to reduced overlap with negative (blue) peaks arising from transitions involving the double-excited states. While the diagonal peaks D_1, D_2, D_3 decrease by a factor of 3.6/ 2.9/ 2.4, the cross peak C_{12} scales down by a factor of 3.1. In contrast the C_{13}, C_{23} cross peaks both decay only slightly by a factor of 0.8. The relative changes of cross and diagonal peak intensity are best visualized by cuts at fixed excitation frequencies in Figure 3.9 (f1-f3). The ratio of C_{12} cross to diagonal peak intensity (Figure 3.9 (f3)) shows a minor decrease by a factor $f(\theta_{12}) = 1.1$ (expected: 1.0). In contrast, the ratio of C_{23} cross to diagonal peak intensity (Figure 3.9 (f2)) shows an increase by a factor $f(\theta_{23}) = 3.8$ (expected: 3.6). These strongly coupled transitions allow one to determine

$f(\theta_{ab})$ with an error around 10% corresponding to an error in relative angle up to 20° (see Figure 2.9). In contrast, the ratio of the weaker C_{13} cross peak to diagonal peak intensity (Figure 3.9 (f3)) shows an increase by a factor $f(\theta_{13}) = 4.9$ (expected: 3.6). This gives the factor $f(\theta_{13})$ with an error of 40%, here corresponding to an deviation in angle by about 30°. Reliable angles require cross peaks clearly separable from any other peaks to prevent systematic errors, and need a good phasing and signal-to-noise interference quality. Moreover, intense cross peaks for both ZZZZ and ZZXX polarization conditions are necessary, which is why this procedure works best for carbonyl stretching vibrations having a transition dipole strength a factor of 4 higher than NH stretching modes with a medium-strong hydrogen bond [52,54,113,141].

It should be noted that in the setup contributions from scattering of pulse k_3 are erased (k_3 is not chopped), while the same is not true for scattering from k_1 and k_2. Here polarization rotation by 90° of the latter two pulse (ZZXX geometry!) with respect to k_{LO} allows one to drastically reduce their scattering contributions to the recorded spectral interferences by about one order of magnitude thanks to the heterodyne detection scheme.

Manual subtraction of the two 2D spectra recorded in ZZZZ and ZZXX geometry, each scaled to their respective diagonal peak maximum, yields the difference plot in Figure 3.9 (d). Here the best scaling factor for the intensity of the ZZXX spectrum was found to be 2.4, slightly below the theoretically predicted value of three[c]. Almost indistinguishable results are obtained from a single 2D spectrum recorded in (60°/-60°/0°/0°) polarization geometry with again a 200 fs waiting time (Figure 3.9 (e)). In both cases, the diagonal peaks as well as the cross peak from parallel transition dipoles are eliminated by about 97%, which compares well to the peak suppression qualities reported by other groups. Diagonal peak suppression works only for nonzero waiting times.

[c]This difference probably results from minor overlap of the D_3 diagonal peak with the C_{23} cross peak where the latter shows an strong enhancement in the ZZXX geometry.

4 Static and dynamical properties of hydrated double-helical DNA

Before presenting the results obtained during this thesis in the next chapters, this chapter highlights those static and dynamic structural and vibrational properties of DNA nucleobases and hydrated DNA, which are of relevance for an understanding of the following chapters.

4.1 Molecular structure

Nucleic acids contain a long sequence of nucleotides with each nucleotide being composed of a nitrogeneous nucleobase that is attached to a backbone composed of a 5-carbon sugar and a negatively charged phosphate group as shown in Figure 4.1. The genetic information is encoded in the sequence of DNA (RNA) nucleobases adenosine, thymidine (uracil), guanine, and cytosine, which are attached along the alternating deoxyribose (ribose) sugar-phosphate backbone [4]. In its native form, DNA comprises two helical antiparallel chains with each chain coiled around the same axis, forming the famous double-helix structure. The two macromolecular strands are bonded to each other via multiple hydrogen-bonds between the DNA nucleobases. The particular hydrogen-donor and -acceptor positions along the different nucleobases ensure complementary base pairing, i.e., only pairing between the conjugate binding partners adenosine (A) and thymidine (T), and between guanine (G) and cytidine (C). Hydrogen-bonding occurs between the NH motifs in the primary or secondary amine group and the carboxylic oxygen or nitrogen of the conjugate binding partner. Base-pairing complementarity is a crucial requirement for the transcription and replication of genetic information. During the process of transcription, well-defined parts of the nucleobase sequence are transformed into single-stranded (antisense) messenger RNA that is read out again at the ribosomes for protein synthesis. Thereby, the sequence of three nucleobases specifies a certain amino acid and, hence, gives the building plan for the synthesis of proteins. The nucleobases are classified into the purines A and G, which contain two fused five- and six-membered heterocyclic rings, and the pyrimidines T and C, which are composed of only one six-membered heterocyclic ring. For G·C base pairs, the most stable base pairing geometry includes three intermolecular hydrogen bonds, while A·T base pairs contain only two. Recent field-ionization mass-spectrometric gas phase analysis, which measure the temperature-dependent evaporation rate of crystalline species, yielded a formation enthalpy of -88 kJ/mol (0.91 eV) for G·C pairs in contrast to only -51 kJ/mol (0.53 eV) for A·T pairs [169]. Though most duplex DNA is composed of complementary strands associating solely through Watson-Crick base pairing, in a small number of DNA structures, especially at places of distortion by proteins or intercalated molecules, Hoogsteen base pairing (cf. Figure 6.1 (b)) has been found [170,171]. In addition, wobble (A·C, G·T) mispairs, triple and quadrupole helices, and parallel dublexes have been observed in exotic cases.

The tertiary DNA structure is not only dependent on hydrogen bonding interactions between the complementary bases adenine-thymidine and guanine-cytosine of the two strands and base stacking interactions among the aromatic π electron systems of the nucleobases (16-58 kJ/mol/stacked pair depending on the DNA sequence [174]), but also significantly influenced by the formation of a water shell at the DNA interface. In biological systems, the B-form DNA structure [175] discovered by Watson and Crick [6] is predominant. It shows a parallel stacking of planar nucleobases with

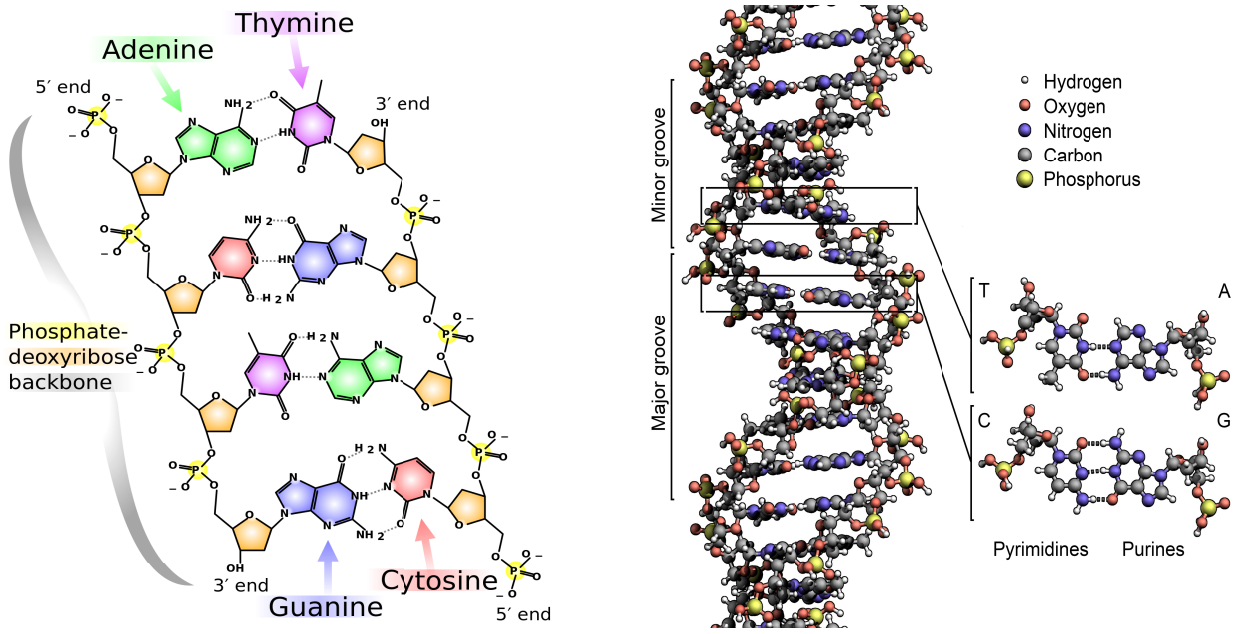

Figure 4.1: *Left: Complementary hydrogen-bonded base pairs of thymine-adenine and guanine-cytidine embedded in a sugar-phosphate backbone (taken from [172]). Right: The tertiary DNA structure of the biologically most abundant B-form (taken from [173]).*

a vertical interbase distance of 3.4 $\AA$ and a total helix diameter around 20 $\AA$ [2] (Figure 4.2). As the two strands are not symmetrically located with respect to each other, the vertical distances of the sugar-phosphate backbones, called the DNA grooves, are distinctly different, with the "major" groove being 22 $\AA$ wide and the "minor" groove spanning only 12 $\AA$ [175] (see Figure 4.3 (b1,c1)). In special environmental conditions, such as for low water content, high salt concentration, or in alcoholic solutions, there exist different DNA conformations [176,177], such as A [178]- and Z [179]-DNA (Figure 4.2) and other very exotic structures. Only B-DNA and Z-DNA have been directly observed in biological systems. The DNA ternary structures differ in helical diameter and twist, the inclination angle of the base pairs relative to the helical axis, and the vertical distance per full turn. While B-DNA shows a total of 10 base-pairs per 360° turn, for A- and Z-form DNA 11 and 12 base-pairs are found, respectively [180]. Moreover, while for B-DNA the major groove greatly exceeds the width of the minor groove, for A-DNA the situation is reversed. To avoid confusions, the groove nomenclature always refers to the situation in B-form DNA. While A- and B-DNA are both right-handed structures, Z-DNA is left-handed. The unusual Z-from structure is distinguished by the zig-zag form of the phosphate and sugar backbone and is only found in GC-rich DNA and for certain purine-pyrimidine base sequences. The detailed structural properties such as groove width, helical twist, and mechanical rigidity of the helix may be influenced by the base sequences. Such structural variations, especially the minor groove width, are predicted to be important recognition motifs for proteins, drugs, or for enzymes in the transcription and replication process of genetic information.

Secondary DNA structure and base pairing geometries have been studied by X-ray diffraction of quasi-crystalline nucleic acid fibers containing oriented DNA polymers and of single-crystal oligonucleotides, the latter providing higher spatial resolution [2,11,14,182,183]. Neutron diffraction measurements, using bright neutron sources as provided by nuclear research reactors, provided

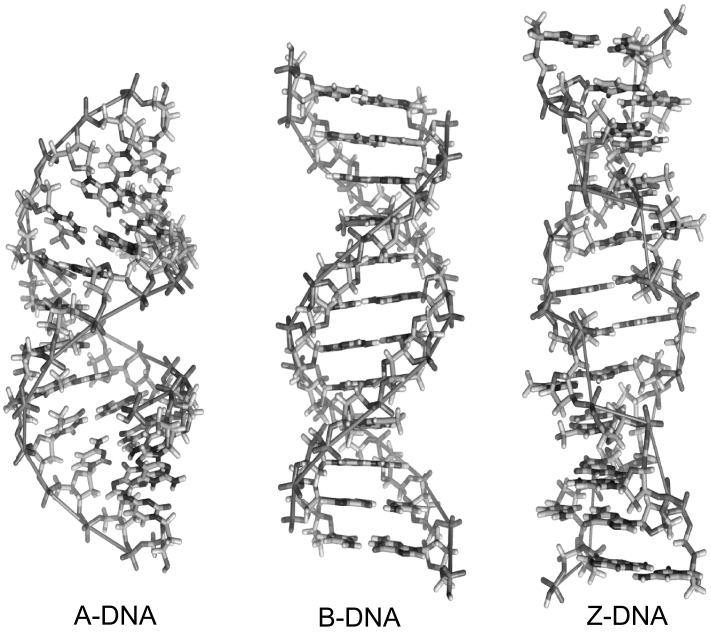

Figure 4.2: *The most important DNA conformations of the A-, B-, and Z-form (taken from [181]). Their formation depends on environmental conditions such as water content and salt concentration.*

complementary information on the hydrogen atom positions [184–186]. Structural information on base pairs in solution has been obtained by linear UV and IR absorption, circular dichroism [176,187], and one-dimensional and multidimensional NMR spectroscopy [18,188]. The combination of NMR results with crystallographic information and quantum chemical calculations allowed for comprehensive insight into the structural equilibrium geometries of DNA.

Hydrogen-bonded base pairs have been investigated in solution phase with Fourier transform IR spectroscopy [189–193] and in gas phase [194–196]. In the latter case, the low density in supersonically expanded molecular beams greatly complicates standard linear absorption measurements. Therefore, mostly resonantly-enhanced multi-photon ionization, especially IR-UV double-resonance spectroscopy, or vibrationally-mediated photodissociation spectroscopy [197] is performed. Resonant excitation by the tunable IR pulse is detected via the observation of the corresponding ion or photofragment signal in the time-of-flight mass spectrum. In order to transfer molecular species in the gas phase, evaporation from a heated oven or laser ablation is typically used, which entails highly elevated temperatures (exceeding those of typical liquid phase experiments) prior to the expansion through a nozzle. Thermodynamically unfavorable isomeric forms become accessible through, e.g., keto-enol or oxo-hydroxy tautomerism, and the formation of base pairing geometries, which are not found in solution-phase systems, becomes possible. Therefore, gas-phase measurements intrinsically measure a mixture a different pairing geometries. Thus care needs to be taken when comparing results from these two situations. E.g., in gas phase the Watson-Crick geometry was found not to be the most stable adenosine-thymidine base pairing geometry [194].

The isolated DNA nucleobases turned out to show a remarkably short lifetime of few hundrets of femtoseconds in the first electronically excited state due to ultrafast internal conversion as measured by UV-pump UV-probe and fluorescence up-conversion spectroscopy [198,199], explaining the high photostability of the DNA nucleobases. Deactivation of the hereby-formed highly-excited vibrational states occurs via intramolecular vibrational redistribution and finally energy transfer to

the surrounding solvent. The last steps of vibrational deactivation can be monitored with ultrafast vibrational spectroscopy. The response of double-helical DNA itself to electronic excitation is significantly different from that of isolated nucleobases. In double-helical DNA oligonucleotides, deactivation of electronic excitation was found to proceed via decay channels involving the formation of long-lived ($\approx$ 100 ps) excimer states located on one of the strands through vertical stacking interactions [57].

For G·C base pairs in crystalline fragments of double-helical RNA oligomers, X-ray diffraction measurements have shown the $G(NH_2)\cdot\cdot C(CO)$ hydrogen bond to be the strongest, reflected in the shortest heavy atom distance of 2.86 $\AA$, followed by the $G(NH_2)\cdot\cdot G(CO)$ hydrogen bond of 2.91 $\AA$ and the $G(NH)\cdot\cdot C(N3)$ hydrogen bond of 2.95 $\AA$ reflecting the weakest bond [11, 12]. For a long time, calculations on the minumum energy structures of isolated G·C base pairs could not reproduce this sequence of hydrogen bond strength, e.g. typically the $G(CO)\cdot\cdot C(NH_2)$ hydrogen bond was calculated to be the strongest bond [200–202]. Systematical density functional studies, which stepwisely increased molecular complexity, showed that neither the inclusion of deoxyribose sugar units nor the addition of phosphate groups yielded significant changes in bond enthalpies and hydrogen bond lengths by more than 0.03 $\AA$. This lead to the conclusion that the backbone itself is not source of changes in hydrogen bond strengths. Only the addition of sodium counterions and, most pronounced, the addition of up to five water molecules provided a reasonable reconciliation with the experimentally measured hydrogen bond lengths in crystalline DNA oligonucleotides [200], which again stressed the important role of the molecular environment, especially water and counterions, for defining the DNA molecular structure.

4.2 Static hydration geometries

The hydration of DNA is governed by local hydrogen bonding interactions as well as long range Coulomb interactions with the charged backbone groups. Early diffraction patterns of DNA fibers realized that the DNA conformation reversibly changes between A and B-form DNA upon a change in water content [203,204]. While B-DNA was found for high relative humidity (R.H.) conditions above 92%, A-DNA structures were found to be formed around 75% R.H.. Gravimetric studies on solid calf-thymus and salmon-sperm DNA as well as vibrational spectroscopic analysis of frequency and intensity changes of IR bands as a function of relative humidity have established an empirical order of water affinity at different bindings sites along the DNA molecule. The charged free phosphate oxygens were found to be the primary hydration sites, followed by esterified phosphate oxygen atoms, followed by sugar O1 atoms, and lastly polar nitrogen, C=O, and amino groups at the nucleobase edges [205] (see the illustration in Figure 4.3). The solvation energy in the first shell around the phosphate backbone was determined to exceed all other hydration sites by $\approx$8 kJ/mol [206]. Crystallographic X-ray studies on AT-rich B-DNA dodecamers found a different order of hydration affinity and determined the polar groups of the minor groove to have the highest water affinity (100% water occupation), followed by the free charged phosphate oxygens (66%), the sugar and major groove bases with similar water occupation (50% and 42%). The esterified phosphate oxygens, surprisingly, showed the lowest degree of hydration [15,207].

The differences is hydration affinity were related to the characteristic hydration structures forming in the minor groove of A·T- and G·C-rich DNA. Measurements on doublex DNA dodecamers revealed for the (narrow) minor groove of A·T-rich regions a regular zig-zag "spine of hydration" running all the way down the minor groove, with the water molecules being associated to the purine N-3 and pyrimidine 0-2 atoms in adjacent base pairs or to the sugar O-4 [14] as shown in Figure 4.3 (b2, d). This extraordinarily stable water spine was found to play a crucial role in stabilization of the B-form structure of A·T-rich DNA and serves as the basis for a less regular outer shell hydration at high humidity. This water spine was also observed in solution phase systems through

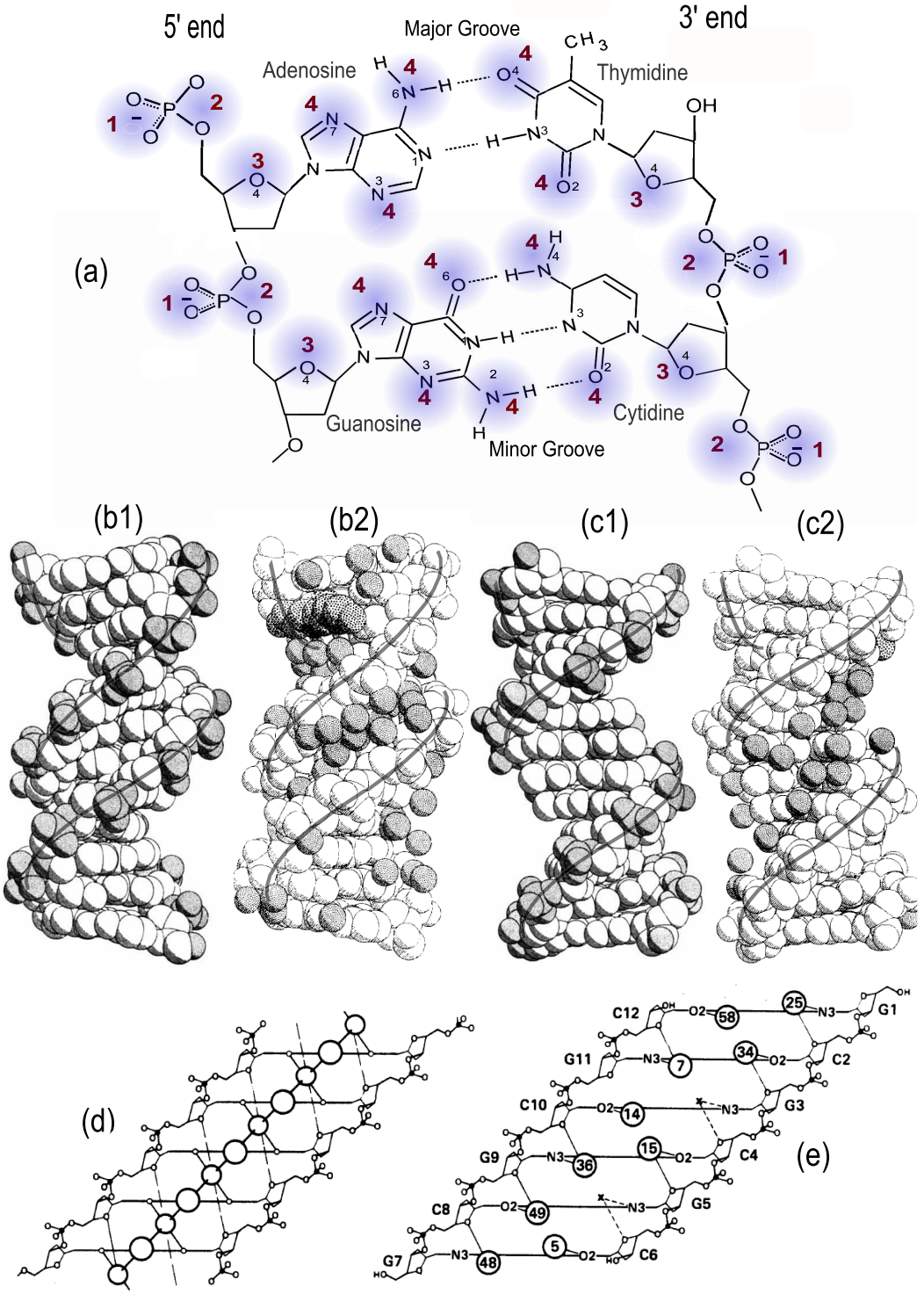

Figure 4.3: *(a) Sketch of the A·T and G·C oligomer molecular structures with the potential hydration sites highlighted with blue color. The red numbering presents the order of water affinity as proposed by Falk et al. [205], with increasing numbers indicating decreasing water affinity. Space-filling drawings of the mixed-base B-DNA CGCGAATTCGCG-dodecamer with the viewer looking on the (b1) minor and (c1) major groove from diametrically opposed directions with the phosphate units marked in black. The atomic positions were obtained from single-crystal X-ray diffraction (modified from ref [175]). In addition, (b2,c2) shows the first-shell associated water molecules as dark shaded spheres with 2.8 Å diameter (modified from ref [14]). The thick structure in top of (b2) is a spermine (polyamine) molecule. (d,e) Unfolded minor groove hydration structures in (d) AT-rich dodecamers and (e) GCGCGC-hexamers, the former showing an idealized spine of hydration (represented by the thick circles) bonding to O-2 pyrimidine and N-3 purines (taken from ref [211]).*

NMR measurements [20,208] and in MD simulations [209,210]. In G·C-rich oligonucleotides such a regular minor groove water spine is missing [15], which was used to explain the ease in structural transition from the B- to the A-form structure in G·C-rich oligonucleotides. Instead, the hydration of the (wider) minor groove in G·C-rich DNA forms two hydration strings running along each wall of the minor groove [14,211], as shown in Figure 4.3 (e), with the overall hydration density being slightly reduced compared to the A·T-rich DNA [14,211]. The minor groove hydration pattern is believed to make B-DNA the preferred structure at high humidity.

Independent of the base sequence, the major groove hydration is less regular, with water molecules forming a first shell around the polar N-7,O-6/N-4 atoms for G·C pairs and around N-7,N-6/O-4 atoms for AT pairs (see Figure 4.3) [14,15]. Here each H_2O often binds in a monodentate fashion, only rarely forming two hydrogen bonds that connect to the polar atoms of different bases in horizontal or vertical (base-stacking) direction. A geometric network of water molecules is missing in the major groove. High level hydration of the major groove leads to formation of water clusters spanning over the major groove from one phosphate group to the other [15].

The hydration geometry around the charged phosphate groups showed a highly disordered hydration structure with fast structual fluctuation [10]. MD simulations showed that on average each charged oxygen atom is hydrated by three water molecules in a tetrahedral arrangement ("cone of hydration") with the water shells of neighboring phosphate groups being spatially separated with neglegible interaction [212,213]. This picture was supported by X-ray and neutron diffraction experiments [207].

The Nucleic Acid Database [13] was used to analyze the principles underlying DNA hydration and to identify average hydration sites independent of the detailed base sequence. Such studies gave the important conclusion that guanine and cytosine bases in A- and B-DNA have the same preferential hydration sites with some variation in hydration densities [214]. The ordered first shell hydration sites were predicted to accommodate a total of 17 water molecules per nucleotide pair (2x6 H_2O on the phosphate group and five ordered water molecules attached to the polar base groups) for B-DNA [215]. Measurements of dielectric relaxation caused by water molecules bound to DNA in mixed water-ethanol solutions determined that 18-19 water molecules per nucleotide are present in B-DNA [177]. It should be noted that diffraction methods can detect only sufficiently localized hydration geometries that exhibit reproducible positions over the ensemble of DNA helices, and, hence, will not detect the full hydration picture and will miss the disordered, randomly distributed water molecules.

4.3 Structural dynamics of the hydration shell

While the static and time-averaged structural properties of the double-helix and its hydration geometry have been studied extensively [7], much less is known about the dynamic processes on the microscopic scale involving structural fluctuations, molecular reorientation, and hydrogen bonding dynamics of the water shell. Early NMR measurements indicated a slowing down in translatory motion of solvating water molecules at the interface of macromolecules such as proteins and DNA [216,217]. Resonant microwave absorption measurements on DNA in aqueous solution [218] as well as temperature-dependent phosphorescence measurements of various DNA-solvent mixtures [219] showed a reduced free water diffusion and solvent mobility in the presence of DNA, which was confirmed by elastic neutron scattering on NaDNA [220]. MD simulations found that the overall diffusion rate at the DNA interface is lower than in bulk water and that translational water mobility is higher in the direction parallel to the solute surface and lower in the direction normal to the surface [221]. The spatial variation of the diffusion coefficient in radial direction to the DNA interface was correlated with peaks in the radial distribution of water molecules [221].

The average residence time of water molecules within a certain radius to their respective DNA

solvation sites were measured via the nuclear Overhauser effect (NOE) between the water protons and the protons in DNA dodecamers in aqueous solution to detect through-space spin-spin couplings, which found hydrating water molecules to reside at the major groove sites shorter than 500 ps, while at the minor groove residence times longer than 1 ns were observed [20]. The relatively short major groove hydration residence times were supported by other groups [208,222,223]. In contrast, measurements of the NOE and nuclear nuclear magnetic relaxation dispersion of the quadrupolar water nuclei ^{17}O and ^{2}H in DNA 17-mers in water at 4°C determined water residence times to be shorter than 1 nanosecond not only for major groove and backbone hydration, but also for the minor groove hydration [21].

MD calculations found average DNA-water hydrogen-bond lifetimes times at the minor groove sites to be only slightly longer than at the major groove sites with a value of (11 ± 11) ps and maximum water residence times of 223 ps [22]. For better comparison with NOE measurements, the average residence time was analyzed by considering water molecules within a NOE distance of 0.35 nm to the DNA interface, which provided average residence times of (100 ± 4) ps with a maximum of 608 ps [22], supporting previous NMR measurements by Sunnerhagen and coworkers [21]. In contrast, hydrogen bond lifetime correlation functions extracted from molecular dynamics simulations exhibited an average lifetime that is longer in the minor groove than in the major groove by a factor of up to 2, while the average hydrogen bond lifetimes was found to significantly depend on the local base pair sequence [24]. Average hydrogen bond lifetimes at the phosphate sites were found to be shorter (but still exceeded the 1 picosecond time scale), attributing an enhanced rigidity to water-DNA geometries in the grooves [24]. In the same work, orientational dynamics of surface water molecules were found to be considerably faster in the major groove positions than in minor grove positions (average rotational time constants of 6 and 26 ps, respectively) with a water orientation dynamics in both grooves being noticeably slower than in bulk water (for bulk water, average rotational time constants are ≈ 2 ps). MD simulations on the hydration of a tRNA anticodon hairpin found water residence times at the solvation sites between 140 and 400 ps [224].

Time-resolved fluorescence Stokes shift (TRSS) measurements focusing on the time range of 1-30 ps with 2-aminopurine[a] [225] as an intrinsic fluorescence probe embedded in a modified B-DNA dodecamer dublex with contributions from hydration dynamics at both minor and major groove positions, revealed two time scales of 1 ps and 10-12 ps, which were attributed to the time scales of molecular rearrangement of bulk-like water and weakly bound water, respectively [226]. TRSS measurements with a fluorescent dye bound exclusively to the minor groove of a DNA dodecamer duplex indicated time constants of 1.5 and 19 ps with similar results for calf thymus DNA [23]. The two times longer 19 ps time constant was explained with a more bulk-like behavior of hydrating water molecules on the major groove side than in minor groove positions, hence indicating a disparity in the dynamics of minor and major groove hydration. The 1.5 and 19 ps dynamic components indicated molecular rearrangement dynamics to be more than one order of magnitude slower than what was observed for the dye in bulk water providing time constants of 0.2 and 1.2 ps [23]. Very similar time constants were obtained through MD simulations on water in the bulk and at the DNA interface [35]. Decomposition into dynamic contributions from the water shell, counterions, and the DNA helix yielded the water dynamics of interfacial water to be a factor of 2-3 slower compared to bulk water, while the long 19 ps time component was attributed to the DNA motion [35]. The dynamic Stokes shift reflects the averaged molecular reorganization dynamics in the fluorophore´s environment over a large spatial volume. This lead to largely controversial interpretations of the observed time scales in terms of the underlying microscopic processes. While Zewail and coworkers attributed the slower reorganization at the DNA interface to decelerated structural solvation dynamics with retarded water motion [23], computational studies on the solvation dynamics in bio-

[a]The use of the natural DNA bases as fluorescent probes is impeded due to their ultrafast lifetimes in the electonically excited state.

logical systems gave conflicting interpretations on the magnitude of contributions from fluctuations of individual water molecules, counterions, and the DNA molecule itself [32,35–37].

TRSS experiments, which were focused on the long time dynamics, with a coumarin dye embedded in DNA oligonucleotides found a molecular reorganization dynamics with a logarithmic time dependence and time constants of 40 ps to 40 ns [33]. Dynamic Stokes shift measurements of coumarin incorporated into an oligonucleotide with a 100 ps time resolution exhibited a multiexponential reorganization dynamics with time components of 300 ps and 13 ns. Such slow dynamics could not be explained by rearrangement of the solvent but were attributed to slow fluctuations within the interior of DNA [34].

The time scales involved in structural fluctuations of hydrated DNA influence the biological activity and chemical reaction rates occurring within the DNA helix as they determine how quickly the DNA structure can adapt to a new product geometry [227,228]. Fast and ultrafast structural fluctuations in the water shell around DNA were predicted to be relevant for DNA-ligand [229] and DNA-protein [230] recognition processes.

As discussed above, the hydrogen bond lifetimes and molecular rearrangement dynamics in the first hydration shell of DNA occur on time scales ranging from few picoseconds to 1 nanosecond, describing the time scales of collective macroscopic molecular rearrangements, exchange with outer solvent molecules, and solvent diffusion over a length of typically few $\AA$. In contrast, the structural dynamics in the second and outer hydration shell of DNA is similar to the behavior of bulk water with the individual solvent molecules showing structural fluctuations such as hydrogen bond breakage and reformation and rotation on the pico- to femtosecond time scale [22,24,51,231]. The behavior of bulk water is shortly discussed in the next paragraph.

Ultrafast structural and vibrational dynamics of bulk water

The microscopic structural dynamics for bulk H_2O water and isotopically-diluted HOD in H_2O or D_2O water are typically faster than for water near biological interfaces ("biological water"). MD simulations and ultrafast IR spectroscopy of bulk water revealed an extended, dynamic, labile hydrogen bond network [8,26–28] with individual water molecules reorienting on the picosecond to femtosecond time scale due to hydrogen bond breaking and reformation events. J. Hynes and coworkers suggested that making and breaking of intermolecular hydrogen bonds occurs in non-diffusive, sudden jumps with hydrogen bond cleavage, reformation and molecular reorientation occurring concertedly [29]. The fluctuating hydrogen bonding Coulomb forces lead to stochastic fluctuations in the OH stretching frequency of individual water molecules within the spectral envelope (spectral diffusion, cf. page 25 f.), which leads to ultrafast decoherence after vibrational excitation. Two-dimensional photon echo spectroscopy revealed that the fastest spectral diffusion processes occur on a time scale of 50 fs, which is much shorter than the average hydrogen bond lifetime of about 1 ps [25,122]. While hydrogen bond modes changing the interwater O··O distance are too slow, such ultrafast spectral diffusion was suggested to arise mainly from ultrafast librational motions (rotations hindered by the water network) and to some extent from near-resonant intermolecular energy transfer between neighboring water molecules (occurring on a 50-100 fs time scale) [25,122,232]. While transient absorption data of H_2O indicated a T_1 lifetime of about 200 fs for the OH stretching oscillators with a decay involving the OH bending vibration [25,105], the OH stretching mode in HDO showed a longer lifetime of about 700 fs due to the absence of efficient relaxation via the HOD bending overtone [233]. In the case of H_2O, the OH bending excitation is transferred to intermolecular librational modes with initially weakened hydrogen bond, which partially break on a ≈ 1 picosecond time scale upon formation of a macroscopically heated water pool ("hot ground state", cf. page 21) [104].

4.4 Ultrafast vibrational spectroscopy of DNA

Structural and vibrational excitation dynamics on the ultrafast time scale can be thoroughly experimentally investigated with ultrafast nonlinear vibrational spectroscopy, which directly follows transient ensemble-averaged changes in vibrational frequencies reflecting dynamic structural changes around the studied vibrational chromophore. The external addition of molecular markers, which potentially disturbed the DNA structure, as in the case of fluorescence studies, is not necessary. The ensemble-averaged vibrational line shapes of DNA in linear and two-dimensional IR spectra are determined by the structural molecular inhomogeneity (diagonal disorder shifting the uncoupled local mode frequencies), the variations in intermode coupling strengths (off-diagonal disorder), and potential interactions with hydrating water molecules.

Ultrafast vibrational two-color pump-probe measurements on artificial double-helical A·T oligomers, investigating the local interactions of phosphate and NH groups with water, have shown that the frequency-time correlation function decays slower than in neat water, which was attributed to decelerated structural fluctuations of the water shell and a reduced rate of resonant OH stretching energy transfer [51]. The water shell of fully hydrated DNA was found to serve as a primary heat sink for vibrational excess energy on the femtosecond time scale, while at low humidity, vibrational energy is delocalized within DNA on a 20 ps time scale [56]. The same oligomers have been investigated with IR-pump anti-Stokes Raman-probe spectroscopy, which revealed a cascaded population transfer from the adenine NH stretching modes to the thymidine NH stretching mode to the NH bending mode and finally to fingerprint and librational modes of the water shell [234]. Moreover, ultrafast pump-probe and 2D-IR experiments were preformed to characterize the vibrational couplings between the NH and NH_2 stretching modes in hydrated A·T oligomers [50,51,235] and G·C base pairs in chloroform [49,236]. Vibrational couplings, anharmonicities, and transition dipole orientations in the carbonyl stretching region of individual nucleobases in D_2O solution were derived from polarization-dependent 2D-IR spectroscopy [48]. Diagonal and off-diagonal anharmonicities encoded in the energy of the double-exited states have been connected to the structure of hydrogen-bonded nucleobase pairs [202]. The dynamics of NH stretching excitations in adenine-uracil base pairs (with chemical modification ensuring exclusively Watson-Crick base pairing) and isolated uracil bases in chloroform have been investigated with pump-probe experiments with a time resolution of 200 fs, showing that interbase hydrogen-bonding leads to accelerated vibrational relaxation on the sub-picosecond time scale [237].

The relative magnitude of interstrand vs. intrastrand vibrational couplings between base pairs in double-helical DNA is a highly debated subject and was focussed mostly on the carbonyl C=O interstrand couplings of hydrogen-bonded pairs compared to intrastrand couplings of stacked nucleobase pairs [52, 54, 238–240]. While FTIR spectra were satisfactorily described through only interbase interstrand couplings [238], Zanni and coworkers interpreted 2D-IR studies of guanine-cytosine double-helical DNA in terms of substantial inter- and intrastrand couplings of similar magnitude of $\approx$ 7-10 cm^{-1} between the carbonyl C=O modes with an excitonic transition dipole coupling model (neglicting hydration effects and frequency disorder) delocalizing the vibrational modes both over the base pair and over the length of the helix [52, 54]. The order of magnitude of interstrand and intrastrand (next-neighbor) vibrational couplings of carbonyl and NH bending modes was reproduced by DFT calculations [241]. These calculation also indicated that the number of stacked nucleobases pairs in the double-helix does not notably affect vibrational linear and 2D-IR line shapes of B-DNA in the carbonyl stretching region, while the reduced vertical distance of stacked base pairs in A-DNA (2.9 $\AA$) was predicted to increase vibrational couplings and the degree of vibrational delocalization along the helix to some extent [241–243]. "Horizontal" vibrational couplings of 5 cm^{-1} between NH stretching oscillators in isolated G·C pairs in solution have been derived from the time scale of an ultrafast energy transfer using Fermi's Golden rule [49]. From

2D-IR spectra of double-helical G·C oligomers presented in chapter 7, we will conclude that the vibrational coupling patterns of NH stretching excitations show negligible influence of intrastrand couplings while there exist weak interbase "horizontal" couplings.

5 Vibrational line shapes and ultrafast dynamics in adenosine and thymidine monomers

The following chapters present the new results obtained during this work. This chapter is devoted to the analysis of the NH stretching excitations in isolated nucleobases adenosine and thymidine in nonpolar chloroform solution. These results will serve as a reference for the effect of interbase hydrogen-bonding in adenosine-thymidine base pairs in chapter 6.

Studies of the isolated nucleobase monomers [48, 237] in solution using ultrafast vibrational spectroscopic approaches are rare and, so far, no diagonal and off-diagonal anharmonicities of the uncomplexed adenosine monomer have been reported. The anharmonicity and coupling parameters are important input parameters for the test and refinement of quantum chemical calculations of nucleoacid bases. We use linear absorption and, in particular, 2D-IR photon echo measurements to determine vibrational couplings and diagonal and off-diagonal anharmonicities of the NH stretching modes. For the adenosine molecule, these parameters will be used as input for an exciton coupling model to determine the proper eigenstate description of the single- and double-excited NH stretching states in the normal or local mode picture. Ultrafast vibrational pump-probe spectroscopy is employed to gain insight into ultrafast population relaxation of the NH stretching states in adenosine and thymidine, and allows to observe quantum beats due to simultaneous coherent excitation of the two NH stretching modes in adenosine. Quantum chemical calculations of adenosine are used to understand the origin of vibrational coupling and anharmonicity values.

5.1 Linear IR spectra of NH and ND stretching modes

We investigate the chemically modified 2´-deoxyadenosine and the chemically modified deoxythymidine nucleoside, which both were synthesized in the group of Prof. Temps in a similar fashion as reported in Ref. [192]. Their molecular structure is shown in Figure 5.1 (a) and 5.3 (a). While adenosine contains a NH_2 amino group attached to a purine ring, thymidine comprises a single NH motif with two close-by C=O carbonyl motifs, which are all attached to a pyrimidine ring. For both molecules, the two hydroxy groups of the deoxyribose unit were subsituted with tert-butyldimethylsilyl (TBMDS) groups in order to ensure sufficient solubility in nonpolar solvents such as chloroform. These 3´,5´-TBDMS protected 2´deoxyadenosine and 3´,5´-TBDMS-protected deoxythymidine molecules will in the following be referred to as A and T, respectively. For the linear and nonlinear IR measurements, the solutes were dissolved in deuterated chloroform $CDCl_3$ and nondeuterated $CHCl_3$, respectively, and held between CaF_2 windows of 1 mm thickness with an absorption path length of 0.2 mm defined by teflon spacers. The nonpolar solvents ensure a weak interaction with the solute[a].

The solvent-corrected linear IR spectrum of the adenosine monomer in deuterochloroform for different concentrations is shown in Figure 5.1 (b). The two vibrational bands at 3413 and 3525 cm^{-1} are assigned to the symmetric $\upsilon(NH_2)_S$ and asymmetric $\upsilon(NH_2)_A$ stretching modes of the

[a]It is interesting to note that the dielectric constant of chloroform ($\epsilon = 4.8$) is comparable to that estimated for the inside of double-helical DNA [244].

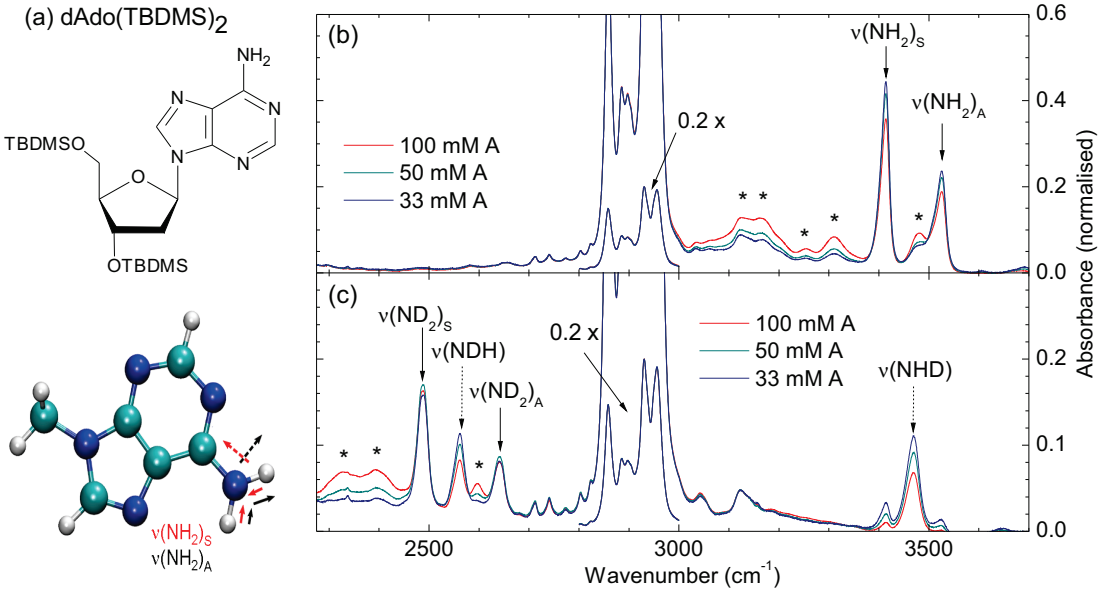

Figure 5.1: *(a) Molecular structure of the TBDMS protected 2´-deoxyadenosine (A). The nuclear displacements following symmetric/asymmetric NH stretching excitations are shown as red/black arrows, while dashed arrows indicate the corresponding transition dipole orientations. Linear FT-IR spectra of (b) A solutions with different concentration in $CDCl_3$ and (d) of 70% deuterated A in $CDCl_3$, both normalised to the CH stretch peak intensity at 2930 cm^{-1}. Asterisks indicate bands resulting from adenosine self-aggregates.*

amino group [189, 245–247] (the definite proof for this assignment will be given below). Their frequency difference indicates a coupling between the two local NH stretching excitations of J_H = -56.0 cm^{-1} = $(\upsilon(NH_2)_S - \upsilon(NH_2)_A)/2$. Due to the perpendicular orientation of the symmetric and asymmetric transition dipoles, dipole-dipole interactions can be ruled out as the origin of this coupling, which points to the dominant role of interactions mediated by the chemical bonds ("mechanical" coupling). While the observed frequency splitting in the linear IR spectra provides only the absolute value of the intermode coupling J_H, its negative sign is derived from quantum chemical calculation, which are discussed in section 5.4. Hence, the symmetric stretching modes are placed at a lower vibrational frequency compared to the asymmetric stretching modes. Our value for J_H is slightly below the values of -57.5 to -59.0 cm^{-1} that have been found in gas-phase 9-H-adenine and 9-methyladenine cooled in a supersonic jet [248–250], 9-H-adenine in helium nano-droplets [196] and in low-temperature Ar matrices [251], and 9-ethyladenine in $CDCl_3$ solution [189]. With increasing A concentration, additional bands around 3125, 3167, 3250, 3310, and 3479 cm^{-1} appear, which are associated with hydrogen-bonded NH stretching modes in A··A dimers or bigger molecular adenosine aggregates [189]. Their reduced transition frequency is a consequence of hydrogen-bonding, which leads to a weakening of the N-H bond and hence to a lowering of its stretching frequency. The intense bands between 2800 and 3050 cm^{-1} are the CH stretching modes located in the TBDMS side groups.

Solvent-corrected linear IR spectra of deuterated samples of A in $CDCl_3$ are shown in Figure 5.1 (c). The symmetric $\upsilon(ND_2)_S$ and antisymmetric $\upsilon(ND_2)_A$ stretching modes appear at 2489 and 2639 cm^{-1}, respectively, which implies a mechanical coupling of J_D = -75.0 cm^{-1} = $(\upsilon(ND_2)_S - \upsilon(ND_2)_A)/2$ between the two ND stretching oscillators. Since the degree of deuteration is only approximately 70%, both fully deuterated ND_2 and partially deuterated NDH groups, as well as a few nondeuterated NH_2 groups contribute to the linear spectrum. Partially deuterated NHD

groups show an effective decoupling between their NH and ND stretching modes, which allows one to observe the transition frequencies of the decoupled local NH and ND stretching oscillators at $\upsilon(NH)$ = 3469 cm^{-1} and $\upsilon(ND)$ = 2564 cm^{-1}, respectively. It is important to note that the mechanical coupling J between the NH and ND stretching modes in the NHD group stays basically unchanged compared to the undeuterated case. It arises from electrostatic electron-core interactions, which are hardly influenced by the core mass. However, due to the large energetic separation between the uncoupled NH and ND local modes, the coupling-induced frequency shift as well as their intermode mixing becomes almost zero (see equations (2.9), (2.10), and (2.11)). We find the "decoupled" frequencies located exactly halfway between those of the symmetric and asymmetric stretching modes, which are observed in the presence of coupling. The degeneracy of the two decoupled local modes in the case of undeuterated NH_2 or fully deuterated ND_2 groups ensures that any intermode coupling between the NH/ND stretching modes will lead to a mixing angle of $\Theta = arctan(J/\hbar(\omega_2 - \omega_1)) = -90°$. This clearly confirms the validity of the normal mode picture for the 0-1 transitions of the ND_2 and NH_2 stretching modes. The frequency positions of the coupled stretching modes are exclusively determined by their intermode coupling $J_{H,D}$, and the normal mode wavefunctions are given by linear combinations of the two local NH/ND stretching modes, with both local modes giving identical contributions. The decoupled local mode NH stretching frequency decreases by a factor of $\upsilon(NH)/\upsilon(ND)$ = 3469/2565 = 1.352 upon deuteration of the amino group (H/D isotope effect), while the coupling between the two local modes at the same time increases by a factor of J_D/J_H = -75/-56 = 1.339. The former observation is in satisfactory agreement with the scaling implied by the harmonic oscillator frequencies $\omega_{NH}/\omega_{ND} = (m_{ND}/m_{NH})^{1/2}$ = 1.37 with $m_{NH,D}$ the reduced masses of the NH,ND system. The reason for the isotope effect on the J coupling will be revealed by ab initio calculations that are presented in section 5.4.

5.2 Population dynamics of NH stretching modes

Time and frequency-resolved transient absorption spectroscopy with pump- and probe pulses of identical linear polarisation was performed to gain insight into ultrafast vibrational population dynamics of the NH stretching modes.

Adenosine

For the A monomer, transient spectra recorded for pump-probe delays of 0.4 - 20 ps are shown in Figure 5.2 (a). A negative absorption change is observed at the fundamental 0-1 transition frequencies of the symmetric stretch $\upsilon(NH_2)_S \approx$ 3415 cm^{-1} and the asymmetric stretch mode $\upsilon(NH_2)_S \approx$ 3525 cm^{-1}, which results from both the bleaching in ground state population and the stimulated emission contribution from the first excited state. Moreover, enhanced absorption signals occur around 3321, 3376, and 3460 cm^{-1}. They arise from 1-2 excitations from the single- into the double-excited states of the NH stretching modes in A. However, their unambiguous assignment into overtone and combination tone transitions is not possible using the pump-probe measurements only. They require a second frequency dimension correlating excitation and detection frequency as given by 2D photon echo spectra (see the following section). These spectra will yield the signals with positive absorbance change at 3321 and 3460 cm^{-1} as the 1-2 overtone transitions of the symmetric and asymmetric stretching modes, respectively.

Additional weak reduced absorption signals, which arise from the free NH stretching mode in A·A adenosine self-associates, are visible at 3470 - 3500 cm^{-1}. The most stable adenosine A·A complexes are cyclic dimers, associated by two NH··N hydrogen bonds with one free and one hydrogen-bonded NH stretching mode per amino group (compare Figure 1 in ref. [189] for possible cyclic dimer structures of adenine). Further weak bleach signals from hydrogen-bonded

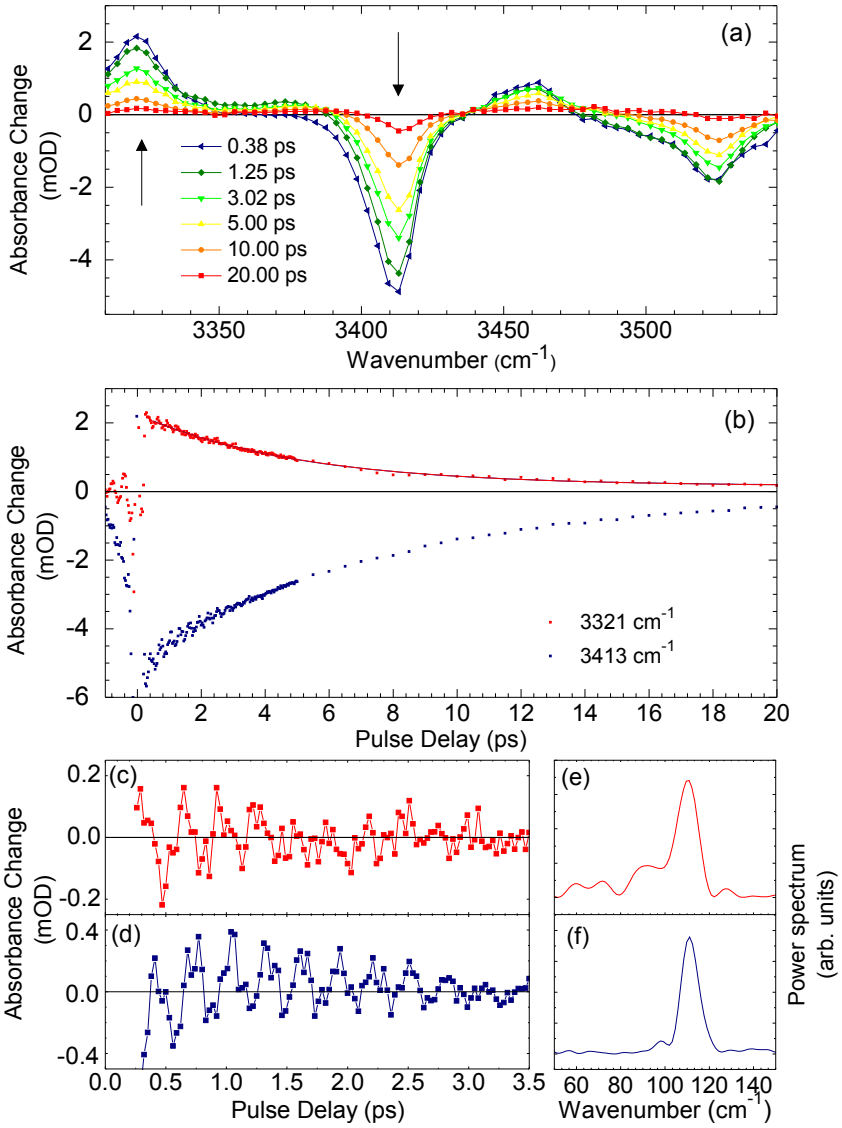

Figure 5.2: *(a) Spectrally-resolved pump-probe transients for different pump-probe delays of 0.4 - 20 ps for A dissolved in $CHCl_3$ at a concentration of 40 mM. (b) Slices at the frequency position of the 0-1 (3413 cm^{-1}) and 1-2 (3321 cm^{-1}) transition of the symmetric NH stretching mode (indicated with arrows in (a)), providing a T_1 lifetime of (6 ± 1) ps. The beating patterns overlaying the transients are shown in (c,d). Their corresponding frequency spectra (Fourier transforms) are shown in (e,f).*

NH stretching modes in adenosine dimers are expected below 3350 cm^{-1}, as marked with asterisks in Figure 5.1 (b). Those hydrogen-bonded NH stretching oscillators carry a slightly higher transition dipole moment μ than the free NH stretching modes, e.g., in monomeric A species. Due to the different scaling behavior of signal intensity in pump-probe ($\propto \mu^4$) compared to linear spectroscopic measurements ($\propto \mu^2$), signals from complexed species become somewhat highlighted against those from monomeric species in third-order experiments. Still, the degree of molecular association is too low to make them visible against superimposed excited state absorption signals from the dominating A monomers.

In order to monitor population dynamics in A, we plot the bleach recovery and excited state decay dynamics in Figure 5.2 (b) for probe frequencies of 3413 and 3321 cm^{-1}, corresponding to

the 0-1 fundamental and 1-2 excited state transitions of the symmetric NH_2 stretching mode. The monoexponential fits (solid lines) indicate for both cases a similar decay time of $T_1 = (6 \pm 1)$ ps, giving the $v = 1$ lifetime of the symmetric stretching mode. Similarly, the time-resolved bleach recovery of the asymmetric stretching oscillator at 3526 cm^{-1} shows a population decay time of $T_1 = (10 \pm 2)$ ps (not shown). These lifetimes are similar with values found for the free NH stretching mode in monomeric 7-azaindole in chloroform [252] and aniline-d5 in CCl_4 (see section 8.6). There is a long-lived weak residual bleaching signal, whose lifetime is way beyond the picosecond time scale monitored in our experiment. It results from additional cascaded decay pathways that do not repopulate the original ground state directly but that intermediately populate other molecular modes.

Quantum beats

The kinetic pump-probe traces of the ground state bleach and excited state absorption transitions of the symmetric and asymmetric normal modes in adenosine each show underdamped oscillations that are superimposed on their exponential decay curves. The beating signal on the 0-1 and 1-2 transition of the symmetric NH stretching mode is isolated by subtracting the dominating slow exponential picosecond population decay, and plotted in Figure 5.2 (c,d). The oscillations persist for several picoseconds with a damping time on the order of one ps. The corresponding power spectrum, given by its Fourier transformation, is shown in Figure 5.2 (e,f). The Fourier tranform of the oscillatory signal is centered around (112 ± 5) cm^{-1} with a FWHM of (12 ± 3) cm^{-1}. The oscillation frequency nicely equals the frequency difference Δv of the fundamental symmetric and asymmetric NH stretching mode $\Delta v = v(NH_2)_A - v(NH_2)_S$. The width of the Fourier transform corresponds to an oscillation damping time of (0.9 ± 0.3) ps, which is similar to the observation from the time-domain data. The beating results from the simultaneous coherent excitation of the $v(NH_2)_S$ and $v(NH_2)_A$ modes by the broadband pump pulse, which has a pulse duration ($\approx$ 100 fs) that is short compared to the wavepacket oscillation period ($\approx$ 298 fs). The impulsive excitation thus induces the formation of a vibrational wavepacket in the $v = 1$ states given by the coherent superposition of both modes (interstate coherence, see also section 2.4 and Figure 2.3 (c) for its Feynman pathway). The evolving wavepacket leads to a temporal modulation of the Frank-Condon overlap with the ground state and $v = 2$ overtone eigenfunctions, which induces a periodically oscillating absorbance change that is observed by the probe pulse when tuning the pump-probe delay. The quantum beat decay rate is a only weakly influenced by T_1 (population) relaxation of both modes due to their long T_1 lifetime of 6-10 ps. The FWHM linewidth Δv of the symmetric and asymmetric NH_2 normal modes in the linear spectra (21 cm^{-1} and 30 cm^{-1}, respectively) hint at a total dephasing time T_2 (neglecting T_1 decay) of $T_2 = 1/(\pi \Delta v)$ as $T_2^S = 500$ fs and $T_2^A = 350$ fs. The much longer quantum beat persistence indicates that there is a high degree of correlation between the temporal development of the two local mode NH stretching frequencies within each molecule of the ensemble. For a system with perfect correlation between both NH stretching modes, i.e. a constant frequency difference between the NH stretching mode frequencies in the amino group of all molecules, there would be no quantum beat decay. Hence, the coupling to the bath seems to shift the two NH stretching modes within each molecule in rather well-correlated way.

Quantum beat oscillations attributed to the direct coherent excitation of two vibrational modes, with a beating frequency given by their difference frequency, have to be distinguished in their microscopic origin from quantum beats arising from anharmonic coupling of the pumped high-frequency vibrations to low-frequency vibrations. Such beatings will be observed and discussed in the context of hydrogen bonded A·T dimers in chapter 6.

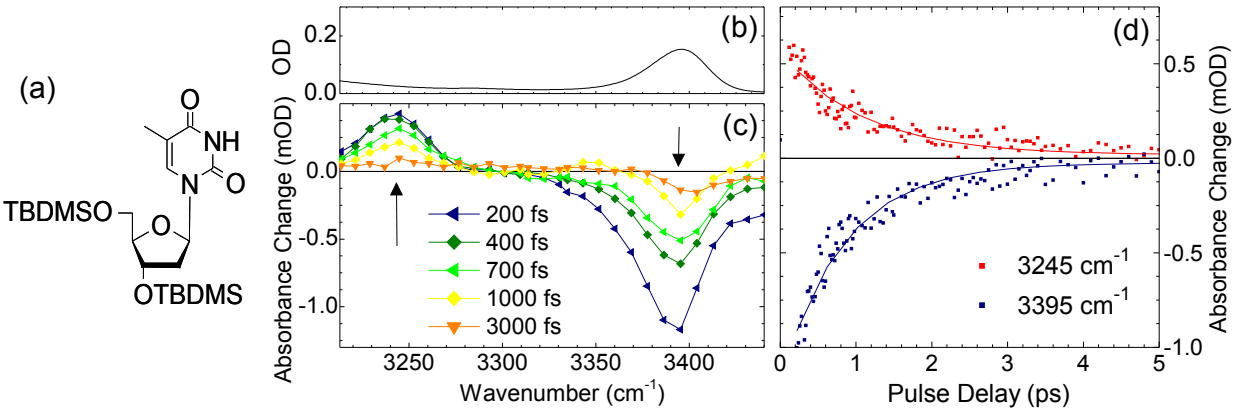

Figure 5.3: *(a) Molecular structure of the TBDMS protected 2´-deoxythymidine (T), showing only one NH stretching oscillator. (b) The linear IR spectrum of a 50 mM solution of T in $CHCl_3$. (c) Transient absorption spectra. (d) shows the kinetic traces in the range of the fundamental 0-1 NH stretching transition at 3395 cm^{-1} and the anharmonically downshifted 1-2 transition at 3245 cm^{-1}. The solid lines are monoexponential fits.*

Thymidine

The linear IR spectrum of T molecules at a concentration of 50 mM in chloroform solution in the region of 3200-3450 cm^{-1} is plotted in Figure 5.3 (b). At this concentration the spectrum is dominated by contributions from T monomers. It shows one NH stretching band at 3395 cm^{-1}. The transient absorption spectra of T (given in (c)) shows a decrease of NH stretching absorption at the same probe frequency due to ground state depletion and stimulated emission from the first excited state, while a red-shifted 1-2 enhanced absorption component occurs at 3245 cm^{-1}, indicating a diagonal anharmonicity of 150 cm^{-1}. The extracted anharmonicity and population lifetime of $T_1 = (0.9 \pm 0.1)$ ps for the NH stretching mode in T (see the monoexponential fits in Figure 5.3 (d)) is similar to values determined for uracil in chloroform solution [237], while the lifetime is about 6 times shorter than the one of NH stretching excitations in the A molecule. This shortening of the populational $\upsilon = 1$ lifetime of the free NH stretching modes in T might result from a Fermi resonance with the C=O carbonyl stretching first overtone, which provides an additional decay channel for the NH stretching excitation in the T molecule. Similar values of T_1 = 1-2.5 ps have been found for the free NH stretching modes in guanosine-cytidine and adenosine-thymidine base pairs in chloroform solution [49, 193].

5.3 Couplings and anharmonicities in adenosine - Local and normal mode description

The absorptive 2D-IR spectra with (k_1, k_2, k_3, k_{LO}) = ZZXX polarization configuration (pulses k_3 and k_{LO} both perpendicular to k_1 and k_2) of A dissolved in $CDCl_3$ were recorded through a scan of the coherence time τ_1 from -600 to 1400 fs (step size 4 fs), which is sufficient to sample the vibrational dephasing dynamics of the NH stretching modes in A fully. The used concentration of A of 40 mM ensures that the A monomer clearly dominates A·A dimers or even bigger homo-molecular aggregates. The 2D spectra are shown in Figure 5.4 for waiting times τ_2 of (c) 0.2, (d) 0.3, (e) 0.5, and (f) 1.0 ps. Each spectrum is scaled to its maximum positive signal intensity at

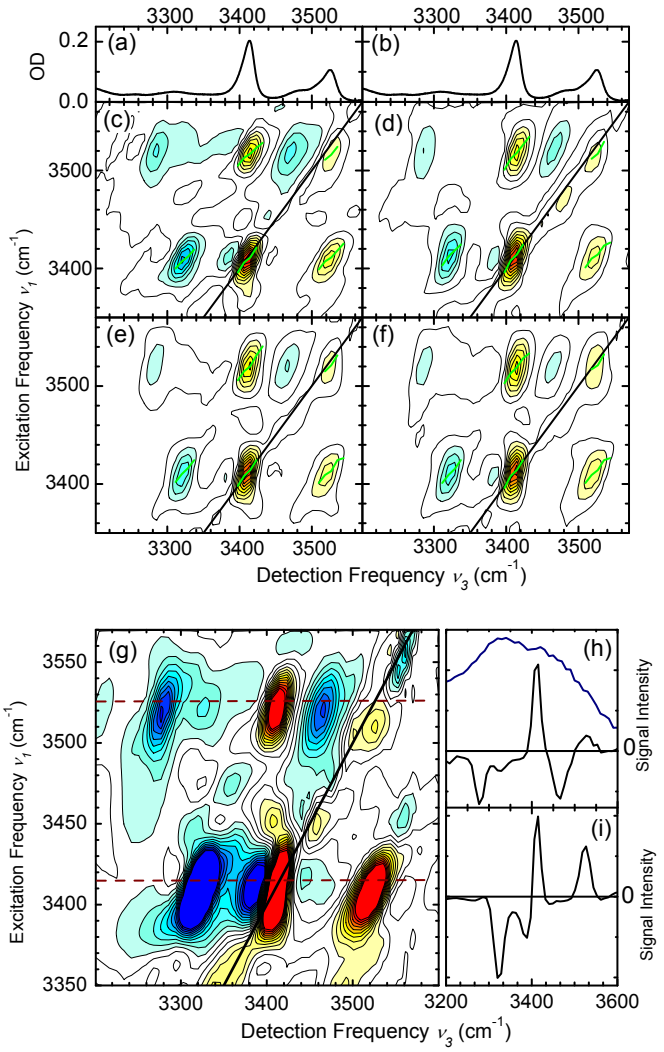

Figure 5.4: *Absorptive 2D-IR spectra of A in $CHCl_3$, recorded in ZZXX polarization geometry for different waiting time of (c) 0.2, (d) 0.3, (e) 0.5, and (f) 1.0 ps. The 2D spectra are each normalized to their maximum positive signal. Center lines connecting the frequency positions with maximum intensity of slices with fixed detection frequency are added to some of the peaks (green lines). The linear IR spectrum is shown in (a,b) for reference. (g) shows the 2D spectra recorded for a 0.2 ps waiting time with blown-up intensity. Slices at fixed excitation frequencies of υ_1 = 3525 cm^{-1} and 3413 cm^{-1} are plotted in (h) and (i). The spectral intensity of the used IR pulses is shown in (h) as blue line.*

the frequency position $(\upsilon_1[cm^{-1}], \upsilon_3[cm^{-1}])$ = (3413,3413). For reference, the top panels in Figure 5.4 (a,b) show the corresponding linear spectrum. The 2D spectra each show 8 dominant peaks, as expected for a system of two coupled anharmonic oscillators (see section 2.5). They are composed of two pairs of "diagonal" peaks and two pairs of cross peaks, each of which are split into a positive and a negative peak. There are two positive diagonal peaks at $\upsilon_1 = \upsilon_3$ = 3413 cm^{-1} and $\upsilon_1 = \upsilon_3$ = 3525 cm^{-1} that arise from Feynman pathways involving only the 0-1 transition of the symmetric $\upsilon(NH_2)_S$ and the asymmetric $\upsilon(NH_2)_A$ NH stretching states, respectively. Moreover, there are positive cross peaks at $(\upsilon_1[cm^{-1}], \upsilon_3[cm^{-1}])$ = (3413,3525) and (3525,3413) as well as negative peaks at (3413,3320), (3413,3390), (3525,3280), and (3525,3465). The origin of these peaks will be discussed later.

The waiting time series of 2D spectra shows no additional negative peaks growing in. The intensities of the positive cross peaks change in accordance with the positive diagonal peaks at the same excitation frequency. This hints at an absence of population transfer (cf. section 2.5) during the waiting time period of 0.2-1.0 ps that is covered by the experiment. In order to evaluate the role of spectral diffusion, the center lines (CL) are added as green lines for the most intense peaks in each 2D spectrum in Figure 5.4 (c,d,e,f). Their slope (CLS) is a measure of the two-point frequency correlation function $C(\tau_2) = \langle \delta\omega(\tau_2)\delta\omega(0)\rangle$, describing dynamic transition frequency changes of the individual oscillators averaged over the molecular ensemble (cf. page 16 and 25). The CLS on all peaks stays roughly constant during one picosecond, at a value of approximately one. This has three interesting repercussions. First, spectral diffusion is absent on the experimental time scale. This points to a weak susceptibility (coupling) of the NH_2 stretching normal modes to fluctuations of the solvent modes. This leads to transition frequency fluctuations of the NH stretching modes much slower than the picosecond time scale and, hence, to a constantly inhomogeneous line broadening. The dielectric constant of the chloroform solvent of $\epsilon = 4.8$ indeed promises rather weak interactions to the solute. Moreover, in the case of a dominating linear solute-solvent interaction term, the pure dephasing rate $1/T_2^*$ was found to be proportional to the vibrational anharmonicity [253]. The latter has a rather small value for free NH stretching modes, and, thus, fluctuating solvent modes will anyway only weakly influence vibrational transition frequencies. Second, the alignment of the CL along the frequency diagonal ($\upsilon_1 = \upsilon_3$) indicates frequency fluctuations being slow on the experimental time scale and thus a dominating inhomogeneous line broadening. This inhomogeneity could be explained by some kind of intramolecular structural inhomogeneity, or different solute-solvent geometries that last over the time scale of one picosecond. Third, the CLS of all positive and negative peaks in the 2D spectrum are identical, which points to correlated fluctuation dynamics of all 0-1 and 1-2 transitions in the system of coupled oscillators. The observation of correlated frequency shifts tells us that in the system Hamiltonian the fluctuations in the off-diagonal coupling terms ("off-diagonal disorder") are weak. Otherwise, e.g. the 0-1 transition frequencies of the two coupled NH stretching modes modes would be shifted in opposite directions by the variable off-diagonal coupling, and the positive cross peaks would show an inverted CLS compared to the positive diagonal peaks [97].

The nonparallel transition dipole orientation of the coupled local NH stretching modes leads to a strong variation in the intensity of 2D-IR spectral signatures with the polarization of the exciting pulses. Absorptive 2D-IR spectra in ZZXX and in ZZZZ (all pulses parallelly polarized) polarization geometry for a waiting time of 200 fs are plotted in Figure 5.5 (b), scaled to their corresponding intensity maximum. The two pairs of cross peaks at $(3413, 3525)^+$,$(3525, 3280)^-$ above the frequency diagonal and $(3525, 3413)^+, (3413, 3390)^-$ below the frequency diagonal (the $\pm$ index indicating the sign of the signal) are significantly increased in ZZXX geometry compared to the other (diagonal) peaks. This increase is consistent with coupled transition dipoles of roughly perpendicular orientation; however, the signal intensities are too low to further specify the relative angle.

The knowledge of the mixing angle Θ for the coupling of two modes allows one to estimate their relative transition dipole angle from their relative peak intensity in the linear IR spectrum. As mentioned before (section 2.1), the local mode transition dipoles $\vec{\mu}_{01}$ and $\vec{\mu}_{10}$ for the 0-1 transitions in the NH stretching modes transform identically as the local mode wavefunctions to form the normal mode transition dipole moments $\vec{\mu}^+$ and $\vec{\mu}^-$ for the symmetric and asymmetric modes:

$$\begin{aligned} \vec{\mu}^+ &= cos\left(\frac{\Theta}{2}\right)\vec{\mu}_{01} + sin\left(\frac{\Theta}{2}\right)\vec{\mu}_{10} \\ \vec{\mu}^- &= -\,sin\left(\frac{\Theta}{2}\right)\vec{\mu}_{01} + cos\left(\frac{\Theta}{2}\right)\vec{\mu}_{10} \end{aligned} \tag{5.1}$$

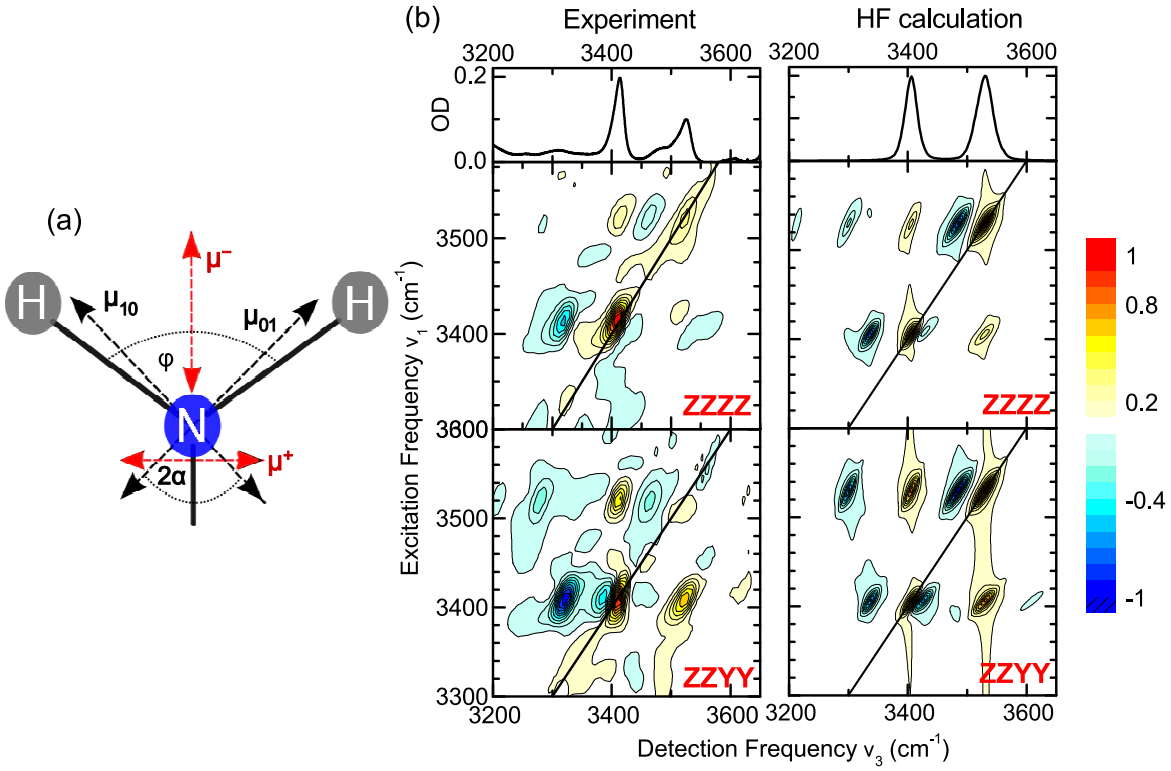

Figure 5.5: *(a) Sketch of the transition dipole orientations for the local NH stretching modes ($\vec{\mu}_{01}$,$\vec{\mu}_{10}$) and the symmetric and asymmetric normal modes ($\vec{\mu}^+$,$\vec{\mu}^-$) in A. $\vec{\mu}_{01}$ and $\vec{\mu}_{10}$ define an angle of 2α, which contrasts with the angle φ between the NH bond vectors. (b) Left column: 2D-IR spectra of A recorded in ZZZZ and ZZXX polarization geometry, validating the assumption of perpendicular normal mode transition dipoles. Right column: Calculated 2D-IR spectra.*

Figure 5.5 (a) shows a sketch of the NH_2 vibrational transition dipole moment orientations for the normal modes and the local NH stretching modes in A. Defining the relative angle between the local mode transition dipoles as 2α, this leads to $\vec{\mu}_{01} = (tan(\alpha), 1)$ and $\vec{\mu}_{10} = (-tan(\alpha), 1)$. With the mixing angle Θ = -90° and equation (5.1), this provides the orthogonal normal modes transition dipole as $\vec{\mu}^+ = (\sqrt{2}tan(\alpha), 0)$ and $\vec{\mu}^- = (0, \sqrt{2})$. The intensity ratio of the symmetric and asymmetric normal modes in the linear absorption (Figure 5.1) is determined to R=1.45 ± 0.2, so that $|\mu^+|^2 = R|\mu^-|^2$. From the latter requirement, the relative angle between the local transition dipoles is estimated as $2\alpha \approx 101°$. This angle differs from the physical H-N-H bond angle $\varphi \approx 120°$, indicating that the NH stretching local mode transition dipole moments are not parallel to the bond vectors. Such differences arise from mode mixing with other overtone or combination states that are not included in our model. This might especially involve mixing with C-N or C=N stretching states from the nearby heteroaromatic ring. Similar differences were found between the orientation of the C=O bond vector and the C=O stretching transition dipole in the amide I mode in proteins [254].

A single 2D spectrum of A carries the complete information about the energy level structure of the single and double excited NH stretching states, hence about the anharmonicity in the system and the degree of mode mixing. In the following section, we will address the question of how to best describe the various quantum eigenstates. This may incorporate either a description in terms of highly coupled and delocalized normal modes, a description as localized excitations with negligible mode mixing, or an intermediate case.

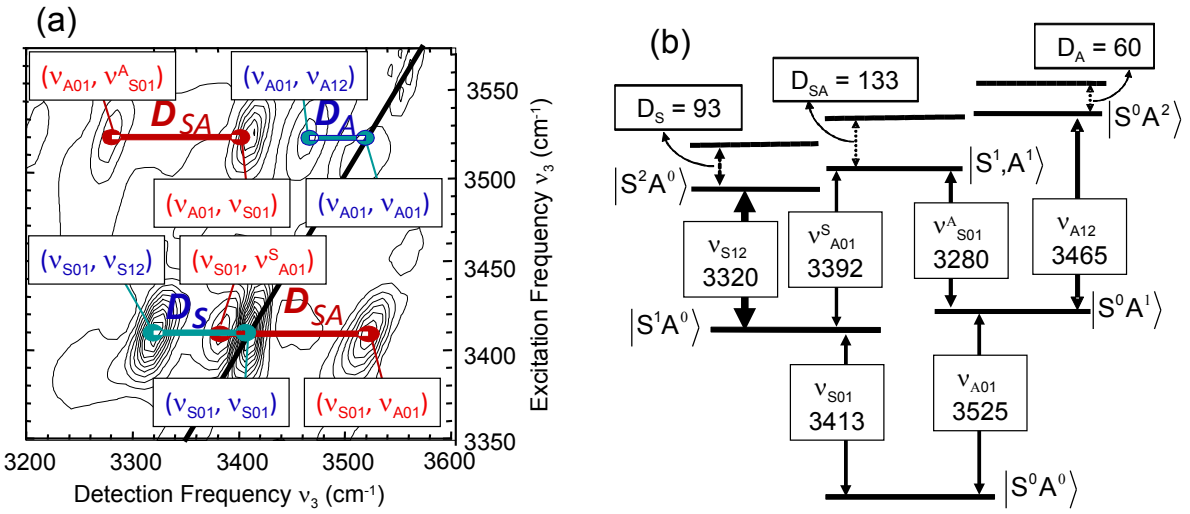

Figure 5.6: *(a) Peak assignment in the 2D spectrum and (b) extracted energy level structure described in the normal mode basis set of two anharmonically coupled symmetric and asymmetric NH stretching modes. Only the six lowest eigenstates accessible with third order experiments are shown, as $|S^nA^m>$ with n and m indicating the number of quanta in the symmetric and asymmetric normal mode, respectively. All transitions are within the bandwidth of the used IR pulses.*

Normal mode picture

In the normal mode representation, we use a basis set $\{|S^nA^m>\}$, with n and m specifying the number of quanta in the symmetric and asymmetric normal modes, respectively. The energy level scheme in the basis set of symmetric and asymmetric NH stretching normal modes as well as its implications on the meaning of the various peaks in the 2D spectrum are shown in Figure 5.6 (a,b). The energy differences between the vibrational levels give information about the anharmonicity of the system. The positive peaks on the frequency diagonal (3413,3413) and (3525,3525) arise from pathways involving excitation of the fundamental 0-1 transition by the first pulse and excitation of the same fundamental frequency by the third pulse. Excitation pathways that in contrast involve transitions into the 1-2 overtone states $|S^0A^2>$ and $|S^2A^0>$ induced by the third pulse explain the negative peaks at (3413,3320) and (3525,3465). These peak positions in the 2D spectra allow one to directly read off the diagonal anharmonicity as $D_S = (3413 - 3320)\ \mathrm{cm}^{-1} = 93\ \mathrm{cm}^{-1}$ and $D_A = (3525 - 3465)\ \mathrm{cm}^{-1} = 60\ \mathrm{cm}^{-1}$ for the symmetric and asymmetric normal modes, respectively. The positive cross peaks (3525,3413) and (3413,3525) are due to excitation pathways involving a mixed excitation of the $\upsilon(NH_2)_S$ and $\upsilon(NH_2)_A$ oscillators. The negative peaks at (3525,3280) and (3413,3390) arise from pathways involving the combination state $|S^1A^1>$, which carries excitation of one quanta in both the symmetric and asymmetric normal modes.[b] The two off-diagonal peak pairs, each composed of a negative and a positive peak at (3525,3413),(3525,3280) and (3413,3525),(3413,3390), have an identical separation (within experimental accuracy) of their detection frequencies by $D_{SA} = (3413 - 3280)\ \mathrm{cm}^{-1} = (3525\text{-}3390)\ \mathrm{cm}^{-1} \approx 135\ \mathrm{cm}^{-1}$. The value D_{SA} specifies how much the fundamental 0-1 excitation of one mode ($\upsilon(NH_2)_S$ or $\upsilon(NH_2)_A$) changes the 0-1 transition frequency of the other mode ($\upsilon(NH_2)_A$ or $\upsilon(NH_2)_S$): the combined

[b] For a more precise description of the microscopic origin of the various peaks in a 2D spectrum of coupled anharmonic oscillators (using the stepwise manipulation of density matrix states in a Feynmann diagram formalism) see section 2.5.

excitation is anharmonically downshifted by D_{SA} compared to the sum of the two fundamental frequencies 3413 +3525 cm^{-1} = 6938 cm^{-1}. As explained in section 2.1, this off-diagonal anharmonic downshift is related to the cubic and quartic derivatives of the molecular potential energy surface, i.e. a result of the anharmonic intermode coupling between the symmetric and asymmetric NH stretching states.

Local mode picture and excitonic modelling

An alternative basis set to describe the eigenfunctions of the single- and double-excited states of A consists of the decoupled local NH stretching states. We describe the excitonic single- and double-excited states in a basis of symmetrized local modes $\{|i,j^{\pm}\rangle\}$ containing the elements

$$|i,j^{\pm}\rangle = \begin{cases} \frac{1}{\sqrt{2}}\left(|i,j\rangle \pm |j,i\rangle\right) & \text{for} \quad i<j \\ |i,i\rangle & \text{for} \quad i=i \end{cases} \tag{5.2}$$

with {i,j} $\in$ {0,1,2} and $(i+j) \leq 2$. i and j specify the degree of excitation in the two local NH stretching states. Figure 5.7 shows schematically the changes in energy positions and vibrational wavefunctions due to intermode coupling in the A molecule. It emphasizes the origin of experimentally observable (coupled) vibrational eigenstates (shown on the right part) as arising from localized (uncoupled) excitations (shown on the left part). On the left part of Figure 5.7, we consider a system without intermode coupling J, but with anharmonicity for the double-excited states. In the absence of intermode coupling J between the two NH stretching states, the first excited states in both oscillators would be degenerate (as we found out by partial deuteration experiments, see above), showing a 0-1 transition frequency of ω_0 = 3469 cm^{-1}. Without diagonal anharmonicity, the energies of the double-excited local mode overtone states |2,0>, |0,2> and combination tone states |1,1> (single quantum excitation in both local oscillators) would coincide. Their energy would be located at twice the 0-1 transition frequency (energy position indicated by the red dashed line in Figure 5.7). In reality, the local overtone states will each be downshifted by the local mode diagonal anharmonicity Δ_0, and the combination state will be downshifted by the combination state anharmonicity Δ_C. Both values give the energetic positions (solid black lines) of the double-excited states in the presence of vibrational anharmonicity, but in the absence of intermode coupling J.

If this coupling is present, the energy levels will shift and their eigenfunctions will mix to a certain extent. In the single-excited states, the strong coupling limit applies with $|J_H| \gg |\omega_1 - \omega_2| = 0$ [46, 69]. The coupling J_H induces a strong mixing of the two $v = 1$ local states, and the 0-1 transitions of both oscillators are shifted to 3413 and 3525 cm^{-1}. Hence, the symmetric $v(NH_2)_S$ and asymmetric $v(NH_2)_A$ normal modes are the proper eigenstates for the one-exciton manifold: in the basis $\{|v(NH_2)_S>, |v(NH_2)_A>\}$, the coupling between the single-excited local modes is removed and the coupling Hamiltonian becomes diagonal with the new one-exciton eigenenergies of $\hbar\omega_0 \pm J_H$.

From each of the one-exciton states, there are two strongly-allowed (i.e. single-photon) excited-state absorption transitions 1-2 (see the thick line arrows in the right of Figure 5.7) that lead to the negative peaks at $(v_1[cm^{-1}], v_3[cm^{-1}])$ = (3413,3320), (3413,3390), and (3525,3280), (3525,3465). From their detection frequencies, the energetic positions of the two-exciton states can be precisely determined as 6733, 6805, and 6990 cm^{-1} (accuracy $\pm$ 5 cm^{-1}). The coupling Hamiltonian (2.14) in the local mode basis shows the |1,1> local combination mode (anharmonically downshifted by Δ_C) to be coupled to the local states |0,2>, |2,0>, which are both lowered in energy by the diagonal anharmonicity Δ_0. A basis transformation towards a new basis set $\{|0,2^{-}>, |0,2^{+}>, |1,1>\}$ yields

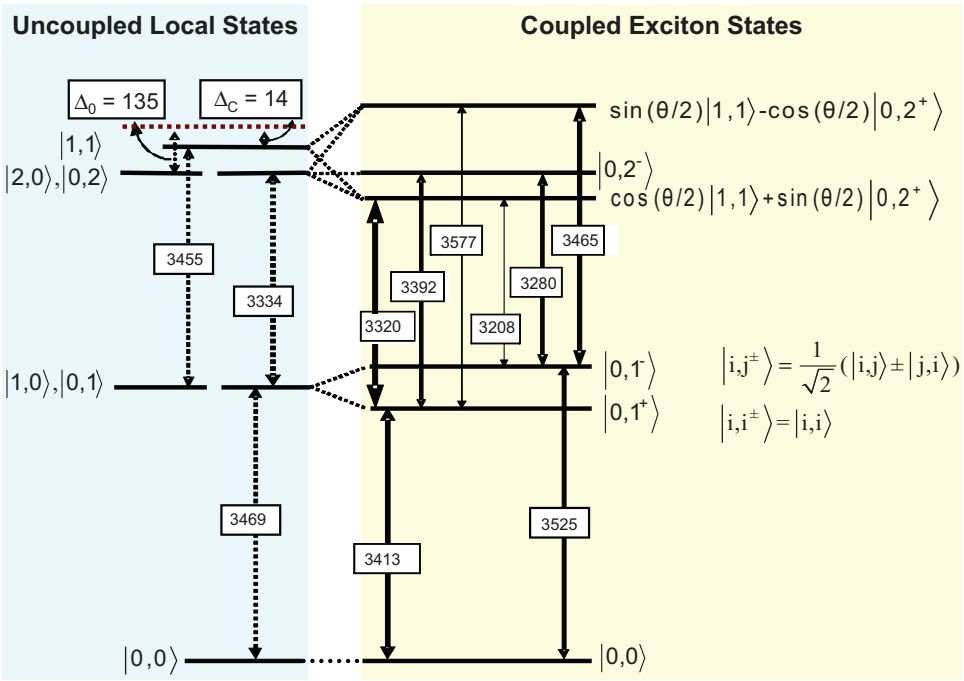

Figure 5.7: *Left: Energy level structure for the uncoupled local modes with local mode (Δ_0) and combination mode (Δ_C) anharmonicity (solid lines), and without any anharmonicity (red dashed line). Right: Energy level structure for the excitonic states in the presence of intermode coupling, leading to mixed states. The mixing angle θ depends on the values of Δ_0, Δ_C, and J. The local states $\{|i,j>\}$ (left) are labelled with the degree of excitation of the two local NH stretching modes, while the excitonic states are best described in a symmetrized local mode basis $\{|i,j^{\pm}>\}$.*

the coupling Hamiltonian of the two-exciton states as:

$$H^{(2)} = \hbar \begin{pmatrix} 2\omega_0 - \Delta_0 & 0 & 0 \\ 0 & 2\omega_0 - \Delta_0 & 2J_H \\ 0 & 2J_H & 2\omega_0 - \Delta_C \end{pmatrix} \quad . \tag{5.3}$$

The coupling between the $|0,2^{-}>$ state to the other two-exciton states is absent; at the same time the coupling between the $|0,2^{+}>$ and |1,1> state is modified to $2J_H$. The two-exciton eigenstates are given by equation (2.16). The degree of mode mixing between the $|0,2^{+}>$ and |1,1> state depends on the mixing angle θ:

$$\theta = arctan\left(\frac{4J}{\Delta_0 - \Delta_C}\right) \tag{5.4}$$

θ can be directly calculated from the knowledge of Δ_0, Δ_C, and the mechanical coupling J, the first two of which still need to be determined. Using the intermode coupling value J_H = -56.0 cm^{-1} as input, the values Δ_0 and Δ_C are used as fit parameters in the diagonalisation of the excitonic Hamiltonian (2.14), to reproduce the eigenenergies determined above. This procedure yields the local mode diagonal anharmonicity $\Delta_0 \approx 135$ cm^{-1} and the anharmonic downshift of the combination state |1,1> to $\Delta_C \approx 14$ cm^{-1}. The local mode combination tone anharmonicity Δ_C is found to be small compared to the local mode diagonal anharmonicity Δ_0 for the A molecule. In fact, in some publications by Hamm and Zanni the anharmonic combination tone downshift is neglected [46], while it is used by Cho, Child and Halonen [255–257]. The value of Δ_0 is similar to

those measured for non-hydrogen-bonded NH stretching vibrations in hetero-cyclic nucleic bases or nucleobase model systems, where the single-excited NH stretching states were described in a local mode representation. The free NH stretching oscillators in G·C base pairs, uracile/thymidine monomers (see page 64), and 7-azaindole in chloroform solution gave a diagonal anharmonicity of 130, 155, and 140 cm^{-1}, respectively [49,237,252].

The determined coupling and local mode anharmonicity values yield for the A molecule the mixing angle θ = -62°. This points to an intermediate coupling regime with medium-strong mode mixing in the two-exciton manifold (θ = 0°/-90°: no/strong mixing), where neither the local nor the normal mode limit applies for the double-excited eigenstates in A. Its eigenfunctions are the asymmetric stretching overtone mode $|0,2^->$ and two states composed of a mixture of the combination tone state |1,1> and the symmetric stretching overtone mode $|0,2^+>$ (c.f. equation (2.16)):

$$\begin{aligned} |\Psi_{20}\rangle &= sin(\theta/2)\,|1,1\rangle - cos(\theta/2)\,\left|0,2^+\right\rangle \\ |\Psi_{11}\rangle &= \left|0,2^-\right\rangle \\ |\Psi_{02}\rangle &= cos(\theta/2)\,|1,1\rangle + sin(\theta/2)\,\left|0,2^+\right\rangle \end{aligned} \tag{5.5}$$

The |1,1> and $|0,2^+>$ wavefunctions contribute $sin^2(\theta/2)$= 27% and $cos^2(\theta/2)$ = 74%, respectively, to the eigenfunction $|\Psi_{20}>$, while the |1,1> and $|0,2^+>$ wavefunctions contribute 74% and 27%, respectively, to the eigenfunction $|\Psi_{02}>$.

This mode mixing in the two-exciton states leads to weak allowance of three-quantum transitions (see thin line arrows in Figure 5.7), which are forbidden in the harmonic oscillator limit. The 2D spectrum of Figure 5.4 (c) is magnified in (g). Slices for two detection frequencies of υ_3 = 3525 and 3413 cm^{-1}, indicated by the dashed lines in (g), are plotted in Figure 5.4(h,i). They reveal weak indications of additional negative peaks at $(\upsilon_1[cm^{-1}], \upsilon_3[cm^{-1}])$ = (3525,3210) and (3413,3575). They show signal intensities just above the detection threshold, which are comparable to those arising from A·A dimers. We assign these additional signals to harmonically forbidden three-quantum 1-2 transitions into the two-exciton manifold, since their frequency positions coincide with the location expected from the level scheme in Figure 5.7. Calculated 2D-IR spectra of A are shown in Figure 5.5 (b) and will be discussed in section 5.4. The calculations predict that the magnitude of the harmonically forbidden signals makes up only few percent of that of the main peaks, which agrees with our experimental findings. Indications of weakly-allowed transitions were reported in the 2D-IR spectra of C≡O stretching bands of dicarbonylacetylacetonato rhodium (I) [112,113,258]. In the latter molecule, the two-exciton states of the CO stretching modes showed a stronger mode mixing since $\Delta_0 \approx |J|$, and, hence, the forbidden three-quantum transitions carried a higher oscillator strength than in the case of the NH stretching transitions in A.

For quantifying the degree of normal or local mode character in the description of the overtone eigenfunctions, Child and Halonen [255–257] defined a parameter ξ (rad) as:

$$\xi = \frac{2}{\pi} arctan\left(\frac{2J}{\Delta_0}\right) \tag{5.6}$$

In the local mode limit ($|J| \ll \Delta_0$), $\xi \approx 0$, while in the normal mode case ($|J| \gg \Delta_0$) $\xi = \pm 1$. As indicated before, the overtone NH stretching eigenstates of A monomer are intermediate between the normal and local mode case, as evidenced by a value $\xi = -0.44$. In contrast, delocalized normal modes turned out to give a more accurate description of the vibrational eigenstates in the C_2D_2 and SO_2 molecule. Weakly-excited overtone states with principle quantum number of n = 2-5 in water and acetylene C_2H_2 were found to be better modeled in a basis of localized excitations due to the highly anharmonic vibrational potential [256,257,259]. A local mode basis has been also used to study OH stretching states of H_2O in the gas phase, where anharmonicities and couplings were found to be of comparable magnitude as for the NH stretching modes in A,

providing a value of $\xi = -0.34$ [255–257]. Moreover, the local mode picture proved successful in the description of overtone states in gas phase amines and anilines [197,260,261]. From studies on aliphatic amines, e.g. methylamine and cyclopropylamine, a local mode coupling and a local mode anharmonicity of $|J_H| = 32\ cm^{-1}$ and $\Delta_0 = 158\ \mathrm{cm}^{-1}$ were derived. In contrast, for aromatic amines with a single aromatic ring such as in aniline, the local mode coupling $|J_H|$ increases to 43.7 cm^{-1}, while $\Delta_0 = 163.4\ \mathrm{cm}^{-1}$ stays unchanged. For the purine A (containing two heteroaromatic rings), we found $|J_H| = 56\ \mathrm{cm}^{-1}$ and $\Delta_0 = 135\ \mathrm{cm}^{-1}$. It seems that there is a general trend towards increasing intermode coupling with increasing size of the delocalized π electron system of an aromatic ring system. At the same time, changes in the magnitude of the local mode anharmonicity stay moderate. Presumably, the increasing interaction between the lone pair of the nitrogen atom with the delocalized π electron system of the sp^2 hybridized aromatic ring orbitals is the reason for this change. Future experiments on different primary amines could be helpful to validate this conclusion.

5.4 Quantum chemical calculations

In order to gain more insight into the microscopic origin of intermode coupling and anharmonicities, and, hence, in the eigenstate character of the excitonic states in the A molecule, Nicholas Preketes, a member of the group of Shaul Mukamel, performed ab initio calculations. To reduce computational time, the molecule was approximated by substitution of the TBDMS-ribose side group with a methyl group (9-methyladenine (9-mA)). Calculations were done for 9-mA and its deuterated variant 9-methyladenine-d_2 (9-mA-d_2) in Gaussian09, using a Hartree-Fock approach with the 6-311++G** basis set. These results were used as input parameters to calculate linear IR and absorptive 2D-IR spectra (waiting time 0 fs) using the software SPECTRON [78], which was developed by the Mukamel group. Gas phase conditions were assumed, so the solvent was considered to have negligible interaction with the solute. Couplings to the fluctuating bath were incorporated phenomenologically by adding a homogenous linewidth of 4 cm^{-1} and inhomogenous broadening components with a FWHM of 21 cm^{-1} and 30 cm^{-1} for the symmetric and asymmetric modes, respectively.

First, the geometry of the A molecule was optimized, minimizing the molecule's internal energy. The calculated anharmonic force constants for the equilibrium geometry then gave the anharmonic potential energy surface. The Hamiltonian was constructed as a Taylor series in the two local NH stretching coordinates Q_i, including the anharmonic correction terms up to sixth order [258,262]:

$$\begin{aligned} H =& \sum_{i}^{2} \frac{p_i^2}{2m_i} + \sum_{i\neq j}^{2} \frac{1}{2} G_{ij} p_i p_j + V_0 + \sum_{i}^{2} f_i Q_i + \frac{1}{2!} \sum_{ij}^{2} f_{ij} Q_i Q_j + \frac{1}{3!} \sum_{ijk}^{2} f_{ijk} Q_i Q_j Q_k \\ &+ \frac{1}{4!} \sum_{ijkl}^{2} f_{ijkl} Q_i Q_j Q_k Q_l + \frac{1}{5!} \sum_{ijklm}^{2} f_{ijklm} Q_i Q_j Q_k Q_l Q_m + \frac{1}{6!} \sum_{ijklmn}^{2} f_{ijklmn} Q_i Q_j Q_k Q_l Q_m Q_n \end{aligned} \tag{5.7}$$

with the nth order force constants $f^{(n)}_{k1k2\ldots k3} = \left(\frac{\partial^n V}{\partial Q_{k1} \partial Q_{k2} \ldots \partial Q_{kn}}\right)_0$ and G_{ij} the Wilson G matrix elements (see section 2.1 and [58–60]). Numerical calculations are simplified when transforming the internal coordinates Q_i and momenta p_i to the bosonic creation ($a^\dagger$) and annihilation (a) operators [70]:

$$Q_i = \sqrt{\frac{\hbar}{2m_i\omega_i}}(a_i + a_i^\dagger) \quad ; \quad p_i = i\sqrt{\frac{\hbar m_i \omega_i}{2}}(a_i^\dagger - a_i) \tag{5.8}$$

with m_i the effective masses taken from the reciprocal diagonal elements of the Wilson G matrix (given by Gaussian). The intrinsic harmonic local mode frequencies ω_i of the internal coordinate

Q_i were calculated from the diagonal elements of the second-order force constants as:

$$\omega_i = \sqrt{\frac{f_{ii}}{m_i}} \tag{5.9}$$

This yields the Hamiltonian (5.7) as:

$$\begin{aligned} H =& \frac{1}{2}\sum_{i}^{2}\frac{\hbar\omega_i}{2}(a_i + a_i^\dagger)^2 - \frac{1}{2}\sum_{i\neq j}^{2}\gamma'_{ij}(a_i^\dagger - a_i)(a_j^\dagger - a_j) + V_0 + \sum_{i}^{2} g_i(a_i + a_i^\dagger) \\ &+ \frac{1}{2}\sum_{i\neq j}^{2}\varphi_{ij}(a_i + a_i^\dagger)(a_j + a_j^\dagger) + \frac{1}{3!}\sum_{ijk}^{2} g_{ijk}(a_i^\dagger + a_i)(a_j^\dagger + a_j)(a_k^\dagger + a_k) \\ &+ \frac{1}{4!}\sum_{ijkl}^{2} g_{ijkl}(a_i^\dagger + a_i)(a_j^\dagger + a_j)(a_k^\dagger + a_k)(a_l^\dagger + a_l) \\ &+ \frac{1}{5!}\sum_{ijklm}^{2} g_{ijklm}(a_i^\dagger + a_i)(a_j^\dagger + a_j)(a_k^\dagger + a_k)(a_l^\dagger + a_l)(a_m^\dagger + a_m) \\ &+ \frac{1}{6!}\sum_{ijklmn}^{2} g_{ijklmn}(a_i^\dagger + a_i)(a_j^\dagger + a_j)(a_k^\dagger + a_k)(a_l^\dagger + a_l)(a_m^\dagger + a_m)(a_n^\dagger + a_n) \end{aligned} \tag{5.10}$$

with $g^{(n)}_{k1k2...kn}$ the dimensionless nth-order force constants and the parameters γ'_{ij} and φ_{ij} defined as:

$$g^{(n)}_{k1k2...kn} = \sqrt{\frac{\hbar^n}{2^n m_{k1}\omega_{k1} m_{k2}\omega_{k2}...m_{kn}\omega_{kn}}} f^{(n)}_{k1k2...kn} \quad , \tag{5.11}$$

$$\gamma'_{ij} = \frac{G_{ij}\hbar}{4}\sqrt{m_i\omega_i m_j\omega_j} \quad , \quad \varphi_{ij} = f_{ij}\sqrt{\frac{\hbar^2}{4m_i\omega_i m_j\omega_j}} \quad . \tag{5.12}$$

Writing out this Hamiltonian in matrix form in a set of harmonic oscillators and diagonalizing it gives the vibrational eigenstates and their corresponding eigenenergies. When $|m_i>$ is the eigenfunction of an harmonic oscillator m excited by i quanta, the Hamiltonian matrix elements are calculated using the functioning of the creation $a_n^\dagger$ and annihilation a_n operators of mode n:

$$\begin{aligned} &< m_i|a_n^\dagger|n_j > = < m_i|\sqrt{j+1}|n_{j+1} > \\ &< m_i|a_n|n_j > = < m_i|\sqrt{j}|n_{j-1} > \end{aligned} \tag{5.13}$$

To calculate intensities in linear and nonlinear IR spectra, the nuclear dipole moment is expanded in the internal local coordinates Q_i up to first order:

$$\mu = \mu_0 + \sum\left(\frac{\partial\mu}{\partial Q_i}\right)_0 Q_i \tag{5.14}$$

with μ_0 the permanent dipole moment.

All expansion coefficients from the Hamiltonian (5.10), calculated for 9-mA and 9-mA-d_2, are summarized in the left side of table 5.1. On the right side of this table, the calculated fundamental frequencies and normal mode and local mode anharmonic downshifts of the overtone levels are compared to the corresponding experimental values. Here the frequencies ω_i and anharmonicities are already scaled with a phenomenological parameter 0.9183. This parameter is an empirical correction factor, which is supposed to account for the neglect of high-order expansion terms in the

g_1	-0.2 (-0.2)	g_{2222}	319.4 (170.6)
g_2	-0.1 (-0.1)	g_{11111}	-140.1 (-64.0)
ω_1	3901.8-0.2 (-0.2)	g_{11112}	14.9 (6.8)
ω_2	3900.7 (2850.2)	g_{11122}	22.6 (10.3)
γ'_{12}	64.6 (88.3)	g_{11222}	22.9 (10.4)
φ_{12}	-6.7 (-4.9)	g_{12222}	15.1 (6.9)
g_{111}	-816.2 (-509.8)	g_{22222}	-140.1 (-64.0)
g_{112}	-6.6 (4.1)	g_{111111}	58.4 (22.8)
g_{122}	5.9 (3.7)	g_{111112}	-8.2 (-3.2)
g_{222}	-815.8 (-509.6)	g_{111122}	-24.2 (-9.4)
g_{1111}	319.6 (170.7)	g_{111222}	-23.7 (-9.2)
g_{1112}	-17.4 (-9.3)	g_{112222}	-24.5 (-9.5)
g_{1122}	-13.5 (-7.2)	g_{122222}	-8.4 (-3.3)
g_{1222}	-17.3 (-9.2)	g_{222222}	58.5 (22.8)

	Experiment	**HF/6-311+G****
ω_A	3525 (2639)	3530 (2627)
ω_S	3413 (2489)	3406 (2483)
D_A	60	46 (31)
D_S	93	69 (35)
D_{AS}	133	106 (68)
D_{tot}	284	219 (134)
Δ_0	135	107 (65)
Δ_C	14	6 (5)

Table 5.1: *Left: Expansion coefficients from the Hamiltonian (5.10) for 9-mA, and $9mA - d_2$ in parentheses, in cm^{-1}. Right: Fundamental frequencies and anharmonicities obtained by experiment and calculations. All calculated values are already scaled with an empirical factor of 0.9183.*

potential energy surface, inaccurate force fields (and hence force constants) and other approximations leading to deviations of the calculated values from the experimental ones [263]. This factor was chosen to provide the best agreement for the experimental values of the 0-1 fundamental transitions. It is bigger than the standard harmonic scaling factor of 0.90 [264], but smaller than the anharmonic scaling factor obtained from second-order vibrational perturbation theory [263,265].

The calculations provide valuable insight into the origin of couplings and anharmonicities. The expansion of equation (5.10) and comparison with equation (2.7) shows[c], that the bilinear coupling parameter J is the sum of two components: a kinetic energy contribution γ'_{12} (resulting from the kinetic energy Hamiltonian $\sum G_{ij}p_ip_j$) and a potential energy contribution φ_{12} (resulting from the bilinear potential energy term $\sum f_{ij}r_ir_j$). Combining equation (6.6) with equation (5.9) shows that the kinetic term is a function of Wilson's G-matrix elements, which are calculated from the optimized molecular geometry, while the potential energy coupling term is dependent on the second-order diagonal force constants f_{11}, f_{22} and on the second-order off-diagonal force constant

[c]Note, that the basic difference between the Hamiltonian (5.10) and the exciton Hamiltonian (2.7) is the neglect of any non-quantum conserving terms and the truncation after the fourth order expansion terms in the latter case.

f_{12} [60,266]:

$$\begin{aligned} J = \gamma'_{12} - \varphi_{12} &= -\hbar\frac{\sqrt{\omega_1\omega_2}G_{12}}{2\sqrt{G_{11}G_{22}}} - \hbar\frac{\sqrt{\omega_1\omega_2}f_{12}}{2\sqrt{f_{11}f_{22}}} \\ &= -\hbar\frac{G_{12}}{2}\left(f_{11}f_{22}m_1m_2\right)^{\frac{1}{4}} - \frac{\hbar}{2}f_{12}\left(f_{11}f_{22}m_1m_2\right)^{-\frac{1}{4}} \end{aligned} \tag{5.15}$$

The calculated values for 9-mA of $\gamma'_{12} \approx 65$ cm^{-1} and $\varphi_{12} \approx$ -7 cm^{-1} clearly indicate that the bilinear coupling J_H is dominated by the momentum/kinetic energy coupling. Moreover, calculations for the deuterated molecule 9-mA-d_2 reproduce the experimentally determined increase in bilinear coupling $J_H \rightarrow J_D$ of roughly a factor of $\sqrt{2}$. The increase is explained by the rising kinetic energy coupling term $\gamma'_{12} \approx 88$ cm^{-1} upon isotopic substitution: because G_{12} and f_{ii} are the same for 9-mA and 9-mA-d_2, equation (5.15) shows γ'_{12} to scale with the square root of the effective mass of the NH (ND) system, leading to a change in γ'_{12} upon deuteration as

$$\frac{\gamma'^{D}_{12}}{\gamma'^{H}_{12}} = \sqrt{\frac{m_1^D}{m_1^H}} \tag{5.16}$$

yielding an enhancement factor of $\approx$ 1.37. In contrast, $\varphi_{12} \approx$ -5 cm^{-1} decreases by the same factor upon deuteration. Similar deuteration effects have been observed for water [267]. Moreover, the dimensionless anharmonic force constants $g^{(n)}$ (n>2) are clearly dominated by the diagonal terms. Their significant decrease with higher order n seems to indicate that the truncation of the Hamiltonian (5.7) after sixth order is justified.

The optimized molecular geometry of 9-mA shows good agreement with previous calculations [268]. The NH_2 group is about 10° out of plane to the aromatic ring system. The ab initio calculations further indicate an angle of $2\alpha = 95°$ between the local transition dipoles of the two NH stretching oscillators, in good agreement with our findings from the analysis of the linear spectrum (101°). The calculated angle between the symmetric and asymmetric transition dipoles is with 84° close to a perpendicular orientation, consistent with implications from the polarization-dependent 2D-IR spectra and with expectations for symmetric and asymmetric NH stretching normal modes.

A comparison between the measured and calculated 2D-IR spectra for ZZZZ and ZZXX polarization condition is shown in Figure 5.5 (b). The calculated spectra shows nice qualitative agreement with the experimental one. In agreement with findings from the excitonic model above, the total anharmonicity of the local modes is dominated by the diagonal local mode anharmonicity Δ_0, while Δ_C is almost negligible. However, the absolute magnitudes of the anharmonic shifts are underestimated in the calculations by roughly a factor of 1.3, while their relative magnitude fits well with the experimental observation. Incorporating additional modes in the calculations could provide a better agreement.

5.5 Conclusions

In summary, we have analyzed the NH stretching modes of chemically-modified adenosine and thymidine monomers in chloroform solution, using linear FT-IR and ultrafast vibrational pump-probe and photon echo spectroscopy.

For adenosine, the linear IR spectra revealed the effectively decoupled NH and ND stretching modes in partially deuterated NHD groups at spectral positions exactly in the middle of the coupled NH_2 and ND_2 stretching modes, respectively. Hence, a mechanical bilinear coupling of J_H = -56 cm^{-1} and J_D = -77 cm^{-1} was deduced (with the negative sign indicated by ab initio calculations), providing the symmetric and asymmetric normal modes as the correct eigenfunctions for the single-excited NH stretching states of the NH_2 and ND_2 amino group in adenosine. Pump-probe

spectroscopy revealed the population (T_1) lifetime of the two NH stretching modes as ≈ 6 and 10 ps and quantum beats due to the coherent simultaneous excitation of the symmetric and asymmetric NH stretching modes by the broadband pump pulse.

2D-IR spectroscopy on adenosine was used to elucidate diagonal and off-diagonal anharmonicities of NH stretching excitations that are encoded in the frequency positions of peaks in the 2D-IR spectrum. Diagonalization of the local mode excitonic coupling Hamiltonian and fitting to the observed energy level structure gave insight into the origin of the two-exciton vibrational eigenenergies and eigenstates. The extracted local mode diagonal anharmonicities of $\Delta_0 = 135$ cm^{-1}, the combination state local mode anharmonicites $\Delta_C \approx 14$ cm^{-1}, and the bilinear intermode coupling J_H show that the intermediate coupling regime applies for the two-exciton states, where the eigenstate wavefunctions can be neither properly described by normal nor local states. The 2D-IR line shapes indicated a high degree of inhomogeneous broadening of the coupled NH stretching modes. Negligible changes in relative intensities and line shapes in 2D-IR spectra with increasing waiting time indicated the absence of intermode population transfer and spectral diffusion on the picosecond time scale. The changes of the cross peaks intensities in 2D spectra with the polarization of the exciting pulses supported the roughly perpendicular orientation of the relative transition dipoles of the symmetric and asymmetric stretching modes. Ab initio Hartree-Fock calculations in the two local NH stretching modes revealed the origin of the mechanical coupling J as arising mostly from kinetic energy coupling contributions. The difference between intermode coupling J_H and J_D was found to result from an increase in the momentum coupling contribution upon deuteration.

For thymidine, the single NH stretching mode shows a population lifetime of about 0.9 ps, which is shorter than the normal mode lifetimes of the adenosine amino group (possibly due to excitation decay via a Fermi resonance with the carbonyl overtone), while the anharmonicity of 150 cm^{-1} for the thymidine NH stretching mode is similar to the adenosine local mode diagonal anharmonicity.

6 Vibrational line shapes and ultrafast dynamics in hydrogen-bonded adenosine-thymidine base pairs

The results of the monomeric adenosine and thymidine nucleobase units of the previous chapter will now be extended to investigate the effects of hydrogen bond mediated base pairing in adenosine-thymidine pairs. Thereby, we will analyze the time-averaged and dynamic properties of their NH stretching manifold. The base pairs will be analyzed in waterfree chloroform solution to specifically study the changes induced by interbase hydrogen bonding in the absence of solvating water molecules, a molecular backbone, or nucleobase stacking as found in native DNA. There exist only a few works on the ultrafast structural and vibrational properties of nucleobase pairs in solution [48, 49, 237, 269], and a 2D-IR spectroscopic study of A·T nucleobase pairs is missing. In particular, the underlying mechanisms leading to the congested vibrational line shape in the NH stretching manifold of adenosine-thymidine base pairs are until now largely unadressed.

In contrast to the situation in double-helical DNA, where typically the well-defined Watson-Crick base pairing geometry is enforced, the absence of the DNA backbone enables formation of a variety of A·T base pairing geometries through spontaneous hydrogen bonding association between nucleobase monomers in solution. Therefore, we first present linear NMR measurements as well as ab initio calculations to estimate the relative abundance of the various base pair geometries. Afterwards, concentration- and temperature-dependent linear IR spectra will be used to extract the complex NH stretching mode pattern of A·T base pairs extending from 2600-3600 cm^{-1}. Two-color IR pump-probe and 2D-IR photon echo spectroscopy will be employed to study intra- and interbase anharmonic couplings between the various NH stretching states and their vibrational dynamics, among them the changes in T_1 lifetimes upon hydrogen-bonding. This experimental data combined with quantum chemical calculations will allow for a qualitative understanding of the various vibrational bands by considering hydrogen bonding effects such as couplings of high-frequency NH stretching excitations to a low-frequency hydrogen-bond mode and the enhanced Fermi resonance mixing with fingerprint combination tone and overtone states, in particular the NH_2 bending overtone.

6.1 Equilibrium A·T base pairing geometries

We investigate the same 3´,5´-TBDMS-protected deoxythymidine (abbreviated as T) and 3´,5´-TBDMS-protected deoxyadenosine (abbreviated as A) nucleosides as in the previous chapter, dissolved in chloroform solution. Their molecular structure is again shown in Figure 6.1 (a). The use of nucleosides (nucleobase and sugar unit) instead of the pure nucleobases ensures on the one hand maximum agreement with the nucleoside structures found in native DNA and on the other hand the formation of additional base pairing geometries and tautomers is suppressed.

For the pairing between A and T nucleobases in solution, there are four cyclic A·T base pairing geometries with two intermolecular hydrogen bonds: The Watson-Crick (WC) geometry (typically found in native DNA), the reverse Watson-Crick (rWC), the Hoogsteen (H), and the reverse Hoogsteen (rH) geometry (see Figure 6.1 (b)). The reverse/nonreverse configrations appear very similar, but especially the Hoogsteen configuration, using the N7 instead of N1 nitrogen atom of A

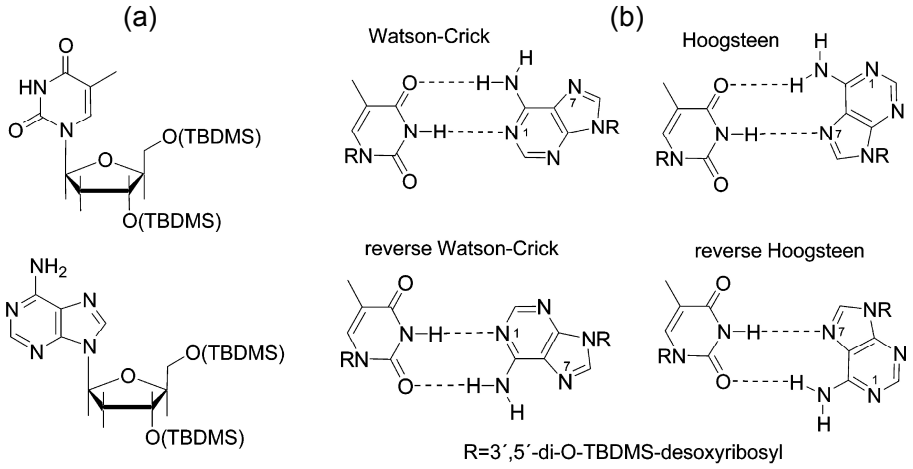

Figure 6.1: *(a) Molecular structure of TBDMS-protected 2´-deoxythymidine (T) (top) and TBDMS-protected 2´-deoxyadenosine (A) (bottom). (b) Possible cyclic base pairing geometries of A and T with two hydrogen bonds.*

for interbase bonding, might show distinctly different hydrogen-bond strength and, hence, different vibrational line shapes and dynamics. The formation of A·A and T·T homodimers is negligible compared to A·T heterodimers in a mixture of A and T in solution, as will be shown later.

Sample composition

For the determination of the relative formation enthalpy and abundance of the different A·T pairing geometries in chloroform solution, we performed low-temperature ^{1}H linear NMR measurements in a Freon solvent mixture ($CDClF_2/CDF_3$) [270,271]. Low-temperature conditions are necessary to slow down the proton and hydrogen-bond exchange kinetics beyond the millisecond time scale. This ensures that the specific magnetic environments around the various proton cores (and hence the molecular structure) shows only moderate changes on the time scale of nuclear spin dephasing. Hence, the slow-exchange regime enables the observation of specific chemical shifts for individual hydrogen-bonded species compared to only broad peaks in the NMR spectrum at elevated temperatures, then reflecting the averaged molecular structure.[a] The chemical shift δ describes the proton Larmor frequency υ_H in the sample in reference to the proton Larmor frequency υ_{Ref} in the residual solvent signal of $CHClF_2$: $\delta = (\upsilon_H - \upsilon_{Ref})/\upsilon_{Ref}$. We measure the ^{1}H chemical shifts of the NH··N imino protons involved in interbase hydrogen-bonding, which provide direct insight into hydrogen bonding geometries. The formation of hydrogen bonds is known to induce a substantial downfield shift of the resonance of the protons involved, i.e., to higher chemical shift values. Figure 6.2 shows NMR spectra at 140 K for mixed solutions of A with slight excess of T in Freon solvent. A detailed discussion can be found in [272]. In summary, there are two signals around 14.9 and 14.2 ppm and two signals around 12 ppm. The former two are assigned to the imino N-H··N protons in the A·T base pairs in WC/rWC and H/rH configuration, respectively, in analogy to measurements on A·U pairs performed under the same experimental conditions [273].[b] The corresponding reverse

[a] These two NMR-regimes of slow and fast exchange are analogous to inhomogeneous and homogenous broadening for optical and vibrational transitions in molecules.

[b] Correlating the observed chemical shifts of bridging protons to interatomic distances through empirical quantitative correlations, NH··N heavy atom distances of 2.85 Å and 2.90 Å for Watson-Crick and Hoogsteen base pairs are predicted. However, the applicability of such correlations to solution phase geometries is questionable, since

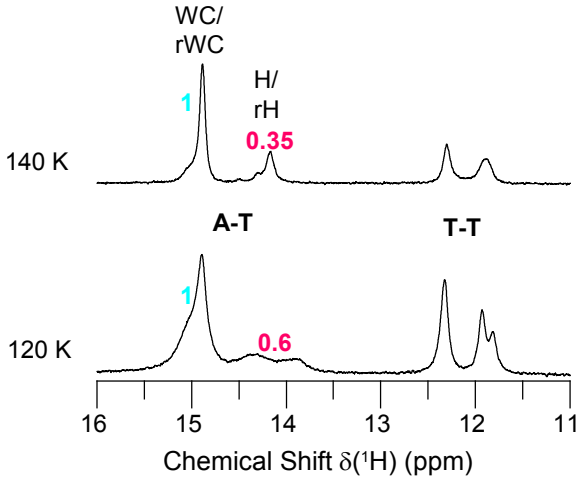

Figure 6.2: *Low-field part of the ^1H NMR spectra of AT mixtures with slight T excess recorded in Freon ($CDClF_3/CDF_3$) solution at various given temperatures. NH··N bridging imino protons in WC/rWC and H/rH configuration can be distinguished with their integrated signal intensities denoted in the Figure.*

and nonreverse configurations cannot be clearly distinguished from each other. The 12 ppm signals belong to T·T dimers. The protons involved in NH··O hydrogen bonds are expected to be found at lower chemical shift, but their signals are too broad to be assigned. Since the integrated NMR signal intensity of a certain peak is directly proportional to the number of protons in a certain environment, the sample composition can be determined in a quantitative way. The relative abundance of the WC/rWC and H/rH configurations, given by the NMR signal ratios of 1:0.35 (1:0.6) at 140 K (120 K), allows one to calculate the free energy differences of the WC/rWC and H/rH geometries, assuming an Arrhenius behavior, as ΔE = -kTln(I_{WC}/I_H) = 1.2-0.5 kJ mol^{-1}. Finding values much smaller than kT at room temperature (2.5 kJ mol^{-1}) hints to the presence of all four types of complexes in room temperature solution.

To validate this conclusion, Nicholas Preketes performed calculations on the relative energetics of the Hoogsteen and Watson-Crick complexes in chloroform, incorporating the full TBDMS-protected nucleobase structures. The solvent was accounted for in a polarizable continuum model [274]. The calculations indicate an elevated stability of the Watson-Crick base pairs by 0.34 kJ mol^{-1} compared to the Hoogsteen configuration. Similar differences in the free energies of association were obtained in recent density functional theory calculations [275] (0.33 kJ mol^{-1}). Both low-temperature NMR spectra and calculated formation enthalpies therefore show that all four dimer configurations in Figure 6.1 will be present in a similar amount in chloroform solution at room temperature. This work will therefore have to answer the question about the spectroscopic distinction of the different species.

6.2 Linear IR spectra of NH and ND stretching modes

The extinction coefficients obtained from linear FT-IR spectra of solutions of A, T, and equimolar AT mixtures at different concentrations in $CHCl_3/CDCl_3$ with CaF_2 windows of 1 mm thickness

these correlations were derived from comparison with diffraction patterns in crystals. It is not clear a priori that hydrogen bonding geometries in crystals and in solution phase are identical.

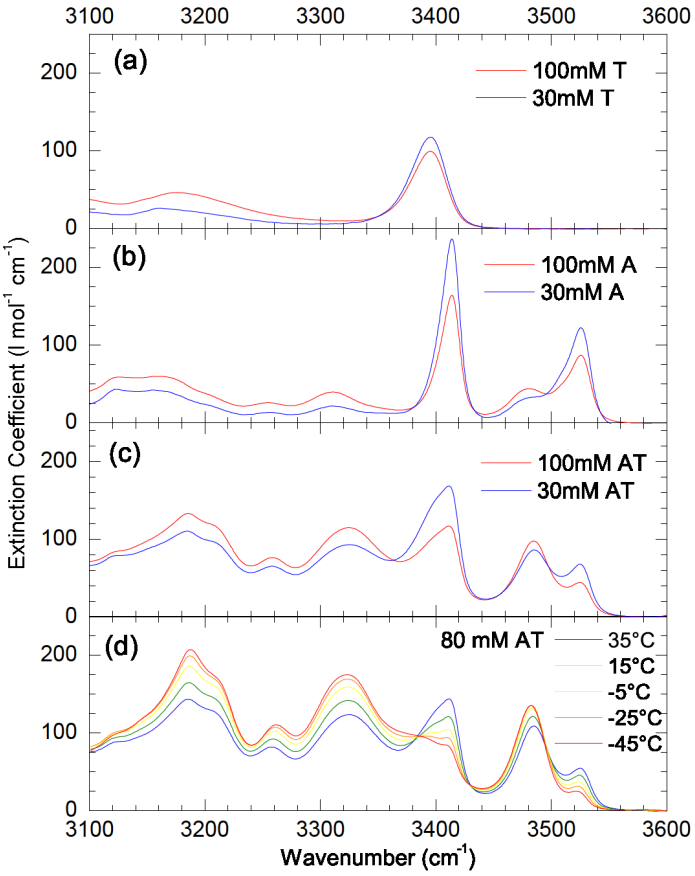

Figure 6.3: *Solvent-corrected room temperature FTIR spectra of solutions of (a) T, (b) A, and (c) equimolar AT mixtures in $CDCl_3$. (d) Temperature-dependent spectra of a 80 mM AT solution in $CHCl_3$.*

(absorption path length of 0.2 mm) are shown in Figure 6.3 (a), (b), and (c). The NH stretching (fundamental) transition in T monomers is found at 3396 cm^{-1}. An increase in T concentration leads to increasing formation of T·T dimers, as reflected in a decrease of the former band and the appearance of two broader red-shifted peaks centered around 3176 and 3068 cm^{-1} (the latter not shown; Figure 6.3 (a)). This observation is in agreement with FTIR studies on the aggregation of 1-cyclohexyluracil in $CDCl_3$ [190]. For A monomer, the symmetric and asymmetric NH stretching bands are observed at 3413 and 3525 cm^{-1}, respectively (see previous chapter). Upon increasing concentration of A, new bands appear at 3126, 3167, 3255, 3311, and 3482 cm^{-1} that are associated to A·A complexes, in agreement with reports on 9-ethyladenine and N-methyladenine in $CDCl_3$ [189]. The linear IR spectra of a mixture of equimolar solutions of A and T (Figure 6.3 (c)) show that with rising A and T concentration the contributions from A and T monomers at 3413 and 3525 cm^{-1} decrease, while new spectral features at 3188, 3211, 3262, 3324, and 3484 cm^{-1} show a synchronous intensity increase. Their spectral positions are distinct from bands found for solutions of only A or T, expect for the 3484 cm^{-1} peak also found in A·A complexes. These peaks are assigned to the NH stretching manifold in A·T dimers. Analysis of complexes of uracil (U) and adenine derivatives in chloroform solution gave NH stretching frequencies at similar spectral positions [245, 276, 277]. At room temperature in chloroform, the association constant for the formation of hydrogen-bonded dimers K_{AU} between A and U was determined to be 15 times larger than the association constants for U·U dimers and even 30 times larger than association to A·A dimers [245]. Similar relative

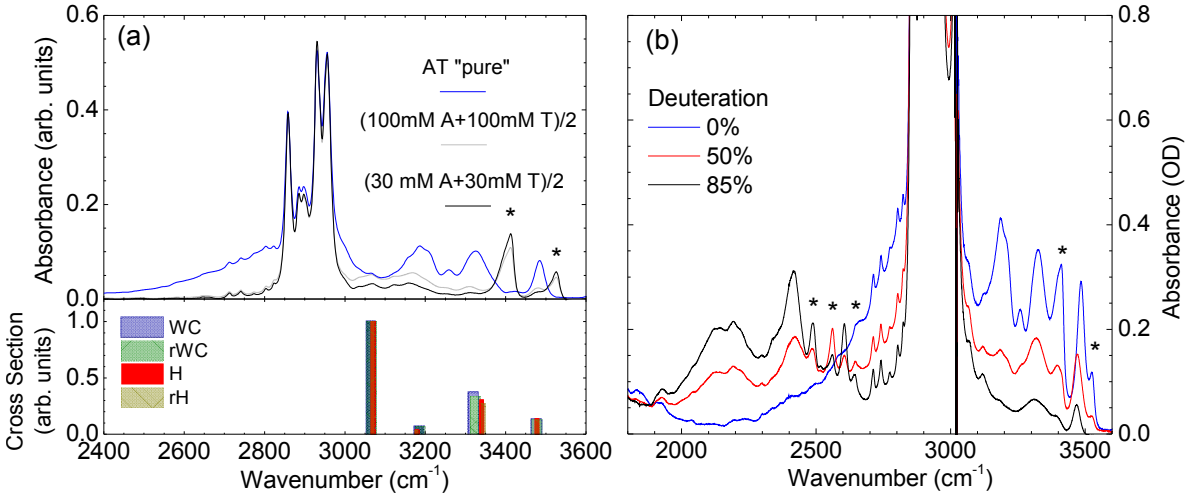

Figure 6.4: *(a) The sum of FTIR spectra for A and T monomers, recorded for 100 amd 30 mM monomer concentration (grey and black lines), is compared to the spectrum of A·T base pairs (blue line), which was corrected for monomer contributions by subtracting the 30 mM monomer sum spectrum. All spectra are normalized to the CH stretching band intensity around 2900 cm^{-1}. The stick spectra below shows the frequency positions and relative intensities of calculated IR spectra for the base pairs. (b) Linear FTIR spectra at different degrees of deuteration. The asterisks indicate ND and NH stretching modes from A and T monomers.*

numbers can be expected for derivatives of A and T, which supports the finding that A·T dimers dominate A·A or T·T homodimers. Upon lowering the sample temperature, the A·T association equilibrium is shifted in favor of complexation of A and T, making the NH stretching manifold of A·T complexes even more pronounced (Figure 6.3 (d)).

Figure 6.4 (a) shows the linear FTIR spectra of A·T dimers (blue line), corrected for the absorbance of both monomeric A and T species, in comparison with the sum of the spectra of A and T monomers for two concentrations (grey and black line). Here the frequency range is shown down to 2400 cm^{-1}, and the spectra are normalized to the absorbance at the position of the CH stretching modes around 2900 cm^{-1} for better comparison. Strikingly, beyond the multitude of NH stretching modes in the 3100 - 3500 cm^{-1} range, the A·T dimers carry significant oscillator strength in the region extending from the CH stretching region down to 2400 cm^{-1}. In contrast, this wing of absorbance is basically absent in the A and T monomer spectra, independent of concentration. This absorption wing is a major feature for the A·T dimers and shows even higher integrated signal strength than the hydrogen-bonded NH stretching modes at 3188 and 3324 cm^{-1}. Although this absorption wing has been reported in the literature before, it has not been thoroughly examined so far.

The spectra of A·T dimers at different degrees of deuteration of the NH_2 amino protons (the "mobile" protons) are shown in Figure 6.4 (b). Upon deuteration, the NH stretching transition described above decrease in intensity. Note that especially the NH stretching bands around 3200 cm^{-1} completely vanish already for moderate degrees of deuteration. New bands related to the ND stretching manifold appear at lower frequencies. Assuming harmonic vibrational modes in first approximation and, hence, a frequency downshift by a factor $\omega_H/\omega_D = (m_D/m_H)^{1/2} = 1.37$ (with $m_{H,D}$ the effective masses of th NH,D system), the bands located at 2488, 2565, 2604, and 2639 cm^{-1} can be assigned to the free ND stretching modes in deuterated monomers and deuterated A·T base pairs. The hydrogen-bonded ND stretching modes appear as red-shifted broad bands at 2419 and 2170 cm^{-1}, both showing significant substructure. The latter peak shows a wing to lower

frequencies, which corresponds to the absorption feature of the non-deuterated A·T dimers in the 3000 - 2400 cm^{-1} range.

Hydrogen bonding localizes NH stretching excitations

In contrast to the situation in the amino group of adenosine monomer, where the decoupled single-excited NH stretching modes were degenerate and, hence, formed the delocalized normal symmetric and asymmetric stretching states, the hydrogen bonding induced frequency redshift (> 200 cm^{-1}) of one of the NH stretching modes leads to an effective decoupling of both NH stretching states in the amino group in A·T base pairs. Both states show a more local character with only little mixing between their wavefunctions (compare equations (2.9), (2.10), and (2.11)). Therefore, the NH stretching modes will be designated with the local mode terminology as the free NH stretching state $\upsilon_A(NH_2)_f$ (f: free) and the hydrogen-bonded NH stretching states $\upsilon_A(NH_2)_b$ (b: bound) of A and the hydrogen-bonded NH stretching states of T $\upsilon_T(NH)$. However, we will show in the following part that mixing with fingerprint overtone states, especially the NH_2 bending overtone, may be significant, which constrains the validity of the local mode picture. The local mode assignments above will therefore primarily reflect the modes that are expected to dominate the wavefunctions.

Linear IR spectroscopy shows that the NH stretching manifold of A·T dimers is composed of at least 5 spectral bands extending from 2400-3500 cm^{-1}. However, a single dimer geometry with three local NH stretching modes should to first approximation produce only three vibrational bands at possibly distinct frequencies. The assignment of this spectral mode pattern is thus far from trivial. The multitude of lines results either from distinctly different NH stretching frequencies in the four different A·T pairing geometries or from couplings to other modes. To gain insight into the origin of vibrational line shapes and the underlying vibrational couplings, we applied femtosecond single- and two-color pump probe as well as 2D photon echo spectroscopy as discussed in the next section.

6.3 Anharmonic coupling between NH stretching excitations and to a low-frequency hydrogen-bond mode

Transient absorption spectra with pump and probe pulses both centered around 3350 cm^{-1} as a function of frequency and time are shown in Figure 6.5. In Figure 6.5 (b), the spectral transients are plotted for pump-probe delays of 100 to 1000 fs. Reduced absorption signals corresponding to ground state $\upsilon = 0$ bleaching and stimulated emission from the excited $\upsilon = 1$ state are located at spectral positions coinciding with the fundamental 0-1 transitions found in the linear IR spectra. The line shapes of these reduced absorption signals show only minor temporal reshaping, e.g., changes in center frequencies and spectral width. This indicates a negligible role of spectral diffusion beyond the spectral width of the various spectral components on the picosecond time scale. This aspect will be discussed later in the context of the 2D-IR measurements. The reduced absorption signals are superimposed on weaker enhanced absorption signatures from excited state 1-2 transitions that are almost invisible in the transient pump-probe spectra. The determination and assignment of excited state transition frequencies and, thus, the derivation of vibrational anharmonicity magnitudes requires the measurement of 2D-IR spectra.

Hydrogen bonding induced T_1 lifetime shortening

The population kinetics at different spectral positions shown in Figure 6.5 (c,d) indicate a faster bleach recovery for the hydrogen bonded fundamental NH stretching transitions compared to the free fundamental NH stretching mode in A·T dimers. While the bleach of the free NH stretching band around 3484 cm^{-1} shows a monoexponential decay with a time constant of 0.8 - 2.1 ps

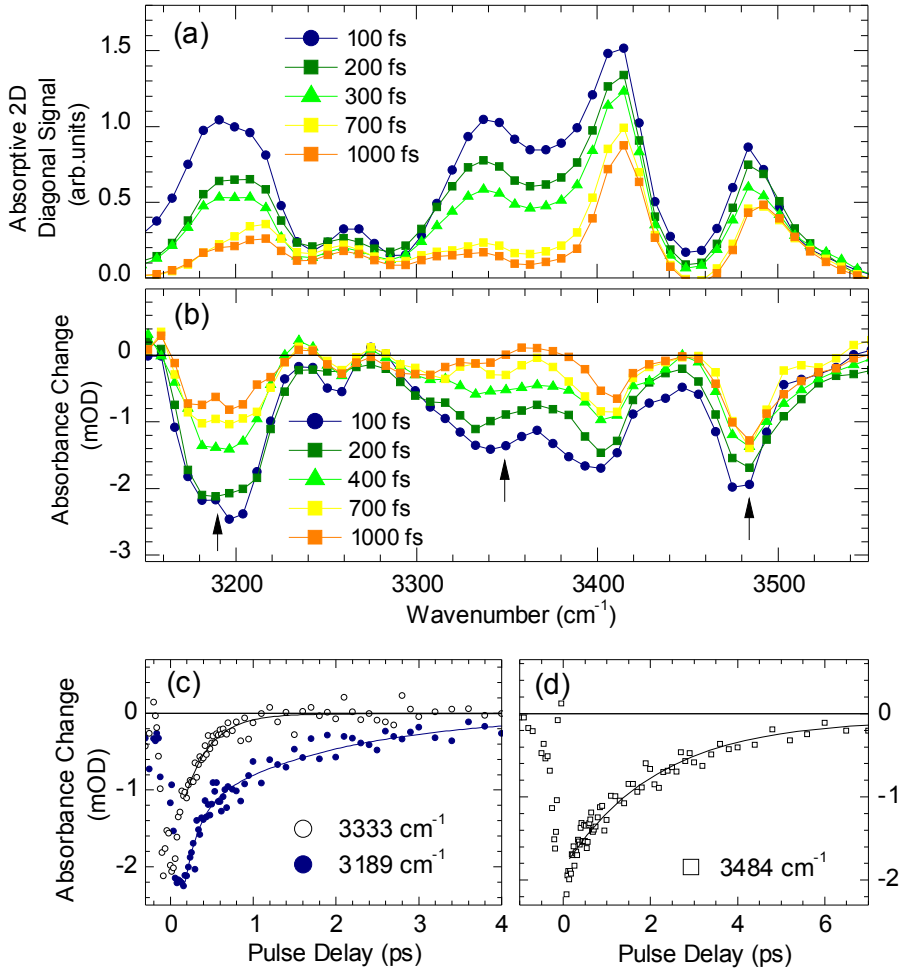

Figure 6.5: *(a) Diagonal cuts of absorptive 2D-IR spectra for different waiting times and (b) transient pump-probe spectra, both recorded with a 120 mM A·T solution in $CHCl_3$. Arrows indicate spectral positions of bleaching signals whose population kinetics is shown in (c,d). Hydrogen-bonded NH stretching modes (transients plotted in (c)) show a sub-picosecond decay component that is missing in the bleach recovery dynamics of free NH stretching modes (transient plotted in (d)), which shows T_1 lifetime shortening through hydrogen bonding.*

(depending on the exact spectral position), hydrogen-bonded NH stretching states located at 3333 and 3189 cm^{-1} show a multiexponential decay with distinctly faster decay components of 0.2 - 0.4 ps (Figure 6.5 (c,d)). T_1 lifetime shortening upon hydrogen bonding was observed in various hydrogen-bonded molecular systems [49, 278, 279]. The hydrogen bonding induced redshift of fundamental NH stretching frequencies leads to a stronger mixing with anharmonically coupled overtone and combination tone fingerprint vibrations, which results in additional population relaxation pathways for the $v = 1$ NH stretching states. The different time scales involved in the cascaded population decay process reflect the multiexponential decay behavior of the bleaching NH stretching signals. The pump-probe kinetics show no pronounced beating due to coherent multimode excitation, in contrast to measurements on A monomer molecules. This results both from the excitation of a multitude of modes, leading to a complicated beating behavior on multiple time scales, and from the shortened lifetime of the hydrogen bonded NH stretching states.

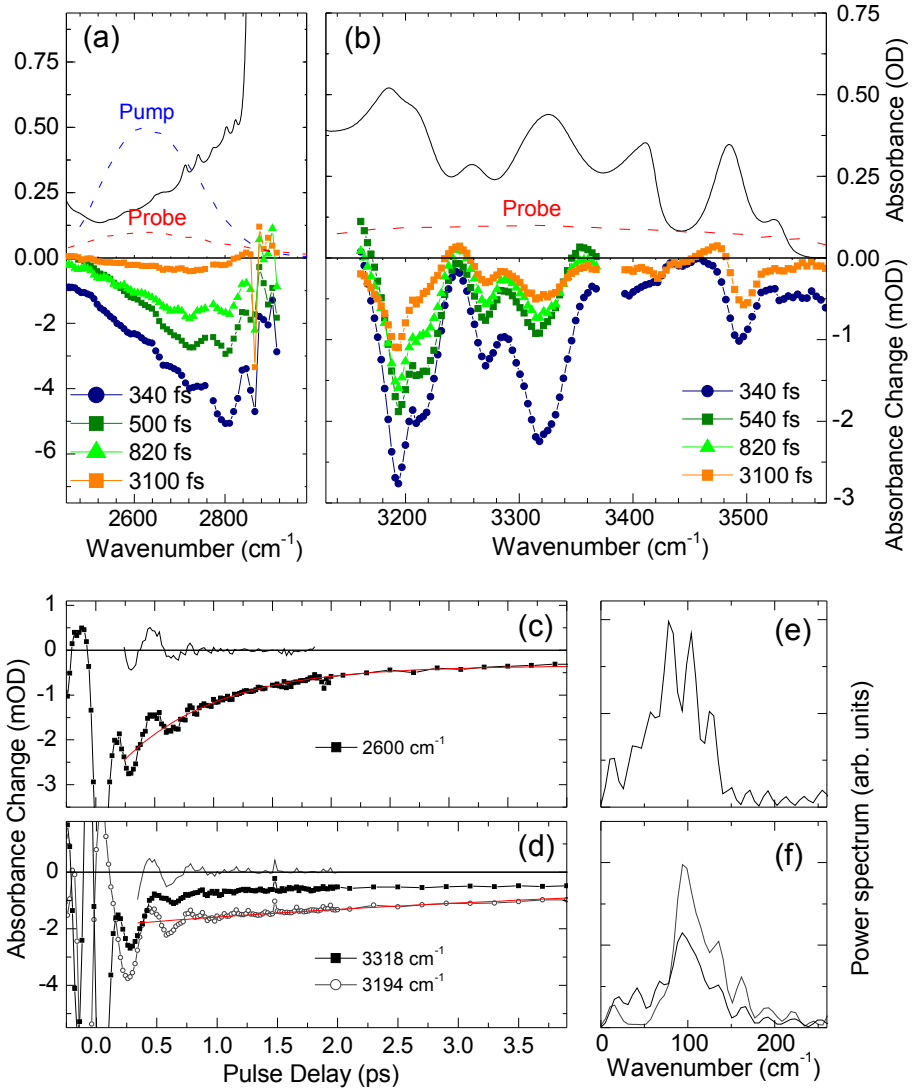

Figure 6.6: *Single- and two-color pump-probe transients for different delays with pump excitation at 2600 cm^{-1}. The instantaneous transient molecular response in the 2500 - 2800 cm^{-1} and 3150 - 3600 cm^{-1} regions in (a) and (b), respectively, shows a multiexponential picosecond and sub-picosecond bleach recovery dynamics (c,d). The instantaneous response in the high frequency spectral region indicates that the NH stretching manifold extends down to 2500 cm^{-1}. The oscillatory contributions to the multiexponential decays are explained with wavepacket motion of coherently excited vibrational sidebands due to anharmonic coupling with an underdamped low-frequency mode, with its frequency spectrum shown in (e,f).*

Origin of the absorption wing below 3000 cm^{-1}

In order to gain insight into the origin of the broad A·T base pair absorption feature between 2400 and 3000 cm^{-1}, we performed a second series of pump-probe experiments with the pump pulses centered at 2600 cm^{-1}.[c] The spectral transients with the probe pulse centered at the same frequency position are plotted in the lower part of Figure 6.6 (a), which shows a broad bleaching

[c] Pump and probe pulses have to avoid the intense CH stretching absorption band to prevent significant pulse distortions.

signal centered at 2800 cm^{-1}. A shift in the probe pulse spectrum to a center frequency of 3300 cm^{-1} enables the observation of transient bleaching signals at spectral positions that coincide with all fundamental NH stretching transitions of A·T base pairs in the 3100 - 3500 cm^{-1} region as shown in Figure 6.6 (b). Within experimental accuracy, the absorption decrease mirrors the A·T base pair related components of the steady-state IR spectrum in frequency position and signal intensities. There are no significantly strong bleaching signals at the frequency position of the free NH stretching modes of A and T monomers. The maximum signal response of all responding modes occurs within the pulse cross correlation width. The pump excitation around 2600 cm^{-1} leads to a shift in the 0-1 transition frequencies of the anharmonically coupled high frequency NH stretching modes, which results in an instantaneous pump-probe response at their unperturbed transition frequencies. An energetically unfavorable uphill population transfer bridging more than 600 cm^{-1} as well as the formation of a vibrationally hot ground state cannot explain the broadband bleaching response. This gives the important conclusion that both the broad absorption wing in the 2400 - 3000 cm^{-1} region and the absorption features at 3188, 3211, 3262, 3324, and 3484 cm^{-1} belong to the NH stretching manifold in the A·T dimers.

Anharmonic couplings to low-frequency hydrogen bond modes revealed by underdamped wavepacket oscillation

The pump-probe transients for excitation at 2600 cm^{-1} are plotted in Figure 6.6 (c,d) for probe frequencies of 2600, 3194, and 3318 cm^{-1}. The multiexponential bleach recovery of these bands each shows a sub-200 fs decay component (only tentatively assignable due to coherent pump-probe coupling contributions near zero delay) and a long time constant beyond 100 ps. At a probe frequency of 2600 and 3194 cm^{-1} additional temporal components of (0.8 ± 0.1) ps and (3.0 ± 0.9) ps, respectively, are found. When probing both above and below the CH stretching region, the multiexponential bleaching decay is overlayed with underdamped beating contributions whose Fourier transforms are centered around 100 cm^{-1} (Figure 6.6 (e,f)).

The origin of these oscillations is explained in Figure 6.7. The beating evidences the anharmonic coupling of the pumped NH stretching excitations to low-frequency intermolecular hydrogen bond modes, e.g., to the symmetric or asymmetric dimer breathing mode, which modulates the two hydrogen bond distances in the A·T dimer synchronously or asynchronously. In a Born-Oppenheimer-like picture, the adiabatic separation of time scales between the fast NH stretching mode and the slow hydrogen bond mode allows one to parametrize the potential energy surface of the slow local coordinate with the degree of excitation of the fast NH stretching local coordinate (see Figure 6.7). This leads to the formation of vibrational sidebands upon NH stretching excitation that are separated by the slow mode frequency, with the degree of excitation into a certain sideband depending on the corresponding Frank-Condon overlap. The broadband pump excitation enables coherent impulsive excitation of several sidebands, resulting in the generation of vibrational wavepackets both in the excited state (Figure 6.7 (b)) and the ground state potential through an impulsive resonantly-enhanced Raman process (Figure 6.7 (c)). The wavepacket, oscillating with the slow mode frequency, translates into a periodically oscillating absorbance change due to the periodic changes in Frank-Condon overlap, which is monitored in the pump-probe experiment.[d] Hence, the observed beating frequency of 100 cm^{-1} is assigned to an unspecified low-frequency intermolecular hydrogen bond mode. Such beating was observed, e.g., in the transmission changes of dyes in solution after electronic excitation [280–282] and in various mid-IR pump-probe studies of molecules in solution carrying intra- [283] or intermolecular hydrogen bonds such as acetic acid dimers [284, 285], 7-azaindole dimer [252] and 2-pyridone dimer [286, 287]. We conclude that the

[d] Alternatively, the oscillating probe pulse absorption can be understood in a classical picture, where the excitation of the anharmonically coupled hydrogen bond mode leads to an oscillating hydrogen bond strength between A and T and, hence, to oscillating spectral positions of the NH stretching absorption bands.

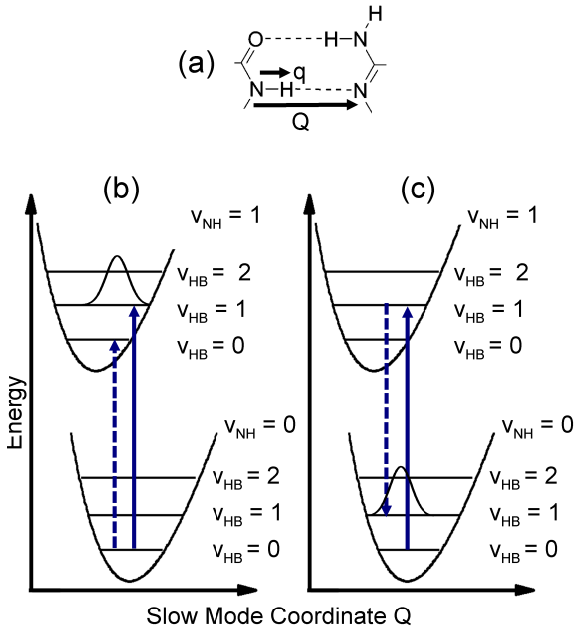

Figure 6.7: *(a) Fast (q) and slow (Q) vibrational coordinates in A·T dimers corresponding to the NH stretching mode and a hydrogen bond mode, respectively, leading to a Born-Oppenheimer-like separation of time scales. (b) Scheme of the potential energy surfaces of the $\upsilon_{NH} = 0$ and 1 states with vibrational energy levels of the low-frequency mode added, where υ_{HB} denotes the excitation state of that low-frequency mode. The two field interactions within the pump pulse (blue arrows) create a vibrational wavepacket in the first excited $\upsilon_{NH} = 1$ state (b) and in the vibrational ground state via an impulsive resonantly-enhanced Raman process (c). The wavepacket oscillation leads to a beating in the pump-probe signal.*

formation of vibrational sidebands upon hydrogen bond formation due to anharmonic coupling to low-frequency modes is one reason for the congested line shapes of A·T base pairs.

6.4 Mapping of the potential energy surface and anharmonic couplings in 2D-IR spectra

So far, we have not addressed the question if the various configurations of A·T dimer geometries show distinctly different NH stretching center frequencies. Now we approach this question with 2D-IR spectroscopy. The occurrence of cross peaks in 2D-IR plots between two localized vibrational bands is indicative of intermode through-bond or dipole-dipole coupling. Only two spatially nearby vibrational modes will exhibit cross peaks, otherwise their anharmonic intermode coupling terms would be zero. Hence, a similar NH stretching manifold in the WC/rWC and H/rH A·T dimer configurations would result in the appearance of cross peaks between all NH stretching modes, while in the case of distinctly different NH stretching mode patterns for different dimer geometries some cross peaks would be absent. The 2D-IR spectra will reveal anharmonic mode couplings and line broadening mechanism for the NH stretching modes in the region of 3100-3500 cm^{-1}.

A series of absorptive 2D-IR spectra of a 120 mM mixture of AT in $CHCl_3$ (as obtained by mixing identical volumes of 240 mM solutions of A and T) with all pulses centered at 3360 cm^{-1}

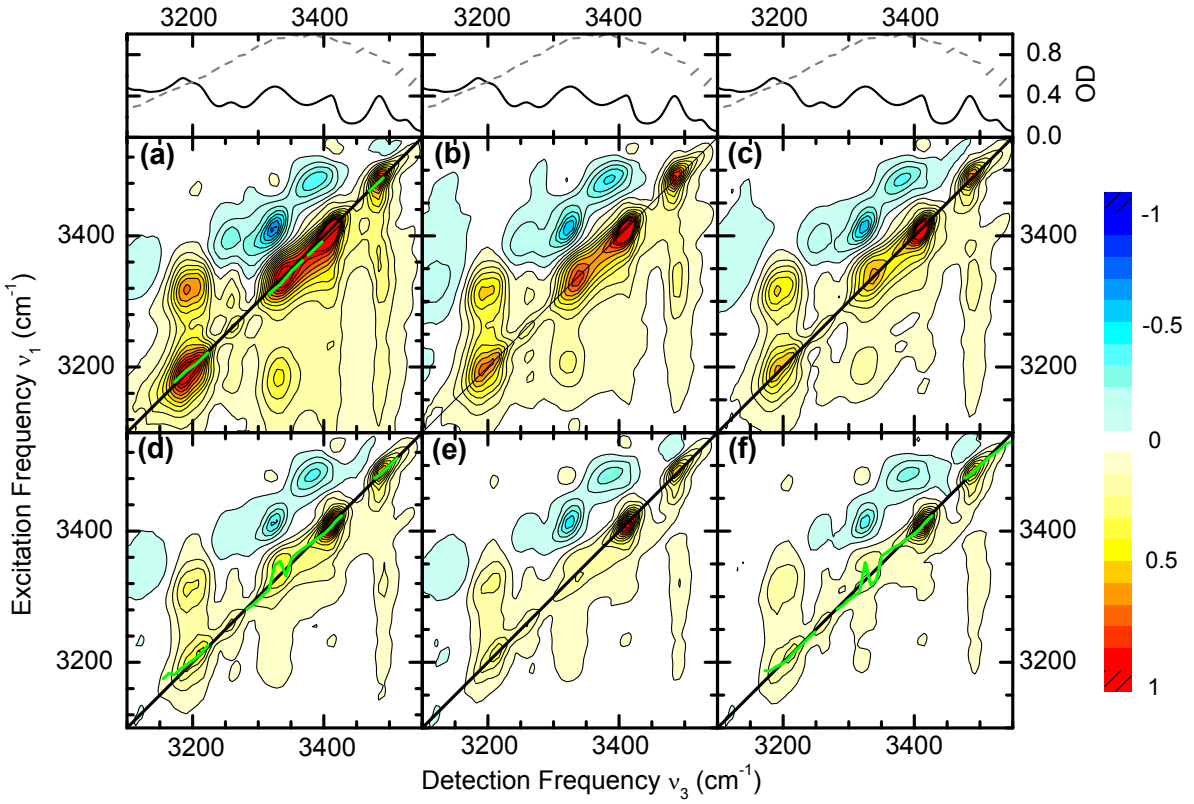

Figure 6.8: *A series of absorptive 2D-IR spectra of a 120 mM AT mixture in $CHCl_3$ in ZZZZ polarization geometry for waiting times T of (a) 100 fs, (b) 200 fs, (c) 300fs, (d) 500 fs, (e) 700 fs, and (f) 1000 fs. The spectra are scaled to 80% of the maximum intensity of the T = 100 fs spectrum. Center lines connecting the frequency positions with maximum intensity of slices with fixed detection frequency are added to some of the peaks (green lines) in (a) (d) and (f). For comparison the linear spectrum of the sample and the excitation laser spectrum is plotted in the top and side panels.*

for waiting times between 0.1 and 1.0 ps is shown in Figure 6.8 recorded with the all-parallel ZZZZ linear polarization scheme for the excitation and local oscillator pulses. The coherence time τ_1 was scanned (in steps of 4 fs) from -400 to 1000 fs until the rephasing and nonrephasing signals decayed to a few percent of the maximum signal at $\tau_1 = 0$. The spectra are scaled to 60% of the maximum signal for the T = 100 fs spectrum, and for comparison the linear spectrum is shown in the top panels. A slice along the frequency diagonal (Figure 6.5 (a)) reveals (positive) peaks at $\upsilon_1 = \upsilon_3 =$ 3200, 3263, 3337, 3415, 3484, and 3525 cm^{-1}, which coincide with peak positions in the linear FT-IR spectrum within experimental accuracy. They arise from various bleaching and stimulated emission Feynman pathways involving only their corresponding 0-1 transitions. Negative off-diagonal peaks are found at $(\upsilon_1[cm^{-1}], \upsilon_3[cm^{-1}]) =$ (3484,3389), (3393,3251) and weaker at (3409,3329). They arise from excitation pathways involving the 1-2 double-excited states of the fundamental 0-1 transitions of the free NH stretching mode in A·T dimers (3484 cm^{-1}), in T monomers (3393 cm^{-1}), and the symmetric stretching mode in A monomers (3415 cm^{-1}), respectively. These features are uniquely resolved in the 2D experiments and not accessible with pump-probe due to the heavy spectral congestion. The derived anharmonic downshift of the free NH stretching mode overtone in the A·T

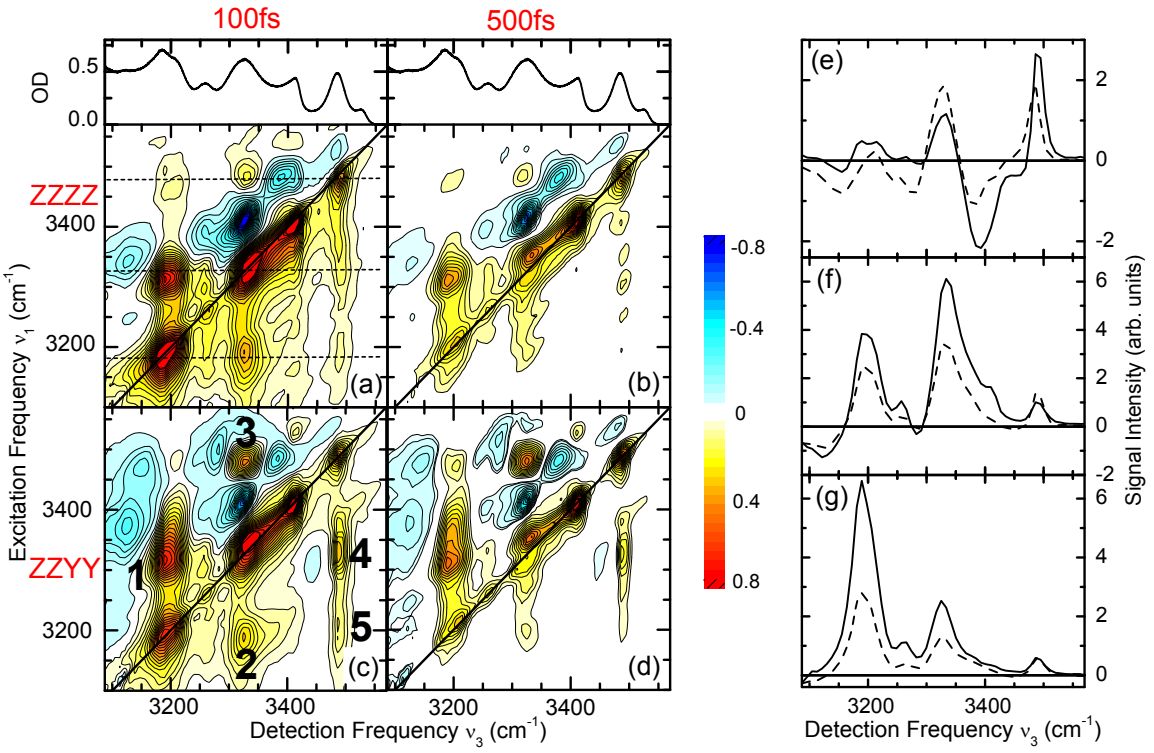

Figure 6.9: *Polarization-dependent absorptive 2D-IR spectra in* (k_1, k_2, k_3, k_{LO}) = *ZZZZ (a,b) and ZZXX (c,d) polarization geometry, each for waiting times T of 100 and 500 fs. The spectra are scaled to 80 % of the maximum intensity in each 2D spectrum. The linear IR spectrum is added to the top panels. A few selected cross peaks are marked with numbers in the panel (c). The change in cross peak intensity upon a change in linear polarization of the excitation and LO pulses is related to the relative transition dipole angle through equations (2.51) and (2.52) with values given in table 6.1. Horizontal slices for the T = 100 fs 2D spectra in ZZZZ (solid lines) and ZZXX geometry (dashed lines) for different excitation frequencies of 3485 cm*$^{-1}$ *(e), 3330 cm*$^{-1}$ *(f), and 3190 cm*$^{-1}$ *(g), as indicated by the dashed lines in (a).*

dimers of $D_{NH,free}$ = 95 cm^{-1} is similar to the value in G·C base pairs [49] (130 cm^{-1}) and to the value of local mode NH stretching anharmonicities of A and T monomers of 135 and 150 cm^{-1}, respectively (see previous chapter). Positive off-diagonal cross peaks are located at (3200,3320), (3320,3200), (3200,3484), (3484,3200), (3320,3484), (3484,3320), and at (3525,3420) (weak).

In order to enhance the visibility of cross peaks between nonparallel transition dipoles and to obtain relative transition dipole angles, we measured 2D-IR spectra in the (k_1, k_2, k_3, k_{LO}) = ZZXX polarization condition, i.e. with two pulses perpendicularly polarized to the other two. These spectra are compared to the ZZZZ polarization geometry in Figure 6.9. In ZZXX configuration, the diagonal peak intensity decreases, while the degree of decrease of the cross peak signals depends on the relative transition dipole angles between the coupled oscillators (see pages 28 ff.). The (3320,3200) and (3200,3320) cross peak intensities drop in accordance with the diagonal peaks. However, the cross peaks at (3320,3484), (3484,3320), (3525,3420), (3420,3525), (3200,3484), and to a lesser extent (3484,3200) increase significantly compared to the diagonal peaks. This is also reflected by spectral cuts for fixed excitation frequencies at 3190, 3330 and 3485 cm^{-1} for 2D spectra in ZZZZ and ZZXX configuration with T = 100 fs in Figure 6.9 (e-f). In addition, in the cross-polarization geometry weak negative signal contributions appear, e.g., at (3482,3155),

(3482,3277), and (3307,3449) (weak). These signals originate from excitation pathways involving the combination state with single-quantum excitation on both involved oscillators and, therefore, provide insight into off-diagonal anharmonic shifts D_{ij}. Positive cross peaks located at (3525,3420) and (3420,3525) arise from through-bond mechanical coupling between the symmetric and asymmetric stretching modes of A monomer (see discussion in the previous chapter). Weak positive cross peak features at (3200,3390) and (3390,3200) in the ZZXX polarization geometry might by due to Fermi resonance coupling of the hydrogen-bonded NH··O stretching state with the carbonyl C=O overtone vibration or due to cross peaks in T·A·T trimers.

The 2D spectra recorded in ZZXX polarization scheme allow us to clearly identify cross peaks between *all* NH stretching excitations in the A·T base pairs, involving both the free NH stretching mode of the adenosine amino group at 3484 cm^{-1} and the hydrogen-bonded NH stretching modes around 3320, 3200, and (very weak) 3263 cm^{-1} (compare Figure 6.9). In addition, the absorption wing at lower frequency is anharmonically coupled to all of the higher frequency NH stretching modes of A·T dimers, as was indicated by the two-color pump-probe measurements. This has two important repercussions:

- The NH stretching manifold of all four A·T pairing geometries WC/rWC/H/rH shows a mode pattern that is identical within the width of the substantially inhomogeneously and lifetime-broadened bands. A purely local mode picture would therefore predict only three major vibrational bands in the NH stretching region of A·T base pairs.
- All NH stretching modes are anharmonically coupled with each other. While the NH stretching excitations in the adenosine amino group are mostly mechanically coupled, there exists notable interbase dipole-dipole couplings between the thymidine and adenosine NH stretching modes.

Fermi resonances with fingerprint overtone and combination tone modes

The sideband generation due to anharmonic coupling to low-frequency modes was already discussed as one contribution to the breakup into four to five major NH stretching bands. As a second mechanism, we assume Fermi resonances with combination and overtones states to play an important role, leading to a strong mixing of vibrational overtone and combination eigenstates with the single-excited NH stretching states. The concomitant transfer of oscillator strength from the dipole-allowed 0-1 fundamental NH stretching transitions to the harmonically-forbidden 0-2 two-quantum transitions could make these Fermi resonance enhanced overtone states a prominent feature in the linear IR spectra. Inspection of the linear spectra and the deuteration experiments, showing an almost complete disappearance of the 3200 cm^{-1} bands already for little H/D exchange with only a slight decrease of the other bands, strongly points to overtone and/or combination tones of the NH_2 bending mode as the most probable candidate experiencing strong Fermi resonance enhancement. As will be discussed below, the polarization-dependent 2D-IR spectra in Figure 6.9 indicate roughly parallel transition dipoles for the 3200 and 3320 cm^{-1} oscillators, which is consistent with the parallel dipole orientation of a Fermi resonance doublet.

Ultrafast population transfer and the absence of spectral diffusion

The population dynamics indicated by the waiting time dependent 2D spectra are plotted in Figure 6.10, which shows the integrated signal intensities around the most intense diagonal and off-diagonal peaks as a function of waiting time (using their maximum signal intensity gives very similar results). In agreement with the pump-probe results above, the decay of the hydrogen-bonded NH stretching states in A·T dimers at 3337 and 3200 cm^{-1} is notably faster than the corresponding decay of free NH stretching modes and the symmetric NH stretching mode of A monomers (3415 cm^{-1}) (Figure

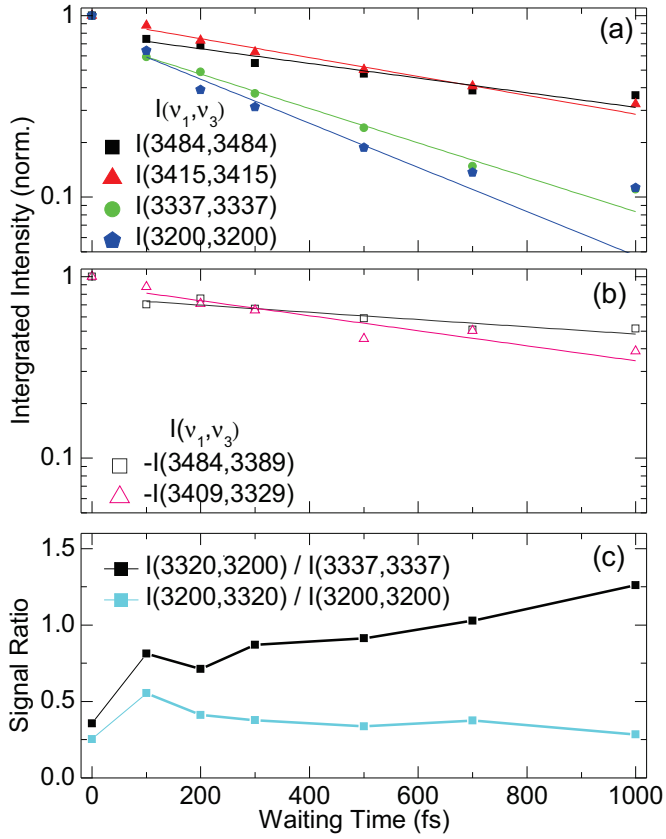

Figure 6.10: *Integrated signal intensity of various peaks in the 2D-IR spectra from Figure 6.8 for different waiting times. Monoexponential fits with floating offset, starting at 100 fs to ensure negligible influence from coherent artifact signals, give an idea of the fast population decay components. Free NH stretching modes decay substantially slower than hydrogen-bonded NH stretching states, as evidenced by bleach recovery (a) and excited-state (b) decay dynamics. (c) Cross-to-diagonal peak intensity ratio of two peaks (specified in the legend) indicating a downhill population transfer.*

6.10 (a)). The rather slow decays of non-hydrogen bonded NH stretching modes are also mirrored by the negative peaks at (3484,3389) and (3409,3329) (Figure 6.10 (b)). Decay times, obtained by monoexponential fits to the integrated temporal signal intensities with a floating offset, as well as the lifetimes from the transient absorption measurements above are summarized in Table 6.1. Both pump-probe and 2D-IR spectra show that while the nonhydrogen bonded NH stretching mode decays with a 1-2 ps time constant, all hydrogen-bonded NH stretching modes show a substantially faster population decay within few hundred femtoseconds.

It is interesting to note that the (3320,3200) cross peak shows an intensity increase with waiting time relative to the (3320,3320) diagonal peak at the same excitation frequency (Figure 6.10 (c)). As explained previously (page 28), this is indicative of a downhill vibrational ultrafast energy transfer from the 3320 cm^{-1} mode to the 3200 cm^{-1} mode. In contrast, such a behaviour is not visible for the ratio of the (3200,3320) cross peak to the (3200,3200) diagonal peak. Similar observations were

0-1 **Frequency** (cm^{-1})	**Lifetime (ps)**	**Type of Measurement**
2600	fast component < 0.2 slow component < 0.8 ± 0.1	Pump-Probe Pump-Probe
3200	0.4 ± 0.1 fast component: 0.18 ± 0.04 slow component: 1.8 ± 0.2	2D Diag. Peak Pump-Probe
3337	0.46 ± 0.06 0.31 ± 0.05	2D Diag. Peak Pump-Probe
3484 3484 3484 band, averaged	1.1 ± 0.4 2.1 ± 0.2 1.8 ± 0.3	2D Diag. Peak Pump-Probe Pump-Probe
Cross Peak (υ_1, υ_3) (cm^{-1}, cm^{-1})		
(3484,3389)	2 ± 1	2D Off-Diag. Peak
(3409,3329)	1.0 ± 0.4	2D Off-Diag. Peak

	1	**2**	**3**	**4**	**5**
f_{ab}	1.1 ± 0.4	1.1 ± 0.2	3.6 ± 1.3	2.5 ± 0.4	2.5 ± 0.3
$\theta_{ab}(^\circ)$	20 ± 20	20 ± 20	90 ± 30	115 ± 10	115 ± 10
Calc. $\theta_{ab}(^\circ)$	4	4	136	136	133

Table 6.1: *Top: Decay times of different vibrational modes measured by frequency-resolved pump-probe and 2D-IR photon echo spectroscopy. Bottom: Enhancement factor of cross-to-diagonal peak intensity ratio in ZZXX compared to ZZZZ polarization configuration and the derived relative transition dipole angles for peaks labeled in Figure 6.9. Calculated angles are given for comparison.*

made for G·C base pairs in chloroform solution [49] and in short-stranded double-helical AT [235] and (to a lesser extent) G·C oligomers (see section 7). For all other peaks there are no significant changes in the cross-to-diagonal peak ratio with waiting time.

The 2D line shapes of all diagonal peaks in Figure 6.8 show a static elongation along the diagonal and exhibit only minor changes with waiting time, as evidenced by the center lines added to the spectra (green lines in Figure 6.8). This points to dominatingly inhomogeneous broadening on the picosecond time scale due to a distribution of rather rigid A·T dimer geometries with only weakly fluctuating hydrogen-bonding geometries, in accordance with implications from the transient absorption measurements above.

Relative transition dipole angles

The measured 2D-IR spectra in ZZZZ and ZZXX polarization condition shown in Figure 6.9 can be used to extract relative transition dipole angles (see pages 28 ff.). An enhancement factor close to 3.6 for the ratio of cross-to-diagonal peak intensities upon a change from ZZZZ to ZZXX polarization would indicate a 90° relative angle, whereas for parallel transitions the ratio would not change. In order to exclude distortions by population or coherence transfer, we recorded polarization-dependent 2D spectra for different waiting times of T = 100, 200, and 500 fs and extrapolated the derived enhancement factor f_{ab} to zero waiting time. Equations (2.51) and (2.52) then allow one to calculate the relative transition dipole angles θ_{ab}. The derived values f_{ab} and θ_{ab} are summarized in Table 6.1.[e] The transition dipole angles between the free NH stretching

[e] The use of integrated signal intensities or maximum intensity values made no significant difference here for determining the third-order signal strength (provided the integration area chosen is not too large).

mode $\upsilon_A(NH_2)_f$ and the modes at 3320/3200 cm^{-1} are 65°-90°. The transition dipoles of the 3200 and 3320 cm^{-1} modes are close to parallel with an angle (20 ± 20)°. For highly localized NH stretching excitations, as expected for A·T dimers due to the localizing effect of hydrogen bonding, the transition dipoles are largely aligned parallel to their corresponding bond vectors (this will be supported by ab initio calculations below). Hence, a relative angle of 120°(60°) is expected between the $\mu(\upsilon_A(NH_2)_b)$ and $\mu(\upsilon_A(NH_2)_f)$ transition dipoles, while the relative angle between the $\mu(\upsilon_T(NH))$ and $\mu(\upsilon_A(NH_2)_b)$ as well as between the transition dipoles of any Fermi resonance doublet should be close to zero. This shows that there exists a clear ambiguity in the assignment of the measured relative transition dipole angles to certain vibrational modes. While the $\upsilon_A(NH_2)_f$ mode is unambiguously fixed to 3485 cm^{-1} through the linear and nonlinear IR measurements, independent calculations are required to assign the remaining vibrational bands.

6.5 Quantum chemical calculations

In order to substantiate the role of the Fermi resonance enhanced NH_2 bending overtone and to help with the assignment of the various NH stretching modes of A·T pairs, ab initio calculations have been performed by Nicholas Preketes. As in the previous chapter, we use the Hartree-Fock approach with the 6-311++G** basis set. For the calculations the A·T dimers are approximated as 9-mA·1-mT dimers, substituting the TBDMS-ribose side groups with a methyl group in both molecules.

The Hamiltonian was calculated as a Taylor series in the three local internal NH stretching states and the NH_2 bending degree of freedom, truncating the anharmonic correction terms after sixth order [258,262]. In the following section, the hydrogen-bonded NH stretching local coordinate of T is addressed as mode 1, while the hydrogen-bonded and the free NH stretching mode of A are designated as mode 2 and 3, respectively. The NH_2 bending coordinate of A is given as mode 4. The Hamiltonian H is set up as a sum of two terms, where H_{123} contains the degrees of freedom of mode one, two, and three, while H_4 contains the internal energy of the NH_2 bending degrees of freedom and its coupling to the NH stretching modes only:

$$H = H_{123} + H_4 \tag{6.1}$$

with

$$\begin{aligned} H_{123} = &\sum_{i,j}^{3} \frac{1}{2} G_{ij} p_i p_j + V_0 + \sum_{i}^{3} f_i Q_i + \frac{1}{2!} \sum_{ij}^{3} f_{ij} Q_i Q_j + \frac{1}{3!} \sum_{ijk}^{3} f_{ijk} Q_i Q_j Q_k \\ &+ \frac{1}{4!} \sum_{ijkl}^{3} f_{ijkl} Q_i Q_j Q_k Q_l + \frac{1}{5!} \sum_{ijklm}^{3} f_{ijklm} Q_i Q_j Q_k Q_l Q_m + \frac{1}{6!} \sum_{ijklmn}^{3} f_{ijklmn} Q_i Q_j Q_k Q_l Q_m Q_n \end{aligned} \tag{6.2}$$

and

$$\begin{aligned} H_4 = &\sum_{i}^{4} \frac{1}{2} G_{i4} p_i p_4 + V_0' + f_4 Q_4 + \frac{1}{2!} \sum_{i}^{4} f_{i4} Q_i Q_4 + \frac{1}{3!} \sum_{i}^{3} f_{i44} Q_i Q_4^2 + \frac{1}{4!} f_{4444} Q_4^4 \\ &+ \frac{1}{5!} f_{44444} Q_4^5 + \frac{1}{6!} f_{444444} Q_4^6 + \frac{1}{3!} \sum_{i}^{3} \left(\frac{\partial G_{i4}}{\partial r_4} \right) p_i p_4 r_4 + \frac{1}{3!} \sum_{i}^{3} \left(\frac{\partial G_{44}}{\partial r_i} \right) r_i p_4^2 \end{aligned} \tag{6.3}$$

with the nth order force constants $f^{(n)}_{k1k2\ldots k3} = \left(\frac{\partial^n V}{\partial Q_{k1} \partial Q_{k2} \ldots \partial Q_{kn}} \right)_0$, the internal coordinates Q_i and momenta p_i, and G_{ij} the Wilson G matrix elements [58–60] (see also section 2.1). In the H_4

Hamiltonian off-diagonal fourth- and higher-order potential energy coupling terms were neglected to reduce calculational complexity. Morover, the first order Taylor expansion terms of the Wilson G matrix around the equilibrium geometry position were included, leading to anharmonic third-order kinetic-potential energy coupling cross terms (the last two terms in (6.3)) [288]. The classical formulas (6.2) and (6.3) are translated into the quantum mechanical analogs through the bosonic creation ($a^\dagger$) and annihilation (a) operators (equation 5.8) [70]. This yields for the H_{123} Hamiltonian the same results as in equation (5.10) (except that the indices i,j run up to number 3), while we obtain for H_4:

$$\begin{aligned} H_4 = {} & \frac{\hbar\omega_i}{2}(a_4 + a_4^\dagger)^2 - \frac{1}{2}\sum_i^3 \gamma'_{i4}(a_i^\dagger - a_i)(a_4^\dagger - a_4) + V_0 + g_4(a_4 + a_4^\dagger) + \frac{1}{2}\sum_i^3 \varphi_{i4}(a_i + a_i^\dagger)(a_4 + a_4^\dagger) \\ & + \frac{1}{3!}\sum_i^3 g_{i44}(a_i^\dagger + a_i)(a_4^\dagger + a_4)^2 + \frac{1}{4!}g_{4444}(a_4^\dagger + a_4)^4 + \frac{1}{5!}g_{44444}(a_4^\dagger + a_4)^5 + \frac{1}{6!}g_{444444}(a_4^\dagger + a_4)^6 \\ & - \frac{1}{3!}\sum_i^3 \gamma'_{i44}(a_i^\dagger - a_i)(a_4^\dagger - a_4)(a_4 + a_4^\dagger) - \frac{1}{3!}\sum_i^3 \gamma''_{i44}(a_i^\dagger + a_i)(a_4^\dagger - a_4)^2 \end{aligned} \tag{6.4}$$

with $g^{(n)}_{k1k2...kn}$ the dimensionless nth-order force constants and the parameters γ'_{ij}, φ_{ij}, γ'_{i44}, and γ''_{i44} defined as:

$$g^{(n)}_{k1k2...kn} = \sqrt{\frac{\hbar^n}{2^n m_{k1}\omega_{k1} m_{k2}\omega_{k2}...m_{kn}\omega_{kn}}} f^{(n)}_{k1k2...kn} \quad , \tag{6.5}$$

$$\gamma'_{ij} = \frac{G_{ij}\hbar}{4}\sqrt{m_i\omega_i m_j\omega_j} \quad , \quad \varphi_{ij} = f_{ij}\sqrt{\frac{\hbar^2}{4m_i\omega_i m_j\omega_j}} \quad , \tag{6.6}$$

$$\gamma'_{i44} = \frac{\hbar^3\omega_i m_i}{2^3}\left(\frac{\partial G_{i4}}{\partial r_4}\right) \quad , \quad \gamma''_{i44} = \frac{\hbar^3\omega_4^2 m_4^2}{\omega_i m_i}\left(\frac{\partial G_{44}}{\partial r_i}\right) \quad . \tag{6.7}$$

Calculation of the optimized minimum energy A·T pair geometry allows one to derive the nth-order force constants and Wilson G-matrix elements. The expansion coefficients are dominated by the diagonal contributions (the interested reader is referred to Table S3 of the supplementary information of ref [193]). Identical to the case of adenosine monomer (chapter 5.4), the bilinear mode couplings $J_{ij} = \gamma'_{ij} - \varphi_{ij}$ between the NH stretching modes can be separated in a kinetic (γ'_{ij}) and potential energy (φ_{ij}) contribution with the kinetic terms dominating. Similarly, the different coupling contributions between the NH_2 bending and NH stretching coordinates are either of kinetic or potential energy origin, where again the kinetic contributions can be shown to dominate. Writing out the Hamiltonian in matrix form in a basis of harmonic oscillator product wavefunctions and matrix diagonalization gives the vibrational eigenstates and their corresponding eigenenergies and, hence, the diagonal and off-diagonal anharmonicities. These values are given in table 6.2, scaled by the same empirical factor (0.9183) used for the adenosine monomer calculations (section 5.4). The calculations show the $\upsilon = 1$ NH stretching state of A at lower frequency to be dominated by the hydrogen-bonded NH stretching eigenstate of A by 86 %, while the NH stretching state of A at higher frequency is dominated by the free NH stretching state of A by 87 %, hence justifying the local mode description of the one-exciton manifold of A·T dimers.

The linear IR cross sections of the fundamental 0-1 NH stretching transitions and 0-2 overtone NH_2 bending transition are calculated by expanding the nuclear dipole moment in the internal coordinates Q_i up to first order as before (equation (5.14)). The transition frequencies with their relative oscillator strength are shown on the bottom in Figure 6.4 (a) for the different A·T dimer configurations. They exhibit only weak variation with the binding geometries within a few wavenumbers,

	WC	**rWC**	**H**	**rH**	**Exp.**
υ_1	3064	3066	3069	3069	2800-3000
υ_2	3319	3324	3340	3344	3320
υ_3	3477	3478	3478	3479	3484
υ_4	1608	1608	1601	1602	1646
D_{11}	211	212	210	206	
D_{22}	72	75	82	82	
D_{33}	77	75	67	67	95±6
D_{44}	31	30	25	25	
D_{12}	6	5	4	3	
D_{13}	1	1	1	1	
D_{23}	48	50	60	65	42±6
D_{14^2}	3	2	1	1	
D_{24^2}	48	47	32	30	60±10
D_{34^2}	60	61	66	67	50±10
Δ_1	211	211	209	204	
Δ_2	130	132	126	125	
Δ_3	107	107	104	108	
Δ_4	6	8	3	4	

Table 6.2: *Left: Calculated fundamental frequencies of the mode 1 ($\upsilon_T(NH)$, mode 2 ($\upsilon_A(NH_2)_b$, mode 3 ($\upsilon_A(NH_2)_f$, mode 4 ($\delta_A(NH_2)$, and the corresponding diagonal (D_{ii}), off-diagonal (D_{ij}), and local mode anharmonicities Δ_i in cm^{-1} for the 9-mA·1-mT dimers in the WC/rWC/H/rH configuration using the Hamiltonian (6.1). The index 4^2 represents the double-excited NH_2 bending state. All values are scaled with a factor of 0.9183. Experimentally derived values from the 2D-IR spectra (reflecting the averaged values over the different dimer geometries) are shown for comparison in the right column.*

except for the hydrogen-bonded NH stretching mode of A that is predicted to have a frequency 25 cm^{-1} higher for the Hoogsteen structure compared to the WC structure. However, this difference is still within the bandwidth of the highly inhomogenously broadened transitions and could not be resolved in the experiment. In agreement with the experiment, these calculations show a similar mode pattern and, hence, intermode couplings for the various dimer geometries.

For all A·T geometries, the $\upsilon_T(NH)$ mode is found to have a dominating integrated oscillator strength and the lowest energy, which indicates the NH··N bond as the strongest hydrogen bond, followed by the $\upsilon_A(NH_2)_b$ mode, and finally by the $\upsilon_A(NH_2)_f$ mode at highest energy.[f] The double-excited NH_2 bending state is found in between the $\upsilon_T(NH)$ mode and the $\upsilon_A(NH_2)_b$ mode. It should be noted that the absolute frequency position of especially the thymine NH stretching state strongly depends on the chosen calculational approach, and, hence, has been the subject of heavy debates in the literature. We performed a normal mode analysis with different exchange-correlation functionals that yielded typically substantially lower $\upsilon_T(NH)$ 0-1 transition frequencies around 2600 cm^{-1} [269] (see supplementary information to Ref. [193]). Therefore, we found the HF approach to give the best agreement with the experimental results.

[f] Note that in the case of double-helical A·T oligomers the presence of the sugar-phosphate backbone with charged counterions and chemically bound water molecules leads to distinctly different results: X-ray and neutron diffraction measurements on AT nucleic acids fibers and single crystal oligonucleotides yielded the NH··N bond as the strongest hydrogen bond only in the case of the WC dimers, while for the Hoogsteen dimers the NH··O bond was found to be the strongest [2].

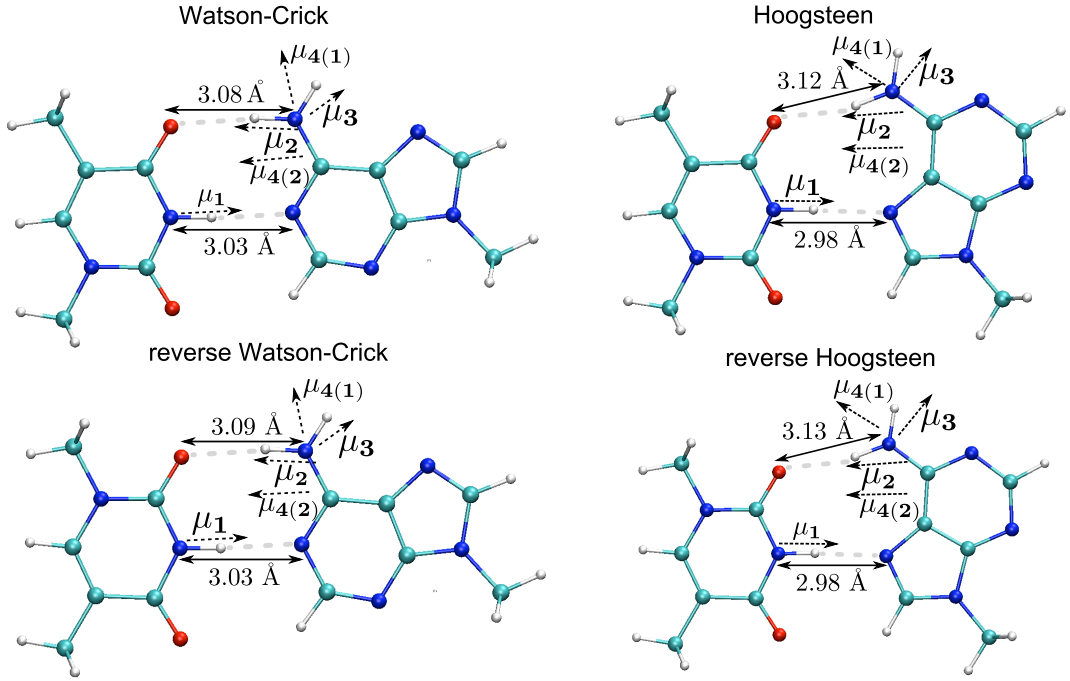

Figure 6.11: *Calculated minimum energy structures of the different WC/rWC/H/rH A·T dimer geometries. The heavy atom distances as well as the dipole orientations of the fundamental 0-1 NH stretching transitions ($\mu_{1,2,3}$) and of the fundamental 0-1 (μ_4) and overtone 0-2 (μ_4^2) NH_2 bending transitions are drawn. The Fermi resonance between the $\upsilon = 2$ NH_2 bending overtone and the $\upsilon = 1$ $\upsilon_A(NH_2)_b$ state leads to a parallel orientation of μ_2 and μ_4^2.*

The calculations seem to underestimate the NH_2 bending overtone oscillator strength, which is probably connected to the truncation of the dipole moment Taylor expansion after the linear order or the underestimation of mixing with other modes. In an excitonic picture, the degree of mixing between two states depends on the energy difference of the decoupled eigenstates and their bilinear intermode coupling. The small diagonal anharmonicity of the NH_2 bending state of $\approx$ 25-31 cm^{-1}, yielding the $\upsilon = 2$ NH_2 bending state around 3185 cm^{-1}, suggests a significant mixing of the NH_2 bending overtone state with the $\upsilon = 1$ $\upsilon_A(NH_2)_b$ state. Apart from the NH_2 bending overtone a multitude of Fermi resonance enhanced fingerprint over- and combination tone states in combination with anharmonically coupled hydrogen bond modes are expected to contribute to the lineshape of A·T dimers in the 2600-3200 cm^{-1} range [289], which calls for further involved theoretic calculations to yield quantitative agreement with the observed lineshape.

Enhanced hydrogen bonding interactions are known to lead to an increase in local mode anharmonicity [290]. Such a behavior is reflected in the calculated local anharmonicities Δ_i in table 6.2, which show only minor variations with dimer geometry. The diagonal and off-diagonal anharmonicities delivered by the 2D-IR spectra are similar to the calculated values, although not all values could be experimentally determined due to substantial signal overlap of the various Feynman excitation pathways.

The calculated equilibrium A·T WC/rWC/H/rH structures and the transition dipole orientations of the three fundamental NH stretching states and the 0-1 fundamental and 0-2 overtone NH_2 bending states are shown in Figure 6.11. The significant differences in energy of the single-excited NH stretching states in mode 1-3 lead to an effective decoupling of all NH stretching oscillators, making the single-excitation NH stretching manifold well-described in a local mode picture. Therefore, only little wavefunction mixing takes place, which makes the NH stretching fundamental

transition dipoles $\mu_{1,2,3}$ largely oriented along their corresponding bond vectors. The Fermi resonance mixing between the NH_2 bending overtone eigenfunction and the single-excited $\upsilon_A(NH_2)_b$ eigenfunction leads to a transfer of oscillator strength to the harmonically forbidden bending overtone transition, which results in an almost parallel orientation of the transition dipole of the 0-2 bending excitation with the μ_2 transition dipole. The calculations predict a N-H-N bond angle in the amino group of A of $\approx 135°$, while the bending overtone and μ_2 transition dipole enclose a negligible 4° angle. Both values are similar to the experimentally derived values (table 6.1).

6.6 Conclusions

We have studied the effect of interbase hydrogen bonding in adenosine-thymidine base pairs in chloroform solution through the analysis of the single- and double-excited NH stretching manifold with linear IR, NMR, ultrafast nonlinear IR spectroscopy, and ab initio calculations. The studied solution contained a similar amount of A·T base pairs in Watson-Crick, reverse Watson-Crick, Hoogsteen, and reverse Hoogsteen configuration, as evidenced by differences in the corresponding formation enthalpy smaller than kT as given by ab initio calculations and low-temperature linear ^1H NMR measurements. Concentration- and temperature-dependent IR spectra allowed us to identify six major bands at 3484, 3324, 3262, 3211, 3188, and 2400-3000 cm^{-1} associated with A·T dimers.

Two-color pump-probe data and the evaluation of cross-peak-patterns in 2D-IR spectra as well as quantum chemical calculations revealed anharmonic couplings between *all* NH stretching oscillators. Apart from dominatingly mechanical coupling between the NH stretching excitations in the adenosine amino group, there exists notable interbase dipole-dipole couplings between the thymidine and adenosine NH stretching modes. 2D-IR spectra and ab initio calculations revealed similar structural and spectroscopic properties for the different A·T dimer geometries: hydrogen stretching frequencies, IR cross sections, vibrational couplings, and, hence, diagonal and off-diagonal anharmonicities exhibited only minor differences. All NH stretching bands were found to be highly inhomogeneously broadened, which indicates a heterogeneous distribution of hydrogen bond lengths in the A·T base pairs. Spectral diffusion is absent on the picosecond time scale, which indicates rather rigid A·T dimer geometries.

A significant reduction of T_1 lifetime through hydrogen bonding from 2.1 ps for the free NH stretching mode to 0.2 - 0.4 ps for the $\upsilon_A(NH_2)_b$ and $\upsilon_T(NH)$ modes was observed. Hydrogen bonding was found to induce anharmonic couplings of the hydrogen bonded NH stretching modes to a low-frequency hydrogen bond mode at ≈ 100 cm^{-1}, as observed through an underdamped beating in the pump-probe transients. The resulting formation of vibrational sidebands significantly contributes to line broadening in the 2400 - 3000 cm^{-1} region. The enhanced mixing with fingerprint overtone and combination tone modes (Fermi resonances), in particular involving the NH_2 bending mode, were determined to allow for a qualitative understanding of the complex NH stretching line shape in A·T dimers. Although the NH stretching modes in the adenosine amino group are largely effectively decoupled from each other due to the effect of hydrogen bonding, couplings with fingerprint overtone and low-frequency vibrations make the local mode picture of only limited validity for the description of the NH stretching manifold in A·T base pairs. The 2D spectra reveal an ultrafast vibrational excitation transfer from the 3330 cm^{-1} to the 3200 cm^{-1} mode.

Ab initio HF/6-311++G** calculations predicted the $\upsilon_T(NH)$ mode to have the lowest frequency, followed by the NH_2 bending overtone, the $\upsilon_A(NH_2)_b$ mode, and finally the $\upsilon_A(NH_2)_f$ mode at highest energy. Transition dipoles of the fundamental NH stretching transitions were found to be largely oriented along the corresponding bond vectors, while the predicted relative transition dipole angles agree with those obtained from polarization-dependent 2D-IR spectra within the error margins. The work calls for comprehensive normal mode theoretical calculations incorpo-

rating Fermi resonance couplings with a multitude of fingerprint modes to provide a quantitative agreement with the congested A·T dimer spectrum.

Compared to the monomeric species, the formation of two interbase hydrogen bonds of different strength in A·T pairs distributes the NH stretching frequencies towards lower values and induces an effective decoupling of the amino NH stretching modes, anharmonic couplings with low-frequency hydrogen-bond modes, and enhanced mixing with fingerprint over- and combination tone modes. Thereby, vibrational relaxation becomes accelerated to sub-picosecond values.

7 Vibrational line shapes and ultrafast dynamics in hydrated double-helical guanine-cytosine DNA oligomers

In the last chapter, we studied the microscopic origin and vibrational dynamics of the congested NH stretching manifold in A·T dimers in chloroform solution by incorporating enhanced mixing and coupling to fingerprint and low-frequency degrees of freedom as induced by the formation of interbase hydrogen bonds. In this chapter, we approach the question of how hydration, the backbone, and potential vertical interbase stacking interactions affect vibrational line shapes and dynamics of NH stretching excitations of the nucleobase pairs, which has been unaddressed so far.

We investigate the nucleobase NH stretching modes of guanine-cytosine base pairs in Watson-Crick geometry in artificial, short-stranded, double-helical DNA oligonucleotide films through linear and ultrafast nonlinear 2D-IR spectroscopy. These measurements are performed at a high and a low degree of hydration with the asymmetric phosphate stretching frequency being used as a sensitive internal molecular probe for the water content. Despite the spectrally overlapping contributions from NH stretching base pair modes and OH stretching modes from solvating water molecules, measurements at different degrees of hydration will enable a separation of base pair and water shell contributions. A comparison of our findings with previous measurements on anhydrous G·C base pairs in chloroform solution [49,236] allows us to evaluate the extent of changes in intra- and interbase vibrational couplings due to the double-helix structure and the effect of hydrating water molecules on vibrational line shapes of NH stretching excitations. Moreover, the role of interbase stacking interactions can be estimated. The response of OH stretching oscillators in first and second hydration shell positions will provide insight into structural dynamics of the water shell and the role of interfacial "biological" water during vibrational relaxation and will be compared to the behavior of bulk water.

7.1 Preparation of thin-film G·C oligomer samples

We investigate artificial double-helical oligonucleotides containing a sequence of 23 guanine-cytosine base pairs (corresponding to about two full helical turns) in Watson-Crick geometry (see Figure 7.1 (a,b)), which were synthesized by Thermo Scientific. For minimized contributions of scattered pump light into the nonlinear signal direction, we synthesized thin film samples (thickness ≈ 20 μm) on Si_3N_4 substrates (thickness 500 nm) of high optical quality (good homogeneity and surface flatness) over the beam diameter of the focused excitation pulses. We replaced the sodium counter cations of the helix backbone with amphiphilic long-chained cethyltrimethylammonium (CTMA) molecules (see Figure 7.1 (c)) as this has been shown to enhance optical sample quality, probably due to reduced DNA aggregation.

The sample preparation procedure is similar as described in ref [291,292]. After complexation with the CTMA surfactants, the complexes were insoluble in water and could hence be separated from the uncomplexed DNA molecules through centrifugation. For intermediate drying, the DNA/CTMA complexes were dissolved in 2-butanol and the mixture was allowed to rest until the 2-butanol solvent was fully evaporated. The dried DNA-surfactant complexes were again dissolved

in 2-methyl-1-propanol and this solution was cast on the Si_3N_4 substrates. After solvent evaporation this lead to thin film samples with a DNA concentration of approximately 10 mM with a thickness around 20 μm. Their linear IR spectra did not show remains of the used solvents. The DNA-surfactant films were then placed in a sealed homebuilt cell [293], connecting the film to a reservoir filled with a properly chosen agent to create an atmosphere of well-defined humidity. The use of P_2O_5 drying powder/a supersaturated $NaBrO_3$ aqueous salt solution leads to a 0%/92% relative humidity (R.H.) atmosphere. After a sufficient equilibration period of several days this leads to a DNA sample with defined water content.

Hydration-dependent conformation changes

Thin film DNA-surfactant complexes with salmon testes and calf thymus DNA, containing about 45% G·C base pairs and prepared in the same fashion as our samples, have been studied by X-ray diffraction and circular dichroism. They showed reversible conformational changes from the B-form under full hydration conditions (relative humidity $> 90\%$) to the A-form in dry samples [292, 294]. Similarly, X-ray diffraction studies on double-helical fibers with sodium counterions containing exclusively G·C pairs, indicated the B-form conformation at a humidity above 90% with a transformation to the A-form at lower humidity [295]. Therefore, our 23 G·C oligonucleotides will show a conformation transition from A- to B-form upon a R.H. increase from 0% to 92%, while the Watson Crick base pairing structure remains. This is in contrast to A·T-rich DNA that has been shown to often retain its conformation over a wide range of humidity due to the extraordinarily stable spine of hydration in the minor groove (cf. section 4). The measurements presented in the following part focus on G·C oligomer films at 0% R.H. (corresponding to ≈ 4 water molecules per base pair) and 92% R.H. (corresponding to more than 20 water molecules per base pair).

7.2 The impact of hydration on linear vibrational spectra

Figure 7.1 (d) shows linear IR spectra of the G·C oligomers at different degrees of hydration. At 0% R.H. the base pair NH stretching modes are the dominant features in the region between 2500 and 3600 cm^{-1}. They are superimposed with strong, narrow CH stretching contributions at 2924, 2854, and 3026 cm^{-1} and the OH stretching band from remaining water molecules. The latter contribution dominates at high 92% R.H.. When drying the sample in vacuum for three days at a pressure of 50 mbar (black solid line), most of the residual water is removed. The difference spectra between the 92% R.H. and vacuum dried samples to the 0% R.H. sample in Figure 7.1 (e) show the broad water OH stretching contribution between 3000 and 3700 cm^{-1} to peak at 3400 cm^{-1} with similar spectral profiles for both humidity ranges. Their line shape shows only small deviations from the case of bulk water, which indicates a similar distribution of hydrogen bonding geometries at the DNA-water interface as was likewise found by Falk [296]. Apart from the significant increase in OH stretching absorption upon hydration, the difference spectra indicate significant changes in the region of the asymmetric phosphate stretching band $\upsilon_{AS}(PO_2)^-$ (around 1240 cm^{-1}) of the phosphate unit at the backbone and less so around the carbonyl C=O stretching modes (1650 - 1700 cm^{-1}).

The asymmetric phosphate stretching band $\upsilon_{AS}(PO_2)^-$ reflects local DNA-water interactions at the DNA backbone in a time-integrated way and has been shown to undergo a characteristic red-shift upon an increase in hydration.[a] The asymmetric phosphate stretching vibration has served as an excellent local probe to investigate the ultrafast energy transfer between DNA and water and the resulting changes of hydrogen bonded structure [56]. The hydration-dependent red-shift

[a] In contrast, the symmetric phosphate stretching vibration $\upsilon_S(PO_2^-)$ has been shown to display only changes of its spectral envelope.

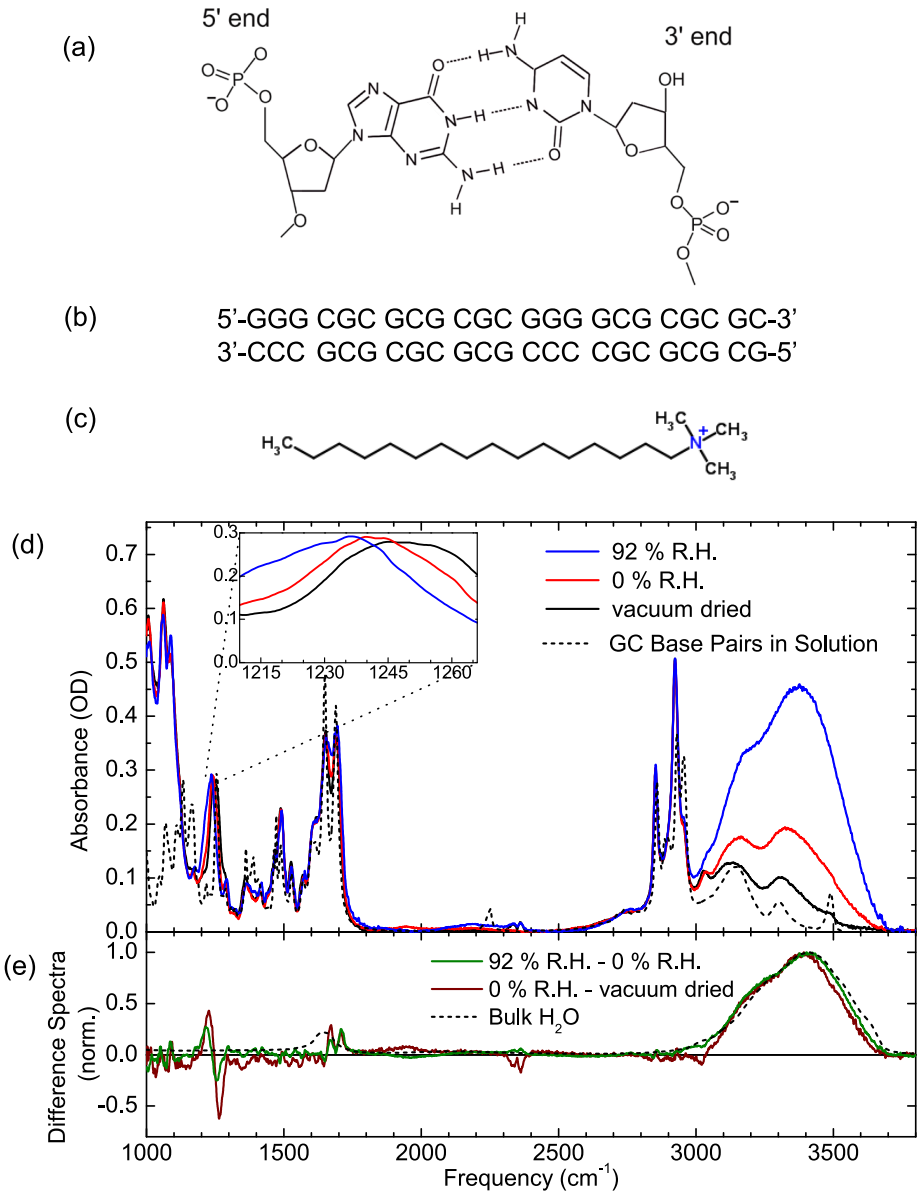

Figure 7.1: *(a) Repetitive molecular motif in G·C 23-oligonucleotides, with the base pair sequence given in (b). (c) Molecular structure of the cethyltrimethylammonium (CTMA) amphipilic surfactants replacing the sodium counterions. (d) FT-IR spectra of G·C oligomers at 92% and 0% relative humidity, and after vacuum drying for a few days. The degree of hydration is reflected in the center frequency of the asymmetric phosphate stretching mode (see inset in (d)) and the intensity of the OH stretching water band. The dashed black line shows the spectra of G·C base pairs in water-free chloroform solution (taken from ref [49], concentration 50 mM). (e) Difference spectra for different degrees of R.H. in comparison to that of bulk water.*

has been determined to be identical for sodium and CTMA couterions [56]. Hence, we can use gravimetric water content calibration measurements by Falk [206], who measured the DNA weight in dependency of humidity on Na-DNA (calf-thymus) and in this way extracted the number of water molecules per nucleotide pair in dependency of humidity. For 0% R.H. the $\upsilon_{AS}(PO_2)^-$ mode peaks at 1242 cm^{-1} exhibiting a red-shift of ≈ 6 cm^{-1} compared to the vacuum dried sample, while

for 92% R.H. the band maximum appears at 1236 cm^{-1} (see the inset of Figure 7.1 (d)). Assuming perfectly dry samples after vacuum drying and using the former $\upsilon_{AS}(PO_2)^-$ shift and the red-shift data from ref [56], we estimate a residual water concentration of roughly four water molecules per base pair in our G·C DNA-CTMA complexes at 0% R.H.. For 92% R.H., the gravimetric studies in ref [206] indicate more than 20 water molecules per base pair, corresponding to fully hydrated DNA with a completely filled first hydration shell (the first shell was predicted to contain up to 17 water molecules per base pair [215]). For such high water content, while most water molecules will be located in first shell positions with strong association to the DNA-CTMA complex through hydrogen bonding, few second shell water molecules will be loosely attached to the DNA interface at larger distances through long-range Coulomb interactions and hydrogen bonding to first shell water molecules. We performed systematic linear IR studies to show that the hydration level in the DNA films can be changed in a fully reversible way between the vacuum dried state, the 0% R.H. state, and the 92% R.H. state.

It is very insightful to compare the linear IR spectra of G·C oligomers at different humidity to that of G·C base pairs in completely waterfree chloroform solution [49] (50 mM) (see dashed black line in Figure 7.1 (d)). G·C pairs in solution - in contrast to A·T base pairs - predominantly form the Watson-Crick structure due to its vastly dominating stability [49, 236]. In the region of NH stretching bands between 2500 and 3550 cm^{-1}, NH stretching band maxima in isolated G·C base pairs appear at similar spectral position in 0% R.H. and, most pronounced, in vacuum dried G·C oligomers. However, it is important to note that the free NH stretching mode around 3490 cm^{-1} is much less pronounced in the case of the G·C oligomer film compared to the situation in G·C base pairs. Moreover, the NH stretching line widths appear broadened, the mechanism of which will be studied with 2D-IR spectroscopy in the next section.

7.3 Ultrafast 2D-IR spectroscopy of NH/OH stretching modes at low hydration level

Heterodyne-detected three-pulse photon echo experiments were used to collect absorptive 2D-IR spectra of the double-helical G·C oligomers with two different excitation pulse center frequencies υ_C of 3260 and 3400 cm^{-1} (bandwidth around 300 cm^{-1}). While for the former case the nonlinear signals from excitation pathways involving the fundamental 0-1 and partly excited state 1-2 transitions in NH and OH stretching modes are addressed, excitation at υ_C = 3400 cm^{-1} allows measurement of nonlinear signatures up to 3600 cm^{-1}, which for high relative humidity conditions particularly highlights the contributions from the OH stretching modes of the water shell. For all measurements the coherence time τ_1 was scanned in steps of 4 fs from -400 to 700 fs until the rephasing and nonrephasing signals decayed to the noise level.

In the previous section, we showed that for 0% R.H. conditions the G·C oligomers contain roughly 4 water molecules per base pair. Their OH stretching oscillator signals spectrally overlap with the base pair NH stretching modes; however, the former contributions to the nonlinear signal are weaker. Because the heterodyne-detected third order signal scales with μ^4 and the linear absorption with $\mu^2 \propto \epsilon$ (with μ the transition dipole moment and ϵ the (linear) extinction coefficient), the ratio R between the third-order 2D signal of the high frequency NH stretching modes ($S^{(3)}_{NH}$) and OH stretching modes ($S^{(3)}_{OH}$) can be estimated as

$$R = \frac{S^{(3)}_{NH,high}}{S^{(3)}_{OH}} = \frac{\mu^4_{NH}}{\mu^4_{OH}} \frac{c(NH,high)}{c(H_2O)} = \left(\frac{\epsilon(NH)}{\epsilon(OH)}\right)^2 \frac{c(NH,high)}{c(H_2O)} \tag{7.1}$$

with $\mu_{NH/OH}$ the transition dipole moments of NH/OH stretching modes and $\epsilon_{NH/OH}$ their respective exctinction coefficients. The extinction coefficient of hydrogen-bonded NH stretching oscillators

in G·C base pairs [49] ($\approx$ 250 l cm^{-1}mol^{-1}) has been shown to exceed that of OH stretching oscillators in water ($\approx$ 100 l cm^{-1}mol^{-1}) by a factor of 2.5. With 4 water molecules per base pair and assuming roughly 3 NH stretching oscillators to absorb below the OH stretching water band, the relative concentration of NH stretching oscillators at higher frequency and water molecules can be estimated as C = $c(NH, high)/c(H_2O) = \frac{3}{4}$. This gives a ratio of R = $2.5^2 \cdot$ 0.75 $\approx$ 4.5, showing that the 2D spectra recorded at 0% R.H. are indeed dominated by the NH stretching mode contributions.

Figure 7.2 shows 2D spectra of 0% R.H. G·C oligomers for different waiting times τ_2 up to one ps, with the top left panel of Figure 7.2 numbering the various peaks. For excitation at υ_C = 3260 cm^{-1} (upper part of Figure 7.2) the 2D spectra show prominent positive peaks (yellow-red contours) of similar intensity at the frequency diagonal $\upsilon_1 = \upsilon_3$ = 3170 cm^{-1} (peak 1) and 3320 cm^{-1} (peak 2), coinciding with the peaks in the linear spectra. They reflect excitation pathways involving the 0-1 transitions of different NH stretching modes and exhibit a high degree of inhomogeneous broadening as will be discussed in section 7.5. The off-diagonal cross peaks with positive sign (blue contours) at (υ_1 [cm^-1], υ_3 [cm^-1]) = (3320, 3170) (peak 3) and (3170, 3320) (peak 4) reflect anharmonic couplings between the NH stretching states. This part of the cross peak patterns is similar to the one exhibited by isolated G·C base pairs in solution [49], the repercussions of which will be discussed on page 108.

At low detection frequencies one observes an extended negative signal with a maximum at (3320,3040) (peak 5), which results from various excitations into the double-excited NH stretching state manifold. Due to the highly broadened bands and, hence, significant overlap between different signal contributions, this band can not be clearly assigned to a certain overtone or combination tone transition. There are only minor changes in line shapes of the 2D spectral structure upon changes in waiting time, which indicates the absence of spectral diffusion on the picosecond time scale (see section 7.5). For long waiting times of T = 750 and 1000 fs, an additional weak negative signal (peak 6) grows in at a blue-shifted detection frequency compared to the fundamental 3320 cm^{-1} transition. It indicates the formation of a vibrationally heated ground state as will be discussed in section 7.5.

Impact of a low water content on population dynamics and 2D-IR spectral signatures

In order to analyze population dynamics, we plot the intensities of the 2D peaks as a function of waiting time in Figure 7.3. Using a monoexponential fit with floating offset (solid lines), the diagonal peaks 1 and 2 show a fast initial decay with a time constant of 250 fs and 210 fs, respectively, while the positive cross peaks 3 and 4 decay with 500 fs and 200 fs, respectively. The peaks 1-4 show a long-lived residual bleaching signal extending beyond the picosecond time scale, which points to complicated vibrational cooling dynamics with branching into different decay channels leading to a delayed ground state refill (see section 7.5).

The cross peaks 3 and 4 show a distinctly different time evolution in comparison to their corresponding diagonal peaks 1 and 2. While the intensities of peaks 1 and 4 decay on a very similar time scale, peak 3 decays notable slower than peak 2, as shown in Figure 7.3 (c). Such an observation indicates a population transfer down in energy from the NH stretching oscillator at 3300 cm^{-1} to the one at 3170 cm^{-1}, while an energetically uphill transfer (despite being in the range of kT) is not clearly observed. Similar findings were made for guanosine-cytidine base pairs in solution [49]. Such measurements realized a continuous increase in the intensity ratio of cross peak 3 to diagonal peak 2 up to the highest waiting time of 1 ps. In contrast, the G·C oligomer measurements only show for this ratio a fast increase within the first 300 fs with only modest changes for higher waiting times. The initial rise may be largely influenced by spectral overlap of peak 3 with decaying excited state enhanced absorption signals and therefore cannot be used as an

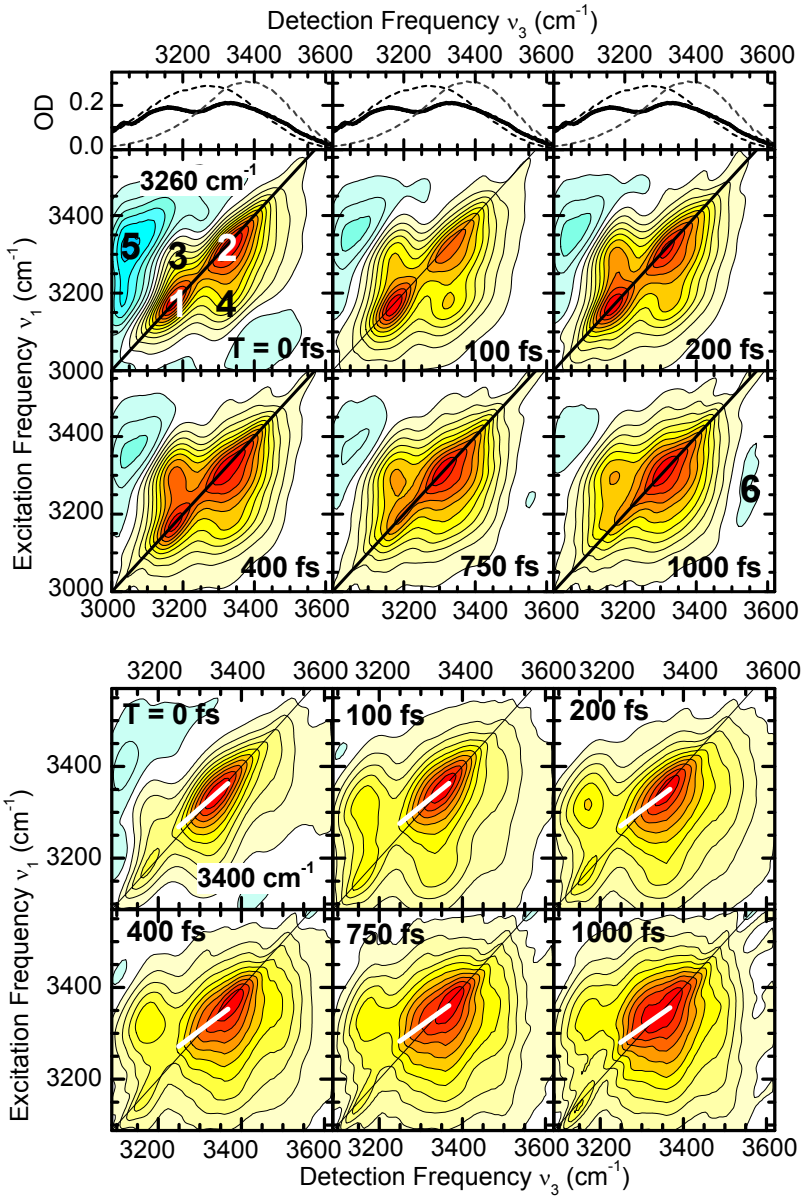

Figure 7.2: *A set of absorptive 2D-IR spectra of 0% R.H. G·C oligomers for different waiting times τ_2 between 0 and 1000 fs. The excitation and LO pulses are centered at 3260 cm^{-1} in the upper part, and at 3400 cm^{-1} in the lower part. The linear IR spectrum is given in the top panels, with the excitation pulse spectra indicated by dashed lines. The dynamics of the intensity of peaks numbered in the top left panel is plotted in Figure 7.3. The white lines in the lower panels provide a linear fit to the center lines (connecting intensity maxima of cuts along the detection frequency axis).*

independent signature of ultrafast energy transfer for the G·C oligomer data.

The negative excited state feature marked as peak 5 decays with a time constant of 200 fs to zero (measured at its maximum position). Since the peak results from contributions of different overtone states, this time constant gives the averaged T_1 lifetimes of the different single-excited NH stretching states. The value agrees quite well with the fast decay constants found for the two diagonal peaks. Such values are similar to the lifetimes found for hydrogen-bonded NH stretching

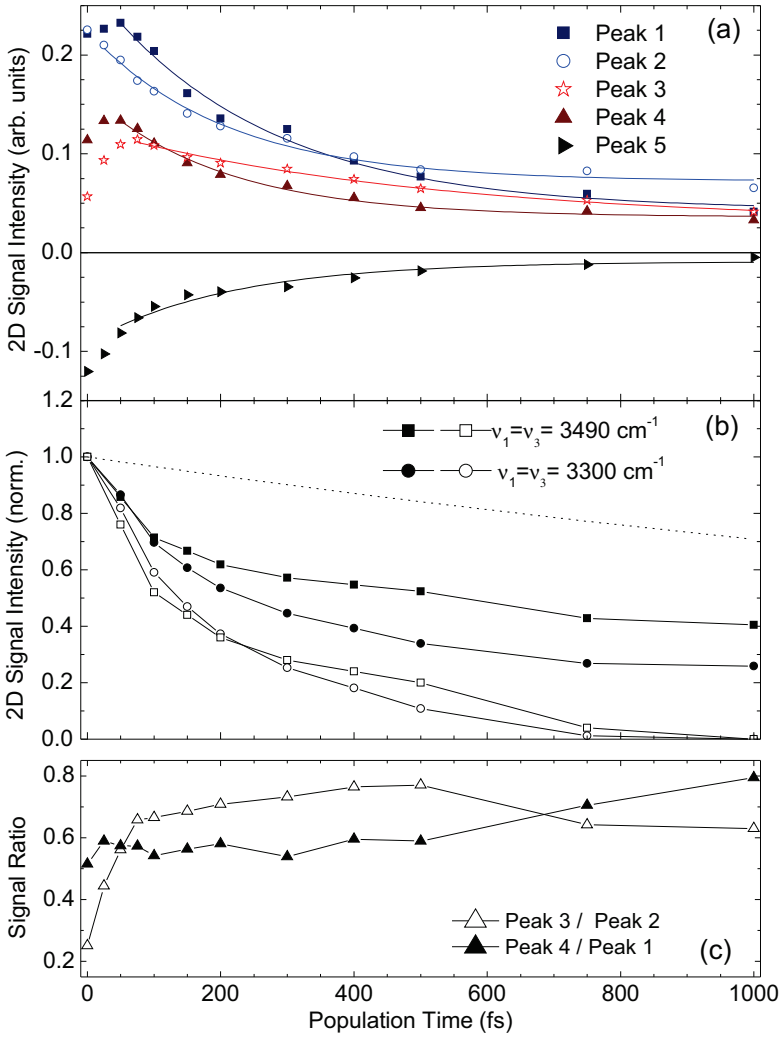

Figure 7.3: *The intensity of the peaks labeled in Figure 7.2 is plotted as a function of waiting time τ_2. (a) The initial decay dynamics are approximated by a monoexponential decay with floating offset, providing T_1 lifetimes between 200 and 500 fs. (b) Comparison of kinetics along the diagonal at $\upsilon_1 = \upsilon_3 = 3300$ and 3490 cm^{-1} before (filled symbols) and after (open symbols) subtraction of the intensity at $T = 1000$ fs (from the 2D spectra of Figure 7.2 with $\upsilon_C = 3400$ cm^{-1}). The dashed line shows the 3 ps decay found for the free NH stretching modes in G·C base pairs for comparison. (c) Cross-to-diagonal peak ratio for the specified peaks.*

oscillators of G·C and A·T base bairs in solution [49,193]. Ultrafast IR-pump/anti-Stokes Raman probe spectroscopy on A·T oligomers showed the decay of NH stretching excitations to proceed via those over- and combination tones that show the smallest energy mismatch to NH stretching states, especially involving NH_2 bending and C=O carbonyl modes, which showed a delayed rise with a rise time close to the NH stretching T_1 decay times [234]. Similar relaxation pathways were found through IR pump-probe experiments for 7-azaindole dimers containing intermolecular hydrogen-bonded NH stretching modes [252,289]. The NH stretch excitations in G·C oligomers are expected to relax in a similar fashion via over- and combination tones of NH/NH_2 bending mode including other fingerprint vibrations.

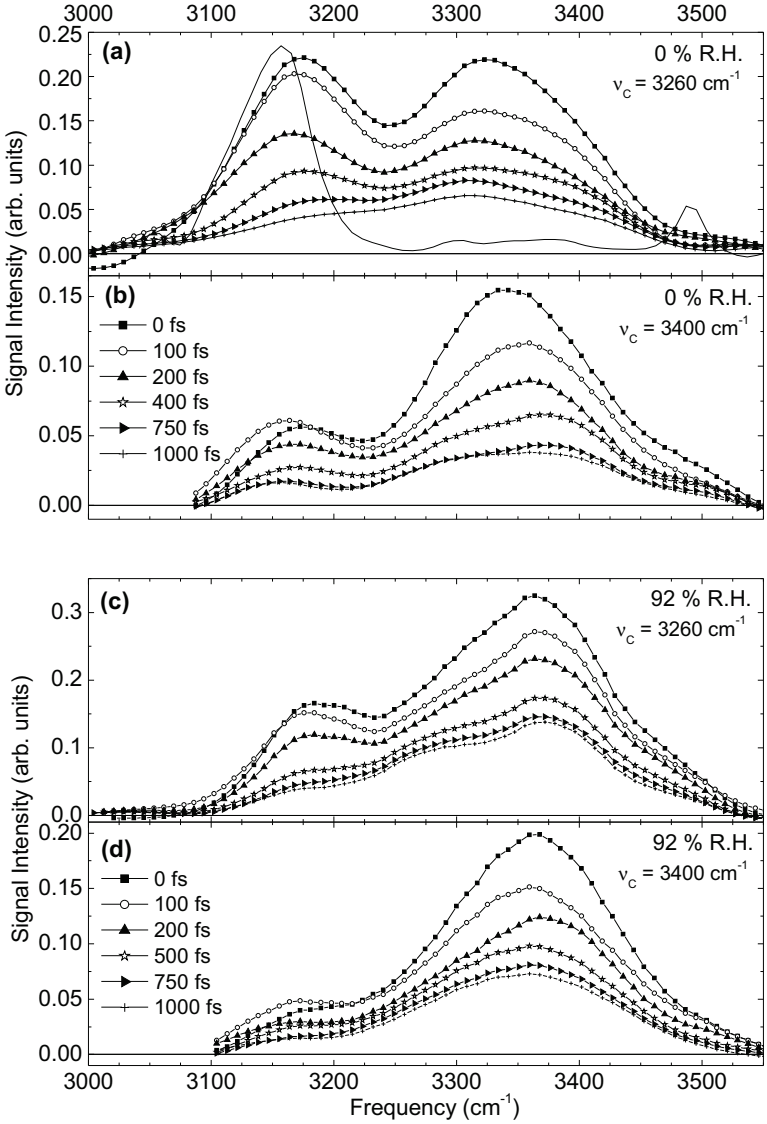

Figure 7.4: *Slices of the G·C oligomers 2D spectra of (a,b) 0% R.H. (from Figure 7.2) and of (c,d) 92% R.H. (from Figure 7.7) along the frequency diagonal $\upsilon_1 = \upsilon_3$ as a function of waiting time. The excitation pulses are centered at 3260 cm^{-1} for (a,c) and at 3400 cm^{-1} for (b,d). The solid line in (a) shows the diagonal cross section of measurements on guanosine-cytidine base pairs in choroform for a waiting time τ_2 = 400 fs, recorded under similar experimental conditions.*

The 2D response of the G·C oligomer sample at 0% R.H. for excitation at 3400 cm^{-1} is shown in the lower part of Figure 7.2. The overall 2D peak pattern remains similar to the 0% R.H. case, while the signal from the hydrogen-bonded NH stretching mode at higher detection frequency dominates the spectra due to its predominant excitation. It is important to note that there are neither distinct cross peaks involving the frequency position $\upsilon_1 = \upsilon_3 = 3490$ cm^{-1}, where the free NH stretching modes of the base pairs would occur, nor are there diagonal peaks involving the free NH stretching mode. The latter becomes clear when plotting 2D spectral cuts along the frequency diagonal: both for excitation at $\upsilon_C = 3260$ cm^{-1} (Figure 7.4 (a)) and 3400 cm^{-1} (Figure 7.4 (b)) these diagonal slices show at most a small shoulder at the position of the free NH stretching mode. Slight differences in the T_1 decay of the NH stretching modes around 3300 cm^{-1} and the OH stretching modes peaking at 3400 cm^{-1} lead to a minor reshaping of the diagonal slices in Figure

7.4 (b). Moreover, it is instructive to compare the decay of the diagonal 2D signal at the frequency position at $\upsilon_1 = \upsilon_2 = 3300$ cm^{-1} (filled round symbols) to the decay at 3490 cm^{-1} (filled square symbols) of potential free NH stretching oscillators as shown in Figure 7.3 (b). After subtraction of their respective offsets (open symbols) at T = 1000 fs, they show basically identical decay dynamics within error margin with a time constant around 200 fs. Preliminary IR pump-probe measurements support the observation of similar population decay dynamics at spectral positions 3300 and 3490 cm^{-1} (not shown). Such findings are in sharp contrast to measurements on G·C base pairs in chloroform solution, where both cross and diagonal peaks involving the free NH stretching mode position were clearly visible. Such discrepancies are illustrated by comparison with the diagonal slices through a 2D spectrum of isolated G·C base pairs (see the solid line in Figure 7.4 (a)). In addition, for G·C base pairs, the population kinetics of the intensity of the 3300 and 3490 cm^{-1} band were distinctly different, with the former peak showing a 210 fs decay and the latter peak a 2.9 ps decay component [49,236] (dashed line in Figure 7.3 (b)).

These findings can be explained with the absence of effective decoupling between the two NH stretching modes in the amino groups of the G·C oligomers. We attribute such a behavior to the influence of solvating water molecules that are partially distributed over the two amino groups in minor and major groove positions even for 0% R.H.. Indeed the polar base groups were found to represent important hydration sites in G·C oligonucleotides, even though the charged phosphate groups exhibit the highest hydration affinity (compare section 4.2). The interaction of the water oxygen atom with that amino proton not involved in interbase hydrogen bonding displaces its fundamental 0-1 NH stretching transition from 3490 cm^{-1} towards lower frequencies, while the arrangement of water molecules over a range of hydration sites and geometries leads to structural disorder. Such additional structural inhomogeneity explains the broadened line shapes of bands, especially the one around 3300 cm^{-1}, in the linear spectra and in the 2D spectral diagonal cuts of G·C oligomers as compared to the case of G·C base pairs in waterfree chloroform solution. We attribute the surprisingly fast $\approx$ 200 fs decay of the diagonal 3490 cm^{-1} signal both to the short T_1 lifetime of OH stretching mode excitations of hydrating water molecules, which exhibit a similar lifetime of around $\approx$ 200 fs for bulk water [104], and to contributions from weakly hydrogen-bonded NH stretching oscillators of the base pairs. The unresolved long-lived decay component may partly result from the slow decay of free NH stretching modes from nonhydrated amino groups.

The induced frequency red-shift upon hydration of the originally free NH stretching modes reduces the energetic separation to the NH stretching modes involved in interbase hydrogen bonding. Therefore, the effect of mode mixing between both NH stretching states in the amino groups due to the mechanical coupling J will become enhanced. The degree of mode mixing, leading to the formation of partly delocalized NH stretching states according to equation (2.10), is described by the mixing angle Θ (equation (2.11)). Realizing that the energy difference between the decoupled local NH stretching states will be around 100 - 200 cm^{-1} and 2J $\approx$ 110 cm^{-1} [49], one estimates a mixing angle Θ between 29° and 47° and, hence, $\upsilon = 1$ eigenstates with a character somewhere between local ($\Theta = 0°$) and normal modes ($\Theta = 90°$). Therefore, for those amino groups, which are hydrogen-bonded to water, the NH stretching excitations will be partly delocalized over both NH motifs.

This observation contrasts with the behavior of both G·C and A·T base pairs in chloroform, where the local mode picture was found to be in first approximation the appropriate description for the single-excited NH stretching states, even though a more detailed analysis showed Fermi resonances with fingerprint combination and overtones states to modify the NH stretching manifold [236] (see chapter 6). The results for the G·C base pairs in solution are summarized in Figure 7.5. The two free NH stretching modes $\upsilon_G(NH_2)_f$ and $\upsilon_C(NH_2)_f$ were both assigned to the narrow 3491 cm^{-1} band. From the three hydrogen bonded NH stretching oscillators, the hydrogen bonded $\upsilon_G(NH_2)_b$ mode was attributed to the 3303 cm^{-1} band; the $\upsilon_G(NH)$ and $\upsilon_C(NH_2)_b$ modes both to

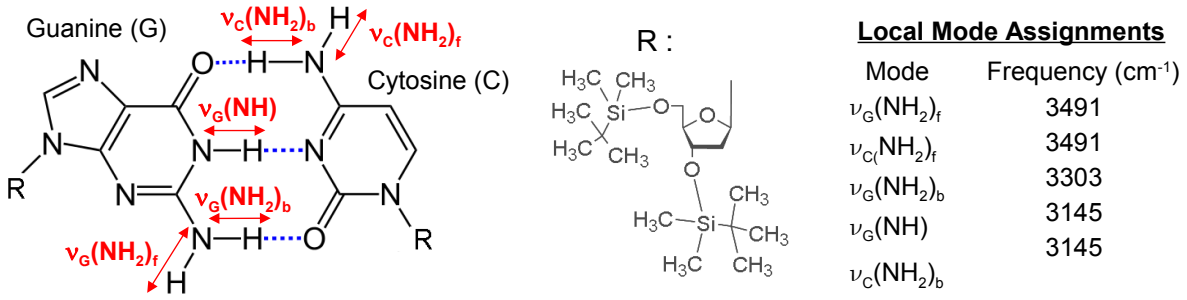

Figure 7.5: *Vibrational band assignment of local NH stretching modes in waterfree G·C base pairs in chloroform solution (from ref [49]).*

the 3145 cm^{-1} band [49]. From the occurrence of vibrational energy transfer on a 200 fs time scale from the $\upsilon_G(NH_2)_b$ to the $\upsilon_G(NH)$ mode, vibrational couplings between the hydrogen-bonded NH stretching oscillators in G of 5 cm^{-1} were estimated. Because the frequency splitting of the hydrogen-bonded NH stretching modes (about 200 cm^{-1} for the $\upsilon_G(NH_2)_b$ mode and 345 cm^{-1} for the $\upsilon_C(NH_2)_b$ mode relative to the free NH stretching modes $\upsilon_{G,C}(NH_2)_f$) was found to clearly exceed the mechanical coupling 2J $\approx$ 110 cm^{-1}, mode mixing between both NH stretching modes in the two amino groups turned out negligible, which proved the local mode picture to be appropriate for G·C base pairs in solution [49].

X-ray diffraction and calculations have predicted significantly different strengths of the individual interbase hydrogen bonding interactions for isolated G·C base pairs and G·C pairs embedded in a double-helix in the presence of water and counterions. Such studies have found the G(NH_2)··C(CO) hydrogen bond to be the strongest, followed by the G(CO)··C(NH_2), and finally the G(NH)··C(N) hydrogen bond. Therefore, one could feel inclined to assign the 3150 cm^{-1} band to the $\upsilon_G(NH_2)b$ mode and the band at 3300 cm^{-1} to the $\upsilon_C(NH_2)_b$ and $\upsilon_G(NH)$ mode. However, due to the failure of the local mode picture the different NH stretching excitations will be highly mixed and such a procedure appears incorrect. Only the excitations in local waterfree base pairs can be still described in the local mode approach. A spectroscopic assignment of the broad bands in the 0% R.H. G·C oligomer spectra requires quantum chemical calculations incorporating specifically the effect of hydrating water molecules, which is beyond the scope of this work.

Minor role of vibrational intrastrand couplings between stacked nucleobase pairs

The off-diagonal cross peaks with positive sign at (3320, 3170) and (3170, 3320) reflect anharmonic couplings between the NH stretching states, in particular between the $\upsilon_G(NH)$ mode and the $\upsilon_C(NH_2)_b/\upsilon_G(NH_2)_b$ modes. The coupling pattern, except for the absence of distinct cross peaks to the position of the free NH stretching mode due to the presence of water, is very similar to that of isolated G·C base pairs in solution [49]. Similar comparisons can be made for the linear and 2D-IR spectral signatures of NH stretching excitations in isolated A·T base pairs in solution (section 6) with those of double-helical A·T oligomers at low water content [51,235][b]. Such comparison for A·T pairs gives a similar conclusion that the overall cross-peak patterns with and without the double-helix structure show only minor differences when discarding the effect of hydration. This leads

[b] Although this does not appear as straightforward since the variety of A·T pairing geometries could create problems (however, in section 6 we showed that the spectral signatures of the different A·T pair configurations are very similar)

to the important conclusion that there are no experimental indications that vibrational couplings of NH stretching excitations between stacked nucleobase pairs - both for A·T- and G·C-rich DNA - play a significant role in double-helical DNA. This finding is consistent with the expectation that transition dipole-dipole couplings (scaling with r^{-3}) between stacked nucleobases are weaker than the interbase couplings in hydrogen-bonded base pairs due to the bigger vertical distance between stacked nucleobases of 3.1 $\AA$ compared to the H··N/O distance of about 1.8 $\AA$ in G·C base pairs [11, 12, 200]. In contrast, cross peaks between carbonyl C=O stretching modes in the 2D-IR spectra of double-helical G·C oligonucleotides have been attributed to both interstrand and intrastrand couplings over similar size (7-10 cm^{-1}) by Zanni and coworkers [52, 54, 241, 242] (cf. discussion in section 4.4).

Diagonal peak suppression

The nonlinear signal strengths of different Feynman pathway contributions are strongly dependent on the relative linear polarization of the exciting pulses. Apart from the possibility of extracting relative transition dipole angles, this allows for certain pulse polarization geometries such as (k_1, k_2, k_3, k_{LO}) = (60°,-60°,0°,0°) to completely suppress the diagonal peak signals as well as cross peak signals of parallel transition dipoles (see section 2.5). While usually the diagonal signals clearly dominate a 2D spectrum and - especially when heavily broadened - partly mask off-diagonal signals, measurements under diagonal peak suppressing conditions enable the exclusive observation of cross peak features. However, as the overall signal intensity is greatly reduced in such measurements, the enhanced influence of scattered pump light may degrade the 2D spectral quality.

Figure 7.6 shows 2D spectra of G·C oligomers at 0% R.H. in (60°,-60°,0°,0°) polarization geometry with excitation pulses centered at 3300 cm^{-1} (upper panels) and 3370 cm^{-1} (lower panels), each for waiting times of T = 100, 300, and 500 fs. For low waiting times, the cross peaks with positive sign at $(\upsilon_1[cm^{-1}], \upsilon_3[cm^{-1}]) \approx$ (3320, 3170) and (3170, 3320) (numbered as peaks I in the bottom panels of Figure 7.6) dominate the spectra. Their clear visibility indicates a nonzero relative angles between the transition dipole vector of the modes at 3320 and 3170 cm^{-1} (polarization-dependent 2D spectra (not shown) revealed a relative angle around 10°). Moreover, we observe a negative cross peak (peak II in Figure 7.6) at ≈ (3150, 3230). It arises from excitation pathways entering the combination state of the 3320 and 3170 cm^{-1} mode and allows the determination of the off-diagonal anharmonicity as 3320-3230 = 90 cm^{-1}. This signal was buried under the diagonal peaks before, just like a cross peak pair at (3380, 3300) and (3300, 3380) (peaks III in Figure 7.6) that appears for increasing waiting times, especially when the excitation pulses are centered at 3370 cm^{-1}. The origin of the latter cross peaks is not perfectly clear. They may arise either from coupling between the NH stretching modes around 3300 cm^{-1} and the OH stretching modes of close-by water molecules hydrating the base pairs in first shell positions. Alternatively, the cross peaks may reflect Fermi-resonance coupling between carbonyl $\upsilon = 2$ overtone transitions in guanine (fundamental at 1690 cm^{-1}) and the NH stretching modes. Such a mechanism was proposed to explain the origin of a diagonal peak at 3380 cm^{-1} in 2D-IR measurements on G·C base pairs (see solid line in Figure 7.4) in solution recorded in ZZZZ polarization geometry [236]. Even with diagonal peak suppression, there are no clear signatures for cross peaks involving the frequency position of potentially free NH stretching modes (around 3490 cm^{-1}).

7.4 Ultrafast 2D-IR spectroscopy of NH/OH stretching modes at full hydration

The change in R.H. from 0 to 92 % is accompanied by a change in DNA conformation from the A- to B-form as discussed before. Both conformations show notable differences in the dimensions

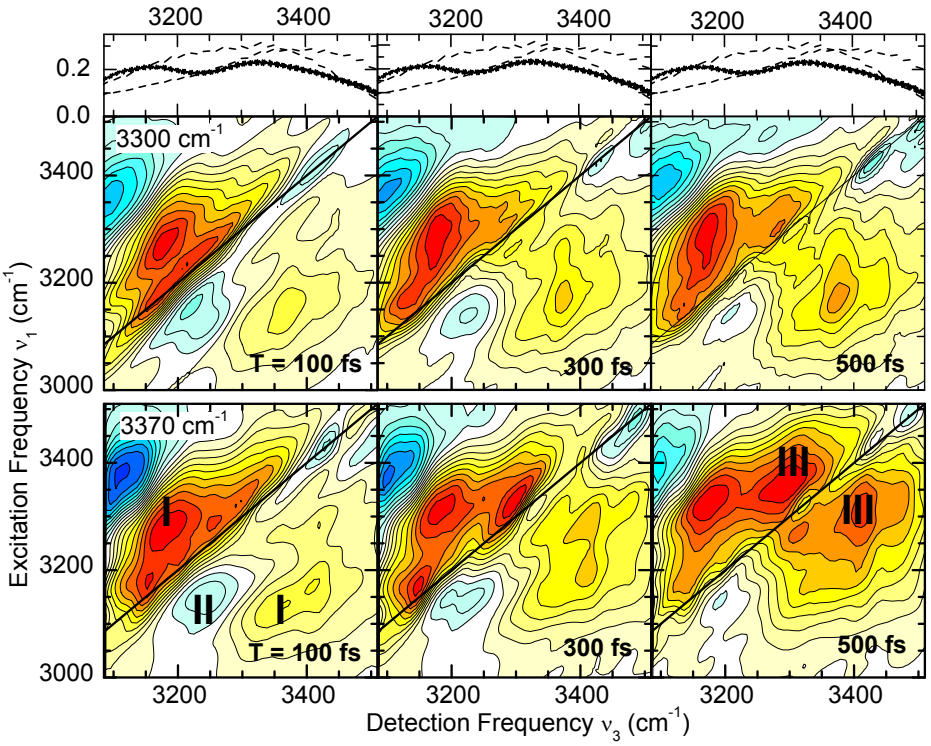

Figure 7.6: *2D spectra at 0% R.H. with excitation pulses centered at 3300 (top pannels) and 3370 (lower panels) in* (k_1, k_2, k_3, k_{LO}) *= (60°/-60°/0°/0°) polarization geometry, suppressing the diagonal peaks. They reveal two cross peaks at* $(\upsilon_1\left[cm^{-1}\right], \upsilon_3\left[cm^{-1}\right])$ *= (3380, 3300) and (3300, 3380) that were previously buried under the dominating diagonal 2D signal.*

of the DNA grooves such as width and depth, defining the steric accessibility of polar nucleobase groups for hydration, which can reflect on the hydration affinities of the polar base groups in the minor and major groove positions. For B-DNA, due to the narrowness and deepness of the minor groove, the minor groove hydration sites are better defined and, hence, higher populated, than the ones in A-DNA, where the minor groove is shallower and wider. Moreover, due to shallow and wide major groove dimensions the hydration sites of the major groove in B-DNA are less populated than in A-DNA, where the major groove becomes narrower. The preferential hydration sites, however, remain the same for A- and B-DNA, while the detailed hydration densities will change to some extent [214] (also see chapter 4.2). Our linear and nonlinear 2D-IR spectra provide an averaged picture over all NH stretching modes in minor and major groove positions. Because the molecular groups located in the minor and major groove position are the same in G·C oligomers (in both cases one carbonyl oxygen and one amino group), the effective vibrational structure of hydrogen-bonded NH stretching modes can be expected to stay to a big extent unaffected from a transition from A- to B-DNA when neglecting the influence of additional water molecules. Considering that vibrational dipole-dipole interactions between stacked nucleobases were found to show no notable influence for the 0 % R.H. measurements of A-DNA (vertical distance between stacked pairs ≈ 2.9 $\AA$), stacking interaction will neither play a notable role for the 92 % R.H. case of B-DNA, where the vertical base pair distance increases to ≈ 3.4 $\AA$. The pure DNA structural changes are not expected to create notable changes in vibrational line shapes but the increased number of hydrating water molecules could. However, in the following section we will show that the formation of a full hydration shell does not notably change the NH stretching excitations compared to the situation of low humidity.

For G·C oligomers at 92 % R.H., the 2D spectra are plotted in Figure 7.7 and show significant

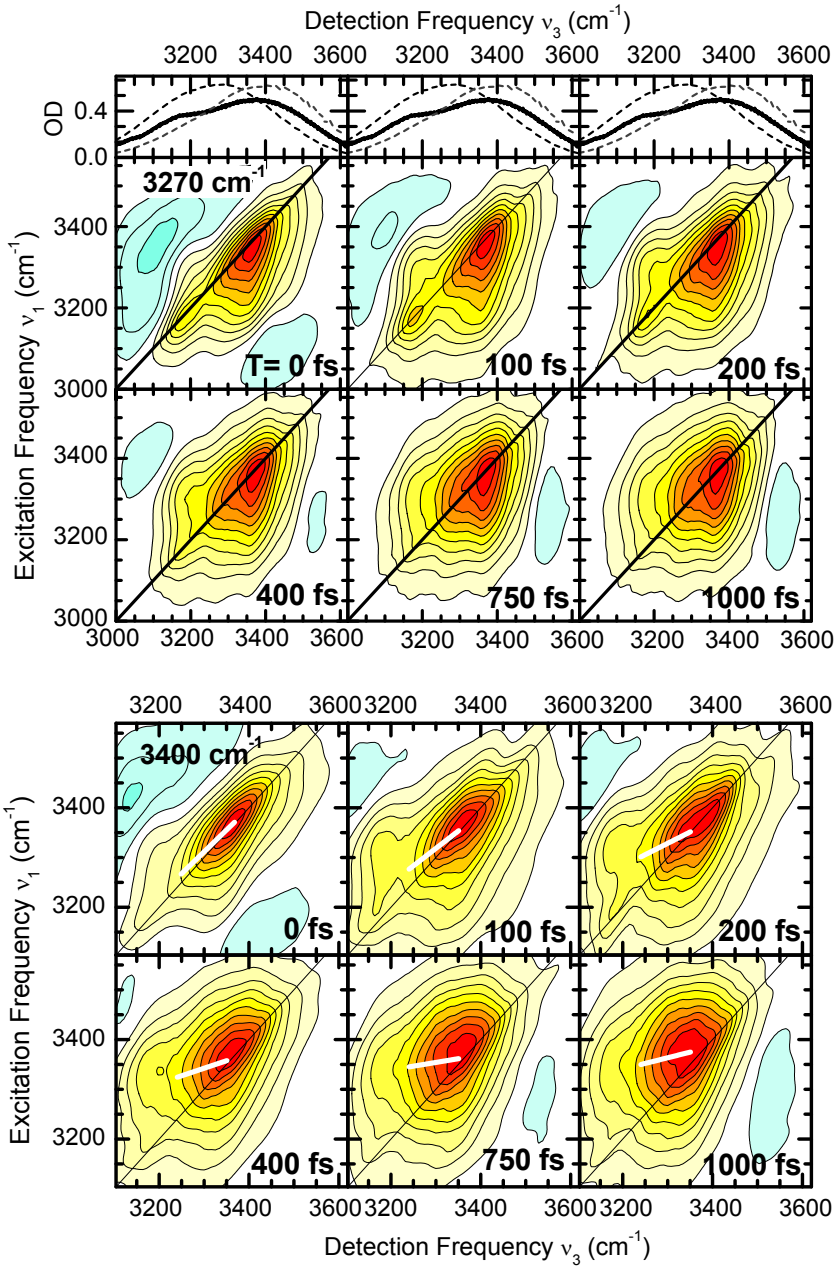

Figure 7.7: *2D spectra of G·C oligomers at 92% R.H. for pulses centered at 3260 cm^{-1} (upper panels) and 3400 cm^{-1} (lower panels) as a function of waiting time. The lower panels contain the linearly fitted center lines (thick white line), whose changes in slope indicate OH stretching mode spectral diffusion in the water shell on the sub-picosecond time scale.*

changes compared to the 0 % R.H. case. Here the NH stretching oscillator response is overlayed by the dominating response of the OH stretching oscillators in more than 20 solvating water molecules. The superimposed OH stretching band peaking at 3400 cm^{-1} leads to a frequency upshift of the maxima of the total nonlinear signal. At this high humidity, the first hydration shell is completely filled with a few additional water molecules associated in second shell positions through long-range interactions to the DNA interface. The corresponding diagonal cuts in Figure 7.4 (c) allow one to

weakly distinguish the overlapping contributions of the OH stretching water band peaking around $\upsilon_1 = \upsilon_2 = 3400$ cm^{-1} from the broad distribution of NH stretching oscillators centered around 3300 cm^{-1}. The 2D spectral signatures with excitation pulses centered at 3260 cm^{-1} (see the top panels of Figure 7.7) of the NH stretching oscillators for early waiting times appear similar to those in the low humidity case, providing similar diagonal and antidiagonal line width as found for the 0% R.H. data. However, the upper diagonal peak now can be divided into a highly inhomogeneous contribution aligned along the diagonal arising from NH stretching modes, that is superimposed on a signal aligned more along the excitation frequency axis. The latter signal thus exhibits a more homogeneous lineshape and results from the OH stretching excitations in the water shell. Therefore the linear and nonlinear response of the NH stretching modes is revealed to be only weakly influenced by the presence of a full hydration shell, as evidenced by the highly similar NH stretching 2D line shapes of diagonal and cross peaks with similar frequency positions and line widths as in the 0% R.H. case (cf. the top panels of Figure 7.2). The NH and OH stretching contributions in the linear and nonlinear response therefore can be considered as additive with the water shell only weakly affecting the NH stretching mode dephasing dynamics and line broadening mechanisms, as was similarly observed for humidity-dependent 2D-IR spectra of A·T oligomers [235].

7.5 Hot ground state formation and spectral diffusion in the water shell

For high waiting times, the water peak in the 2D spectra shows a substantial reshaping with increasing waiting time, transforming from an initially elliptical shape aligned parallel to the frequency diagonal into a more round shape at high waiting times, which reveals significant spectral diffusion of OH stretching oscillators in the extended hydration shell at the DNA interface. Moreover, a strong negative signal appears with increasing waiting time at blue-shifted detection frequencies, which is much stronger than the weak signal observed for 0% R.H. (cf. peak 6 in Figure 7.2). The latter results from OH stretching oscillators whose 0-1 transition frequency becomes blue-shifted upon population of anharmonically coupled low-frequency modes during vibrational energy redistribution. This "hot ground state signal" as well as the origins of spectral diffusion will be discussed in the following section.

Hot ground state formation

The positive diagonal and cross peaks showed a long-lived residual bleaching signal extending beyond the picosecond time scale (compare peaks 1-4 in Figure 7.3), which reveals that the initial vibrational ground state is not repopulated directly after excitation. In a cascaded relaxation process the NH stretching excitation energy is finally delocalized over several low-frequency intramolecular G·C oligomer modes, intermolecular DNA-water modes, and librational (hindered rotational) modes in solvating water molecules, reflecting the state of a macroscopically vibrationally heated sample. The delocalization of the excess vibrational NH stretching energy into various low-frequency modes - especially those of the water shell - leads to a hot ground state, which is characterized by a slightly elevated vibrational temperature. Its effects are sketched in Figure 7.8. The onset of population of low-frequency modes induces changes in the NH and OH stretching line shapes due to their anharmonic coupling. Such a heated ground state will show an enhanced fraction of weakened or even broken hydrogen bonds in the hydration shell, which shifts the frequencies of the affected oscillators to higher values. This shift will manifest both in an enhanced absorption signal (negative sign) at the position of the transiently blue-shifted shifted 0-1 transition arising from hydrogen-bonded oscillators whose hydrogen bond became weakened due to coupling to the vibrationally heated bath modes (see peak 6 in Figure 7.2, and Figure 7.8

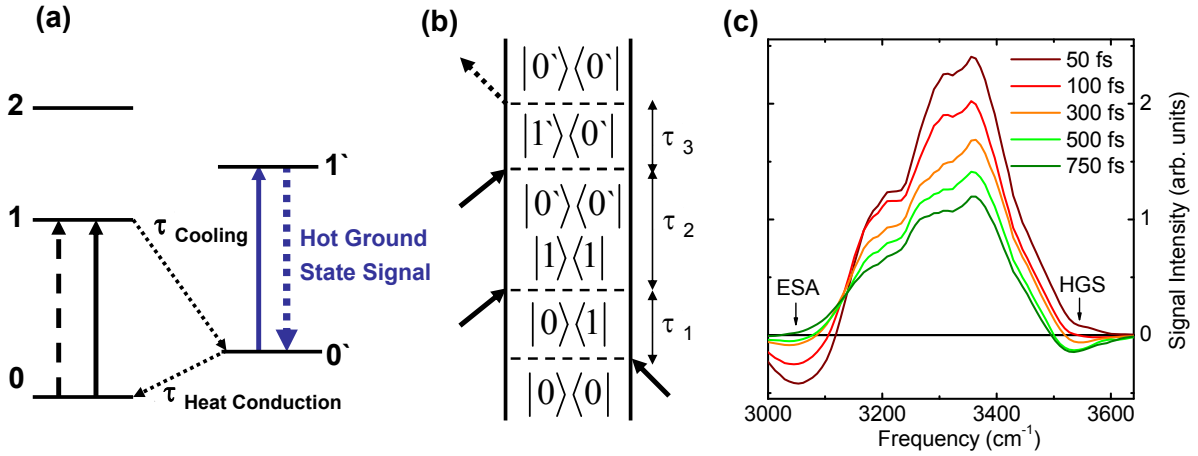

Figure 7.8: *(a) Ladder diagram describing the formation of the blue-shifted hot ground state (HGS) signal, with the corresponding Feynman pathway shown in (b). Vibrational energy redistribution during the waiting time may lead to population of low-frequency bath modes that are anharmonically coupled to nonexcited OH stretching oscillators and therefore shift their 0-1 transition energy. The equilibrium situation is restored on the time scale of macroscopic heat conduction out of pumped volume. (c) Slices of the 2D spectra in Figure 7.7 (upper panels) at a fixed excitation frequency of 3270 cm^{-1}, showing the ingrowing HGS signal.*

(c)). At the same time, a reduced absorption signal (positive sign) will be left in the region of the original (unperturbed) 0-1 OH or NH stretching frequencies, i.e. extending over the full range of the positive 2D diagonal peak. As the detailed relaxation pathway of any individual oscillator is a random process with the possibility of accessing various intermediate states, there are no correlations between the initial excitation frequency and the final occurrence in a hot ground state signal at a certain detection frequency. Hence, the hot ground state signals will exhibit a homogeneous, i.e. round, 2D-IR lineshape. The measurements at high 92% R.H. shows the blue-shifted hot ground signal much more pronounced than at 0% R.H.. This indicates that vibrational heating, following relaxation of NH/OH stretching modes, primarily affects OH stretching oscillators in the water shell and less so the hydrogen-bonded NH stretching modes in the base pairs.

The dynamic intensities of these characteristic hot ground state features give independent information on vibrational cooling dynamics. The network of water molecules in the DNA solvation shell shows the signatures of a vibrationally heated water pool already few hundred femtoseconds after excitation of the OH and NH stretching oscillators (see Figure 7.8 (c)), which proves effective energy delocalization into the hydration shell on an ultrafast time scale. Therefore, the "biological" water at the DNA interface serves as a highly efficient heat sink and thereby contributes to the photostability of DNA as was similarly observed in fully hydrated *AT* oligomers [56] and nano-sized water pools in reverse micelles [297].

Spectral diffusion

In order to quantify the reshaping of 2D line profiles and thereby evaluate the extent of spectral diffusion on the experimental time scale, we studied the center lines in the 2D spectra. The center lines were generated by determining the intensity maxima of vertical 2D spectral slices at fixed detection frequencies and connecting such positions from slices along different detection frequencies. Their linear fits are added to the 2D-IR spectra of the 0% R.H. samples (lower panels in Figure

7.2) and 92% R.H. samples (lower panels in Figure 7.7) as white lines. As spectral diffusion is only observed in the water shell and not for the NH stretching modes of the bases (see below), such analysis is restricted to the frequency range of OH stretching oscillators, while distortions due to the sign change of the hot ground state signal prevent analysis for detection frequencies above 3380 cm^{-1}. We therefore restrict the analysis to a range of 3250-3370 cm^{-1}. The development of the center line slope (CLS) with waiting time is plotted in Figure 7.9 and approximates the ensemble-averaged two-point frequency-frequency correlation function (FFCF) C(t)=$\langle\delta\omega(t)\delta\omega(0)\rangle$ as discussed before (cp. page 16 and 25).

Low hydration

For the case of weakly hydrated G·C oligomers at 0% R.H., there are only minor changes in the center line slope, staying roughly constant around a value of 0.75 as shown in Figure 7.9 (open circle symbols). This is indicative of a high degree of structural inhomogeneity in the G·C base pair geometries, which stay static on the picosecond time scale. Particularly towards the ends of the 23-oligomers molecular structure, interbase hydrogen bonding strengths can be expected to show slight deviations to the case in the center of the oligomer structure, with possibly better accessibility of polar base groups for hydration. In addition, the low number of water molecules will be highly inhomogeneously distributed over the phosphate and groove binding sites. Such processes contribute to the highly inhomogeneous line broadening.

Although dominated by NH stretching base pair contributions (see previous discussion), in the analyzed frequency range there are also contributions from water OH stretching oscillators. The constant FFCF therefore evidences the minor role of spectral diffusion both for the NH stretching modes in the base pairs and for the $\approx$ 4 most tightly bound first shell water molecules on the picosecond time scale. It points to a fairly rigid hydration geometry at the DNA interface for the most tightly bound $\approx$ 4 molecules, sitting in the first solvation shell around the phosphates and to some extend distributed around the base edges at minor and major groove positions. The lifetime of the water-DNA hydrogen bonds thus clearly exceeds 1 ps, as was similarly observed for double-helical adenine-thymine oligomers [235] at low hydration level. It also agrees with theoretical MD calculations that found average DNA-water hydrogen-bond lifetimes times at the minor groove sites to be only slightly longer than at the major groove sites with a value around 11 ps [22]. Average residence times at the phosphate sites were found to be shorter but still exceeding the 1 picosecond time scale [24].

Full hydration

The 92% R.H. 2D spectra with excitation at 3400 cm^{-1} are dominated by the OH stretching contributions from the DNA water shell and, hence, show the spectral diffusion dynamics most clearly. The filled square symbols in Figure 7.9 show the CLS to decay within the first 400 fs from an intial value of 0.9 to a value of 0.3 with a slower decay or even constant offset for higher waiting times. The initial decay can be satisfactory described through a single-exponential decay with a 250 fs lifetime and an offset of 0.19 (solid line in Figure 7.2). This initial decay, though still in the sub-picosecond regime, is substantially slower than the spectral diffusion dynamics observed for OH stretching modes in bulk H_2O water, which showed a fast sub-100fs component [25]. Similarly, MD simulations calculating the FFCF for bulk water indicated a fast ($\approx$ 100 fs) initial decay followed by a slower decay with a time constant influenced by the extent of intermolecular vibrational energy transfer [298] (cf. dashed and dotted line in Figure 7.2). Such a fast initial component is obviously absent in our data, while the slower component predicted by MD calculations is found in our data. This shows that the high level hydration does not lead to extended water pools but that water is spread over and strongly interacts with the DNA interface.

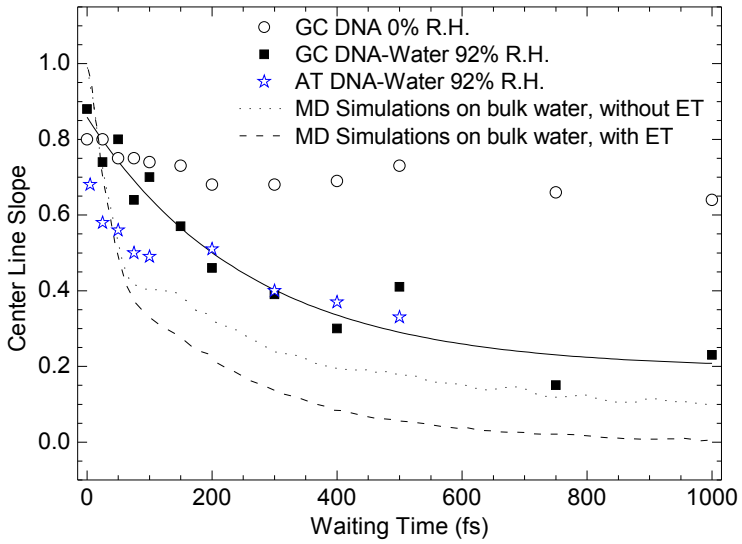

Figure 7.9: *Slopes of the center lines at 0% R.H. (open circles, cf. Figure 7.7) and 92% R.H. (black squares, cf. Figure 7.2) in the frequency position of NH and OH stretching modes as a function of waiting time for G·C oligomers (excitation centered at 3400 cm^{-1}), reflecting the frequency-fluctuation correlation function (FFCF). The center lines for the measurements on 92% R.H. roughly follow a monoexponential decay with a 250 fs time constant (black line) and a long-lived component (here approximated by an offset of 0.19). In contrast, the FFCF of OH stretching oscillators in bulk H_2O showed a sub-100 femtosecond initial decay as reproduced by molecular dynamics simulations in ref [298] including (dashed line) and excluding (dotted line) resonant energy transfer between different OH stretching oscillators. A similar analysis on A·T oligomers at 92% R.H. yielded a decay of the FFCF (blue star symbols) that is similar to the decay found for 92 % R.H. G·C oligomers.*

Two mechanisms contribute to transient changes in the 0-1 transition frequencies (spectral diffusion) of OH stretching modes in the water shell: first, structural fluctuations leading to temporal deformations of the potential energy surface of individual oscillators, hereby temporally shifting the transition frequencies of the affected oscillators. Because fast structural fluctuations require a floopy binding geometry, mostly more weakly bound water molecules in the first and, especially, second hydration shell will contribute here. Those water molecules directly interacting with the DNA interface exhibit decelerated structural fluctuation dynamics due to steric hinderance effects (which especially refers to those embedded in the shallow and deep minor groove) and due to the strong electrostatic interactions with the polar base and charged phosphate groups. Second, resonant energy transfer of OH stretching excitations in different water molecules with slightly different center frequencies may lead to a decay in the frequency correlation function. Due to the lower water concentration in the fully hydrated DNA samples of 10 M (as compared to 55 M in the bulk), the average water-water distance can be expected to be significantly higher, which in the picture of Förster-resonance energy transfer greatly reduces energy transfer rates [51, 299] and makes energy transfer a less prominent mechanism for spectral diffusion of OH stretching modes in hydrated DNA. A similar behavior (maybe with a slightly slower decay of the FFCF) was observed for OH stretching excitations in the water shell around A·T oligomers in 2D-IR measurements [51] (see blue star symbols in Figure 7.9). Our findings support predictions from recent molecular dynamics simulations finding a deceleration in the frequency fluctuation correlation function by a factor of

2-3 [35].

Moreover, the influence of the overlaid hot ground state signal has to be considered as an additional contribution to the dynamic reshaping of the diagonal 2D signal for higher waiting times. This contribution does not reflect any spectral diffusion dynamics but is merely related to the increasing intensity of the hot ground state signal, which shows a homogeneous, i.e. round, 2D line shape as explained above. Hence, the 2D spectral reshaping of the diagonal signal may be partly due to the residual bleaching signal of OH stretching oscillators experiencing a bath of elevated temperature for higher waiting times. 2D-IR measurements on water nano-droplets confined in reverse micelles showed the ingrowing hot ground state signal as the dominant mechanism for the observed 2D band reshaping [297]. In contrast, our G·C oligomer measurements provide the frequency-fluctuation dynamics of the water OH stretching modes consistent with MD simulations [35], which is why we assume the hot ground state contribution to be of minor importance.

7.6 Conclusions

We have analyzed the vibrational and structural dynamics of NH and OH stretching modes in double-helical guanine-cytosine (G·C) 23-mers in Watson Crick geometry at different levels of relative humidity (R.H.). The frequency position of the asymmetric phosphate stretching mode $\upsilon_{AS}(PO_2)^-$, providing an internal molecular measure of the water content, indicates 4 water molecules per base pair at 0% R.H. and more than 20 water molecules per base pair at 92% R.H. conditions.

At low humidity, contributions from the base pair NH stretching modes dominate the nonlinear 2D spectra, exhibiting a highly inhomogeneous lineshape and T_1 population times of 200-300 fs similar to those of hydrogen-bonded NH stretching excitations in isolated G·C base pairs in chloroform solution. However, there are no indicators for a full decoupling of NH stretching excitations in the two amino groups as evidenced by the absence of pronounced diagonal or cross peak signals in the 2D-IR spectra in the frequency range where free NH stretching modes would appear (3490 cm^{-1}), in contrast to observations in G·C base pairs in solution. Moreover, the slow population dynamics in the 3490 cm^{-1} range, characteristic of free NH stretching states, is missing. We conclude that already at 0 % R.H. the residual water molecules have a substantial impact on vibrational line shapes through the formation of local hydrogen bonds to the "free" NH motif in the base amino groups. This hydrogen bonding leads to a reduction in the decoupled local energies of the amino NH stretching modes, therefore enhancing the effect of mechanical intermode coupling and creating partly delocalized eigenstates that show a character intermediate between local and normal mode. There is no ultrafast spectral diffusion of the NH stretching modes and OH stretching excitations of the residual (most tightly bound) interfacial water molecules at low humidity on the picosecond time scale, hinting to rather rigid G·C base pair and DNA-water geometries. We find weak inter-base "horizontal" vibrational couplings between NH stretching oscillators in the hydrogen-bonded G·C pairs, while intrastrand "vertical" couplings between neighboring NH stretching modes are negligible. Similar conclusions can be drawn for the coupling scheme of stacked A·T base pairs in double-helical DNA.

For a fully occupied first hydration shell and a few additional waters weakly coordinated in second shell positions at 92% R.H., the nonlinear response is dominated by OH stretching modes of the water shell. The 2D spectra show an additive behavior of nonlinear NH stretching and OH stretching contributions, i.e. the condition of full hydration does not significantly alter the NH stretching line shapes as compared to the low humidity case. We observe a 250 fs decay of the OH stretching frequency-fluctuation correlation function, i.e. slowed-down compared to the sub-100fs fast decay component found for bulk water. We attribute this decelerated decay to reduced structural fluctuations in the water shell on the DNA interface due to steric constraints and tight

DNA-water interactions and to the creation of a vibrationally hot ground state forming in the process of vibrational cooling. The formation of a hot ground state with an enhanced fraction of weakened and/or broken hydrogen bonds in the DNA hydration shell is found to occur on the time scale of few hundred femtoseconds, which points to the important role of the DNA hydration shell as a highly efficient heat sink. The overall dynamics in the water shell is similar to the situation in hydrated double-helical adenine-thymine oligomers [235].

8 Enhancement of Fermi resonances upon hydrogen bonding in aniline-d5

Our linear and 2D-IR studies on A·T base pairs in solution revealed the important role of Fermi resonance enhanced overtone/combination tone states, in particular involving the NH_2 bending mode, for the understanding of vibrational line shapes and energy relaxation pathways. Therefore, we decided on a separate investigation of the influence of hydrogen bonding on the intensity of harmonically-forbidden overtone vibrations and the manifestation of Fermi resonances in 2D-IR spectra. Aniline-d5[a] (abbreviated as An) provides a perfect model system to study the enhancement of Fermi resonances upon hydrogen bonding because the small mode density in An allows one to observe basically only a single Fermi-resonance - the NH_2 bending overtone - while the effective coupling to NH stretching single-excited states can be tuned through hydrogen bonding with dimethylsulfoxide (DMSO) molecules.

In this chapter, we present a quantitative analysis of the pronounced Fermi-resonance effect on the NH_2 bending overtone absorption strength in aniline-d5 upon hydrogen bonding to DMSO. We will show that in ternary mixtures of An-d5, DMSO, and CCl_4 the proper choice of DMSO concentration allows to form predominantly nonhydrogen-bonded An monomers, single-hydrogen-bonded An·DMSO complexes, or double-hydrogen-bonded An·$(DMSO)_2$ complexes. The frequency red-shift of the NH stretching combined with a blue-shift of the NH_2 bending fundamental upon hydrogen bond formation will be shown to lead to a drastic enhancement of the Fermi-resonance effect. The changes in oscillator strength are modeled in an excitonic approach to extract the intermode couplings and vibrational eigenstates in the single-excited NH stretching manifold, providing in particular the degree of mode mixing between fundamental NH stretching states and the NH_2 bending overtone state. Polarization-dependent 2D-IR spectroscopy will be used to map out the single- and double-excited state manifold of NH stretching transitions revealing anharmonicities, couplings and relative transition dipole orientations. We illustrate the superiority of nonlinear 2D-IR spectroscopy over standard linear overtone spectroscopy in extracting overtone energy level schemes due to the mostly unambiguous band assignment in the former case.

8.1 Kinetic analysis and spectral decomposition of the linear infrared spectrum

First, we analyze the concentration-dependent IR spectra of ternary An/DMSO/CCl_4 mixtures, which will reveal the An-DMSO complexation constants and the isolated linear spectra of An monomer, An·DMSO, and An·$(DMSO)_2$. The FT-IR spectral region of the NH stretching modes in ternary mixtures An/DMSO/CCl_4 is plotted in Figure 8.1 (a) as a function of DMSO concentration, while the An concentration is kept constant at 0.4 M. In the absence of DMSO, the symmetric and asymmetric NH stretching modes in An monomer appear at 3395 and 3480 cm^{-1}. A very weak feature around 3212 cm^{-1} signifies the NH_2 bending first overtone. The linear spectra of An at different concentrations shows no significant changes up to 0.4 M, therefore self-association of An

[a] It is advantageous to use the deuterated compound as the single-excited NH_2 bending state is then effectively decoupled from the $\upsilon(CC)$ ring mode because the separation of both modes is enhanced compared to the situation in An-h7.

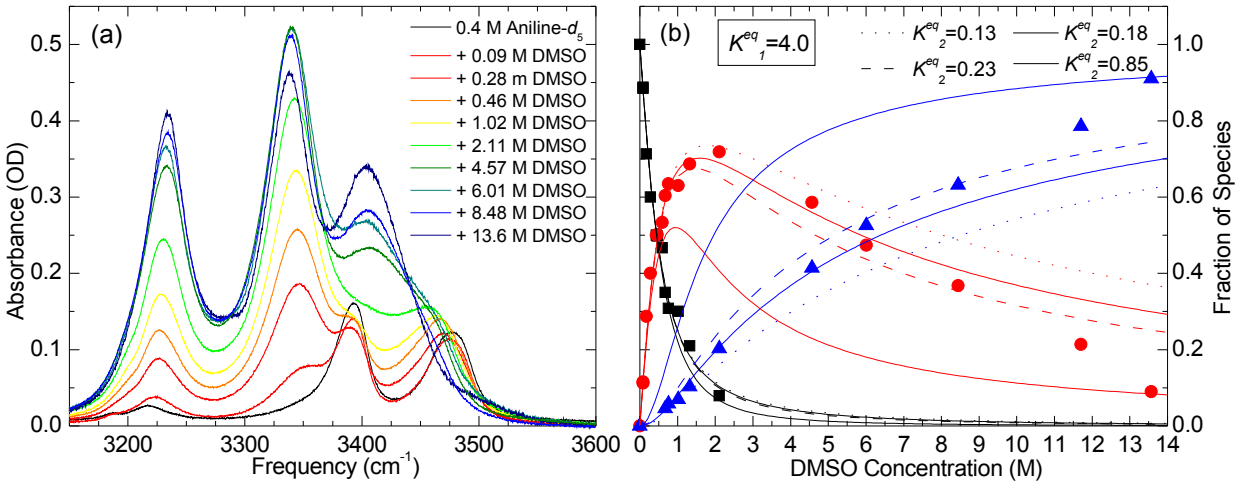

Figure 8.1: *(a) Linear FT-IR spectra of 0.4 M An in CCl_4 with variable concentration of DMSO, reflecting the increasing complexation of An and DMSO in the NH stretching region. (b) Decomposition of the linear spectra into different contributions of An monomers, An·DMSO, and An·$(DMSO)_2$ complexes allows one to determine their relative fractions as a function of DMSO concentration for a ternary An/DMSO/CCl_4 mixture with 0.4 M An. The black/red/blue symbols represent the fraction of An monomers/An·DMSO complexes/An·$(DMSO)_2$ complexes. The different lines reproduce their relative fraction with rate equations using the equilibrium constants given in the Figure (b).*

can be neglected for the covered concentration ranges. Upon increasing DMSO concentration, An starts to form hydrogen-bonded complexes with DMSO, which leads to gradual changes in the overall linear response in the NH stretching region with the different complexes absorbing at different spectral positions. Already for low DMSO concentrations, a new band around 3345 cm^{-1} arises, increases up to a DMSO concentration of 6 M, and decreases for higher values again. At the same time, the Fermi resonance enhanced NH_2 bending overtone around 3212 cm^{-1} increases in intensity and upshifts slightly. In addition, the asymmetric NH stretching mode from An monomers disappears upon increasing DMSO concentration, forming a new band centered around 3400 cm^{-1} for DMSO concentrations above 4.6 M. In order to decompose the linear IR spectra in Figure 8.1 (a) into the spectral contributions of An monomer, An·DMSO, and An·$(DMSO)_2$ complexes and to determine their relative abundance as a function of DMSO concentration, consider the following complexation scheme:

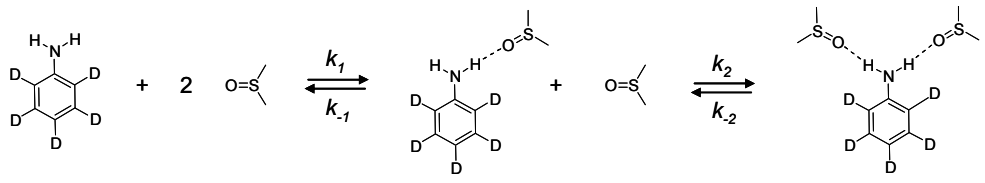

with the equilibrium constants $K_1^{eq} = (k_1/k_{-1})$ and $K_2^{eq} = (k_2/k_{-2})$. Therefore, the initially arising band for low DMSO concentration is assigned to the An·DMSO complexes and the band appearing only for high DMSO concentrations to the An·$(DMSO)_2$ complexes. Considering only the DMSO concentration range between 0 and 0.6 M, the IR absorption spectra can be separated into a sum with variable contributions of the An monomer spectrum and the An·DMSO spectrum. Knowing the sum of the concentrations of the An, An·DMSO, and An·$(DMSO)_2$ complexes to stay constant

at 0.4 M, the third contribution of An·$(DMSO)_2$ complexes relevant for high DMSO concentrations can be extracted, hence providing a complete decomposition of the total IR spectra in Figure 8.1 (a) into three different contributions. The knowledge of their individual spectral signatures also allows for the determination of their individual concentrations as a function of DMSO concentration as shown in Figure 8.1 (b). The lines represent the relative concentrations of the three species as given by the system of coupled rate equations with the equilibrium constants K_1^{eq} and K_2^{eq} as free parameters. Best agreement is obtained for $K_1^{eq} = 4.0$ l mol^{-1} and $K_2^{eq} = 0.18$ l mol^{-1} for DMSO concentrations up to ≈ 4 M (see the thick solid lines). Deviations for higher DMSO concentrations indicate a change in the equilibrium constant K_2^{eq} towards higher values, the data suggest that K_2^{eq} $= 0.85$ l mol^{-1} is required for 0.4 M An in DMSO (thin solid lines). As Figure 8.1 (b) illustrates, a change in DMSO concentration enables to shift the predominant species from monomeric An over An·DMSO complexes to almost exclusively An·$(DMSO)_2$ complexes in pure DMSO.

8.2 Linear fundamental and overtone IR spectra of NH stretching modes

The kinetic analysis above directly provides the individual linear IR spectra of the different species (An monomer, An·DMSO, and An·$(DMSO)_2$). Figure 8.2 shows their linear IR extinction coefficient in the spectral region of the NH_2 bending mode between 1540 and 1690 cm^{-1} in (a) and the NH stretching mode pattern between 3210 and 3620 cm^{-1} in (b). Additionally, the inset in (b) shows the highly structured weak band around 3220 cm^{-1} of An monomers on a magnified scale. Ab initio calculations [300] allow for an unambiguous mode assignment in the NH_2 bending fundamental region (a), assigning the narrow intense band at 1573 cm^{-1} to the $\upsilon(CC)$ ring mode and the upshifting bands at 1616 cm^{-1} (An monomer), 1629 cm^{-1} (An·DMSO), and 1641 cm^{-1} (An·$(DMSO)_2$) to the NH_2 bending mode of An in the presence of 0, 1, and 2 hydrogen bonds to DMSO molecules. For the An spectra in (b) this suggests the 3216 cm^{-1} peak as the $\delta(NH_2^{0-2})$ bending overtone transition and the weaker shoulder at 3187 cm^{-1} as the $\upsilon(CC) + \delta(NH_2)$ combination mode. The latter becomes almost invisible when An is complexed to DMSO, probably because the combination mode experiences less Fermi resonance enhancement and because of the increasing broadening of the bending overtone band. For the following discussion we will mostly neglect the $\upsilon(CC) + \delta(NH_2)$ combination mode.

The spectral changes of the mode pattern in the NH stretching region shown in Figure 8.2 (b) reflect the characteristic effects of hydrogen bonding on XH stretching modes: a drastic frequency red-shift, an enhancement in line width, and an enhancement in integrated oscillator strength (cf. section 2.3). At the same time, the NH_2 bending mode shows a frequency upshift with line broadening upon hydrogen bonding (Figure 8.2 (a)), while its integrated oscillator strength only shows mild changes. In contrast, the NH stretching modes show a significant oscillator strength increase, which is even much more pronounced for the Fermi resonance enhanced bending overtone around 3220 cm^{-1}. The latter increase results not only from the increased oscillator strength of the coupled NH stretching modes, but also from the increased effective Fermi-resonance-induced mixing due to the reduced energetic separation of NH_2 bending overtone and the NH stretching states. While the integrated oscillator strength of the total absorbance in the 3100-3600 cm^{-1} region scales as 1/4.9/5.7 for the An/An·DMSO/An·$(DMSO)_2$ species, the integrated absorbance of the bending overtone $\delta(NH_2)$ increases about 4 times more, scaling as 1/17/24 for the An/An·DMSO/An·$(DMSO)_2$ species.

Knowing that the oscillator strength scales quadratically with the transition dipole moment and considering that An·DMSO complexes contain one free and one hydrogen-bonded NH stretching mode and the An·$(DMSO)_2$ complexes two hydrogen-bonded NH stretching modes, we can calculate the transition dipole moment enhancement per hydrogen-bonded NH stretching mode

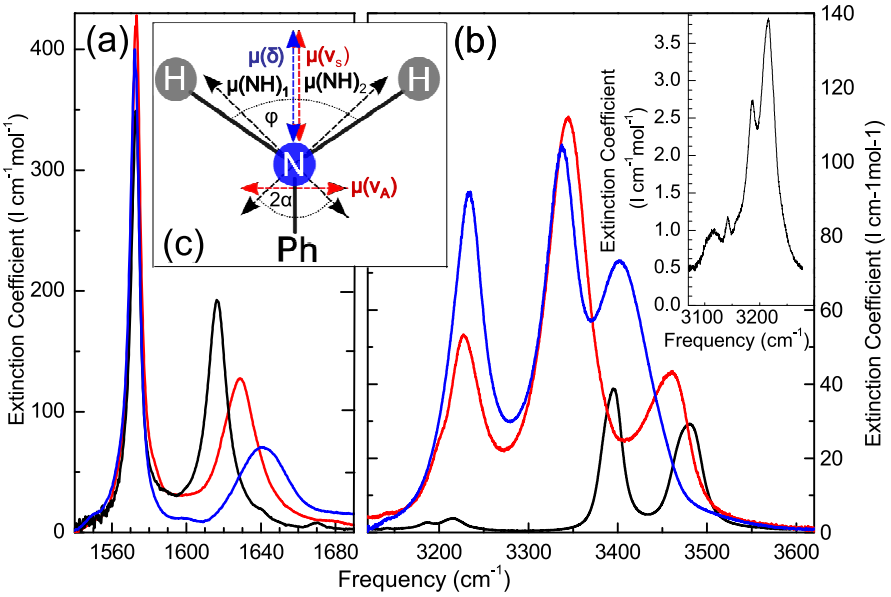

Figure 8.2: *Decomposed isolated IR spectra of An monomer (black lines), single hydrogen-bonded An·DMSO (red lines), and double-hydrogen-bonded An·$(DMSO)_2$ (blue lines). Their corresponding NH_2 bending fundamental region is shown in (a), while the NH stretching fundamental and NH_2 bending 0-2 overtone bands are shown in (b). The latter mode around 3220 cm^{-1} shows an impressive oscillator strength enhancement upon hydrogen bonding due to increased Fermi resonance coupling to the fundamental 0-1 NH stretching mode transitions. The NH stretching modes also show a notable absorbance enhancement upon hydrogen bonding. The sketch in (c) illustrates the transition dipole moment orientations of the normal modes (symmetric $\upsilon(NH_2)_S$, asymmetric $\upsilon(NH_2)_A$, NH_2 bending mode δ), and of the local NH stretching modes $\upsilon(NH)_1$ and $\upsilon(NH)_2$, which enclose an angle φ differing from the H-N-H bond angle 2 α.*

in the different molecular complexes compared to the transition dipole of the free NH stretching modes in An monomer. We obtain an enhancement of transition dipole strength for the single hydrogen-bonded NH stretching modes in An·DMSO as $\sqrt{2} \cdot \sqrt{(4.9 - 0.5)} = 3.0 \pm 0.2$ and for the double hydrogen-bonded NH stretching modes in An·$(DMSO)_2$ as $\sqrt{5.7} = 2.4 \pm 0.2$. The smaller increase for the double hydrogen-bonded amino group indicates a reduced NH··O hydrogen bond strength for the An·$(DMSO)_2$ species in comparison to the single hydrogen bond in An·DMSO. This conclusion is supported by thermodynamic analysis measuring linear IR spectra as a function of concentration and temperature in order to obtain the standard enthalpy change per hydrogen bond ΔH using the Van´t Hoff equation. Such analysis yields the enthalpy reduction per hydrogen bond largest for An·DMSO (-32.6 kJ/mol) and weaker for An·$(DMSO)_2$ (-27.5 kJ/mol), which proves the hydrogen bond in An·DMSO as the strongest. This can be understood by considering that the formation of a first hydrogen bond can polarize one NH bond most effectively, while a second hydrogen bond to the remaining free NH motif will be weaker because the second hydrogen atom will be more strongly associated to the (now more negative) N atom. Therefore, this second hydrogen atom will carry a smaller positive partial charge.

Figure 8.3 shows the linear overtone spectra in the region 6200-7000 cm^{-1} of the 0-2 NH stretching transitions decomposed into the spectral profiles of An monomer in CCl_4, An·DMSO complexes in CCl_4, and An·$(DMSO)_2$ complexes in DMSO. With increasing vibrational energy, the number of possibilities of reaching nearly energetic degeneracy between coupled various combination and

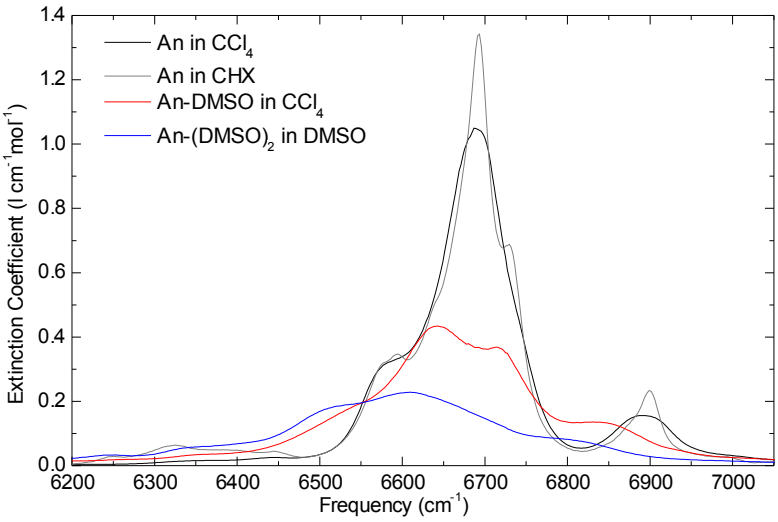

Figure 8.3: *Decomposed extinction coefficient spectra of An monomer (black line), An·DMSO (red line), and An·(DMSO)$_2$ (blue line) in the region of the 0-2 overtone NH stretching transitions. The enhanced line broadening combined with the multitude of overtone and combination states greatly complicates band assignments in the linear overtone spectra. The spectra of An monomer in cyclohexane (CHX, grey line) shows more fine structure due to reduced solvent-induced line broadening.*

overtone states greatly increases: considering only the NH_2 bending and NH stretching degrees of freedom, in the region of double-excited NH stretching states there are already 6 different possibilities of forming overtone and combination tone states. As such states appear line-broadened in Figure 8.3, their unambiguous mode assignment is extremely difficult. Only for An monomer is the peak assignment straightforward. The strongest 6692 cm^{-1} peak can be assigned to the symmetric NH stretching overtone $\upsilon(NH_2)_S^{0-2}$ and the 6892 cm^{-1} peak to the asymmetric NH stretching overtone $\upsilon(NH_2)_A^{0-2}$. The shoulder around 6579 cm^{-1} is tentatively ascribed to the 0-4 NH_2 bending overtone $\delta(NH_2)^{0-4}$. The reduced line broadening in the completely nonpolar cyclohexane (CHX) solvent allows the observation of additional substructure such as a shoulder at 6730 cm^{-1} that we assign to the combination mode $\upsilon(NH_2)_S + \upsilon(NH_2)_A$.

While the fundamental NH stretching transitions show a remarkable increase in integrated oscillator strength upon hydrogen bonding, it is quite the opposite for the first overtone region of NH stretching states as seen in Figure 8.3. Assuming that only NH stretching and bending degrees of freedom contribute in the first overtone region of NH stretching oscillators, the integrated absorbance in the 6200 - 7000 cm^{-1} region scales for An/An·DMSO/An·(DMSO)$_2$ as 1/0.76/0.52, and therefore decreases by about 25% per newly formed hydrogen bond. This observation is surprising since hydrogen bonding is expected to enhance the vibrational anharmonicity of NH stretching states, therefore making harmonically-forbidden overtone transitions more allowed. A calculation for hydrogen-bonded phenol complexes, expanding the potential energy surface up to third order in the XH stretching coordinate Q and truncating the dipole moment expansion $\mu(Q) = \mu_0 + \mu_1 Q + \mu_2 Q^2$ after the quadratic term (cf. equation (2.12)), was used to explain the enhanced oscillator strength in the fundamental NH stretching region. Both the linear μ_1 and quadratic μ_2 terms gave an enhanced positive contribution upon hydrogen bonding to the overall oscillator strength for the 0-1 transition to the single-excited XH stretching states. In contrast, a partial

cancellation was observed of these two contributions with the two terms showing for the 0-2 overtone transition an opposite sign, while hydrogen bonding increases the cancellation of both contributions [96]. This explains the opposite effects of hydrogen bonding on the linear cross section of single-quantum and two-quantum transitions in NH stretching oscillators.

8.3 Quantitative analysis of hydrogen bonding induced changes through excitonic modelling

Knowing the extinction coefficients of the monomeric, single-, and double-hydrogen bonded An species, we can provide a quantitative analysis of the spectral changes in the linear spectra induced by hydrogen bonding. An excitonic model will be constructed to reproduce the observed frequency shifts as well as the changes in oscillator strength upon hydrogen bonding in order to obtain the decoupled eigenenergies, eigenfunctions, coupling constants, and transition dipole vector orientations for the two single-excited NH stretching states and the bending overtone state.

Our excitonic model Hamiltonian, describing the states in the 3100-3600 cm^{-1} region, incorporates only three vibrational states, namely the two fundamental NH stretching states and the bending first overtone state with a mechanical coupling J between the amino NH stretching oscillators and a Fermi resonance coupling V between the fundamental NH stretching states and the NH_2 bending overtone state. We define a hybrid mode basis set, i.e. a mixture of local and normal mode states, consisting of the two one-quantum NH stretching local mode states $\left|\upsilon(NH)_1^1\right\rangle$ and $\left|\upsilon(NH)_2^1\right\rangle$ and the two-quantum NH_2 bending state $\left|\delta(NH_2)^2\right\rangle$ with the exponent specifying the number of quanta in the respective mode. In this basis $\{\left|\upsilon(NH)_1^1\right\rangle, \left|\upsilon(NH)_2^1\right\rangle, \left|\delta(NH_2)^2\right\rangle\}$, the coupling Hamiltonian is written as

$$H = \hbar \begin{pmatrix} \omega_1 & J & V \\ J & \omega_2 & V \\ V & V & \delta^{0-2} \end{pmatrix}. \tag{8.1}$$

The local mode approach for the NH stretching states is most appropriate for the An·DMSO complexes, where the diagonal frequency downshift of the hydrogen-bonded NH stretching oscillator leads to an effective decoupling of both NH stretching states, localizing the vibrational excitation.

Alternatively, we could use a purely normal mode basis set using the one-quantum symmetric $\left|\upsilon(NH_2)_S^1\right\rangle = \left(\left|\upsilon(NH)_1^1\right\rangle + \left|\upsilon(NH)_2^1\right\rangle\right)/\sqrt{2}$ and asymmetric $\left|\upsilon(NH_2)_A^1\right\rangle = \left(\left|\upsilon(NH)_1^1\right\rangle - \left|\upsilon(NH)_2^1\right\rangle\right)/\sqrt{2}$ NH stretching normal mode states and the $\upsilon = 2$ bending overtone mode. In this basis set $\{\left|\upsilon(NH_2)_S^1\right\rangle, \left|\upsilon(NH_2)_A^1\right\rangle, \left|\delta(NH_2)^2\right\rangle\}$ we obtain the coupling Hamiltonian as:

$$H = \hbar \begin{pmatrix} \omega_S & 0 & \sqrt{2}V \\ 0 & \omega_A & 0 \\ \sqrt{2}V & 0 & \delta^{0-2} \end{pmatrix} \tag{8.2}$$

Now the coupling of the $\left|\upsilon(NH_2)_A^1\right\rangle$ state to both the $\left|\upsilon(NH_2)_S^1\right\rangle$ and the $\left|\delta(NH_2)^2\right\rangle$ state is eliminated and the two decoupled local NH stretching modes are energetically degenerate with $\omega_1 = \omega_2 =: \omega_0$ and $\hbar\omega_S = \hbar\omega_0 + J$ and $\hbar\omega_A = \hbar\omega_0 - J$. The latter degeneracy is best fulfilled for the equivalent NH stretching oscillators in An monomers and An·$(DMSO)_2$ complexes.

Vibrational eigenenergies and the corresponding eigenstates are independent of the chosen basis set and are obtained by diagonalization of the coupling Hamiltonian (8.1) or (8.2). The coupling parameters J and V, the decoupled local NH stretching energies $\hbar\omega_0$, and the decoupled bending overtone eigenenergy $\hbar\delta^{0-2}$ (required to be smaller than twice the bending fundamental mode $2{\cdot}\delta(NH_2) = 3233$ cm^{-1}) are used as fit parameters to reproduce the observed center frequencies of the An monomer bands. This yields J = -51 cm^{-1}, V = -37 cm^{-1}, and ω_0 = 3429.5 cm^{-1}.

A similar coupling term J was found for the amino group in adenosine monomer (-56 cm^{-1}, cf. chapter 5). In chapter 5.4 and 6.5 we showed that the bilinear coupling terms J_{ij} (creating the splitting between symmetric and asymmetric eigenstates) and the coupling of the bending overtone to the NH stretching modes are dominated by their kinetic contributions, which were shown to depend exclusively on the Wilson G-matrix elements, which can be derived from the molecular structure. As the molecular An structure stays largely unaffected in the presence of hydrogen bonding, the coupling values J and V are also expected to stay roughly unchanged. Therefore, for the excitonic modeling of the linear spectra of An·DMSO and An·$(DMSO)_2$ complexes, the parameters J and V stay fixed at the values obtained from the An monomer calculations. In the case of An··DMSO, the energy of the decoupled $|\upsilon(NH)_2^1\rangle$ stretching states is kept at a value identical to that of An monomer, while the decoupled eigenenergy of the $|\upsilon(NH)_1^1\rangle$ mode is allowed to decrease by Δ_{HB}. In the case of An·$(DMSO)_2$, both decoupled local NH stretching eigenenergies are allowed to downshift by the same amount Δ'_{HB}. Apart from the hydrogen-bonding diagonal frequency downshift Δ_{HB}, Δ'_{HB}, the An·DMSO and An·$(DMSO)_2$ calculations each have only their respective decoupled bending overtone energy $\hbar\delta(NH_2)^{0-2}$ as a second fitting parameter.

Despite the simple excitonic ansatz, such an analysis reproduces the central vibrational band position with perfect agreement for the An monomer case and with only minor deviations ($\leq$ 6 cm^{-1}) for the An·DMSO and An·$(DMSO)_2$ complexes as shown in table 8.1. The extracted downshift Δ_{HB} of the NH stretching local mode frequency upon hydrogen bonding is stronger in An·DMSO (88 cm^{-1}) than in An·$(DMSO)_2$ (80 cm^{-1}), confirming that the hydrogen bond in An·DMSO is stronger than those in the An·$(DMSO)_2$ complex, in agreement with the kinetic and thermodynamic analysis above. The analysis also provides the vibrational eigenstates as a linear combination of the basis states $|\upsilon(NH)_1^1\rangle$, $|\upsilon(NH)_2^1\rangle$, and $|\delta(NH_2)^2\rangle$ (see supplement in ref [168]). The obtained eigenstates show the normal mode description to be a fairly good starting point for the description of An monomer and the double hydrogen-bonded complex An·$(DMSO)_2$. In particular, the NH stretching mode with the highest frequency is almost perfectly described by the asymmetric normal mode in An and An·$(DMSO)_2$. In contrast, the NH stretching excitations in An·DMSO are to a high degree (70-85%) localized on the free and hydrogen-bonded NH stretching oscillators. Especially for the single and double hydrogen-bonded An complexes, the $\upsilon = 2$ NH_2 bending state is strongly mixed with the NH stretching state at lower frequency ($|\upsilon(NH_2)_b\rangle$ or $|\upsilon(NH_2)_S\rangle$).

The transition dipole moments for transitions from the ground state to a certain endstate $\psi = a|\upsilon(NH)_1^1\rangle + b|\upsilon(NH)_2^1\rangle + c|\delta(NH_2)^2\rangle$ can be written as a sum of transition dipoles $\mu(NH)_1$, $\mu(NH)_2$ and $\mu(\delta^{0-2})$ with their respective amplitudes given by the amplitude factors a, b, c. Therefore, knowing the excitonic vibrational eigenstates, we can calculate their transition dipole moments and, hence, determine the integrated oscillator strength of the different transitions in the linear spectrum. The orientations of the transition dipole vectors $\mu(NH)_1$, $\mu(NH)_2$, and $\mu(\delta^{0-2})$ are defined in Figure 8.2 (c). Best agreement with the experimental data is obtained by assuming identical transition dipoles for the two free NH stretching modes in An monomer with a dark 0-2 (forbidden) bending overtone transition. The oscillator strength of the bending overtone is assumed to result exclusively from a partial transfer of oscillator strength due to Fermi-resonance mixing with the NH stretching states. Therefore, the following transition dipole vectors are associated to the basis set elements:

$$\begin{aligned} |\upsilon(NH)_1^1\rangle: &\quad \mu(NH)_1 = (cos(\alpha), sin(\alpha)); \\ |\upsilon(NH)_2^1\rangle: &\quad \mu(NH)_2 = (cos(\alpha), -sin(\alpha)); \\ |\delta(NH_2)^2\rangle: &\quad \mu(\delta^{0-2}) = (0,0). \end{aligned} \tag{8.3}$$

The angle 2α between the local NH stretching transition dipole vectors is estimated from the observed ratio 0.93 to 1 of the symmetric to asymmetric NH stretching peak intensities in the An monomer linear spectrum as $2\alpha = 89.2°$, i.e. much smaller than the H-N-H amino group

bonding angle. This strong angular deviation (also found for adenosine monomer, chapter 5) reflects the neglected contribution of CN stretching modes to the NH stretching modes. We can calculate the absorption intensities for the transitions in the 3100-3600 cm^{-1} spectral region of the linear spectra using both the detailed knowledge of the excitonic vibrational eigenstates (i.e. of the amplitudes a, b, c) obtained from diagonalization of the coupling Hamiltonian and the transition dipole moment enhancement factor for each hydrogen-bonded NH stretching mode from the evaluation of the linear spectrum above. The $\upsilon = 2$ NH_2 bending state in the An complexes with 0 and 2 hydrogen bonds shows mixing only with the symmetric NH stretching mode $|\upsilon(NH_2)_S\rangle$ at lower frequency. Therefore, the transition dipole vector of the bending overtone is aligned parallel to the symmetric stretching transition dipole vector, both oriented perpendicular to the asymmetric stretching transition dipole. For the An·DMSO complexes, there is a small deviation by 6° from the parallel alignment of bending overtone and $\upsilon(NH)_b$ transition dipole due to weak mixing with the free NH stretching mode $\upsilon(NH_2)_f$. In this case, the angle between both bending overtone and the fundamental $\upsilon(NH_2)_b$ transition dipoles to the free NH stretching mode $\upsilon(NH_2)_f$ transition dipole is predicted to differ significantly from 90° (calculated values are approximately 50°). These predicted relative transition dipole angles will be compared to the measured values obtained from polarization-dependent 2D-IR spectra below.

The quantitative agreement of the experimentally observed oscillator strengths with those predicted by the excitonic model gives a measure of the applicability and quality of the excitonic model. Figure 8.1 shows a comparison between the calculated and experimental parameters. Roughly 2/3 of the observed Fermi resonance-enhanced intensity of the NH_2 bending overtone in the single and double hydrogen-bonded complexes is reproduced in our calculations. A slight increase by a few wavenumbers in the coupling strength parameters J and V leads to quantitative agreement with the observed Fermi band intensity. The 1/3 discrepancy results mainly from contributions from other modes not contained in the model, particularly the combination mode $\upsilon(CC) + \delta(NH_2)$, which was found to be responsible for about a quarter of the Fermi band intensity in An monomer.

In summary, the excitonic model above provides a good description of the fundamental N-H stretching manifold using a hybrid mode representation consisting of two local N-H stretching states and the two-quantum NH_2 bending normal mode. With the extracted coupling parameters of J = -51 cm^{-1} between the two local N-H stretching modes and a Fermi resonance coupling value V = -37 cm^{-1}, we achieve a good agreement between the observed frequency positions and integrated band intensities of all investigated species. The frequency of the local N-H stretching mode shifts from ω_0 = 3429.5 cm^{-1} for An monomer to $\omega_0 - \Delta_{HB}$ = 3342 cm^{-1} for An·DMSO to $\omega_0 - \Delta'_{HB}$ = 3350 cm^{-1} for An·$(DMSO)_2$ as a consequence of hydrogen bonding. The eigenstates obtained by diagonalization of the coupling Hamiltonian reveal the normal mode picture as appropriate to first approximation for the N-H stretching manifold for An monomer and An·$(DMSO)_2$, but not for the single-hydrogen bonded An·DMSO complex.

8.4 NH stretching overtone manifold revealed by 2D-IR spectra

In principle, the linear overtone spectra in the region 6200-7000 cm^{-1} presented above contains all information about the energy level scheme of the double-excited NH stretching state manifold. As discussed above, in practice the decreasing overtone cross section of stretching transitions upon hydrogen bonding, combined with a significant band broadening, makes an unambiguous band assignment impossible. Therefore, we have recorded polarization-dependent 2D-IR spectra for three samples (each dominated by a single species) in ZZZZ and ZZXX polarization geometry at a fixed waiting time τ_2 of 125 fs, which exceeds the cross-correlation pulse width in order to suppress coherent artifact signals from mixed pulse interaction sequences that occur during pulse overlap. The 2D-IR spectra, each scaled to the maximum peak intensity, are plotted in Figure 8.4. As

	An		**An·DMSO**		**An·(DMSO)$_2$**	
Mode	Exp.	Calc.	Exp.	Calc.	Exp.	Calc.
$\upsilon(NH_2)_A/\upsilon(NH_2)_f$	3481 (0.96)	3481 (0.986)	3461 (2.24)	3454.7 (2.10)	3402 (4.47)	3401 (5.62)
$\upsilon(NH_2)_S/\upsilon(NH_2)_b$	3396 (0.90)	3395 (0.919)	3344 (5.2)	3344 (6.22)	3337 (3.5)	3340 (3.55)
δ^{0-2}	3216 (0.11)	3216 (0.095)	3227 (2.34)	3227 (1.49)	3233 (3.43)	3233 (2.23)
$\delta + \upsilon(CC)$	3187 (0.03)					
Transition Dipole Enhancement Factors						
$\mu(NH)_b$	(1.00)		2.97		2.39	
Excitonic Model Fitting Parameters						
Fixed by An Monomer Calculations						
$\upsilon(NH)_{local}(cm^{-1})$		3429.5				
J (cm^{-1})		-51				
V (cm^{-1})		-37				
$2\alpha(^\circ)$		89.2				
Parameters Varied for all Species						
$\delta(NH_2)^{0-2}$	3233 (=2 $\delta(NH_2)$)	3233	3258 (=2 $\delta(NH_2)$)	3255	3282 (=2 $\delta(NH_2)$)	3274
Δ_{HB}		(0)		88		80

Table 8.1: *Comparison between experimental data and excitonic model calculations for the linear IR spectra of An monomer, An·DMSO, and An·(DMSO)$_2$. The values in parenthesis give the integrated band intensities normalized to the intensity of the NH stretching modes in An monomer. For more details see the text.*

the decomposition of the linear spectra showed (Figure 8.1), An in pure CCl_4 contains exclusively nonhydrogen-bonded monomeric An molecules, while in pure DMSO roughly 90% of An exists as An·(DMSO)$_2$ complex. For the analysis of the single-hydrogen bonded An·DMSO complexes, we have chosen a ternary mixture of 0.4 M An and 0.7 M DMSO in CCl_4, which contains about 36 % An, 60 % An·DMSO, and 4% An·(DMSO)$_2$ complexes. Although the An·DMSO concentration is maximized at higher DMSO concentrations, the chosen concentrations fulfill the demand for a large fraction of An·DMSO complexes with a reasonably low concentration of double hydrogen-bonded An·(DMSO)$_2$ complexes. The latter tend to dominate the third-order response quickly because of their enhanced transition dipoles due to hydrogen bonding.

The cross sections of the 2D signal in Figure 8.4 along the frequency diagonal reflect the peak maxima in the linear spectrum with each 2D spectra being dominated by a single species (which is An monomer in panels (a-0, b-0), An·DMSO in panels (c-1, d-1), and An·(DMSO)$_2$ in panels (e-2, f-2)). The enhancement in NH stretching oscillator strength upon hydrogen bonding is confirmed by the 2D-IR spectra. Moreover, they reveal the existence of cross peaks between the Fermi resonance enhanced bending overtone state and *both* NH stretching modes in all complexes. As dipole-dipole coupling can be ruled out as mechanism for the interaction between two modes with perpendicular transition dipole moment, the coupling between the Fermi band and the asymmetric NH stretching mode at highest frequency is of mainly mechanical origin ("through bond coupling"). In addition, it is important to note that all diagonal peaks show "standard" cross peaks with positive sign at the crossing point of their diagonal peak frequencies. A recent introductory textbook [46] on

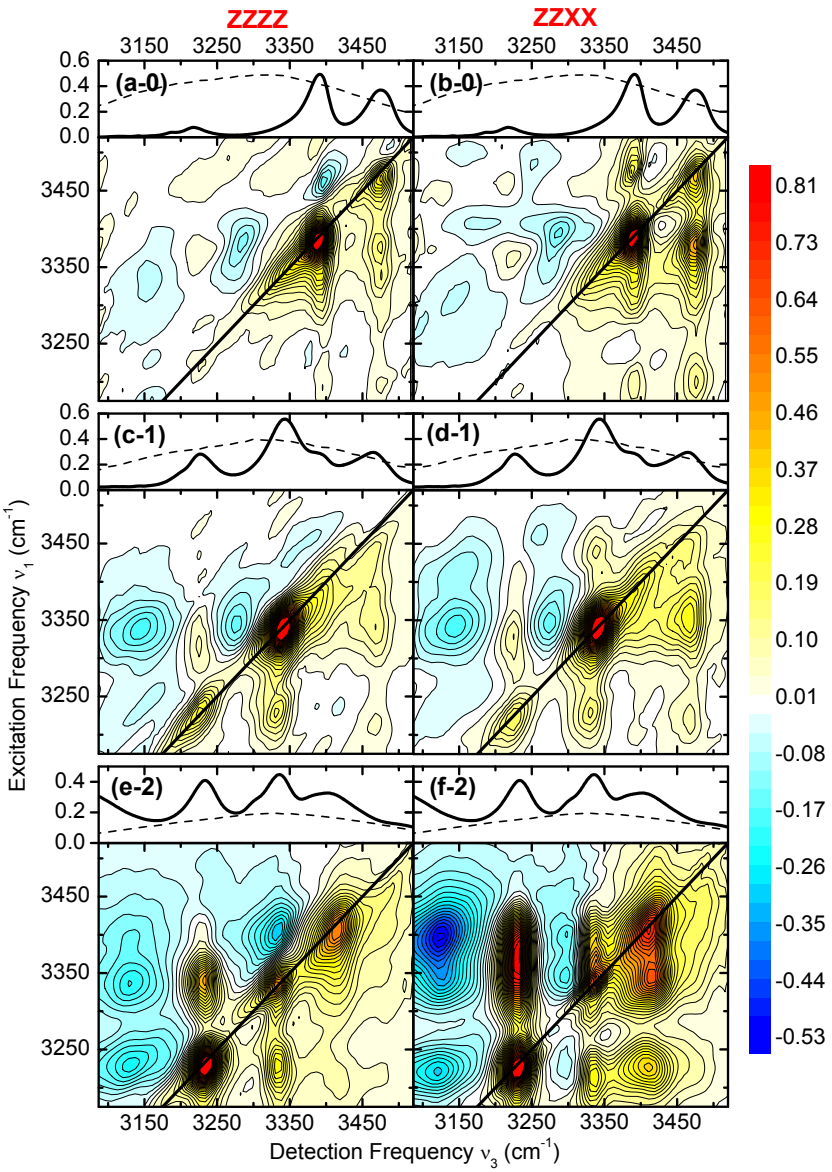

Figure 8.4: *Absorptive 2D-IR spectra in the NH stretching region for samples with 0.7 M An in CCl_4 (a-0, b-0; containing only An monomer), 0.4 M An and 0.7 M DMSO in CCl_4 (c-1, d-1; dominated by An·DMSO (60%)), and 0.4 M An in DMSO (e-2, f-2; dominated by An·$(DMSO)_2$ (90%)). The left and right columns show measurements in ZZZZ and ZZXX polarization geometry, respectively, each at waiting time of 125 fs. Above each 2D spectrum, the corresponding linear IR spectrum is shown together with the intensity profile of the used laser pulses.*

2D-IR predicted, based on a simple harmonic oscillator approach, distinct cross peak pattern with inverted sign for Fermi resonances, which contrasts with our experimental observations.

The 2D-IR spectra for An monomer in ZZZZ polarization geometry (panel (a-0)) exhibits two strong excited state signals (ESA, with negative sign, blue contours) at $(\upsilon_1(cm^{-1}, \upsilon_3(cm^{-1}) =$ (3380,3280) and (3455,3395) arising from excitation pathways entering the NH stretching overtone states. This gives anharmonicities of $D_S = 115$ cm^{-1} and $D_A = 85$ cm^{-1} for the symmetric and

asymmetric stretching modes, respectively, which are slightly higher than values found for adenosine mononer (chapter 5). The two diagonal peaks at $\upsilon_1 = \upsilon_3 = 3387$ and 3476 cm^{-1}, corresponding to the symmetric and asymmetric NH stretching normal modes, show two strong positive cross peaks at (3465,3385) and (3385,3475) in the ZZXX measurement, the latter peak becoming enhanced by roughly a factor of three compared to the 3387 cm^{-1} diagonal peak for the perpendicular polarization condition. Such an increase in cross-to-diagonal peak intensity is in agreement with the expected perpendicular orientation of both normal modes. The intensity of the (3465,3385) cross peak is weaker than its equivalent below the diagonal due to a strong overlap with the excited state peak of the asymmetric stretching mode visible only in the ZZZZ spectrum. In addition, even though the intensity of the Fermi bending overtone diagonal signal barely exceeds the noise limit, we observe cross peaks between the two NH stretching normal modes and the Fermi band, which become enhanced in the ZZXX polarization spectrum.

The 2D-IR spectra of An·DMSO and An·$(DMSO)_2$ complexes in (c-1,d-1) and (e-2,f-2), respectively, show enhanced signal-to-noise ratios due to the transition dipole increase for the hydrogen-bonded NH stretching modes. Below the diagonal, we can clearly identify positive cross peaks between all transitions. The changes in cross-to-diagonal peak intensities with polarization confirm for both complexes approximately parallel transition dipoles of the bending overtone Fermi band $\mu(\delta^{0-2})$ and the NH stretching transition at lowest frequency. Moreover, both of these transitions appear more or less perpendicular to the NH stretching mode at highest frequency, as reflected by the increase in cross-to-diagonal intensity ratio by a factor of 3-4 when going from ZZZZ to ZZXX polarization geometry. These relative orientations are in agreement with the predicted angles from the excitonic model analysis, considering the experimental error margins.

For all species, the positive cross peak between the two NH stretching modes above the diagonal is superimposed by the negative exited state absorption peak of the upper NH stretching state, which dominates over the positive cross peak in the ZZZZ measurements. The relative intensity increase of the positive cross peak in the ZZXX 2D spectrum leads to a cancellation of the negative ESA peak to a large extent. The obtained diagonal anharmonicities for the upper NH stretching mode of ≈ 80 cm^{-1} for the single and double hydrogen-bonded complexes are similar to the value in An monomer. The ESA peak of the lower (hydrogen-bonded) NH stretching mode $\upsilon(NH_2)_b$ at (3344,3274) in An··DMSO implies a ≈ 70 cm^{-1} diagonal anharmonic shift, significantly smaller than the $D_S = 115$ cm^{-1} shift in An monomer. We do not observe an increase in diagonal anharmonicity for the hydrogen-bonded NH stretching modes as compared to the nonhydrogen-bonded modes, but partially even a clear reduction in diagonal anharmonicity. This observation may appear to conflict with the generally observed trend of increasing *local mode* anharmonicity upon increased hydrogen bonding interactions [290]. However, realize that we observe *diagonal* anharmonicities, which reflect the influence of both the local mode decoupled anharmonicities and the intermode coupling strengths affecting the single and double-excited NH stretching energy levels (see section 2.1 and the local vs. normal mode discussion in chapter 5). The interplay of both aspects may lead to highly unpredictable values for the diagonal anharmonicities. We could not identify the lower NH stretching ESA peak in An·$(DMSO)_2$.

For An·$(DMSO)_2$, we observe the diagonal Fermi resonance enhanced NH_2 bending overtone as the most intense feature. Moreover, the overtone ESA peak at (3233,3125) arising from transitions from the two-quantum $\delta(NH_2)^2$ state to the four-quantum $\delta(NH_2)^4$ state is prominent, while it is hardly noticeable for the An·DMSO complex. This reflects the significant transition dipole enhancement of the bending overtone states due to increased mode mixing with hydrogen-bonded NH stretching states, the formation of the second hydrogen bond, and the nonlinear nature of the 2D-IR experiment.

It its interesting to compare results of the 2D spectra with those of the linear overtone spectra. Peaks with negative sign in the 2D spectra correspond to sequential single-quantum excitation

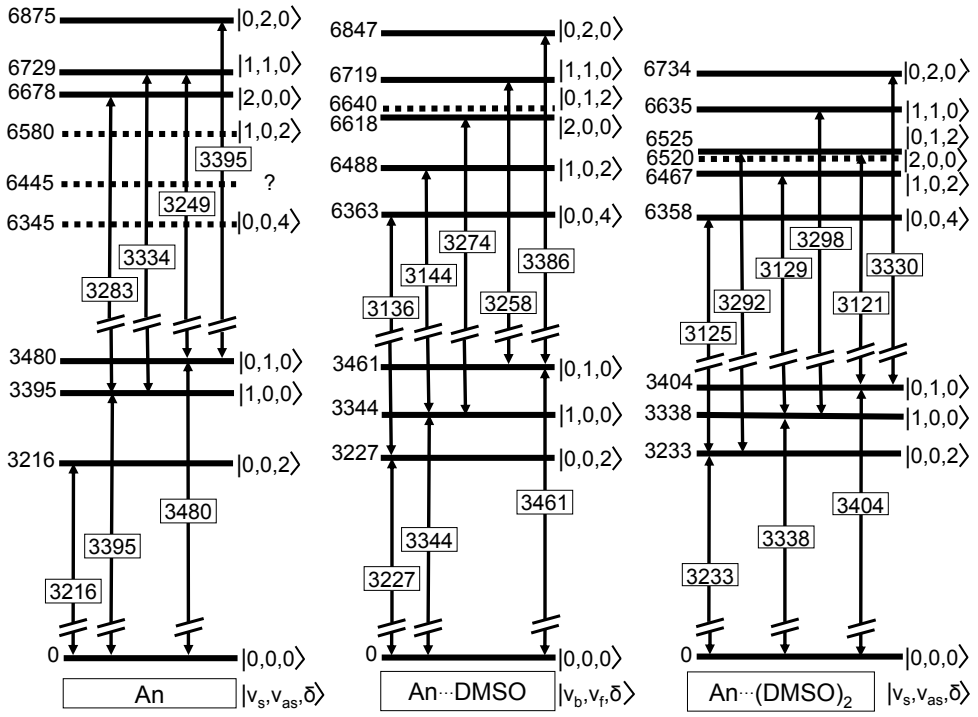

Figure 8.5: *Energy level scheme for An, An·DMSO, and An·(DMSO)$_2$. Those levels extracted from the polarization-dependent 2D-IR spectra are show as solid with the arrows indicating the transition frequencies, while levels identified through the linear overtone spectra are illustrated with dotted lines. The states are labeled with the number of quanta in the corresponding modes, reflecting the dominant wavefunction contributions.*

pathways accessing overtone and combination states with the third field interaction. In contrast, linear overtone spectroscopy creates amplitude on the same endstates through a direct transition with a single photon. Therefore, nonlinear 2D spectra and linear overtone spectra contain complementary information on overtone states. However, the intensity of their spectral signatures will be significantly different. In contrast to linear overtone spectra, 2D spectroscopy provides more reliable and precise information on the energy level scheme with the polarization dependence of 2D spectra being a helpful tool for peak assignments. The overall dramatically reduced ambiguity is of particular relevance for higher excited states, because the number of energy levels leading to Fermi resonances dramatically increases with the total vibrational energy.

Six energy levels due to overtone and combination modes of the NH stretching and NH_2 bending modes are expected in the first NH stretching overtone region. With the assignment of peaks in the 2D spectra above, we can construct the energy level scheme of the single- and double-excited NH stretching excitations, including the bending overtone states in the different molecular species. Figure 8.5 shows the level scheme for An monomer, An·DMSO, and An·(DMSO)$_2$ as extracted from the linear IR and nonlinear 2D spectra. The corresponding transitions identified through the 2D spectra are indicated with arrows. The single-excited NH stretching manifold and the first bending overtone states are most accurately determined from the linear spectra. In none of the three molecular species were we able to extract all six states in the first NH stretching overtone region from the 2D-IR spectra alone. For An monomer, we could identify only the over and combination tone states with purely NH stretching mode character, while limited mixing with bending overtone states prevented detection of states with bending mode character due to their

minute signal intensities.

The states in Figure 8.5 are labeled with the number of quanta in the normal modes $|\upsilon(NH_2)_S$, $\upsilon(NH_2)_A$, $\delta(NH_2)$ for An monomer and An·$(DMSO)_2$, while the different states are represented by the degree of excitation in the modes $|\upsilon(NH_2)_b, \upsilon(NH_2)_f, \delta(NH_2)\rangle$ for An·DMSO. As noted before, such labeling indicates only the dominant wave function components, while the relative contribution of these components can vary and mixing with other modes may be substantial. The excitonic approach for the single-excited NH stretching manifold described above yielded good agreement with the linear spectra and provided couplings, decoupled local mode frequencies, and the detailed eigenstate wavefunctions. A similar approach on the NH stretching overtone manifold could in principle reveal diagonal and off-diagonal local mode anharmonicities as well as the overtone eigenstates. However, we refrain from such an analysis: even in the 2D spectra the high density of overtone states, leading to spectral overlap, combined with partially too low signal intensities prevents the identification of all states with a precision necessary for highly reliable results. Considering the high number of unknown parameters (6 local mode anharmonicities + 6 decoupled local mode transition frequencies) as well as the uncertainties about the correct coupling Hamiltonian, we skip such an excitonic approach for the NH stretching overtone manifold.

For An monomer, the linear overtone and 2D-IR spectra give agreeing results on the spectral position of the symmetric (6689 vs 6678 cm^{-1}) and asymmetric (6892 vs 6875 cm^{-1}) NH stretching first overtone state considering the experimental accuracy (for each method $\approx \pm$ 10 cm^{-1}). As expected, the relative intensities of the 0-2 symmetric and asymmetric stretching overtone band in the linear spectra greatly differ from the relative intensity of the corresponding excited state absorption peaks in the 2D spectrum. The combination level $\upsilon(NH_2)_S + \upsilon(NH_2)_A$ is clearly identified through the 2D spectra at 6729 cm^{-1} but not obvious in the linear overtone spectra for An in CCl_4. However, the reduced line broadening for An in cyclohexane (CHX) allows one to observe a local maxima at a very similar position (6730 cm^{-1}). The assignment of these three bands is consistent with previous results [301]. The remaining three unidentified energy levels in the 2D spectra of An monomer can be tentatively assigned through the linear overtone spectra in Figure 8.3 and are added as dashed lines in Figure 8.5. The three peaks at 6580 cm^{-1} (strong), 6445 cm^{-1} (weak), and 6345 cm^{-1} (weak) in the linear overtone spectra are ascribed to the An states $|\upsilon(NH_2)_S, \upsilon(NH_2)_A, \delta(NH_2)\rangle = |0,1,2\rangle$, $|1,0,2\rangle$, and $|0,0,4\rangle$, respectively, although this assignment is ambiguous.

The reduction in oscillator strength of overtone transitions upon hydrogen bonding combined with a spectrally more dense mode structure in the single-excited NH stretching manifold of the hydrogen-bonded complexes (resulting in increased spectral overlap) complicates the assignments of overtone and combination tone states for the An·DMSO and An·$(DMSO)_2$ species in their linear overtone spectra. The energy level of the $|\upsilon(NH_2)_b, \upsilon(NH_2)_f, \delta(NH_2)\rangle = |0,1,2\rangle$ state in An·DMSO complexes, which was not clearly identified in the 2D-IR spectra, is attributed to the peak at 6640 cm^{-1} in the linear overtone spectrum. Actually, this assignment is consistent with the observation of very weak features with negative sign in the 2D-IR spectra at (3452,3160) and (3238,3419). The $|2,0,0\rangle$ state for An·$(DMSO)_2$ was not identified in the 2D spectra, but is tentatively assigned to the shoulder at 6520 cm^{-1} in the linear overtone spectra. This predicts an excited state absorption peak at (3338,3182) and, hence, two partly overlapping negative peaks contributing to the (3338,3129) negative peak in the An·$(DMSO)_2$ 2D-IR spectrum.

8.5 Conclusions

Stimulated by our indications of significant Fermi resonance contributions for the line shapes of A·T base pairs, we have analyzed the effect of hydrogen bonding on the single- and double-excited NH stretching manifold in aniline-d5. This revealed a dramatic increase in the oscillator strength

of the NH_2 bending first overtone transition upon hydrogen-bonding to DMSO due to a Fermi resonance with the NH stretching levels. For the first time, the magnitude of this Fermi resonance effect and the NH stretching transition dipole enhancement due to hydrogen bond formation has been experimentally quantified for the single and double hydrogen-bonded complexes of An with DMSO. Decomposing the linear spectra into contributions from monomeric An, An·DMSO, and An·$(DMSO)_2$, we observed an increase in integrated oscillator strength for transitions into the one-quantum NH stretching manifold by a factor 4.9 and 5.7 in the presence of one and two hydrogen bonds, respectively, while the integrated absorbance of the NH_2 bending first overtone grows by a factor of 17 and 24, respectively.

The origin of this dramatic Fermi resonance enhancement was quantitatively captured with an excitonic model using only the two local NH stretching modes and the NH_2 bending first overtone mode, revealing a mechanical coupling of J = -55 cm^{-1} between the two NH stretching modes and a Fermi resonance coupling between the NH stretching states and the first bending overtone state of V = -37 cm^{-1}. The extracted redshift Δ_{HB} of the local single-excited NH stretching modes was determined to be slightly larger for An·DMSO (Δ_{HB} = 88 cm^{-1}) than for An·$(DMSO)_2$ (Δ_{HB} = 80 cm^{-1}), signifying a slightly stronger hydrogen bond for the single hydrogen-bonded complexes. Diagonalization of the coupling Hamiltonian yielded the eigenstate wavefunctions, demonstrating that the single-excited NH stretching manifold in An monomer and An·$(DMSO)_2$ can be appropriately described through normal modes of symmetric and asymmetric NH stretching and NH_2 bending modes. In contrast, the formation of a single hydrogen bond leads to an effective decoupling of both NH stretching modes, leading to the local mode picture of free and hydrogen-bonded NH stretching modes in An·DMSO complexes. The oscillator strength increase and frequency red-shift of the NH stretching modes upon hydrogen bonding combined with the frequency upshift of the NH_2 bending overtone was found to lead to enhanced mode mixing between the (basically dark) bending overtone state and the one-quantum NH stretching states and was used to explain quantitatively the strong increase in bending overtone absorption strength in the An·DMSO and An·$(DMSO)_2$ complexes. At the same time, a moderate decrease in the cross section of the 0-2 first overtone NH stretching transitions upon hydrogen bonding was observed.

We also demonstrated the potential of 2D-IR spectroscopy for analysis of the overtone levels in large molecules in the liquid phase. Most overtone levels in the NH stretching overtone manifold of An, An·DMSO, and An·$(DMSO)_2$ complexes were unambiguously determined from the peaks in the 2D-IR spectra, which arise from sequential single-quantum transitions along the various Feynman pathways. In contrast, linear overtone spectra did not allow for unambiguous state assignments and suffered from highly overlapping states and low signal strength of the harmonically-forbidden multiquantum transitions sampled in linear overtone spectra. Polarization-dependent 2D-IR spectra were used to support the relative orientations of the various transition dipole vectors predicted by the excitonic model. Moreover, the 2D-IR spectra demonstrated that Fermi resonance multiplets exhibit a 2D-IR signature that is indistinguishable (except for the parallel transition dipole) from conventional coupled fundamental transitions. The results of this section suggest that hydrogen bonding can indeed cause overtone vibrations to become dominant spectral features, which supports our previous conclusion that Fermi resonance contributions are significant for the line shapes of A·T base pairs.

8.6 Outlook: Vibrational relaxation pathways in aniline-d5 and its hydrogen-bonded complexes with DMSO

So far, in this chapter we have used linear and nonlinear 2D-IR spectroscopy to gain insight into vibrational couplings and anharmonicities, i.e., properties of the potential energy surface of An monomers and hydrogen-bonded complexes with DMSO. The magnitude of couplings within NH_2

stretching and bending excitations and couplings with other intramolecular degrees of freedom are reflected in the vibrational energy flow pathways, which are best deciphered with ultrafast vibrational pump-probe and 2D-IR spectroscopy. Fermi resonances with bending overtones have been postulated to play a key role in the vibrational energy redistribution of hydrogen stretching oscillators, ranging from CH stretching modes in organic molecules [103] to OH stretching modes in liquid water [104].

We have studied the population kinetics of the NH stretching excitations, the NH_2 bending fundamental band (1617-1641 cm^{-1}), and the $\upsilon(CC)$ ring mode (1573 cm^{-1}) through single and two-colour pump-probe measurements. Whereas for An monomer the NH stretching lifetime is 5.5 ps, it shortens to 0.6-0.9 ps in An·$(DMSO)_2$ (see Figure 8.6 (a)). We have not found such a significant lifetime shortening for the NH_2 bending fundamental mode, which varies from 0.6 ps in An to 0.4 ps in An·$(DMSO)_2$. For An monomer, we find a drastically decelerated decay of the transient absorption of the NH_2 bending mode with a 6 ps time constant after exciting the NH stretching modes. Interestingly, for An·$(DMSO)_2$ we observe a delayed rise in the response of both the NH_2 bending mode and (even further delayed) the $\upsilon(CC)$ ring mode upon pump excitation of the Fermi resonance enhanced NH_2 bending overtone (Figure 8.6 (b,c)). The delay becomes even more evident when pumping only the NH stretching modes. These findings seem to suggest that vibrational energy deactivation proceeds from the fundamental NH stretching states via the NH_2 bending first overtone to the fundamental NH_2 bending state and finally over the $\upsilon(CC)$ ring stretching state. The initial ultrafast energy transfer from the upper NH stretching mode to the NH_2 bending overtone mode mode can be followed with 2D-IR spectroscopy.

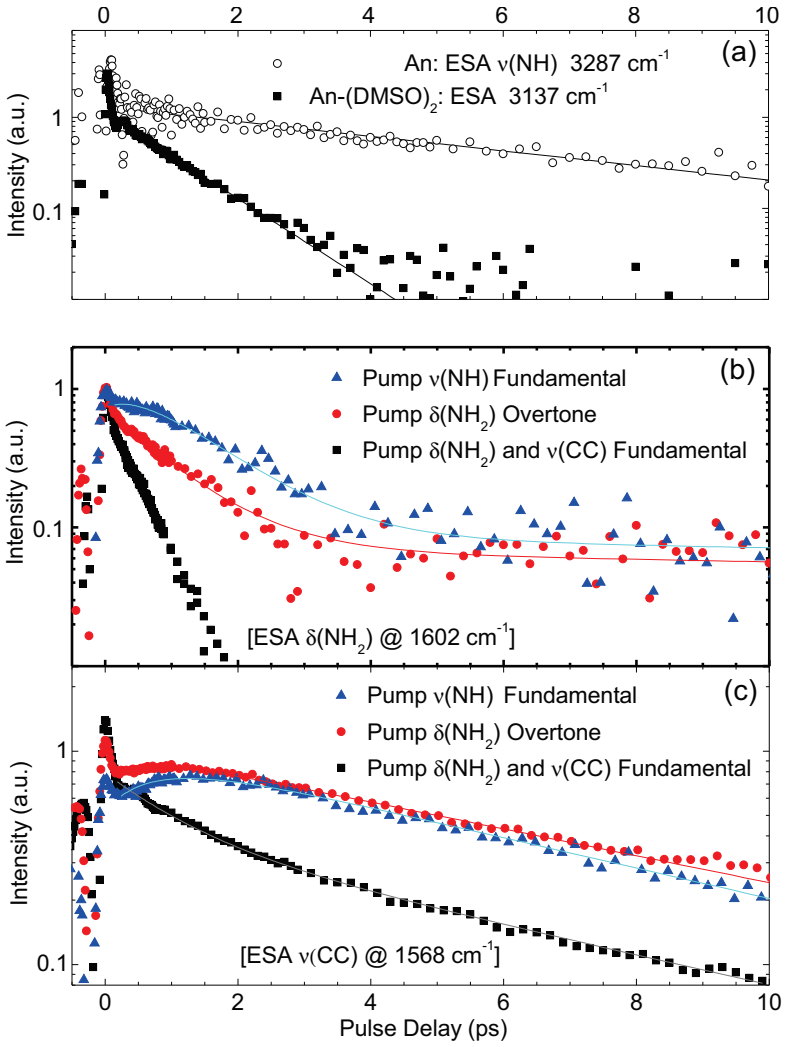

Figure 8.6: *(a) Semi-logarithmic plot of the kinetic pump-probe response for the NH stretching excited state absorption (ESA) signal (3287 cm^{-1}) in An monomer and the ESA signal at 3137 cm^{-1} in An·$(DMSO)_2$ upon simultaneous excitation of the NH stretching and NH_2 bending overtone. (b) Population kinetics of the NH_2 bending ESA signal (1602 cm^{-1}) on semi-logarithmic scale when pumping the NH stretching states (blue symbols), the NH_2 bending overtone state (red symbols), or directly the NH_2 bending fundamental and $\upsilon(CC)$ ring mode (black symbols) in An·$(DMSO)_2$ complexes. (c) The same as in (b) with probing of the ESA response of the $\upsilon(CC)$ ring mode (1568 cm^{-1}).*

9 Summary

This work contributes to a deeper understanding of the vibrational potential energy surface and ultrafast vibrational dynamics of DNA. Excitations of NH stretching vibrations were used as sensitive local probes for hydrogen bonding, vibrational intra- and interbase couplings, energy relaxation, and dynamical changes in the environment in linear and ultrafast nonlinear infrared (IR) pump-probe and - most importantly - two-dimensional photon echo experiments. The latter sample vibrational coherence dynamics along two different evolution periods in order to correlate vibrational excitation frequencies with their detection frequencies at a later time. The experiments were supported by exciton model and quantum chemical ab initio calculations. The DNA constituents were analyzed at variable levels of molecular complexity to quantify the impact of interbase hydrogen bonding and mode couplings separately from the influence of vertical stacking interactions and hydrating water molecules in double-helical DNA. First, the NH stretching excitations in isolated nucleobase monomers adenosine and thymidine in nonpolar waterfree solution were analyzed. These measurements served as a reference for the study of various hydrogen bonding effects in adenosine-thymidine nucleobase pairs. A study of double-helical hydrated guanine-cytosine oligomer films enabled to analyze the effect of hydration and nucleobase stacking on vibrational line shapes and dynamics, while providing additional insight into ultrafast structural fluctuations in the water shell and the water shell's role in vibrational relaxation. Moreover, the hydrogen bonding induced enhancement of Fermi resonances was quantitatively studied in ternary mixtures of aniline, DMSO, and CCl_4.

Adenosine and thymidine nucleobase monomers

The monomeric nucleobases adenosine and thymidine in chloroform solution are used to analyze the NH stretching modes in the absence of hydrogen bonding. In adenosine, H/D exchange experiments show that the NH stretching states in the amino group exhibit a mechanical coupling of J_H = -56 cm^{-1}, which is dominated by the kinetic coupling contribution and increases to J_D= -77 cm^{-1} for the ND stretching modes in the deuterated amino group. Linear vibrational spectra of partially deuterated adenosine reveal the symmetric and asymmetric normal NH stretching modes as the correct eigenfunctions for the single-excited states. In contrast, the energy positions of the two-exciton states, as provided by the 2D-IR spectra, in combination with an excitonic coupling model show the double-excited states as intermediate between the local and normal mode case through the interplay of mechanical coupling J_H and local mode diagonal (Δ_0 = 135 cm^{-1}) and combination mode anharmonicities (Δ_C = 14 cm^{-1}). The 2D-IR spectra show no signatures of population transfer and spectral diffusion on the picosecond time scale. Pump-probe measurements show population lifetimes of the symmetric and asymmetric NH stretching modes in adenosine of $\approx$ 6 and 10 ps, respectively, and reveal underdamped quantum beats due to simultaneous coherent excitation of both modes with the beating dephasing on a time scale of a few picoseconds. The single NH stretching mode of the thymidine monomer shows a diagonal anharmonicity of 150 cm^{-1} with a shorter population lifetime of 0.9 ps, possibly due to vibrational energy relaxation via the carbonyl overtone.

Hydrogen-bonded adenosine-thymidine nucleobase pairs

The formation of hydrogen-bonded adenosine-thymidine nucleobase pairs in chloroform solution leads to pronounced changes in vibrational line shapes and population kinetics in the NH stretching manifold. Hydrogen bonding leads to a red-shift of the involved NH stretching oscillator frequencies, forming 5-6 major bands in the 2400-3500 cm^{-1} region. As indicated by ^{1}H NMR

measurements and ab initio calculations, all four double hydrogen-bonded A·T pairing geometries, that is Watson-Crick, reverse Watson-Crick, Hoogsteen, and reverse Hoogsteen, occur in solution with similar abundance. Their spectroscopic and structural properties are very similar with only minor differences in hydrogen stretching frequencies, cross sections, vibrational couplings, and anharmonicities, as evidenced by 2D-IR cross peak patterns, pump-probe measurements and Hartree-Fock calculations. All NH stretching oscillators are found to be anharmonically coupled either by mechanical through-bond or interbase dipole-dipole couplings between thymidine and adenosine NH stretching modes.

Hydrogen bonding is found to induce anharmonic couplings of NH stretching modes to a low-frequency hydrogen bond mode at $\approx$ 100 cm^{-1} (indicated by underdamped beatings in the pump-probe transients), which results in the formation of vibrational sidebands contributing to line broadening in the 2400-3000 cm^{-1} region. The red-shift of NH stretching frequencies leads to enhanced mixing with fingerprint overtone and combination tone modes (Fermi resonances), in particular involving the NH_2 bending mode. Incorporating both effects enables a qualitative understanding of the high number of A·T dimer-associated vibrational bands, which exceeds the number of local NH stretching modes. Although the NH stretching modes in the adenosine amino group are effectively decoupled from each other due to hydrogen bonding, mixing with fingerprint and low-frequency degrees of freedom slightly limits the validity of the local mode picture for the NH stretching manifold of A·T base pairs.

A significant hydrogen-bonding induced population lifetime shortening due to the increase in effective coupling with fingerprint degrees of freedom is observed in the pump-probe transients. While the nonhydrogen-bonded $\upsilon_A(NH_2)_f$ mode exhibits a 2.1 ps lifetime, the lifetime of hydrogen-bonded NH stretching modes $\upsilon_T(NH)_b$ and $\upsilon_A(NH_2)_b$ is determined as 0.2 - 0.4 ps. The 2D spectra reveal an ultrafast vibrational excitation transfer from the 3330 cm^{-1} to the 3200 cm^{-1} mode. All NH stretching bands are found to be highly inhomogeneously broadened, which indicates a heterogeneous distribution of hydrogen bond lengths in the A·T base pairs or different local environments. Fluctuations in the hydrogen-bonding geometries are negligible on the picosecond time scale as displayed by the static inhomogeneous 2D lineshape.

Hydrated guanine-cytosine base pairs in double-helical DNA

A study of artificial DNA oligomers containing 23 guanine-cytosine (G·C) base pairs in Watson-Crick geometry at variable water content in comparison to measurements on isolated G·C base pairs in chloroform solution shows that the presence of the double-helix structure in combination with already a few hydrating water molecules has a notable impact on vibrational line shapes and dynamics.

At a low water content of about 4 water molecules per base pair, contributions from the base pair NH stretching modes dominate the 2D-IR spectra. Highly inhomogeneous line shapes reflect a high degree of structural inhomogeneity. There is no ultrafast spectral diffusion of the NH stretching modes and the OH stretching excitations of the residual most tightly bound water molecules, which evidences fairly rigid G·C base pair and DNA-water structures. Weak interbase "horizontal" vibrational couplings between NH stretching oscillators in the hydrogen-bonded G·C pairs are found, while there are no indications for notable intrastrand "vertical" couplings between the NH stretching modes of stacked nucleobase pairs. T_1 population times are measured as 200-300 fs, in agreement with observations of hydrogen-bonded NH stretching modes in the isolated nucleobases, but without major changes over the NH stretching spectral region. Neither the linear nor the 2D-IR measurements show evidence of a pronounced free NH stretching mode, as indicated by the absence of distinct diagonal and cross peaks and the absence of a significantly enhanced T_1 lifetime at the spectral positions expected for nonhydrogen bonded NH stretching modes. The conclusion is drawn that already at low humidity several of the "free" NH motifs in the base amino

groups are hydrogen-bonded to water, which shows the high water affinity of polar groups in major and minor groove positions. The decrease in energy difference of the decoupled local NH stretching modes in the amino groups creates party delocalized eigenstates with a mode character intermediate between local and normal modes.

At a high water content of more than 20 water molecules per base pair, the 2D spectra show an additive, dominating contribution of water shell OH stretching modes, while the NH stretching excitations are largely unchanged. Therefore, the formation of a fully occupied first hydration shell with few water molecules in outer shell positions has minor impact on interbase hydrogen bonding and vibrational coupling within the NH stretching excitations. A 250 fs decay of the OH stretching frequency-fluctuation correlation function is observed through the dynamic reshaping of the 2D spectra, which is slowed down compared to the sub-100 fs fast decay found in bulk water. This decelerated decay is attributed to reduced structural fluctuations in the water shell due to strong interactions with the DNA interface and steric constraints, to a reduction in resonant intermolecular energy transfer rate, and to the formation of a vibrationally heated ground state in the water shell created in the process of vibrational cooling. The formation of the hot ground state on the femtosecond time scale points to the important role of the hydration shell as an efficient heat sink for high-energy vibrational excitations.

Fermi resonance enhancement upon hydrogen bonding in aniline-d5

In order to quantitatively study the Fermi resonance effect of the NH_2 bending overtone with fundamental NH stretching modes, aniline-d5 (An) hydrogen-bonded to 0, 1, and 2 DMSO molecules was analyzed. Hydrogen bonding of the amino NH_2 motifs to one or even two DMSO molecules leads to a significant increase in integrated oscillator strength of the NH stretching transitions, which nonetheless pales in comparison to the increase in the absorption strength of the NH_2 bending first overtone. The dramatic Fermi resonance enhancement was quantitatively captured with an excitonic model using only the two local NH stretching modes and the NH_2 bending first overtone mode. Thereby, a mechanical coupling between the two NH stretching modes of J = -55 cm^{-1} and a Fermi resonance coupling between the NH stretching states and the first bending overtone state of V = -37 cm^{-1} is revealed. The oscillator strength increase and frequency red-shift of the NH stretching modes upon hydrogen bonding combined with the frequency upshift of the NH_2 bending overtone explains the enhanced mode mixing and oscillator strength transfer from the one-quantum NH stretching states to the bending overtone state. The excitonic model reveals the single-excited NH stretching manifold in the 3100-3600 cm^{-1} range in An monomer and An·$(DMSO)_2$ as appropriately described through normal modes of symmetric and asymmetric NH stretching and NH_2 bending modes. In contrast, for An·DMSO the effective decoupling resulting from formation of a single hydrogen bond leads to the local mode description of free and hydrogen-bonded NH stretching modes. Polarization-dependent 2D-IR spectroscopy is demonstrated as an important tool for the analysis of vibrational overtone spectra and is used to unambiguously determine most overtone levels in the NH stretching overtone manifold of An, An·DMSO, and An·$(DMSO)_2$ complexes and the relative transition dipole orientations. One- and two-color pump-probe and 2D-IR measurements are used to analyze the vibrational energy relaxation pathways of NH stretching excitations in the An molecule and double-hydrogen An·$(DMSO)_2$ complexes. The data suggest that energy flow proceeds over the NH_2 bending overtone to the NH_2 bending fundamental and υ(CC) ring mode.

The results of this work can serve as a reference for the analysis of other DNA model systems and as a benchmark for comprehensive DFT calculations incorporating a large number of degrees of freedom and molecular dynamics simulations of DNA. The research presented in this thesis constitutes a first step towards the analysis of bigger macromolecular DNA aggregates and the role of ultrafast dynamics in complex biological processes.

10 Zusammenfassung

Diese Arbeit trägt zu einem tieferen Verständnis der Schwingungsstruktur und ultraschnellen Schwingungsdynamik von DNA bei. Anregungen von NH Streckvibrationen der DNA Nukleinbasen wurden als empfindliche Sonden für Wasserstoffbrückenbindungen, inter- und intramolekulare Vibrationskopplungen, Energierelaxation, und dynamische Umgebungsänderungen in linearen und ultraschnellen nichtlinearen infrarot (IR) Anrege-Abtastexperimenten und insbesondere zweidimensionalen Photonen-Echo Experimenten verwendet. Letztere tasten die Dynamik von Schwingungskohärenzen über zwei verschiedene Zeitperioden ab, um die Vibrationsfrequenzen bei Anregung und späterer Detektion zu korrelieren. Diese Experimente wurden von exzitonischen Modellrechnungen und quantenchemischen ab-intio-Rechnungen begleitet. Die DNA Bestandteile wurden bei einem variablen Grad von molekularer Komplexität untersucht, um den Einfluss von intermolekularen Wasserstoffbrückenbindungen und intra- und intermolekularen Kopplungen von Vibrationsmoden separat von vertikalen Stapelwechselwirkungen und umgebenden Wassermolekülen in der DNA Doppelhelix zu untersuchen. Zunächst wurden die NH Streckanregungen in den isolierten Nukleinbasen Adenosin und Thymidin in nichtpolarer wasserfreier Lösung untersucht. Diese Messungen fungierten als Referenz für die Untersuchung von verschiedenen wasserstoffbrückeninduzierten Effekten in Adenosin-Thymidin Nukleinbasenpaaren. Die Analyse von doppelhelixartiger DNA mit Guanin-Cytosin Basenpaaren bei variablem Wassergehalt ermöglichte, den Einfluss von Hydration und Stapelwechselwirkungen auf die Vibrationslinienformen und Vibrationsdynamik zu untersuchen, während gleichzeitig interessante Einsichten in ultraschnelle strukturelle Fluktuationen der Hydrathülle und in die Funktion der Hydrathülle bei Schwingungsrelaxationsprozessen gewonnen wurden. Außerdem wurde die wasserstoffbrücken-induzierte Verstärkung von Fermi-Resonanzen in einer tertiären Lösung aus Anilin, DMSO und CCl_4 quantitativ untersucht.

Adenosin und Thymidin Nukleinbasen

Die monomeren Nukleinbasen Adenosin und Thymidin in Chloroform werden verwendet, um die NH Streckmoden in Abwesenheit von Wasserstoffbrückenwechselwirkungen zu untersuchen. In Adenosin zeigen die NH Streckzustände der Aminogruppe eine mechanische Kopplung von J_H = -56 cm^{-1}, welche durch den kinetischen Energiekopplungsbeitrag domiert ist. Die mechanische Kopplung steigt auf J_D = -77 cm^{-1} für die ND Streckschwingungen bei vollständiger Deuterierung. Die linearen Schwingungsspektren von partiell deuteriertem Adenosin zeigen die symmetrischen und asymmetrischen NH Strecknormalbewegungen als die richtigen Eigenfunktionen der einfach angeregten Zustände. Im Gegensatz dazu beweisen die von 2D-IR Messungen gelieferten Energiepositionen der doppelt angeregten Zustände in Kombination mit exzitonischen Modellrechnungen, dass die Zweiquantenzustände aufgrund des Zusammenspiels von mechanischer Kopplung J_H und lokaler diagonaler Anharmonizität (Δ_0 = 135 cm^{-1}) und Anharmonizität der Kombinationsmode (Δ_C = 14 cm^{-1}) einen intermediären Charakter zwischen dem von streng lokalisierten Moden und dem von delokalisierten Normalmoden aufweisen. Die 2D-IR Spektren zeigen keine Anzeichen von Populationstransfer oder spektraler Diffusion auf der Pikosekundenzeitskala. Anrege-Abtastexperimente zeigen Populationslebensdauern der beiden NH Streckanregungen in Adenosin von $\approx$ 6 und 10 ps und offenbaren unterdämpfte Quantenbeats aufgrund der kohärenten Anregung der symmetrischen und asymmetrischen NH Streckzustände, welche auf der Zeitskala von wenigen Pikosekunden dephasieren. Die einzelne NH Streckmode von Thymidin zeigt eine diagonale Anharmonizität von 150 cm^{-1} bei einer verkürzten Lebensdauer von 0.9 ps, was vermutlich durch Schwingungsrelaxation

über den Carbonyloberton erklärt werden kann.

Wasserstoffverbrückte Adenosin-Thymidin Nukleinbasenpaare

Die Bildung von wasserstoffverbrückten Adenosin-Thymidin Nukleinbasenpaaren in Chloroform führt zu signifikanten Änderungen in der Schwingungslinienform und Populationskinetik der mannigfachen NH Streckanregungen. Wasserstoffbrücken führen zu einer Rotverschiebung der involvierten NH Streckoszillationsfrequenzen, was zur Ausbildung von 5-6 bedeutenden Schwingungsbanden im Bereich von 2400-3500 cm^{-1} führt. Wie ^1H NMR Messungen und ab-initio-Rechnungen zeigen, treten alle vier doppelt wasserstoffverbrückten A·T Paargeometrien (Watson-Crick, rückseitiges Watson-Crick, Hoogsteen, rückseitiges Hoogsteen) in Lösung mit ähnlicher Häufigkeit auf. Ihre spektroskopischen und strukturellen Eigenschaften sind sehr ähnlich mit nur kleineren Unterschieden in den NH Streckschwingungsfrequenzen, Wirkungsquerschnitten, Schwingungskopplungsstärken und Anharmonizitäten, worauf die Kreuzpeaksignaturen in 2D Experimenten, Anrege-Abtast-Experimente sowie Hartree-Fock-Rechnungen hindeuten. Es wurde gezeigt, das alle NH Streckoszillatoren miteinander anharmonisch gekoppelt sind, entweder über mechanische Kopplungen über die chemischen Bindungen oder über Dipol-Dipolkopplungen zwischen Thymidin und Adenosin NH Streckanregungen.

Unterdämpfte Oszillationen in den Pump-Probetransienten haben gezeigt, dass die Formation von Wasserstoffbrücken anharmonische Kopplungen zwischen NH Streckmoden und niederfrequenten Wasserstoffbrückenmoden bei etwa 100 cm^{-1} induziert, was zur Bildung von Vibrationsseitenbanden führt, welche zur Linienverbreiterung insbesondere im 2400-3000 cm^{-1} beitragen. Die Rotverschiebung der NH Streckfrequenzen führt zu einer verstärkten Mischung mit Fingerprint Ober- und Kombinationstönen (Fermi-Resonanzen), insbesonderen mit der NH_2 Biegemode. Die Berücksichtigung beider Effekte ermöglicht ein qualitatives Verständnis der hohen Anzahl an A·T Dimer assozierten NH Streckschwingungsmoden, welche die Anzahl an lokalen NH Streckfreiheitsgrade übertifft. Obwohl die NH Streckmoden der Adenosinaminogruppe effektiv voneinander entkoppelt sind, schränkt die Mischung mit Fingerprintfreiheitsgraden und niederfrequenten Schwingungsmoden die Gültigkeit des Bildes von lokalen NH Streckanregungen ein.

Weiterhin wurde eine signifikante Verkürzung der Populationslebensdauer in den Anrege-Abtasttransienten nachgewiesen und mit der wasserstoffbrückeninduzierten Zunahme von effektiven Kopplungen mit Fingerprintfreiheitsgraden erklärt. Während die nichtwasserstoffverbrückte Schwingungsmode $\upsilon_A(NH_2)_f$ eine Anregungslebensdauer von etwa 2 ps zeigt, wurden die Lebensdauern der wasserstoffverbrückten NH Streckmoden $\upsilon_A(NH_2)_b$ und $\upsilon_T(NH)$ zu 0.2-0.4 ps bestimmt. Die 2D Spektren zeigen einen ultraschnellen Transfer von Schwingungsenergie von der 3330 cm^{-1} zur 3200 cm^{-1} Mode. Es wurde festgestellt, dass alle NH Streckmoden hochgradig inhomogen verbreitert sind, was auf eine heterogene Verteilung von Wasserstoffbrückenlängen in den A·T Basenpaaren zugeführt wird. Die Fluktuationen in den intermolekularen Wasserstoffbrückengeometrien sind auf der Pikosekundenzeitskala vernachlässigbar, wie die statische Inhomogenität der 2D Spektren zeigt.

Hydratisierte Guanin-Cytosin Basenpaare in doppelhelixartiger DNA

Der Vergleich von linearen und 2D Messungen an künstlicher DNA mit 23 guanine-cytosine (G·C) Basenpaaren in Watson-Crick Geometrie bei variablen Wasseranteil mit ähnlichen Messungen an isolierten G·C Basenpaaren in Chloroform zeigt, dass in Gegenwart der DNA Doppelhelix bereits ein niedriger Wassergehalt signifikante Auswirkungen auf Vibrationslinienformen und Schwingungsdynamik hat.

Bei einem niedrigen Wassergehalt von 4 Wassermolekülen pro Basenpaar werden die 2D Spektren von den NH Streckmoden der Basenpaare dominiert. Die elliptische Linienform in den 2D Spektren deutet auf ein hohes Maß von struktureller Inhomogenität hin. Es findet keine ultraschnelle spektrale Diffusion der NH Streckmoden der Basenpaare und der OH Streckmoden der

verbleibenden stark gebundenen Wassermoleküle statt, was auf weitgehend starre G·C Basenpaar- und DNA-Wasser-Strukturen hindeutet. Schwache "horizontale" Schwingungskopplungen zwischen NH Streckoszillatoren in den wasserstoffverbrückten G·C Basenpaaren werden beobachtet, während die linearen und 2D Spektren keine Anzeichen für signifikante "vertikale" Intrastrangkopplungen zwischen den NH Streckmoden der gestapelten Nukleinbasenpaare geben. Es werden T_1 Populationszeiten von 200-300 fs gemessen, in Übereinstimmung mit Ergebnissen an wasserstoffverbrückten NH Streckmoden in isolierten Basenpaaren, aber unabhängig von der genauen spektralen Postion. Weder die linearen noch die 2D-IR Messungen zeigen Anzeichen für ausgegrägte freie NH Streckmoden, worauf die Abwesenheit von deutlich sichtbaren Diagonal- und Kreuzpeaks und das Fehlen von deutlich verlängerten T_1 Lebensdauern bei den erwarteten spektralen Positionen von freien NH Streckmoden hindeutet. Dies führt zu dem Schluss, dass bereits bei niedrigem Wassergehalt viele der "freien" NH Motife der Aminogruppen von Wassermolekülen hydratisiert sind, was eine hohe Wasseraffinität der polaren Gruppen in den Positionen der großen und kleinen DNA Furche anzeigt. Die durch die Hydratisierung reduzierte Energiedifferenz der entkoppelten lokalen NH Streckmoden in den Aminogruppen führt zu teilweise delokalisierten Eigenzuständen mit einem Zustandscharakter, der intermediär zwischen lokalen und normalen Schwingungsmoden liegt.

Bei einem hohen Wasseranteil mit mehr als 20 Wassermolekülen pro Basenpaar zeigen die 2D Spektren einen additiven, dominierenden Beitrag von OH Streckanregungen der DNA-Hydrathülle, während die NH Streckanregungen weitgehend ungeändert bleiben. Somit hat die Ausbildung einer vollständig gefüllten ersten Wasserschale und die vereinzelte Besetzung von weiter aussenliegenden Hydratisierungsplätzen nur einen geringen Einfluss auf Wasserstoffbrücken in den Baasenpaaren und Schwingngskopplungen zwischen den NH Streckanregungen. Die dynamische Verformung innerhalb der 2D Spektren erlaubt die Beobachtung des Zerfalls der OH Streck-Frequenzfluktuationskorrelationsfunktion mit einer Zerfallsdauer von 250 fs, was verglichen mit dem in Volumenwasser beobachteten sub-100 fs schnellem Zerfall eine Verlangsamung darstellt. Dieser verlangsamte Zerfall wird reduzierten strukturellen Fluktutionen in der Hydrathülle aufgrund von starken Wechselwirkungen mit der DNA und sterischen Einschränkungen zugeordnet sowie mit der verringerten Rate von resonantem Energietransfer und der Bildung eines schwingungsmäßig aufgeheiztem Grundzustandes in der Wasserschale erklärt. Die Bildung eines heißen Grundzustandes während des Prozesses der Vibrationsrelaxation auf der Femtosekundenzeitskala beweist die wichtige Rolle der Hydrathülle als effiziente Wärmesenke for hochenergetische Vibrationsanregungen.

Wasserstoffbrückeninduzierte Verstärkung von Fermi-Resonanzen in Aniline-d5

Um den Fermi-Resonanzeffekt des NH_2 Biegeobertons mit fundamentalen NH Streckmoden quantitativ zu untersuchen, wurde Aniline-d5 (An) wasserstoffverbrückt mit 0, 1 und 2 DMSO Molekülen untersucht. Die Bildung von Wasserstoffbrücken der NH_2 Aminogruppe mit einem oder zwei DMSO Molekülen führt zu einem erheblichen Anstieg der integrierten Oszillatorstärke der NH Streckübergänge, der dennoch verblasst gegenüber der Oszillatorstärkenzunahme des ersten NH_2 Biegeobertons. Diese dramatische Fermiresonanzerhöhung wurde quantitativ mit einem exzitonischen Model beschrieben, welches die zwei lokalen NH Streckmoden und den ersten NH_2 Biegeoberton verwendet. Damit wurde die mechanische Kopplung zu J = -55 cm^{-1} sowie die Fermiresonanzkopplung zwischen den NH Streckzuständen und dem ersten Biegeoberton zu V = -37 cm^{-1} bestimmt. Die Zunahme der Oszillatorstärke der fundamentalen NH Streckmoden und deren Frequenzrotverschiebung erklärt zusammen mit dem Frequenzanstieg des NH_2 Biegeobertons die verstärkte Zustandsmischung zwischen Biegeoberton und den einfach angeregten NH Streckzuständen und somit den Transfer von Absorptionsstärke. Wie das exzitonische Modell zeigt, lassen sich die NH Streckzustände im Bereich 3100-3600 cm^{-1} in An und An··$(DMSO)_2$ angemessen über die symmetrischen und asymmetrischen NH Strecknormalschwingungen sowie den NH_2 Biegeober-

ton beschreiben. Im Gegensatz dazu führt die effektive Entkopplung der NH Streckzustände in An··DMSO zur Beschreibung als lokale Moden von freien und wasserstoffverbrückten NH Streckschwingungen. Es wird gezeigt, dass polarisationabhängige 2D-IR Spektroskopie ein wichtiges Werkzeug zur Analyse von Vibrationsobertonspektren darstellt und es erlaubt, die meisten Obertonniveaus von NH Streckanregungen sowie die relativen Übergangsdipolorientierungen in An, An··DMSO und An··$(DMSO)_2$ eindeutig zu bestimmen.

Einfarben- und Zweifarben-Anrege-Abtastexperimente sowie 2D-IR Messungen werden verwendet, um die Relaxationskanäle von NH Streckanregungen in An und An··$(DMSO)_2$ zu untersuchen. Die Messungen deuten darauf hin, dass der Energiefluss über den NH_2 Biegeoberton zu der NH_2 Biegefundamentalmode und schließlich über die υ(CC) Ringmode verläuft.

Die in dieser Arbeit präsentierten Forschungsergebnisse stellen eine Referenz für die Analyze von DNA Modelsystemen dar sowie für umfangreiche Dichtefunktionalrechnungen unter Berücksichtigung einer großen Anzahl an Freiheitsgraden und für Rechnungen zur molekularen Dynamik in DNA. Die Ergebnisse dieser Arbeit bereiten den Weg für die Analyse von größeren makromolekularen DNA-Aggregaten und der Rolle von ultraschneller Dynamik in komplexen biologischen Prozessen.

11 Publications

Peer-reviewed articles

- C. Greve and T. Elsaesser, *Ultrafast Two-Dimensional Infrared Spectroscopy of Guanine-Cytosine Base Pairs in DNA Oligomers, Journal of Physical Chemistry B* **117** (2013) 14009-14017

- C. Greve, E.T.J. Nibbering, and H. Fidder, *Hydrogen-Bonding-Induced Enhancement of Fermi Resonances: A Linear IR and Nonlinear 2D-IR Study of Aniline-d5, The Journal of Physical Chemistry B* **117** (2013) 15843-15855

- C. Greve, N. K. Preketes, H. Fidder, R. Costard, B. Koeppe, I. A. Heisler, S. Mukamel, F. Temps, E.T.J. Nibbering, and T. Elsaesser, *N-H Stretching Excitations in Adenosine-Thymidine Base Pairs in Solution: Pair Geometries, Infrared Line Shapes, and Ultrafast Vibrational Dynamics, Journal of Physical Chemistry A* **117** (2013) 594-606

- C. Greve, N. K. Preketes, R. Costard, B. Koeppe, H. Fidder, E. T. J. Nibbering, F. Temps, S. Mukamel, and T. Elsaesser, *N-H Stretching Modes of Adenosine Monomer in Solution Studied by Ultrafast Nonlinear Infrared Spectroscopy and Ab Initio Calculations, Journal of Physical Chemistry A* **116** (2012) 7636-7644

- R. Costard, C. Greve, I. A. Heisler, and T. Elsaesser, *Ultrafast Energy Redistribution in Local Hydration Shells of Phospholipids: A Two-Dimensional Infrared Study, Journal of Physical Chemistry Letters* **3** (2012) 3646-3651

Conference proceedings

- C. Greve, N. K. Preketes, R. Costard, B. Koeppe, H. Fidder, E. T. J. Nibbering, F. Temps, S. Mukamel, and T. Elsaesser, *Ultrafast IR Pump-Probe and 2D-IR Photon Echo Spectrocopy of Adenosine-Thymidine Base Pairs, EPJ Web Conf.* **41** (2013) 05019

- R. Costard, C. Greve, N. E. Levinger, E. T. J. Nibbering, and T. Elsaesser, *Vibrational Dynamics of Water Confined in Phospholipid Reverse Micelles, EPJ Web Conf.* **41** (2013) 06003

Other peer-reviewed articles

- C. Greve, M. Kroener, S. Trippel, P. Woias, R. Wester, and M. Weidemueller, *Storage of Protonated Water Clusters in a Biplanar Multipole RF Trap, New Journal of Physics* **12** (2010) 065035

12 Bibliography

[1] S. Neidle, *Oxford Handbook of Nucleic Acid Structure.* Oxford University Press: New York, 1999.

[2] W. Saenger, *Principles of Nucleic Acid Structure.* Springer: New York, 1984.

[3] T. Creighton, *Proteins, 2nd edn.* Freeman: New York, 1993.

[4] L. Stryer, *Biochemistry.* Freeman: San Francisco, 1981.

[5] P. Schuster, G. Zundel, and C. Sandorfy, *The Hydrogen Bond: Recent Developments in Theory and Experiments.* North Holland: Amsterdam, 1976.

[6] J. Watson and F. Crick, *Molecular Structure of Nucleic Acids - A Structure For Deoxyribose Nucleic Acid*, *Nature* **171** (1953) 737–738.

[7] E. Westhof, *Water - An Integral-Part of Nucleic Acid Structure*, *Annual Review of Biophysics and Biophysical Chemistry* **17** (1988) 125–144.

[8] B. Bagchi, *Water Dynamics in the Hydration Layer Around Proteins and Micelles*, *Chemical Reviews* **105** (2005) 3197–3219.

[9] C. Robinson and S. Sligar, *Molecular Recognition Mediated by Bound Water - A Mechanism for Star Activity of the Restriction-Endonuclease Ecori*, *Journal of Molecular Biology* **234** (1993) 302–306.

[10] M. Eisenstein and Z. Shakked, *Hydration Patterns and Intermolecular Interactions in A-DNA Crystal-Structures - Implications for DNA Recognition*, *Journal of Molecular Biology* **248** (1995) 662–678.

[11] J. Rosenberg, N. Seeman, R. Day, and A. Rich, *RNA Double-Helical Fragments at Atomic Resolution - Crystal-Structure of Sodium Guanylyl-3',5'-Cytidine Nonahydrate*, *Journal of Molecular Biology* **104** (1976) 145–167.

[12] H. Sobell, K. Tomita, and A. Rich, *Crystal Structure of an Intermolecular Complex Containing a Guanine and a Cytosine Derivative*, *Proceedings of the National Academy of Sciences of the United States of America* **49** (1963) 885–892.

[13] H. Berman, W. Olson, D. Beveridge, J. Westbrook, A. Gelbin, T. Demeny, S. Hsieh, A. Srinivasan, and B. Schneider, *The Nucleic Acid Database - A Comprehensive Relational Database of 3-Dimensional Structures of Nucleic Acids*, *Biophysical Journal* **63** (1992) 751–759.

[14] H. Drew and R. Dickerson, *Structure of a B-DNA Dodecamer III. Geometry of hydration*, *Journal of Molecular Biology* **151** (1981) 535–556.

[15] M. Kopka, A. Fratini, H. Drew, and R. Dickerson, *Ordered Water-Structure Around a Beta-DNA Dodecamer - A Quantitative Study*, *Journal of Molceular Biology* **163** (1983) 129–146.

[16] G. Otting and K. Wuthrich, *Studies of Protein Hydration in Aqueous Solution by Direct NMR Observation of Individual Protein-Bound Water Molecules*, *Journal of the American Chemical Society* **111** (1989) 1871–1875.

[17] G. Otting, E. Liepinsh, and K. Wuthrich, *Protein Hydration in Aqueous Solution*, *Science* **254** (1991) 974–980.

[18] B. Halle and V. Denisov, *Water and Monovalent Ions in the Minor Groove of B-DNA Oligonucleotides as Seen By NMR*, *Biopolymers* **48** (1998) 210–233.

[19] A. Kornberg and T. A. Baker, *DNA Replication, Second Edition.* University Science Books, 1992.

[20] E. Liepinsh, G. Otting, and K. Wuthrich, *NMR Observation of Individual Molecules of Hydration Water Bound to DNA Dublexes: Direct Evidence for a Spine of Hydration Water Present in Aqueous Solution*, *Nucleic Acids Research* **20** (1992) 6549–6553.

[21] M. Sunnerhagen, V. Denisov, K. Venu, A. Bonvin, J. Carey, B. Halle, and G. Otting, *Water Molecules in DNA Recognition I: Hydration Lifetimes of trp Operator DNA in Solution Measured by NMR Spectroscopy*, *Journal of Molecular Biology* **282** (1998) 847–858.

[22] A. Bonvin, M. Sunnerhagen, G. Otting, and W. van Gunsteren, *Water Molecules in DNA recognition II: A Molecular Dynamics View of the Structure and Hydration of the trp Operator*, *Journal of Molecular Biology* **282** (1998) 859–873.

[23] S. Pal, L. Zhao, and A. Zewail, *Water at DNA Surfaces: Ultrafast Dynamics in Minor Groove Recognition*, *Proceedings of the National Academy of Sciences of the United States of America* **100** (2003) 8113–8118.

[24] S. Pal, P. K. Maiti, and B. Bagchi, *Exploring DNA Groove Water Dynamics Through Hydrogen Bond Lifetime and Orientational Relaxation*, *Journal of Chemical Physics* **125** (2006) 234903.

[25] M. L. Cowan, B. D. Bruner, N. Huse, J. R. Dwyer, B. Chugh, E. T. J. Nibbering, T. Elsaesser, and R. J. D. Miller, *Ultrafast Memory Loss and Energy Redistribution in the Hydrogen Bond Network of Liquid H_2O*, *Nature* **434** (2005) 199–202.

[26] I. Ohmine and H. Tanaka, *Fluctuation, Relaxations, and Hydration in Liquid Water - Hydrogen-Bond Rearrangement Dynamics*, *Chemical Reviews* **93** (1993) 2545–2566.

[27] C. Fecko, J. Eaves, J. Loparo, A. Tokmakoff, and P. Geissler, *Ultrafast Hydrogen-Bond Dynamics in the Infrared Spectroscopy of Water*, *Science* **301** (2003) 1698–1702.

[28] R. Rey, K. Mller, and J. Hynes, *Hydrogen Bond Dynamics in Water and Ultrafast Infrared Spectroscopy*, *Journal of Physical Chemistry A* **106** (2002) 11993–11996.

[29] D. Laage and J. Hynes, *A Molecular Jump Mechanism of Water Reorientation*, *Science* **311** (2006) 832–835.

[30] V. Denisov and B. Halle, *Protein Hydration Dynamics in Aqueous-Solution - A Comparison of Bovine Pancreatic Trypsin-Inhibitor and Ubiquitin by O-17 Spin Relaxation Dispersion*, *Journal of Molecular Biology* **245** (1995) 682–697.

[31] V. Denisov and B. Halle, *Protein Hydration Dynamics in Aqueous Solution*, *Faraday Discussions* **103** (1996) 227–244.

[32] S. Pal, P. K. Maiti, B. Bagchi, and J. T. Hynes, *Multiple Time Scales in Solvation Dynamics of DNA in Aqueous Solution: The Role of Water, Counterions, and Cross-Correlations*, *The Journal of Physical Chemistry B* **110** (2006) 26396–26402.

[33] E. Brauns, M. Madaras, R. Coleman, C. Murphy, and M. Berg, *Complex Local Dynamics in DNA on the Picosecond and Nanosecond Time Scales*, *Physical Review Letters* **88** (2002).

[34] E. Brauns, M. Madaras, R. Coleman, C. Murphy, and M. Berg, *Measurement of Local DNA Reorganization on the Picosecond and Nanosecond Time Scales*, *Journal of the American Chemical Society* **121** (1999) 11644–11649.

[35] K. E. Furse and S. A. Corcelli, *The Dynamics of Water at DNA Interfaces: Computational Studies of Hoechst 33258 Bound to DNA*, *Journal of the American Chemical Society* **130** (2008) 13103–13109.

[36] T. Li, A. A. Hassanali, Y.-T. Kao, D. Zhong, and S. J. Singer, *Hydration Dynamics and Time Scales of Coupled Water-Protein Fluctuations*, *Journal of the American Chemical Society* **129** (2007) 3376–3382.

[37] A. A. Golosov and M. Karplus, *Probing Polar Solvation Dynamics in Proteins: A Molecular Dynamics Simulation Analysis*, *Journal of Physical Chemistry B* **111** (2007) 1482–1490.

[38] C. Rischel, A. Rousse, I. Uschmann, P. Albouy, J. Geindre, P. Audebert, J. Gauthier, E. Forster, J. Martin, and A. Antonetti, *Femtosecond Time-Resolved X-ray Diffraction From Laser-Heated Organic Films*, *Nature* **390** (1997) 490–492.

[39] H. Ihee, V. Lobastov, U. Gomez, B. Goodson, R. Srinivasan, C. Ruan, and A. Zewail, *Direct Imaging of Transient Molecular Structures with Ultrafast Diffraction*, *Science* **291** (2001) 458–462.

[40] M. Bargheer, N. Zhavoronkov, Y. Gritsai, J. Woo, D. Kim, M. Woerner, and T. Elsaesser, *Coherent Atomic Motions in a Nanostructure Studied by Femtosecond X-ray Diffraction*, *Science* **306** (2004) 1771–1773.

[41] M. Karplus and J. A. McCammon, *Molecular Dynamics Simulations of Biomolecules*, *Nature Structural Biology* **9** (2002) 646–652.

[42] E. T. J. Nibbering and T. Elsaesser, *Ultrafast Vibrational Dynamics of Hydrogen Bonds in the Condensed Phase*, *Chemical Reviews* **104** (2004) 1887–1914.

[43] T. Elsaesser and H. Bakker, *Ultrafast Hydrogen Bonding Dynamics and Proton Transfer Processes in the Condensed Phase*. Kluwer Academic Publishers, 2002.

[44] E. Nibbering, H. Fidder, and E. Pines, *Ultrafast Chemistry: Using Time-Resolved Vibrational Spectroscopy For Interrogation of Structural Dynamics*, *Annual Review of Physical Chemistry* **56** (2005) 337–367.

[45] S. Mukamel, *Multidimensional Femtosecond Correlation Spectroscopies of Electronic and Vibrational Excitations*, *Annual Review of Physical Chemistry* **51** (2000) 691–729.

[46] P. Hamm and M. Zanni, *Concepts and Methods of 2D Infrared Spectroscopy*. Cambridge University Press, 2011.

[47] M. Khalil, N. Demirdöven, and A. Tokmakoff, *Coherent 2D IR Spectroscopy: Molecular Structure and Dynamics in Solution*, *Journal of Physical Chemistry A* **107** (2003) 5258–5279.

[48] C. S. Peng, K. C. Jones, and A. Tokmakoff, *Anharmonic Vibrational Modes of Nucleic Acid Bases Revealed by 2D-IR Spectroscopy*, *Journal of the American Chemical Society* **133** (2011) 15650–15660.

[49] M. Yang, Ł. Szyc, K. Röttger, H. Fidder, E. T. J. Nibbering, T. Elsaesser, and F. Temps, *Dynamics and Couplings of N-H Stretching Excitations of Guanosine-Cytidine Base Pairs in Solution*, *Journal of Physical Chemistry B* **115** (2011) 5484–5492.

[50] Ł. Szyc, M. Yang, E. Nibbering, and T. Elsaesser, *Ultrafast Vibrational Dynamics and Local Interactions of Hydrated DNA*, *Angewandte Chemie International Edition* **49** (2010) 3598–3610.

[51] M. Yang, Ł. Szyc, and T. Elsaesser, *Decelerated Water Dynamics and Vibrational Couplings of Hydrated DNA Mapped by Two-Dimensional Infrared Spectroscopy*, *Journal of Physical Chemistry B* **115** (2011) 13093–13100.

[52] A. T. Krummel and M. T. Zanni, *DNA Vibrational Coupling Revealed with Two-Dimensional Infrared Spectroscopy: Insight into why Vibrational Spectroscopy is Sensitive to DNA Structure*, *Journal of Physical Chemistry B* **110** (2006) 13991–14000.

[53] S. Woutersen, Y. Mu, G. Stock, and P. Hamm, *Subpicosecond Conformational Dynamics of Small Peptides Probed by Two-Dimensional Vibrational Spectroscopy*, *Proceedings of the National Academy of Sciences* **98** (2001) 11254–11258.

[54] A. Krummel, P. Mukherjee, and M. Zanni, *Inter and Intrastrand Vibrational Coupling in DNA Studied with Heterodyned 2D-IR Spectroscopy*, *Journal of Physical Chemistry B* **107** (2003) 9165–9169.

[55] T. Elsaesser, *Ultrafast Memory Loss and Relaxation Processes in Hydrogen-Bonded Systems*, *Biological Chemistry* **390** (2009) 1125–1132.

[56] L. Szyc, M. Yang, and T. Elsaesser, *Ultrafast Energy Exchange via Water-Phosphate Interactions in Hydrated DNA*, *Journal of Physical Chemistry B* **114** (2010) 7951–7957.

[57] C. Crespo-Hernandez, B. Cohen, and B. Kohler, *Base Stacking Controls Excited-State Dynamics in A-T DNA*, *Nature* **436** (2005) 1141–1144.

[58] E. B. Wilson, J. C. Decius, and P. Cross, *Molecular Vibrations*. Dover Publications: New York, 1980.

[59] E. Wilson, *Some Mathematical Methods for the Study of Molecular Vibrations*, *Journal of Chemical Physics* **9** (1941) 76–84.

[60] H. G. Kjaergaard, A. L. Garden, G. M. Chaban, R. B. Gerber, D. A. Matthews, and J. F. Stanton, *Calculation of Vibrational Transition Frequencies and Intensities in Water Dimer: Comparison of Different Vibrational Approaches*, *Journal of Physical Chemistry A* **112** (2008) 4324–4335.

[61] H. Nielsen, *The Vibration-Rotation Energies of Molecules*, *Review of Modern Physics* **23** (1951) 90–136.

[62] A. Willetts and N. Handy, *The Anharmonic Constants for a Symmetric Top*, *Chemical Physics Letters* **235** (1995) 286–290.

[63] P. Hamm, S. M. Ohline, and W. Zinth, *Vibrational Cooling after Ultrafast Photoisomerization of Azobenzene Measured by Femtosecond Infrared Spectroscopy*, *The Journal of Chemical Physics* **106** (1997) 519–529.

[64] M. Khalil and A. Tokmakoff, *Signatures of Vibrational Interactions in Coherent Two-Dimensional Infrared Spectroscopy*, *Chemical Physics* **266** (2001) 213–230.

[65] J. Pliva, *Anharmonic Constants for Degenerate Modes of Symmetric Top Molecules*, *Journal of Molecular Spectroscopy* **139** (1990) 278–285.

[66] J. D. Patterson and B. C. Bailey, *Solid-State Physics, Introduction to the Theory.* Springer, 2007.

[67] E. B. Wilson, *The Normal Modes and Frequencies of Vibration of the Regular Plane Hexagon Model of the Benzene Molecule*, *Physical Review* **45** (1934) 706–714.

[68] D. L. Rousseau, R. P. Bauman, and S. P. S. Porto, *Normal Mode Determination in Crystals*, *Journal of Raman Spectroscopy* **10** (1981) 253–290.

[69] M. Cho, *Two Dimensional Optical spectroscopy.* CRC Press: Boca Raton, 2009.

[70] C. Cohen-Tannoudji, B. Diu, and F. Laloe, *Quantum Mechanics.* W de gruyter, 1999.

[71] L. Halonen, *Local Mode Vibrations in Polyatomic Molecules.* Wiley, 2007.

[72] M. S. Child and L. Halonen, *Overtone Frequencies and Intensities in the Local Mode Picture.* Wiley, 2007.

[73] G. Herzberg, *Molecular Spectra and Molecular Structure I. Spectra of Diatomic Molecules.* Van Nostrand, 1950.

[74] I. Mills and A. Robiette, *On The Relationship of Normal-Modes to Local Modes in Molecular Vibrations*, *Molecular Physics* **56** (1985) 743–765.

[75] M. L. Sage and J. Jortner, *Bond Modes*, pp. 293–322. Wiley, 2007.

[76] M. J. Frisch, G. W. Trucks, H. B. Schlegel, G. E. Scuseria, M. A. Robb, J. R. Cheeseman, G. Scalmani, V. Barone, and B. M. et al., "Gaussian 09 Revision A.1." Gaussian Inc. Wallingford CT 2009.

[77] T. Brixner, T. Manal, I. V. Stiopkin, and G. R. Fleming, *Phase-Stabilized Two-Dimensional Electronic Spectroscopy*, *The Journal of Chemical Physics* **121** (2004) 4221–4236.

[78] S. Mukamel, *Principles of Nonlinear Optical Spectroscopy*, *Oxford University Press* (1995).

[79] R. Vangrondelle, J. Dekker, T. Gillbro, and V. Sundstrom, *Energy Transfer and Trapping in Photosynthesis*, *Biochimica et Biophysica acta-Bioenergetics* **1187** (1994) 1–65.

[80] V. Sundstrom, T. Pullerits, and R. van Grondelle, *Photosynthetic Light-Harvesting: Reconciling Dynamics and Structure of Purple Bacterial LH2 Reveals Function of Photosynthetic Unit*, *Journal of Physical Chemistry B* **103** (1999) 2327–2346.

[81] R. Marcus and N. Sutin, *Electron Transfers in Chemistry and Biology*, *Biochimica et Biophysica Acta (BBA) - Reviews on Bioenergetics* **811** (1985) 265–322.

[82] A. G. Redfield *Advances in Magnetic Resonance* **1** (1965).

[83] W. T. Pollard and R. A. Friesner, *Solution of the Redfield Equation for the Dissipative Quantum Dynamics of Multilevel Systems*, *The Journal of Chemical Physics* **100** (1994) 5054–5065.

[84] M. Khalil, N. Demirdöven, and A. Tokmakoff, *Vibrational Coherence Transfer Characterized with Fourier-Transform 2D IR Spectroscopy*, *Journal of Chemical Physics* **121** (2004) 362–373.

[85] D. W. Oxtoby, *Vibrational Population Relaxation in Liquids*. Wiley, 2007.

[86] F. E. Figueirido and R. M. Levy, *Vibrational Relaxation and Bloch-Redfield Theory*, *The Journal of Chemical Physics* **97** (1992) 703–706.

[87] A. Tokmakoff, *Lecture: Introductory Quantum Mechanics 2*. MIT Department of Chemistry, 2008.

[88] J. L. Skinner, *Semiclassical Approximations to Golden Rule Rate Constants*, *The Journal of Chemical Physics* **107** (1997) 8717–8718.

[89] D. Oxtoby, *Vibrational Relaxation in Liquids - Quantum States in a Classical Bath*, *Journal of Physical Chemistry* **87** (1983) 3028–3033.

[90] F. Bloch, *Nuclear Induction*, *Physical Review* **70** (1946) 460–474.

[91] R. Kubo, *A Stochastical Theory of Line Shapes*. 1967.

[92] M. Born and R. Oppenheimer, *Zur Quantentheorie der Moleküle*, *Annalen der Physik* **389** (1927) 457–484.

[93] P. Schuster, G. Zundel, and C. Sandorfy, *The Hydrogen Bond: Recent Developments in Theory and Experiments II. Structure and Spectroscopy*, *North Holland: Amsterdam* 565–611.

[94] F. A. Lauti, A.and Froment and A. Novak, *Relationship Between NH Stretching Frequencies and NO Distances of Crystals Containing NHO Hydrogen Bonds*, *Spectroscopy Letters: An International Journal for Rapid Communication* **9** (1976) 289–299.

[95] A. Novak, *Hydrogen Bonding in Solids. Correlation of Spectroscopic and Crystallographic Data*, *Plenary Lecture, First European Crystallographic Meeting* (1973) 177–212.

[96] N. Leroux, C. Samyn, and T. Zeegers-Huyskens, *Mid- and Near-IR Study of the Hydrogen Bond Interaction Between N-Methyldiacetamide and Phenols*, *Journal of Molecular Structure* **448** (1998) 209–220.

[97] N. Demirdöven, M. Khalil, and A. Tokmakoff, *Correlated Vibrational Dynamics Revealed by Two-Dimensional Infrared Spectroscopy*, *Physical Review Letters* **89** (2002).

[98] A. Laubereau and W. Kaiser, *Vibrational Dynamcis of Liquids and Solids Investigated by Picosecond Light-Pulses*, *Review of Modern Physics* **50** (1978) 607–665.

[99] W. Zinth, R. Leonhardt, W. Holzapfel, and W. Kaiser, *Fast Dephasing Processes Studied with a Femtosecond Coherent Raman System*, *IEEE Journal of Quantum Electronics* **24** (1988) 455–459.

[100] A. Zumbusch, G. Holtom, and X. Xie, *Three-Dimensional Vibrational Imaging by Coherent Anti-Stokes Raman Scattering*, *Physical Review Letters* **82** (1999) 4142–4145.

[101] D. J. Ulness, J. C. Kirkwood, and A. C. Albrecht, *Competitive Events in Fifth Order Time Resolved Coherent Raman Scattering: Direct versus Sequential Processes*, *The Journal of Chemical Physics* **108** (1998) 3897–3902.

[102] R. Inaba, H. Okamoto, K. Yoshihara, and M. TasumiI, *Femtosecond Time-Resolved Coherent Anti-Stokes Raman Scattering of the C-Equivalent-to-C Stretching in Liquid Alkynes*, *Journal of Physical Chemistry* **97** (1993) 7815–7819.

[103] D. Dlott, *Vibrational Energy Redistribution in Polyatomic Liquids: 3D infrared-Raman Spectroscopy*, *Chemical Physics* **266** (2001) 149–166.

[104] S. Ashihara, N. Huse, A. Espagne, E. T. J. Nibbering, and T. Elsaesser, *Ultrafast Structural Dynamics of Water Induced by Dissipation of Vibrational Energy*, *Journal of Physical Chemistry A* **111** (2007) 743–746.

[105] A. Lock and H. Bakker, *Temperature Dependence of Vibrational Relaxation in Liquid H_2O*, *Journal of Chemical Physics* **117** (2002) 1708–1713.

[106] P. Hamm, *Coherent Effects in Femtosecond Infrared-Spectroscopy*, *Chemical Physics* **200** (1995) 415–429.

[107] M. Chachisvilis, H. Fidder, and V. Sundstrom, *Electronic Coherence in Pseudo-2-Color Pump-Probe Spectroscopy*, *Chemical Physics Letters* **234** (1995) 141–150.

[108] S. Yan, M. T. Seidel, and H.-S. Tan, *Perturbed Free Induction Decay in Ultrafast Mid-IR Pump-Probe Spectroscopy*, *Chemical Physics Letters* **517** (2011) 36–40.

[109] H. Graener, G. Seifert, and A. Laubereau, *Direct Observation of Rotational Relaxation Times by Time-Resolved Infrared Spectroscopy*, *Chemical Physics Letters* **172** (1990) 435–439.

[110] A. Tokmakoff, R. S. Urdahl, D. Zimdars, R. S. Francis, A. S. Kwok, and M. D. Fayer, *Vibrational Spectral Diffusion and Population Dynamics in a Glass-Forming Liquid: Variable Bandwidth Picosecond Infrared Spectroscopy*, *The Journal of Chemical Physics* **102** (1995) 3919–3931.

[111] J. Hybl, Y. Christophe, and D. Jonas, *Peak Shapes in Femtosecond 2D Correlation Spectroscopy*, *Chemical Physics* **266** (2001) 295–309.

[112] O. Golonzka, M. Khalil, N. Demirdöven, and A. Tokmakoff, *Vibrational Anharmonicities Revealed by Coherent Two-Dimensional Infrared Spectroscopy*, *Physical Review Letters* **86** (2001) 2154–2157.

[113] O. Golonzka, M. Khalil, N. Demirdöven, and A. Tokmakoff, *Coupling and Orientation Between Anharmonic Vibrations Characterized with Two-Dimensional Infrared Vibrational Echo Spectroscopy*, *Journal of Chemical Physics* **115** (2001) 10814–10828.

[114] C. S. Peng, K. C. Jones, and A. Tokmakoff, *Anharmonic Vibrational Modes of Nucleic Acid Bases Revealed by 2D-IR Spectroscopy*, *Journal of the American Chemical Society* **133** (2011) 15650–15660.

[115] S. Woutersen and P. Hamm, *Nonlinear Two-Dimensional Vibrational Spectroscopy of Peptides*, *Journal of Physics-Condensed Matter* **14** (2002) R1035–R1062.

[116] H. S. Chung, Z. Ganim, K. C. Jones, and A. Tokmakoff, *Transient 2D IR Spectroscopy of Ubiquitin Unfolding Dynamics*, *Proceedings of the National Academy of Sciences* **104** (2007) 14237–14242.

[117] S. Woutersen and P. Hamm, *Time-Resolved Two-Dimensional Vibrational Spectroscopy of a Short Alpha-Helix in Water*, *Journal of Chemical Physics* **115** (2001) 7737–7743.

[118] P. Hamm, M. Lim, and R. M. Hochstrasser, *Structure of the Amide I Band of Peptides Measured by Femtosecond Nonlinear-Infrared Spectroscopy*, *The Journal of Physical Chemistry B* **102** (1998) 6123–6138.

[119] M. C. Thielges and M. D. Fayer, *Protein Dynamics Studied with Ultrafast Two-Dimensional Infrared Vibrational Echo Spectroscopy*, *Accounts of Chemical Research* **45** (2012) 1866–1874.

[120] Y. S. Kim and R. M. Hochstrasser, *Applications of 2D-IR Spectroscopy to Peptides, Proteins, and Hydrogen-Bond Dynamics*, *The Journal of Physical Chemistry B* **113** (2009) 8231–8251.

[121] P. Hamm, J. Helbing, and J. Bredenbeck, *Two-Dimensional Infrared Spectroscopy of Photoswitchable Peptides*, *Annual Review of Physical Chemistry* **59** (2008) 291–317.

[122] D. Kraemer, M. L. Cowan, A. Paarmann, N. Huse, E. T. J. Nibbering, T. Elsaesser, and R. J. D. Miller, *Temperature Dependence of the Two-Dimensional Infrared Spectrum of Liquid H_2O*, *Proceedings of the National Academy of Sciences* **105** (2008) 437–442.

[123] S. T. Roberts, K. Ramasesha, and A. Tokmakoff, *Structural Rearrangements in Water Viewed Through Two-Dimensional Infrared Spectroscopy*, *Accounts of Chemical Research* **42** (2009) 1239–1249.

[124] M. D. Fayer, *Dynamics of Water Interacting with Interfaces, Molecules, and Ions*, *Accounts of Chemical Research* **45** (2012) 3–14.

[125] J. Bredenbeck, A. Ghosh, H.-K. Nienhuys, and M. Bonn, *Interface-Specific Ultrafast Two-Dimensional Vibrational Spectroscopy*, *Accounts of Chemical Research* **42** (2009) 1332–1342.

[126] M. Khalil, N. Demirdöven, and A. Tokmakoff, *Obtaining Absorptive Line Shapes in Two-Dimensional Infrared Vibrational Correlation Spectra*, *Physical Review Letters* **90** (2003) 047401.

[127] S. T. Roberts, J. J. Loparo, and A. Tokmakoff, *Characterization of Spectral Diffusion from Two-Dimensional Line Shapes*, *Journal of Chemical Physics* **125** (2006) 084502.

[128] K. Lazonder, M. S. Pshenichnikov, and D. A. Wiersma, *Easy Interpretation of Optical Two-Dimensional Correlation Spectra*, *Optical Letters* **31** (2006) 3354–3356.

[129] K. Kwak, D. E. Rosenfeld, and M. D. Fayer, *Taking Apart the Two-Dimensional Infrared Vibrational Echo Spectra: More Information and Elimination of Distortions*, *The Journal of Chemical Physics* **128** (2008) 204505.

[130] K. Kwak, S. Park, I. J. Finkelstein, and M. D. Fayer, *Frequency-Frequency Correlation Functions and Apodization in Two-Dimensional Infrared Vibrational Echo Spectroscopy: A New Approach*, *The Journal of Chemical Physics* **127** (2007) 124503.

[131] M. Cho, J. Yu, T. Joo, Y. Nagasawa, S. Passino, and G. Fleming, *The Integrated Photon Echo and Solvation Dynamics*, *Journal of Physical Chemistry* **100** (1996) 11944–11953.

[132] J. Stenger, D. Madsen, P. Hamm, E. Nibbering, and T. Elsaesser, *A Photon Echo Peak Shift Study of Liquid Water*, *Journal of Physical Chemistry A* **106** (2002) 2341–2350.

[133] T. Joo, Y. Jia, J. Yu, M. Lang, and G. Fleming, *Third-Order Nonlinear Time Domain Probes of Solvation Dynamics*, *Journal of Chemical Physics* **104** (1996) 6089–6108.

[134] M. Khalil, N. Demirdöven, and A. Tokmakoff, *Vibrational Coherence Transfer Characterized with Fourier-Transform 2D IR Spectroscopy*, *The Journal of Chemical Physics* **121** (2004) 362–373.

[135] T. Brixner, J. Stenger, H. Vaswani, M. Cho, R. Blankenship, and G. Fleming, *Two-Dimensional Spectroscopy of Electronic Couplings in Photosynthesis*, *Nature* **434** (2005) 625–628.

[136] W. Zhang, T. Meier, V. Chernyak, and S. Mukamel, *Exciton-Migration and Three-Pulse Femtosecond Optical Spectroscopies of Photosynthetic Antenna Complexes*, *Journal of Chemical Physics* **108** (1998) 7763–7774.

[137] R. Costard, N. E. Levinger, E. T. J. Nibbering, and T. Elsaesser, *Ultrafast Vibrational Dynamics of Water Confined in Phospholipid Reverse Micelles*, *Journal of Physical Chemistry B* **116** (2012) 5752–5759.

[138] R. M. Hochstrasser, *Two-dimensional IR-spectroscopy: Polarization Anisotropy Effects*, *Chemical Physics* **266** (2001) 273–284.

[139] S. Woutersen and P. Hamm, *Structure Determination of Trialanine in Water using Polarization Sensitive Two-Dimensional Vibrational Spectroscopy*, *Journal of Physical Chemistry B* **104** (2000) 11316–11320.

[140] M. Zanni, N. Ge, Y. Kim, and R. Hochstrasser, *Two-Dimensional IR Spectroscopy Can Be Designed to Eliminate the Diagonal Peaks and Expose only the Crosspeaks needed for Structure Determination*, *Proceedings of the National Academy of Sciences of the United States of America* **98** (2001) 11265–11270.

[141] M. Zanni, S. Gnanakaran, J. Stenger, and R. Hochstrasser, *Heterodyned Two-Dimensional Infrared Spectroscopy of Solvent-Dependent Conformations of Acetylproline-NH_2*, *Journal of Physical Chemistry B* **105** (2001) 6520–6535.

[142] E. Fulmer, P. Mukherjee, A. Krummel, and M. Zanni, *A Pulse Sequence for Directly Measuring the Anharmonicities of Coupled Vibrations: Two-Quantum Two-Dimensional Infrared Spectroscopy*, *Journal of Chemical Physics* **120** (2004) 8067–8078.

[143] J. Faist, F. Capasso, D. L. Sivco, C. Sirtori, A. L. Hutchinson, and A. Y. Cho, *Quantum Cascade Laser*, *Science* **264** (1994) 553–556.

[144] P. Moulton, *Spectroscopic and Laser Characteristics of $Ti : Al_2O_3$*, *Journal of the Optical Society of America B - Optical Physics* **3** (1986) 125–133.

[145] R. Kaindl, M. Wurm, K. Reimann, P. Hamm, A. Weiner, and M. Woerner, *Generation, Shaping, and Characterization of Intense Femtosecond Pulses Tunable from 3 to 20 μm*, *Journal of the Optical Society of America B- Optical Physics* **17** (2000) 2086–2094.

[146] J. Midwinter and J. Warner, *Effects of Phase Matching Method and of Uniaxcial Crystal Symmetry on Polar Distribution of Second-Order Nonlinear Optical Polarisation*, *British Journal of Applied Physics* **16** (1965) 1135–1142.

[147] R. R. Alfano and S. L. Shapiro, *Observation of Self-Phase Modulation and Small-Scale Filaments in Crystals and Glasses*, *Physical Review Letters* **24** (1970) 592–594.

[148] G. Yang and Y. Shen, *Spectral Broadening of Ultrashort Pulses in a Nonlinear Medium*, *Optics Letters* **9** (1984) 510–512.

[149] P. Hamm, R. Kaindl, and J. Stenger, *Noise Suppression in Femtosecond Mid-Infrared Light Sources*, *Optics Letters* **25** (2000) 1798–1800.

[150] R. R. Ernst, G. Bodenhausen, and A. Wokaun, *Principles of Nuclear Magnetic Resonance in One and Two Dimensions*. Oxford University Press: Oxford, 1987.

[151] B. Vogelsanger, M. Andrist, and A. Bauder, *Two-Dimensional Correlation Experiments in Microwave Fourier Transform Spectroscopy*, *Chemical Physics Letters* **144** (1988) 180–186.

[152] R. F. Loring and S. Mukamel, *Selectivity in Coherent Transient Raman Measurements of Vibrational Dephasing in Liquids*, *The Journal of Chemical Physics* **83** (1985) 2116–2128.

[153] S. Mukamel, A. Piryatinski, and V. Chernyak, *Two-Dimensional Raman Echoes: Femtosecond View of Molecular Structure and Vibrational Coherence*, *Accounts of Chemical Research* **32** (1999) 145–154.

[154] Y. Tanimura and S. Mukamel, *2-Dimensional Femtosecond Vibrational Spectroscopy of Liquids*, *Journal of Chemical Physics* **99** (1993) 9496–9511.

[155] A. Tokmakoff, M. Lang, D. Larsen, G. Fleming, V. Chernyak, and S. Mukamel, *Two-Dimensional Raman Spectroscopy of Vibrational Interactions in Liquids*, *Physical Review Letters* **79** (1997) 2702–2705.

[156] A. Tokmakoff, M. Lang, D. Larsen, and G. Fleming, *Intrinsic Optical Heterodyne Detection of a Two-Dimensional Fifth Order Raman Response*, *Chemical Physics Letters* **272** (1997) 48–54.

[157] L. P. DeFlores, R. A. Nicodemus, and A. Tokmakoff, *Two Dimensonal Fourier Transform Spectroscopy in the Pump-Probe Geometry*, *Optics Letters* **32** (2007) 2966–2968.

[158] S.-H. Shim and M. T. Zanni, *How to Turn your Pump-Probe Instrument into a Multidimensional Spectrometer: 2D IR and Vis Spectroscopies via Pulse Shaping*, *Physical Chemistry Chemical Physics* **11** (2009) 748–761.

[159] W. P. de Boeij, M. S. Pshenichnikov, and D. A. Wiersma, *Heterodyne-Detected Stimulated Photon Echo: Applications to Optical Dynamics in Solution*, *Chemical Physics* **233** (1998) 287–309.

[160] L. Lepetit, G. Chériaux, and M. Joffre, *Linear Techniques of Phase Measurement by Femtosecond Spectral Interferometry for Applications in Spectroscopy*, *Journal of the Optical Society of America B* **12** (1995) 2467–2474.

[161] S. M. Gallagher, A. W. Albrecht, J. D. Hybl, B. L. Landin, B. Rajaram, and D. M. Jonas, *Heterodyne Detection of the Complete Electric Field of Femtosecond Four-Wave Mixing Signals*, *Journal of the Optical Society of America B* **15** (1998) 2338–2345.

[162] L. Lepetit, G. Cheriaux, and M. Joffre, *Linear Techniques of Phase Measurement by Femtosecond Spectral Interferometry for Applications in Spectroscopy*, *Journal of the Optical Society of America B-Optical Physics* **12** (1995) 2467–2474.

[163] M. Cowan, J. Ogilvie, and R. Miller, *Two-Dimensional Spectroscopy using Diffractive Optics Based Phased-Locked Photon Echoes* , *Chemical Physics Letters* **386** (2004) 184–189.

[164] V. I. Prokhorenko, A. Halpin, and R. J. D. Miller, *Coherently-Controlled Two-Dimensional Photon Echo Electronic Spectroscopy*, *Optics Express* **17** (2009) 9764–9779.

[165] V. Volkov, R. Schanz, and P. Hamm, *Active Phase Stabilization in Fourier-Transform Two-Dimensional Infrared Spectroscopy*, *Optics Letters* **30** (2005) 2010–2012.

[166] R. Trebino, K. DeLong, D. Fittinghoff, J. Sweetser, M. Krumbugel, B. Richman, and D. Kane, *Measuring Ultrashort Laser Pulses in the Time-Frequency Domain Using Frequency-Resolved Optical Gating*, *Review of Scientific Instruments* **68** (1997) 3277–3295.

[167] N. Demirdöven, M. Khalil, O. Golonzka, and A. Tokmakoff, *Dispersion Compensation with Optical Materials for Compression of Intense Sub-100-fs Mid-Infrared Pulses*, *Optics Letters* **27** (2002) 433–435.

[168] C. Greve, E. T. J. Nibbering, and H. Fidder, *Hydrogen-Bonding-Induced Enhancement of Fermi Resonances: A Linear IR and Nonlinear 2D-IR Study of Aniline-d5*, *The Journal of Physical Chemistry B* **117** (2013) 15843–15855.

[169] I. Yanson, A. Teplitsky, and L. Sukhodub, *Experimental Studies of Molecular-Interactions betweeen Nitrogen Bases of Nucleic Acids*, *Biopolymers* **18** (1979) 1149–1170.

[170] A. Wang, G. Ughetto, G. Quigley, T. Hakoshima, G. Vandermarel, J. Vanboom, and A. Rich, *The Molecular-Structure of a DNA Triostin-A Complex*, *Science* **225** (1984) 1115–1121.

[171] D. Gilbert, G. Vandermarel, J. Vanboom, and J. Feigon, *Unstable Hoogsteen Base-Pairs Adjacent to Echinomycin Binding-Sites Within a DNA Dublex*, *Proceedings of the National Academy of Sciences of the United States of America* **86** (1989) 3006–3010.

[172] M. P. Ball, *DNA Chemical Structure*, *http://en.wikipedia.org* (retrieved 17.04.2014).

[173] R. Wheeler, *DNA Structure Key Labelled*, *http://en.wikipedia.org* (retrieved 17.04.2014).

[174] R. Ornstein, R. Rein, D. Breen, and R. Macelroy, *Optimized Potential Function for Calculation of Nucleic-Acid Interaction Energies. I. Base Stacking*, *Biopolymers* **17** (1978) 2341–2360.

[175] R. Wing, H. Drew, T. Takano, C. Broka, S. Tanaka, K. Itakura, and R. Dickerson, *Crystal-Structure Analysis of a Complete Turn of B-DNA*, *Nature* **287** (1980) 755–758.

[176] V. Ivanov, L. Minchenk, A. Schyolki, and A. Poletaye, *Different Conformations of Double-Stranded Nucleic Acid in Solution as Revealed by Circular Dichroism*, *Biopolymers* **12** (1973) 89–110.

[177] T. Umehara, S. Kuwabara, S. Mashimo, and S. Yagihara, *Dielectric Study on Hydration of B-DNA, A-DNA, and Z-DNA*, *Biopolymers* **30** (1990) 649–656.

[178] W. Fuller, M. Wilkins, H. Wilson, and L. Hamilton, *Molecular Configuration of Deoxyribonucleic Acid. IV. X-ray Diffraction Study of A Form*, *Journal of Molecular Biology* **12** (1965) 60–76.

[179] A. Wang, G. Quigley, F. Kolpak, J. Crawford, J. Vanboom, G. Vandermarel, and A. Rich, *Molecular-Structure of a Left-Handed Double Helical DNA Fragment at Atomic Resolution*, *Nature* **282** (1979) 680–686.

[180] S. Arnott, P. Smith, and R. Chandrasekaran, *Handbook of Biochemistry and Molecular Biology 2.* CRC: Cleveland, 1976.

[181] R. Wheeler, *A-DNA, B-DNA and Z-DNA*, *http://en.wikipedia.org* (retrieved 17.04.2014).

[182] H. Drew, R. Wing, T. Takano, C. Broka, S. Tanaka, K. Itakura, and R. Dickerson, *Structure of a B-DNA Dodecamer - Conformation and Dynamics*, *Proceedings of the National Academy of Sciences of the United States of America-Biological Sciences* **78** (1981) 2179–2183.

[183] R. Dickerson and H. Drew, *Structure of a B-DNA Dodecamer II. Influence of Base Sequence on Helix Structure*, *Journal of Molecular Biology* **149** (1981) 761–786.

[184] M. Frey, T. Koetzle, M. Lehmann, and W. Hamilton, *Precision Neutron-Diffraction Structure Determination of Protein and Nucleic-Acid Components. XII. Study of Hydrogen-bonding in Purine-Pyrimidine Base Pair 9-Methyladenine·1-Methylthymine*, *Journal of Chemical Physics* **59** (1973) 915–924.

[185] S. Arai, T. Chatake, T. Ohhara, K. Kurihara, I. Tanaka, N. Suzuki, Z. Fujimoto, H. Mizuno, and N. Niimura, *Complicated Water Orientations in the Minor Groove of the B-DNA Decamer d(CCATTAATGG)(2) Observed by Neutron Diffraction Measurements*, *Nucleic Acids Research* **33** (2005) 3017–3024.

[186] M. Shotton, L. Pope, T. Forsyth, P. Langan, R. Denny, U. Giesen, M. Dauvergne, and W. Fuller, *A High-Angle Neutron Fibre Diffraction Study of the Hydration of Deuterated A-DNA*, *Biophysical Chemistry* **69** (1997) 85–96.

[187] K. M. Knee, S. B. Dixit, C. E. Aitken, S. Ponomarev, D. L. Beveridge, and I. Mukerji, *Spectroscopic and Molecular Dynamics Evidence for a Sequential Mechanism for the A-to-B Transition in DNA*, *Biophysical Journal* **95** (2008) 257–272.

[188] C. D. Bloomfield, VA and I. J. Tinoco, *Physical Chemistry of Nucleic Acids.* Harper & Row: New York, 1974.

[189] L. Biemann, T. Haeber, D. Maydt, K. Schaper, and K. Kleinermanns, *Structural Assignment of Adenine Aggregates in $CDCl_3$*, *Journal of Chemical Physics* **128** (2008).

[190] L. Biemann, T. Haeber, and K. Kleinermanns, *Fourier Transform Infrared Spectroscopy of 1-Cyclohexyluracil Aggregates in $CDCl_3$ Solutions*, *Journal of Chemical Physics* **130** (2009).

[191] N. K. Schwalb and F. Temps, *Ultrafast Electronic Relaxation in Guanosine is Promoted by Hydrogen Bonding with Cytidine*, *Journal of the American Chemical Society* **129** (2007) 9272–9273.

[192] N. K. Schwalb, T. Michalak, and F. Temps, *Ultrashort Fluorescence Lifetimes of Hydrogen-Bonded Base Pairs of Guanosine and Cytidine in Solution*, *Journal of Physical Chemistry B* **113** (2009) 16365–16376.

[193] C. Greve, N. K. Preketes, H. Fidder, R. Costard, B. Koeppe, I. A. Heisler, S. Mukamel, F. Temps, E. T. J. Nibbering, and T. Elsaesser, *N-H Stretching Excitations in Adenosine-Thymidine Base Pairs in Solution: Pair Geometries, Infrared Line Shapes, and Ultrafast Vibrational Dynamics*, *Journal of Physical Chemistry A* **117** (2013) 594–606.

[194] C. Plutzer, I. Hunig, K. Kleinermanns, E. Nir, and M. de Vries, *Pairing of Isolated Nucleobases: Double Resonance Laser Spectroscopy of Adenine-Thymine*, *ChemPhysChem* **4** (2003) 838–842.

[195] E. Nir, K. Kleinermanns, and M. de Vries, *Pairing of Isolated Nucleic-Acid Bases in the Absence of the DNA Backbone*, *Nature* **408** (2000) 949–951.

[196] F. Dong and R. Miller, *Vibrational Transition Moment Angles in Isolated Biomolecules: A Structural Tool*, *Science* **298** (2002) 1227–1230.

[197] R. Marom, U. Zecharia, S. Rosenwaks, and I. Bar, *Vibrational Overtone Spectra of N-H Stretches and Intramolecular Dynamics on the Ground and Electronically Excited States of Methylamine*, *Journal of Chemical Physics* **128** (2008) 154319.

[198] J. Pecourt, J. Peon, and B. Kohler, *DNA Excited-State Dynamics: Ultrafast Internal Conversion and Vibrational Cooling in a Series of Nucleosides*, *Journal of the America Chemical Society* **123** (2001) 10370–10378.

[199] C. Crespo-Hernandez, B. Cohen, P. Hare, and B. Kohler, *Ultrafast Excited-State Dynamics in Nucleic Acids*, *Chemical Reviews* **104** (2004) 1977–2019.

[200] C. Guerra, F. Bickelhaupt, J. Snijders, and E. Baerends, *Hydrogen Bonding in DNA Base Pairs: Reconciliation of Theory and Experiment*, *Journal of the American Chemical Society* **122** (2000) 4117–4128.

[201] C. Guerra, F. Bickelhaupt, J. Snijders, and E. Baerends, *The Nature of the Hydrogen Bond in DNA Base Pairs: The Role of Charge Transfer and Resonance Assistance*, *Chemistry-A European Journal* **5** (1999) 3581–3594.

[202] G.-x. Wang, X.-y. Ma, and J.-p. Wang, *Anharmonic Vibrational Signatures of DNA Bases and Watson-Crick Base Pairs*, *Chinese Journal of Chemical Physics* **22** (2009), no. 6 563–570.

[203] R. Franklin and R. Gosling, *The Structure of Sodium Thymonucleate Fibers. I. The Influence of Water Content*, *Acta Crystallographica* **6** (1953) 673–677.

[204] M. Falk, K. Hartman, and R. Lord, *Hydration of Deoxyribonucleic Acid III. A Spectroscopic Study of Effect of Hydration on Structure of Deoxyribonucleic Acid*, *Journal of the American Chemical Society* **85** (1963) 391–394.

[205] M. Falk, K. Hartman, and R. Lord, *Hydration of Deoxyribonucleic Acid II. An Infrared Study*, *Journal of the American Chemical Society* **85** (1963) 387–391.

[206] M. Falk, R. Lord, and K. Hartman, *Hydration of Deoxyribonucleic Acid I. A Gravimetric Study*, *Journal of the American Chemical Society* **84** (1962) 3843–3846.

[207] B. Schneider, K. Patel, and H. Berman, *Hydration of The Phosphate Group in Double-Helical DNA*, *Biophysical Journal* **75** (1998) 2422–2434.

[208] M. Kubinec and D. Wemmer, *NMR Evidence for DNA Bound Water in Solution*, *Journal of the American Chemical Society* **114** (1992) 8739–8740.

[209] P. Subramanian and D. Beveridge, *A Theoretical-Study of the Aqueous Hydration of Canonical-B D(CGCGAATTCGCG): Monte-Carlo Simulation and Comparison with Crystallographic Ordered Water Sites*, *Journal of Biomolecular Structure and Dynamics* **6** (1989) 1093–1122.

[210] M. Young, G. Ravishanker, and D. Beveridge, *A 5-Nanosecond Molecular Dynamics Trajectory for B-DNA: Analysis of Structure, Motions, and Solvation*, *Biophysical Journal* **73** (1997) 2313–2336.

[211] G. Prive, U. Heinemann, S. Chandrasegaran, L. Kan, M. Kopka, and R. Dickerson, *Helix Geometry, Hydration, and G·A Mismatch in a B-DNA Decamer*, *Science* **238** (1987) 498–504.

[212] B. Pullman, A. Pullman, H. Berthod, and N. Gresh, *Quantum-Chemical Studies of Environmental Effects on Biomolecules. VI. Ab-Initio Studies on Hydration Scheme of Phosphate Group*, *Theoretica Chimica Acta* **40** (1975) 93–111.

[213] Y. Duan, P. Wilkosz, M. Crowley, and J. Rosenberg, *Molecular Dynamics Simulation Study of DNA Dodecamer d(CGCGAATTCGCG) in Solution: Conformation and Hydration*, *Journal of Molecular Biology* **272** (1997) 553–572.

[214] B. Schneider, D. Cohen, L. Schleifer, A. Srinivasan, W. Olson, and H. Berman, *A Systematic Method for Studying the Spatial Distribution of Water Molecules around Nucleic-Acid Bases*, *Biophysical Journal* **65** (1993) 2291–2303.

[215] B. Schneider and H. Berman, *Hydration of the DNA Bases is Local*, *Biophysical Journal* **69** (1995) 2661–2669.

[216] I. Kuntz, T. Brassfie, G. Law, and G. Purcell, *Hydration of Macromolecules*, *Science* **163** (1969) 1329–1331.

[217] R. E. Dehl and C. A. J. Hoeve, *Broad-Line NMR Study of H_2O and D_2O in Collagen Fibers*, *The Journal of Chemical Physics* **50** (1969) 3245–3251.

[218] G. Edwards, C. Davis, J. Saffer, and M. Swicard, *Resonant Microwave Absorption of Selected DNA Molecules*, *Physical Review Letters* **53** (1984) 1284–1287.

[219] J. Milton and W. Galley, *Evidence for Heterogeneity in DNA-Associated Solvent Mobility From Acridine Phosphorescence Spectra*, *Biopolymers* **25** (1986) 1673–1684.

[220] L. Schreiner, M. Pintar, A. Dianoux, F. Volino, and A. Rupprecht, *Hydration of NaDNA by Neutron Quasi-Elastic Scattering*, *Biophysical Journal* **53** (1988) 119–122.

[221] V. Makarov, M. Feig, B. Andrews, and B. Pettitt, *Diffusion of Solvent Around Biomolecular Solutes: A Molecular Dynamics Simulation Study*, *Biophysical Journal* **75** (1998) 150–158.

[222] V. Denisov, K. Venu, J. Peters, H. Horlein, and B. Halle, *Orientational Disorder and Entropy of Water in Protein Cavities*, *Journal of Physical Chemistry B* **101** (1997) 9380–9389.

[223] S. Fawthrop, J. Yang, and J. Fisher, *Structural and Dynamic Studies of a Non-Self-Complementary Dodecamer DNA Dublex*, *Nucleic Acids Research* **21** (1993) 4860–4866.

[224] P. Auffinger and E. Westhof, *RNA Hydration: Three Nanoseconds of Multiple Molecular Dynamics Simulations of the Solvated tRNA(Asp) Anticodon Hairpin*, *Journal of Molecular Biology* **269** (1997) 326–341.

[225] S. Pal, J. Peon, and A. Zewail, *Ultrafast Decay and Hydration Dynamics of DNA Bases and Mimics*, *Chemical Physics Letters* **363** (2002) 57–63.

[226] S. Pal, L. Zhao, T. Xia, and A. Zewail, *Site- and Sequence-Selective Ultrafast Hydration of DNA*, *Proceedings of the National Academy of Sciences of the United States of America* **100** (2003) 13746–13751.

[227] J. T. Hynes, *Theory of Chemical Reaction Dynamics Vol . IV*, *CRC Press: Boca Raton* (1985).

[228] P. Rossky and J. Simon, *Dynamics of Chemical Processes in Polar Solvents*, *Nature* **370** (1994) 263–269.

[229] T. Chalikian, G. Plum, A. Sarvazyan, and K. Breslauer, *Influence of Drug-Binding on DNA Hydration - Acoustic and Densimetric Characterizations of Netropsin Binding to the Poly(dAdT)·Poly(dAdT) and Poly(dA)·Poly(dT) Dublexes and the Poly(dT)·Poly(dA)·Poly(dT) Triplex at 25 Degrees C*, *Biochemistry* **33** (1994) 8629–8640.

[230] M. Billeter, P. Guntert, P. Luginbuhl, and K. Wuthrich, *Hydration and DNA Recognition by Homeodomains*, *Cell* **85** (1996) 1057–1065.

[231] C. Greve and T. Elsaesser, *Ultrafast Two-Dimensional Infrared Spectroscopy of Guanine-Cytosine Base Pairs in DNA Oligomers*, *Journal of Physical Chemistry B* **117** (2013) 14009–14017.

[232] A. Paarmann, T. Hayashi, S. Mukamel, and R. J. D. Miller, *Probing Intermolecular Couplings in Liquid Water With Two-Dimensional Infrared Photon Echo Spectroscopy*, *Journal of Chemical Physics* **128** (2008).

[233] S. Woutersen, U. Emmerichs, H. Nienhuys, and H. Bakker, *Anomalous Temperature Dependence of Vibrational Lifetimes in Water and Ice*, *Physical Review Letters* **81** (1998) 1106–1109.

[234] V. Kozich, Ł. Szyc, E. T. J. Nibbering, W. Werncke, and T. Elsaesser, *Ultrafast Redistribution of Vibrational Energy After Excitation of NH Stretching Modes in DNA Oligomers*, *Chemical Physics Letters* **473** (2009) 171–175.

[235] M. Yang, Ł. Szyc, and T. Elsaesser, *Femtosecond Two-Dimensional Infrared Spectroscopy of Adenine-Thymine Base Pairs in DNA Oligomers*, *Journal of Physical Chemistry B* **115** (2011) 1262–1267.

[236] H. Fidder, M. Yang, E. T. J. Nibbering, T. Elsaesser, K. Röttger, and F. Temps, *N-H Stretching Vibrations of Guanosine-Cytidine Base Pairs in Solution: Ultrafast Dynamics, Couplings, and Line Shapes*, *Journal of Physical Chemistry A* **117** (2013) 845–854.

[237] S. Woutersen and G. Cristalli, *Strong Enhancement of Vibrational Relaxation by Watson-Crick Base Pairing*, *Journal of Chemical Physics* **121** (2004) 5381–5386.

[238] F. B. Howard, J. Frazier, and H. T. Miles, *Interbase Vibratational Coupling in G:C Polynucleotide Helices*, *Proceedings of the National Academy of Sciences of the United States of America* **64** (1969) 451–458.

[239] M. Gulotta, D. J. Goss, and M. Diem, *Conformational Studies of the Smallest Structural Motifs of DNA Detectable via Vibrational Circular Dichroism: Cytidylyl-(3'-5')-Guanosine and Guanylyl-(3'-5')-Cytidine*, *Biopolymers* **28** (1989) 2047–2058.

[240] W. Zhong, M. Gulotta, D. J. Goss, and M. Diem, *DNA Solution Conformation via Infrared Circular Dichroism: Experimental and Theoretical Results for B-Family Polymers*, *Biochemistry* **29** (1990) 7485–7491.

[241] C. Lee, K.-H. Park, and M. Cho, *Vibrational Dynamics of DNA. I. Vibrational Basis Modes and Couplings*, *Journal of Chemical Physics* **125** (2006) 114508.

[242] C. Lee, K.-H. Park, J.-A. Kim, S. Hahn, and M. Cho, *Vibrational Dynamics of DNA. III. Molecular Dynamics Simulations of DNA in Water and Theoretical Calculations of the Two-Dimensional Vibrational Spectra*, *Journal of Chemical Physics* **125** (2006) 114510.

[243] C. Lee and M. Cho, *Vibrational Dynamics of DNA : IV. Vibrational Spectroscopic Characteristics of A-, B-, and Z-form DNA's*, *Journal of Chemical Physics* **126** (2007) 145102.

[244] H. DeVoe and I. Tinoco Jr., *The Stability of Helical Polynucleotides: Base Contributions*, *Journal of Molecular Biology* **4** (1962) 500–517.

[245] Y. Kyogoku, R. Lord, and A. Rich, *An Infrared Study of Hydrogen Bonding Between Adenine and Uracil Derivatives in Chloroform Solution*, *Journal of the American Chemical Society* **89** (1967) 496–504.

[246] Y. Kyogoku, R. Lord, and A. Rich, *Hydrogen Bonding Specificity of Nucleic Acid Purines And Pyrimidines in Solution*, *Science* **154** (1966) 518–520.

[247] J. H. Miller and H. M. Sobell, *Infrared Demonstration of Hydrogen Bonding between Purine and Pyrimidine Base Analogues in Solution*, *Journal of Molecular Biology* **24** (1967) 340–350.

[248] C. Plutzer, E. Nir, M. de Vries, and K. Kleinermanns, *IR-UV Double-Resonance Spectroscopy of the Nucleobase Adenine*, *Physical Chemistry Chemical Physics* **3** (2001) 5466–5469.

[249] C. Plutzer and K. Kleinermanns, *Tautomers and Electronic States of Jet-Cooled Adenine Investigated by Double Resonance Spectroscopy*, *Physical Chemistry Chemical Physics* **4** (2002) 4877–4882.

[250] M. Kabelac, C. Plutzer, K. Kleinermanns, and P. Hobza, *Isomer Selective IR Experiments and Correlated ab Initio Quantum Chemical Calculations Support Planar H-bonded Structure of the 7-methyl Adenine···Adenine and Stacked Structure of the 9-Methyl Adenine···Adenine Base Pairs*, *Physical Chemistry Chemical Physics* **6** (2004) 2781–2785.

[251] M. Nowak, L. Lapinski, J. Kwiatkowski, and J. Leszczynski, *Molecular Structure and Infrared Spectra of Adenine. Experimental-Matrix Isolation and Density Functional Theory Study of Adenine N-15 Isotopomers*, *Journal of Physical Chemistry* **100** (1996) 3527–3534.

[252] J. R. Dwyer, J. Dreyer, E. T. J. Nibbering, and T. Elsaesser, *Ultrafast Dynamics of Vibrational N-H Stretching Excitations in the 7-Azaindole Dimer*, *Chemical Physics Letters* **432** (2006) 146–151.

[253] J. Stenger, D. Madsen, P. Hamm, E. Nibbering, and T. Elsaesser, *Ultrafast Vibrational Dephasing of Liquid Water*, *Physical Review Letters* **87** (2001) 027401.

[254] H. Torii and M. Tasumi, *Model Calculations on the Amide I Infrared Bands of Globular Proteins*, *The Journal of Chemical Physics* **96** (1992) 3379–3387.

[255] M. Child, *Local Mode Overtone Spectra*, *Accounts of Chemical Research* **18** (1985) 45–50.

[256] M. Child and L. Halonen, *Overtone Frequencies and Intensities in the Local Mode Picture*, *Advances in Chemical Physics* **57** (1984) 1–58.

[257] L. Halonen, *Local Mode Vibrations in Polyatomic Molecules*, in *Advances in Chemical Physics*, vol. 104 of *Advances in Chemical Physics*, pp. 41–179. 1998.

[258] A. Moran, J. Dreyer, and S. Mukamel, *Ab Initio Simulation of the Two-Dimensional Vibrational Spectrum of Dicarbonylacetylacetonato Rhodium(I)*, *Journal of Chemical Physics* **118** (2003) 1347–1355.

[259] R. Lemus, *Vibrational Excitations in H_2O in the Framework of a Local Model*, *Journal of Molecular Spectroscopy* **225** (2004) 73–92.

[260] D. Howard, T. Robinson, A. Fraser, and H. Kjaergaard, *The Effect of NH_2-Inversion Tunneling Splitting on the NH-Stretching Overtone Spectra of Aniline Vapour*, *Physical Chemistry Chemical Physics* **6** (2004) 719–724.

[261] B. Niefer, H. Kjaergaard, and B. Henry, *Intensity of CH-Stretching and NH-Stretching Transitions in the Overtone Spectra of Cyclopropylamine*, *Journal of Chemical Physics* **99** (1993) 5682–5700.

[262] T. Hayashi and S. Mukamel, *Multidimensional Infrared Signatures of Intramolecular Hydrogen Bonding in Malonaldehyde*, *Journal of Physical Chemistry A* **107** (2003) 9113–9131.

[263] R. D. Johnson, K. K. Irikura, R. N. Kacker, and R. Kessel, *Scaling Factors and Uncertainties for Ab Initio Anharmonic Vibrational Frequencies*, *Journal of Chemical Theory and Computation* **6** (2010) 2822–2828.

[264] J. P. Merrick, D. Moran, and L. Radom, *An Evaluation of Harmonic Vibrational Frequency Scale Factors*, *Journal of Physical Chemistry A* **111** (2007) 11683–11700.

[265] V. Barone, P. Carbonniere, and C. Pouchan, *Accurate vibrational spectra and magnetic properties of organic free radicals: The case of H_2CN*, *Journal of Chemical Physics* **122** (2005).

[266] H. G. Kjaergaard and B. R. Henry, *The Relative Intensity Contributions of Axial and Equatorial CH Bonds in the Local Mode Overtone Spectra of Cyclohexane*, *The Journal of Chemical Physics* **96** (1992) 4841–4851.

[267] F. Li and J. L. Skinner, *Infrared and Raman Line Shapes for Ice Ih. I. Dilute HOD in H_2O and D_2O*, *Journal of Chemical Physics* **132** (2010) 204505.

[268] P. Hobza and J. Šponer, *Structure, Energetics, and Dynamics of the Nucleic Acid Base Pairs: Nonempirical ab Initio Calculations*, *Chemical Reviews* **99** (1999) 3247–3276.

[269] G. M. Krishnan and O. Kuehn, *Identifying Adenine-Thymine Base Pairing by Anharmonic Analysis of the Hydrogen-Bonded NH Stretching Vibrations*, *Chemical Physics Letters* **435** (2007) 132–135.

[270] I. Shenderovich, P. Tolstoy, N. Golubev, S. Smirnov, G. Denisov, and H. Limbach, *Low-Temperature NMR Studies of the Structure and Dynamics of a Novel Series of Acid-Base complexes of HF with Collidine Exhibiting Scalar Couplings Across Hydrogen Bonds*, *Journal of the American Chemical Society* **125** (2003) 11710–11720.

[271] P. M. Tolstoy, J. Guo, B. Koeppe, N. S. Golubev, G. S. Denisov, S. N. Smirnov, and H.-H. Limbach, *Geometries and Tautomerism of OHN Hydrogen Bonds in Aprotic Solution Probed by H/D Isotope Effects on C-13 NMR Chemical Shifts*, *Journal of Physical Chemistry A* **114** (2010) 10775–10782.

[272] B. Koeppe, E. T. J. Nibbering, and P. M. Tolstoy, *NMR and FT-IR Studies on the Association of Derivatives of Thymidine, Adenosine, and 6-N-Methyl-Adenosine in Aprotic Solvents*, *Zeitschrift fur Physikalische Chemie - International Journal of Research in Physical Chemistry and Chemical Physics* **227** (2013) 723–749.

[273] A. Dunger, H. Limbach, and K. Weisz, *Geometry and Strength of Hydrogen Bonds in Complexes of 2 '-Deoxyadenosine with 2 '-Deoxyuridine*, *Journal of the American Chemical Society* **122** (2000) 10109–10114.

[274] V. Barone and M. Cossi, *Quantum Calculation of Molecular Energies and Energy Gradients in Solution by a Conductor Solvent Model*, *Journal of Physical Chemistry A* **102** (1998) 1995–2001.

[275] R. F. Ribeiro, A. V. Marenich, C. J. Cramer, and D. G. Truhlar, *The Solvation, Partitioning, Hydrogen Bonding, and Dimerization of Nucleotide Bases: a Multifaceted Challenge for Quantum Chemistry*, *Physical Chemistry Chemical Physics* **13** (2011) 10908–10922.

[276] R. Hamlin, R. Lord, and A. Rich, *Hydrogen-Bonded Dimers of Adenine and Uracil Derivatives*, *Science* **148** (1965) 1734–1737.

[277] G. Nagel and S. Hanlon, *Higher-Order Associations of Adenine and Uracil by Hydrogen-Bonding. II. Formation of Complexes in Mixed Solutions of 9-Ethyladenine and 1-Cyclohexyluracil*, *Biochemistry* **11** (1972) 823–830.

[278] V. Kozich, J. Dreyer, S. Ashihara, W. Werncke, and T. Elsaesser, *Mode-Selective O-H Stretching Relaxation in a Hydrogen Bond Studied by Ultrafast Vibrational Spectroscopy*, *Journal of Chemical Physics* **125** (2006).

[279] V. Kozich, J. Dreyer, and W. Werncke, *Mode-Selective Vibrational Redistribution after Spectrally Selective N-H Stretching Mode Excitation in Intermolecular Hydrogen Bonds*, *Journal of Chemical Physics* **130** (2009).

[280] J. Ha, H. Maris, W. Risen, J. Tauc, C. Thomsen, and Z. Vardeny, *Observation of Molecular Vibrations in Real Time*, *Physical Review Letters* **57** (1986) 3302–3302.

[281] M. Rosker, F. Wise, and C. Tang, *Femtosecond Relaxation Dynamics of Large Molecules*, *Physical Review Letters* **57** (1986) 321–324.

[282] K. A. Nelson and L. R. Williams, *Femtosecond Time-Resolved Observation of Coherent Molecular Vibrational Motion*, *Physical Review Letters* **58** (1987) 745–745.

[283] D. Madsen, J. Stenger, J. Dreyer, E. T. Nibbering, P. Hamm, and T. Elsaesser, *Coherent Vibrational Ground-State Dynamics of an Intramolecular Hydrogen Bond*, *Chemical Physics Letters* **341** (2001) 56–62.

[284] K. Heyne, N. Huse, J. Dreyer, E. T. J. Nibbering, T. Elsaesser, and S. Mukamel, *Coherent Low-Frequency Motions of Hydrogen Bonded Acetic Acid Dimers in the Liquid Phase*, *The Journal of Chemical Physics* **121** (2004) 902–913.

[285] N. Huse, B. Bruner, M. Cowan, J. Dreyer, E. Nibbering, R. Miller, and T. Elsaesser, *Anharmonic Couplings Underlying the Ultrafast Vibrational Dynamics of Hydrogen Bonds in Liquids*, *Physical Review Letters* **95** (2005) 147402.

[286] Ł. Szyc, J. Guo, M. Yang, J. Dreyer, P. M. Tolstoy, E. T. J. Nibbering, B. Czarnik-Matusewicz, T. Elsaesser, and H.-H. Limbach, *The Hydrogen-Bonded 2-Pyridone Dimer Model System. 1. Combined NMR and FT-IR Spectroscopy Study*, *Journal of Physical Chemistry A* **114** (2010) 7749–7760.

[287] M. Yang, Ł. Szyc, J. Dreyer, E. T. J. Nibbering, and T. Elsaesser, *The Hydrogen-Bonded 2-Pyridone Dimer Model System. 2. Femtosecond Mid-Infrared Pump-Probe Study*, *Journal of Physical Chemistry A* **114** (2010) 12195–12201.

[288] L. Halonen and T. Carrington, *Fermi Resonances and Local Modes in Water, Hydrogen-Sulfide, and Hydrogen Selenide*, *Journal of Chemical Physics* **88** (1988) 4171–4185.

[289] J. Dreyer, *Unraveling the Structure of Hydrogen Bond Stretching Mode Infrared Absorption Bands: An Anharmonic Density Functional Theory Study on 7-Azaindole Dimers*, *Journal of Chemical Physics* **127** (2007).

[290] C. Sandorfy, *Hydrogen Bonding: How Much Anharmonicity?*, *Journal of Molecular Structure* **790** (2006) 50–54.

[291] J. R. Dwyer, L. Szyc, E. T. J. Nibbering, and T. Elsaesser, *Ultrafast Vibrational Dynamics of Adenine-Thymine Base Pairs in DNA Oligomers*, *Journal of Physical Chemistry B* **112** (2008) 11194–11197.

[292] K. Tanaka and Y. Okahata, *A DNA-Lipid Complex in Organic Media and Formation of an Aligned Cast Film*, *Journal of the American Chemical Society* **118** (1996) 10679–10683.

[293] J. R. Dwyer, L. Szyc, E. T. J. Nibbering, and T. Elsaesser, *Note: An Environmental Cell for Transient Spectroscopy on Solid Samples in Controlled Atmospheres*, *Review of Scientific Instruments* **84** (2013).

[294] C. Yang, D. Moses, and A. Heeger, *Base-Pair Stacking in Oriented Films of DNA-Surfactant complex*, *Advanced Materials* **15** (2003) 1364–1367.

[295] S. Arnott and E. Selsing, *Structure of Polydeoxygluanylic Acid Polydeoxycytidylic Acid*, *Journal of Molecular Biology* **88** (1974) 551–552.

[296] M. Falk, A. Poole, and C. Goymour, *Infrared Study of State of Water in Hydration Shell of DNA*, *Canadian Journal of Chemistry* **48** (1970) 1536–1542.

[297] R. Costard, C. Greve, I. A. Heisler, and T. Elsaesser, *Ultrafast Energy Redistribution in Local Hydration Shells of Phospholipids: A Two-Dimensional Infrared Study*, *Journal of Physical Chemistry Letters* **3** (2012) 3646–3651.

[298] T. L. C. Jansen, B. M. Auer, M. Yang, and J. L. Skinner, *Two-Dimensional Infrared Spectroscopy and Ultrafast Anisotropy Decay of Water*, *Journal of Chemical Physics* **132** (2010).

[299] S. Woutersen and H. Bakker, *Resonant Intermolecular Transfer of Vibrational Energy in Liquid Water*, *Nature* **402** (1999) 507–509.

[300] W. Tzeng, K. Narayanan, K. Shieh, and C. Tung, *A Study of the Structures and Vibrations of $C_6H_5NH_2$, C_6H_5NHD, $C_6H_5ND_2$, $C_6D_5NH_2$, C_6D_5NHD, and $C_6D_5ND_2$ in the S_1 State by Ab Initio Calculations*, *Journal of Molecular Structure: THEOCHEM* **428** (1998) 231–240.

[301] J. Lady and K. Whetsel, *New Assignments for First Overtone N-H and N-D Stretching Bands of Anilines and Effect of Intramolecular Hydrogen Bonding on Anharmonicities of N-H Vibrations*, *Spectrochimica Acta* **21** (1965) 1669–1679.

Selbstständigkeitserklärung

Ich erkläre hiermit, dass ich die vorliegende Arbeit selbständig und nur unter Verwendung der angegebenen Literatur und Hilfsmittel angefertigt habe.

Ich habe mich anderwärts nicht um einen Doktorgrad beworben und besitze keinen entsprechenden Doktorgrad.

Desweiteren erkläre ich die Kenntnisnahme der dem Verfahren zugrunde liegenden Promotionsordnung der Mathematisch-Naturwissenschaftlichen Fakultät der Humboldt-Universität zu Berlin.

Berlin, den 10.05.14

Danksagung

Mein besonderer Dank geht an **Prof. Dr. Thomas Elsässer** für die Möglichkeit, diese Arbeit im Max-Born-Institut für Kurzzeitdynamik und nichtlineare Spektroskopie in Berlin anfertigen zu können und so ein sehr vielseitiges und für mich anfangs weitgehend unbekanntes Gebiet der Physik kennenzulernen. Diverse hilfreiche und zielführende Gespräche sowie eine kritische Lektüre dieser Abhandlung haben entscheidend zum Gelingen dieser Arbeit beigetragen.

Weiterhin danke ich **Dr. Erik Nibbering** für die gute Zusammenarbeit, unzählige erhellende wissenschaftliche Gespräche sowie seine Hilfe bei organisatorischen Problemen.

I am particularly indebted to **Dr. Henk Fidder** for his precise and engaged scientific work. Thank you for uncountable very interesting and fruitful discussions and for giving very helpful comments to my thesis, I enjoyed working with you very much.

Dr. René Costard danke ich für das Beitragen der wichtigen Zwei-Farben Pump-Probe-Messungen und seine Einführung in den praktischen Umgang mit nichtlinearer Optik und zeitaufgelösten Pump-Probe Messungen zu Beginn meiner Arbeit am MBI. Thank you **Dr. Nicholas K. Preketes** for doing a great job on the ab initio calculations. Moreover, I want to thank **Dr. Ismael Heisler** for his important contributions in the programming of labview and for the very productive and pleasant cooperation. Moreover, I thank **Dr. Ming Yang** for his introduction into the 2D world at the beginning of my thesis and help with experimental problems. **Dr. Łukas Szyc** danke ich für seine entscheidende Hilfe und Wissensweitergabe zur DNA-Probenherstellung, für interessante Gespräche und die angenehme, kollegiale Zusammenarbeit. **Dr. Thorsten Siebert** und **Dr. Benjamin Fingerhut** danke ich für viele interessante Diskussionen und Feedback zu Teilen dieser Arbeit. **Dr. Benjamin Köppe** danke ich für den Beitrag der NMR Messungen, unzählige Diskussionen über NMR Spektroskopie und die angenehme gemeinsame Zeit im Büro mit verschiedensten Unterhaltungen auch abseits der Physik.

Besonderer Dank geht außerdem an **Tobias Tyborski**, **Sebastian Friede**, **Dr. Vincent Juvé**, **Bastian Borchers**, **Simon Birkholz** und **Dr. Mirabelle Premont-Schwarz** für viele interessante Diskussionen und die unterhaltsame Zeit abseits des MBI und beim Mittagessen. Thank you also to **Micheline Soley** for your endurance and patience in teaching me the fine details of **E**nglish grammar and the interesting exchange of thoughts on various social and political subjects. Mein Dank gilt weiterhin diversen technischen Mitarbeitern des MBI, insbesondere **Regina Lendt, Regina Goleschny, Peter Scholze** sowie **Helmut Walz** für ihre stetige Bereitschaft, im Chemielabor oder bei Bestellungen zu helfen bzw. die schnelle Hilfe bei Problemen in der Werkstatt oder mit Elektronikkomponenten.

Inbesondere danke ich sehr **meiner Familie**, die mich zu jeder Zeit perfekt unterstützt hat, sowie diversen Personen aus meinem privaten Umfeld, die einen wunderbaren Gegenpol zur wissenschaftlichen Arbeit darstellen.